SOLAR-TERRESTRIAL PHYSICS

Founders: Institute of Solar-Terrestrial Physics of Siberian Branch of Russian Academy of Sciences
Siberian Branch of the Russian Academy of Sciences

CONTENTS

20th Annual Conference "Plasma Physics in the Solar System"
February 10–14, 2025, Space Research Institute RAS

15th Russian-Chinese Workshop on Space Weather,
September 9–13, 2024, Institute of Solar-Terrestrial Physics SB RAS

PROCESSES OF ACCELERATION AND TRANSFER
OF ELECTRONS IN A PULSE CIRCULAR RIBBON FLARE

A.T. Altyntsev (iD)
Institute of Solar-Terrestrial Physics SB RAS,
Irkutsk, Russia, altyntsev@iszf.irk.ru

N.S. Meshalkina (iD)
Institute of Solar-Terrestrial Physics SB RAS,
Irkutsk, Russia, nata@iszf.irk.ru

S.A. Anfinogentov
Institute of Solar-Terrestrial Physics SB RAS,
Irkutsk, Russia, anfinogentov@iszf.irk.ru

D.A. Zhdanov
Institute of Solar-Terrestrial Physics SB RAS,
Irkutsk, Russia, zhdanov@iszf.irk.ru

I.I. Myshyakov (iD)
Institute of Solar-Terrestrial Physics SB RAS,
Irkutsk, Russia, ivan_m@iszf.irk.ru

E.F. Ivanov (iD)
Institute of Solar-Terrestrial Physics SB RAS,
Irkutsk, Russia, eugenessrt@gmail.com

Chengming Tan
State Key Laboratory of Solar Activity and Space Weather,
National Space Science Center CAS,
Beijing, China, tanchengming@nssc.ac.cn

Zhao Wu
School of Space Science and Physics,
Shandong University,
Weihai, China, wuzhao@sdu.edu.cn
Laboratory for Electromagnetic Detection,
Institute of Space Sciences,
Shandong University,
Weihai, China

Abstract. We discuss acceleration and transport of electrons in the circular flare SOL2024-03-25T06:37:00 of the M4.4 X-ray class, characterized by a record-short duration of hard X-ray emission pulse. We have used radio data in the 0.1–40 GHz range, including images of the flare region in the Siberian Radio Heliograph frequency range. Microwave and hard X-ray emissions are generated in the vicinity of the magnetic domain by the interaction of ropes visible at 1600 Å. The impulsive stage ended with a short peak <5 s long, recorded simultaneously at 35 GHz and in the 100–300 keV range. After the peak, a long loop in the ultraviolet (UV) rises and a broad plasma ejection appears which is directed along the outer spine observed before the flare. Large loops connect the spine and the remote source. There is a broadband microwave source at the remote footpoint at 215 arcsec, with the delay of its maximum from the peak in the flare core being ~5 s, and the electron prop- agation velocity along the large loops estimated at one-third of the velocity of light. A distinctive feature of the radiation of the remote source was high degree of its circular polarization. The meter flare emission indicates that tops of large loops are filled with non-thermal electrons with large pitch angles. The set of spatial, spectral, and polarization characteristics of microwave sources obtained for the first time is discussed in the context of the known results on the nature of circular ribbon flares.

Keywords: Sun, acceleration mechanisms, microwave bursts, meter bursts, circle ribbon flare.

INTRODUCTION

Recent observations have revealed that among main flares are circular ribbon ones, which occur in a special magnetic configuration with a photospheric magnetic field domain included in an area with fields of opposite magnetic polarity. Above such a domain is a dome separatrix surface at the top of which there is a point with a null magnetic field [Priest, Titov, 1996; Masson et al., 2009; Sun et al., 2013]. From this point, the so-called spines extend into the dome and up from it. Magnetic field vectors in the vicinity of the spines are directed along them and are opposite in sign. The fields near the inner spine are directed away from the photosphere from the center of the domain, and the fields in the vi-

cinity of the outer spine are manifested in EUV (extreme ultraviolet) observations as large-scale loops whose remote footpoints are closed on regions of the photosphere with vertical fields of the same sign as the domain field. The remote footpoints of these loops can be located hundreds of arcsec away from the domain, i.e. from the flare core. Circular ribbon flares are often accompanied by coronal jets, type III radio bursts, coronal mass ejections, shock waves, coronal dimmings, and kink oscillations of coronal loops and filaments (see, for example, the recent review [Zhang, 2024]).

The energy release of circular flares is assumed to occur in the magnetic reconnection processes not only during the interaction between structures within the domain, but also in current sheets formed on separatrix surfaces near the null point [Pontin et al., 2013]. Anoth-

er feature of circular flares is the response to energy release in the flare core in remote sources. The energy for their activation in EUV and radio emissions is transferred by particles and waves. In the case of plasma ejections, the features of circular flares are related to their closed dome magnetic structure. Plasma ejections should be accompanied by a significant change in the topology of the magnetic field above the domain.

One of the underexplored questions in physics of circular flares is the acceleration and transport of particles in the fundamentally three-dimensional topology of energy release regions. To study the processes of electron acceleration, it is natural to use radio data that allows us to record non-thermal electron fluxes in coronal magnetic structures with a plasma density insufficient to detect the free-free X-ray emission of nonthermal electrons. To date, there are relatively few publications on the results of radio observations of circular flares. Meshalkina et al. [2009] discussed the configuration and scenario of two such flares, which were mapped by the Nobeyama Radioheliograph (NoRH [Torii et al., 1979]) at 17 and 34 GHz. The flares under study were driven by the interaction between magnetic ropes located inside the dome separatrix surface. The response to electron acceleration during a flare was ~1 min pulse of hard X-ray emission in the 50–100 keV channel of the satellite RHESSI (Reuven Ramaty High Energy Solar Spectroscopic Imager) and microwave emission at 17 GHz. At that time in the microwave emission there was a remote source with a high degree of circular polarization (up to 50 %) located 120 arcsec from the flare core. The polarization sign of the emission from the remote source corresponded to an extraordinary wave. In the flare examined in [Altyntsev et al., 2022], ~8 s oscillations of microwave emission at a frequency of 5.7 GHz were observed both in the remote source and in the flare core. The emission oscillations in the flare core were explained by modulation of the acceleration process during the interaction between current ropes inside the domain, and the response in the source that was 60 arcsec away was caused by nonthermal electrons coming from the core at a velocity of $(1.5 \div 2)10^{10}$ cm/s.

A flare with another driver — magnetic reconnection in the vicinity of the null point — has been discussed in [Kumar et al., 2016]. During the flare, ~3 min quasi-periodic pulsations of hard X-ray and microwave emissions were recorded. The authors believe that the oscillations were triggered by variations in electron acceleration in the vicinity of the null point. In that event, the remote source was not identified.

Microwave sources in the circular ribbon flare SOL2014-12-17T04:51 of the M8.7 X-ray class have been examined in more detail [Chen et al., 2019; Lee et al., 2020]. In addition to AIA/SDO data, sequences of radio maps from MUSER (MingantU SpEctral Radioheliograph) [Yan et al., 2009], available in the 1–2 GHz range, and NoRH [Nakajima et al., 1994] were used to study the dynamics of the flare structure. Comparison of fluxes at frequencies of 17 and 34 GHz has shown that at the beginning of the flare the increase in radio emission can be explained by thermal heating of plasma in-

side the magnetic domain due to reconnection at the magnetic null point. Signs of nonthermal energy release appear during a stepwise increase in the microwave flux a few minutes before the impulsive phase. During the impulsive phase lasting ~10 min, the emission from the rope inside the dome dominates, microwave sources with circular polarization of opposite signs appearing near the rope's footpoints. The remote source was observed on the maps at a frequency of 17 GHz, yet the impulsive phase does not show up in the emission intensity profile of the remote source. The emission flux from the remote source increased gradually during the flare, similar to the increase in EUV emission. This allowed the authors to assume that the microwave emission from a remote source is generated by a bremsstrahlung mechanism. It follows from MUSER maps that the sources emitting at 1.2–2.0 GHz were located above the null point of the magnetic domain.

In our work, we discuss the scenario and dynamics of electron acceleration and transport during the circular flare SOL2024-03-25T06:37 of the M4.4 X-ray class, characterized by a record-short duration of hard emission (~5 s at half-height in the 100–300 keV channel).

INSTRUMENTS

AIA/SDO UV and EUV images and SDO HMI (Helioseismic and Magnetic Imager) magnetograms have been employed to analyze the dynamics of the spatial structure of the flare [Lemen et al., 2012]. Note that the ~12 s periodicity of AIA/SDO observations is insufficient to observe the dynamics of this flare. Moreover, almost all images in all AIA channels were overexposed just during the flare energy release pulse.

Microwave sources were observed by three antenna arrays of the Siberian Radioheliograph (SRH) [Lesovoi et al., 2014; Lesovoi, Kobets, 2017; Altyntsev et al., 2020]. The mapping was carried out by frequency scanning independently in each range (3–6, 6–12, 12–24 GHz) at an interval of 3.5 s. The spatial resolution of the mapping depends on the frequency and local time of observations. In this work, we have used frequencies from 2.8 to 12.2 GHz with beamwidths varying from 23×83 to 10×18 arcsec. Anfinogentov's software package was employed to construct the images [https://radiomag.iszf.irk.ru/books/sibirskii-radiogeliograf/page/sintez-radioizobrazenii-s-pomoshhiu-paketa-srh-synth]. To analyze time profiles of radio emission, we used measurements of the total SRH flux [https://badary.iszf.irk.ru/srhCorrPlot.php].

Integral solar radio emission spectra were measured with a time resolution of 1 s by NoRP (Nobeyama Radio Polarimeters) [Torii et al., 1979] at five frequencies in the range 1.0–17.0 GHz, the Badary Broadband Microwave Spectropolarimeter (BBMS), [Zhdanov, Zandanov, 2011] at 26 frequencies in the range 4–8 GHz.

In our study, we have used spectra from the 50–3000 MHz SRH spectropolarimeter SOLARSPEL with a time resolution of 0.5 s and a frequency resolution of 1 MHz.

Fluxes at high frequencies 35.25–39.75 GHz were available during the impulsive phase in observations

from CBS (Chashan Broadband Solar millimeter spectrometer) [Shang et al., 2022, 2023], recording the dynamic spectrum in the range 35–40 GHz. We utilized data with a frequency resolution of 0.5 GHz and a time resolution of 0.537 s.

Integral spectra in the range 1.6–2.0 GHz were obtained with the radio interferometer MUSER-I (China). The MUSER-I frequency range covers 0.4–2.0 GHz [Yan et al., 2016]. The March 25, 2024 event was observed in the left circular polarization with a spectral resolution of 16 MHz and a time resolution of 3.125 ms.

We also employed data from the radio telescope in Learmonth (Australia), which overlaps in time with other radio data. The telescope is part of RSTN (United States Air Force Radio Solar Telescope Network) [Guidice et al., 1981] whose instruments measure intensity at eight frequencies (245, 410, 610, 1415, 2695, 4995, 8800, and 15400 MHz) with a resolution of 1 s.

Hard X-ray fluxes were measured using Fermi/GBM (Fermi Gamma-Ray Burst Monitor) [Meegan et al., 2009] with a time resolution of 1 s.

OBSERVATIONS

The magnetic structure with domain, isolated by a compact region of a positive vertical field, surrounded by fields of reverse polarity, was formed in the southern part of active region (AR) 13615 on March 24. In AIA/SDO images in EUV lines from 10:00 UT on March 24, 2024, a ring structure appeared around the domain and at times a jet is seen moving away from this structure in a southerly direction. This configuration can be traced continuously until 00:00 UT on March 26, when the domain of the positive field is significantly reduced in size, and the ring structure in EUV lines disappears. No large flares, except for the event under study, were observed during these days.

Figure 1 shows three time points of AR evolution in the vicinity of the magnetic domain. The time hereafter is given in UT. The magnetic structure is seen to develop over time: on March 24, a fragment begins to stand out in the north of the domain, and it separated on the day of the flare. By March 26, this fragment had moved away to the north, and another fragment had separated to the west.

An M4.4 X-ray flare occurred in this structure on March 25, 2024. Soft X-ray emission began to increase at 06:37, and ceased to decrease at 06:48. The peak of the impulsive phase, when a short pulse of hard X-ray emission with photon energy above 100 keV was observed, was recorded at 06:43:24. During the flare, AR
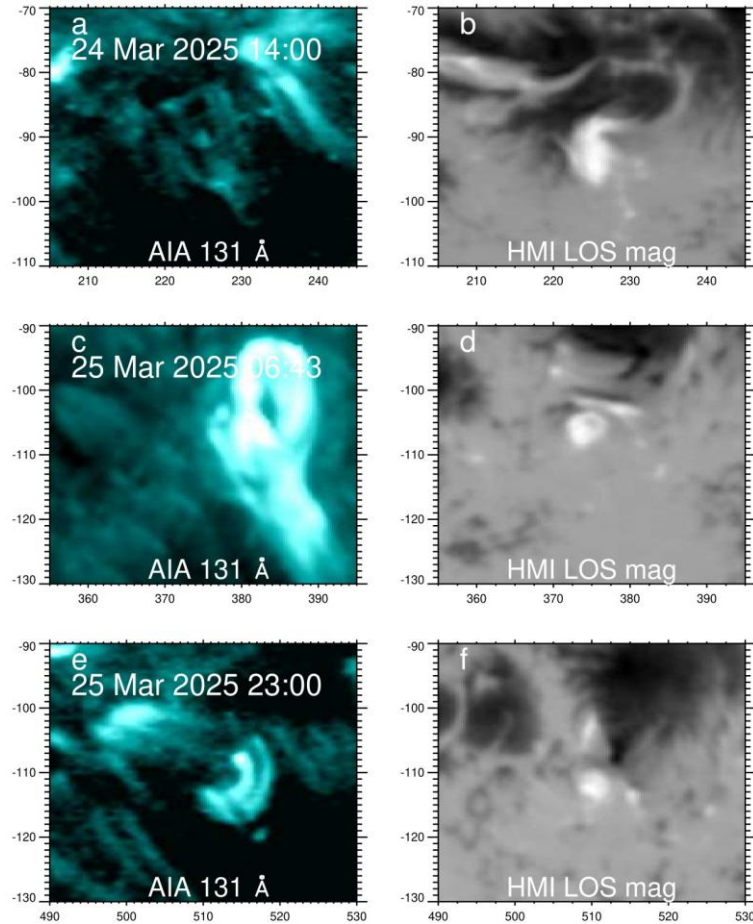

Figure 1. AIA/SDO images in the 131 Å channel at different time points (on the left) and SDO/HMI magnetograms at the time points closest to those indicated in the left column (on the right). On the axes are arcseconds relative to the center of the solar disk

was located in the central part of the solar disk. The flare is noted for its high brightness in all AIA/SDO UV and EUV ranges.

Sequences of not overexposed EUV images in the 304 and 131 Å lines during the impulsive phase are shown in Figure 2. At the first two time points, the flare structures have a loop-like shape. Note that a narrow jet extending southward in the plane of the sky was observed for the first time in the 171 Å line at 06:40:57. The jet's brightness and length, which can be considered as a manifestation of the outer spine of the magnetic structure, began to increase after 06:42. Between 06:43:17 and 06:43:30, the jet's transverse size increased significantly, indicating a modification of the magnetic structure near the zero point and the outer spine. Then, the bright region of plasma ejection expanded, with marked fragments elongated along the magnetic field.

The ejection plasma filled large-scale loops, which became visible in EUV emission 4 min after the start of the ejection (Figure 3). In panel *a* at footpoints of large loops, contours depict microwave sources emitting at the maximum of the microwave flux (06:43:24) at a frequency of 8 GHz. In the flare core there is a structure characteristic of a magnetic flux rope: a source in intensity along the edges of which there are sources with different circular polarization. The remote footpoints of the loops were located at a distance of ~215 arcsec east of the flare core in the region with northward magnetic field. Panel *b* shows magnetic field lines calculated by the Green function method in a potential approximation from the HMI/SDO vector magnetogram for 06:48 UT. There is a good agreement between the observed and calculated structures, which allows us to use the calculation results to estimate plasma and magnetic field parameters in large loops.

Let us take a closer look at the structure of the flare core. Figure 4 displays the image in the 131 Å line at 06:43:18 a few seconds before the peak of the hard X-ray emission (*a*); the magnetogram of the longitudinal magnetic field and the image of the flare core in the 1600 Å line at 06:43:26 (*b*). The domain field was positive, its value reached 800 G. The flare was probably
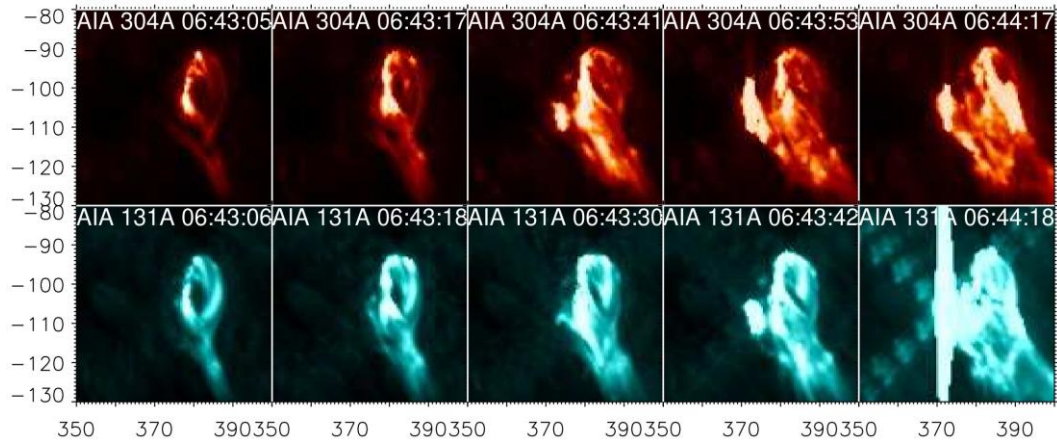
Figure 2. Sequences of images of the flare core in the 304 Å and 131 Å lines. The time is given in UT. The image size is 50×50 arcsec. Image centers are 378/–104 arcsec from the center of the solar disk
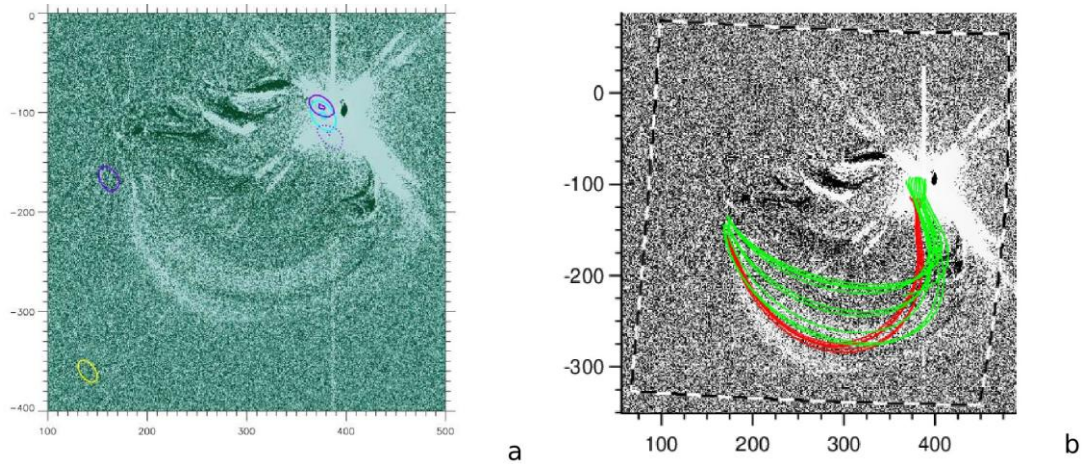
Figure 3. Flare region with a remote source: *a* is the difference image at 06:46 in the 94 Å line. The 06:41 image is subtracted. The contours at the levels (0.5, 0.95) from the maximum/minimum indicate microwave sources. Blue contours show the intensity at a frequency of 8 GHz (SRH); purple, circular polarization: solid contour is the right circular polarization (RCP); dotted, the left circular polarization (LCP). The yellow oval in the lower left corner is the antenna beamwidth at 8 GHz, its size is 15×25 arcsec; green and red lines denote the magnetic field lines calculated in a potential approximation (*b*). The black and white contour is the boundary of the computational domain. The background is a difference image from the left figure

6
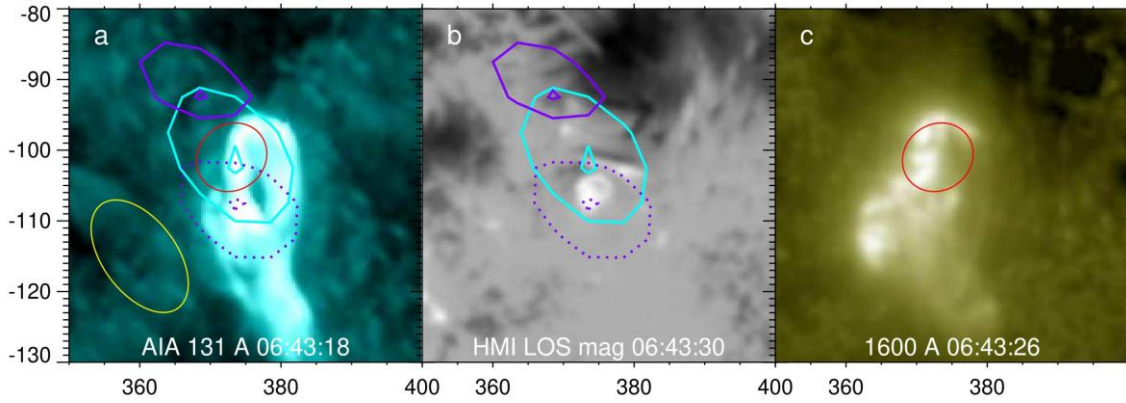
Figure 4. Flare region structure in the 131 Å line at 06:43:18 (*a*); longitudinal magnetic field magnetogram at 06:43:30 (*b*); an image in the 1600 Å line (*c*). The red oval in panels *a*, *c* marks a real source with dimensions 9.3×10.4 arcsec after deconvolution with antenna beamwidth at 12 GHz. The yellow oval in the lower left corner indicates the antenna beamwidth 10.5×18.3 arcsec at 12 GHz. Contours in *a* and *b* outline microwave sources at a frequency of 12 GHz at 06:43:24 in intensity (R+L, blue contour), and polarization (purple contour; solid — RCP (0.5, 0.95 from maximum); dotted — LCP (0.5, 0.95 from minimum))

initiated by separation of a small fragment from the northern part of the domain (see Figure 1, *d*). In EUV emission there is a ring structure in which the brightness depression corresponds to the location of the magnetic domain. The ring's size and shapes are similar in different EUV ranges. In the south, the ring is bordered by a bright region of plasma outflow along the magnetic field lines in the vicinity of the outer spine.

Contours show microwave sources in intensity and polarized microwave emission at a frequency of 12.2 GHz. In the lower left corner, the yellow contour outlines an oval that corresponds to the half-height of the antenna beamwidth. The size of the beamwidth is comparable to the size of the sources. The result of deconvolution under the assumption that the shapes of the pattern and the source are two-dimensional Gaussian functions is depicted by the red oval in panels *a*, *c*. Note that the location of the center of brightness of the microwave source remains unchanged in time. At the edges of the center of brightness in intensity (blue contour) there are sources with opposite directions of circular polarization (purple contours), i.e. the microwave emission structure indicates the existence of loops or ropes.

Panel *c* presents an image in the AIA 1600 Å range almost at the maximum of hard X-ray emission. The main radio source is seen to be above a part of a long flux rope located near the magnetic field domain and extended northwestward. In UV emission, as in EUV emission, southward plasma flow is observed, but the transverse size of the flow has become much wider.

The time profiles of electromagnetic emission of nonthermal electrons accelerated during the flare are presented in Figure 5. High energies of the accelerated electrons are indicated by the microwave emission, recorded with CBS at 35–40 GHz, and by hard X-ray emission, recorded with the FERMI/GBM spectrometer in the 100–300 keV channel. Measurements of the integral solar flux by SRH antennas with a resolution of 3.5 s are given for frequencies of 2.8, 8, and 23.4 GHz. Triangles mark the times of recording at these frequencies. Fluxes at 17 (NoRP), 8.1 GHz (BBMS), and hard X-ray emission intensity (FERMI/GBM) were measured with a resolution of 1 s. The Chinese spectrometer CBS had

the best time resolution of 0.5 s.

A noticeable increase in flare emission begins at about 06:42:48 (dash-dotted line) at frequencies below 8 GHz at photon energies below 20 keV. After 16 s at photon energies to 50 keV, the emission in the range 8–17 GHz begins to increase, reaching a local intensity maximum in 9 s at 06:43:13. In the channels recording harder emissions, the signal begins to grow a few seconds later, at 06:43:19 (dash-dotted line) and reaches a maximum in 5.5 s. In channels of 35 GHz and >50 keV, the signal decreases most rapidly, for 2–3 s, and then the rate of decrease slows down. At the same time, in the top panels of Figure 5, which show the emission of lower-energy electrons, the intensity of signals increases rather than decreases after a pulse of hard emission. Notice that pulses of microwave and hard X-ray emissions are observed at the front of increasing soft X-ray emission whose maximum was recorded at 06:44:35, i.e. more than 1 min later. A similar dependence is characteristic of the Neupert effect when soft X-ray emission is generated by plasma heated by accelerated electron fluxes.

As shown above (see Figure 4, *c*), the microwave source is projected onto a long rope observed in the range of 1600 Å. The dynamics of rope formation can be traced in the images in Figure 6. It can be seen (top row) that before the impulsive phase there are two ropes extended one after another in a northwesterly direction. In the region, where their footpoints approach each other, there is a bright region that rises slightly upward during the impulsive phase. During this phase (middle row), the brightness is distributed along the emerging common flux rope and the region of plasma outflow widens. After the impulsive phase (bottom row), the plasma flow region expands to the length of the rope. The velocity of the leading front of the flow can be estimated from the images in the bottom row as 330 km/s in the plane of the sky.

SRH observations allowed us to identify microwave fluxes from the flare core and remote source. With a distance of 215 arcsec between the sources, the delay between maxima of the time profiles of these sources is ~5 s. Spectra of the sources at the maximum of the impulsive phase are presented in Figure 7, *a*.
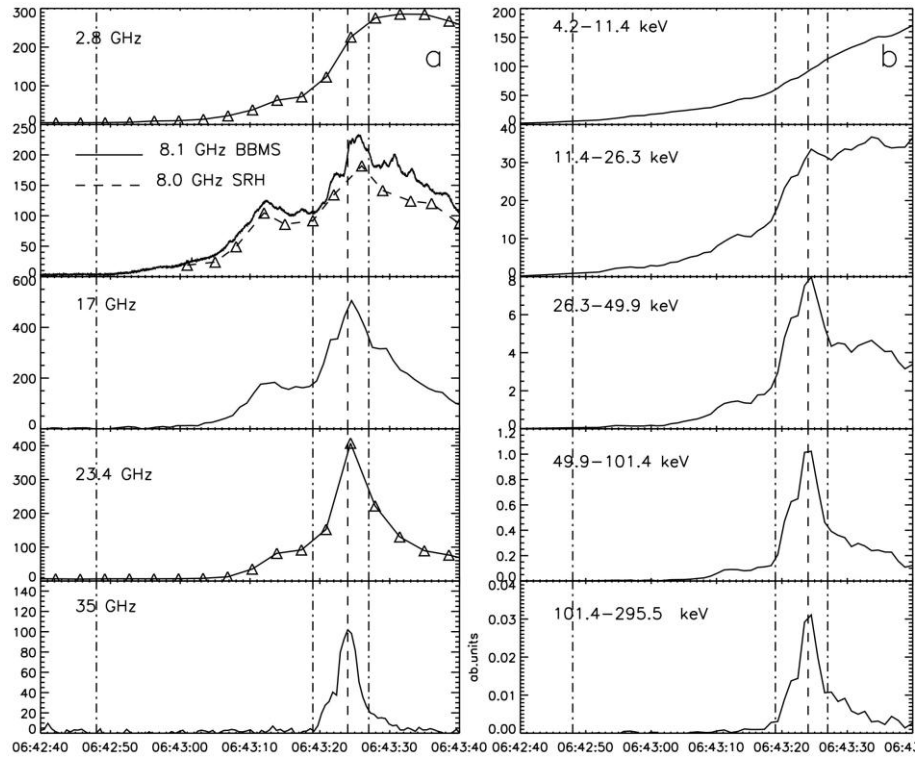
Figure 5. Time profiles of microwave (*a*) and hard X-ray (*b*) emissions. Receiving frequencies and channel boundaries in energies are shown. The instruments in use and the time resolution of the measurements are described in the text. Triangles mark measurement time points at these frequencies in SRH curves of 2.8, 8, and 23.4 GHz. The time points 06:42:48, 06:43:19, 06:43:28 are indicated by vertical dash-dotted lines. The dashed line is the peak of hard X-ray emission at 06:43:24
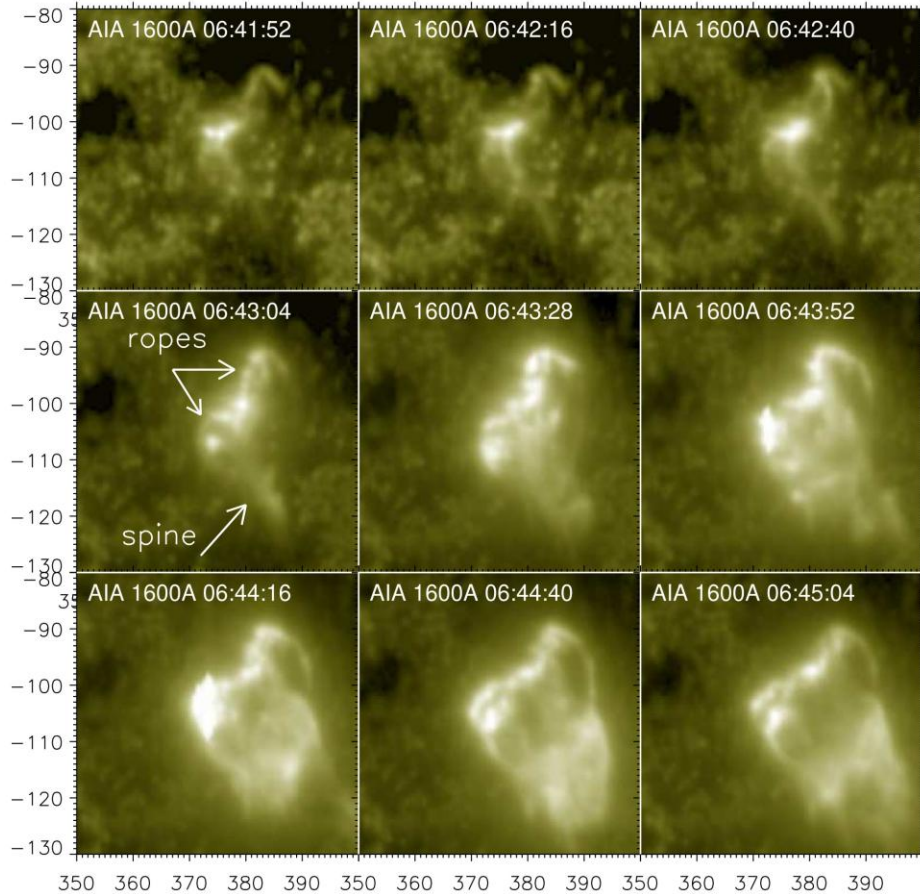
Figure 6. Development of the rope in the flare region; images in the AIA/SDO 1600 Å channel at different time points
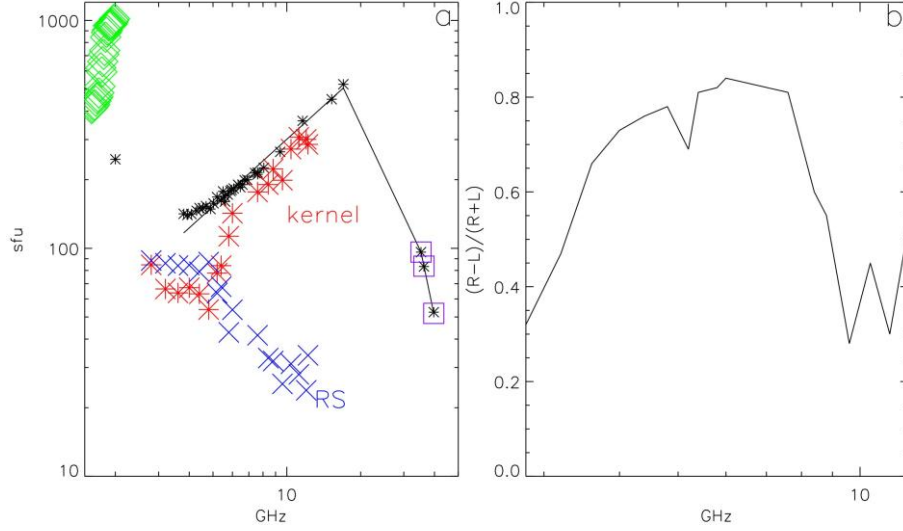
Figure 7. Composite spectrum at the peak of the flare at 06:43:25 (*a*). Red asterisks indicate SRH data, fluxes are collected from images in the flare core; blue crosses, in a remote source; black asterisks mark the integral spectrum from SRH, BBMS, NoRP data; black asterisks in purple squares, CBS data; green rhombs, MUSER-I data. Spectrum of the degree of polarization for a remote source (*b*)
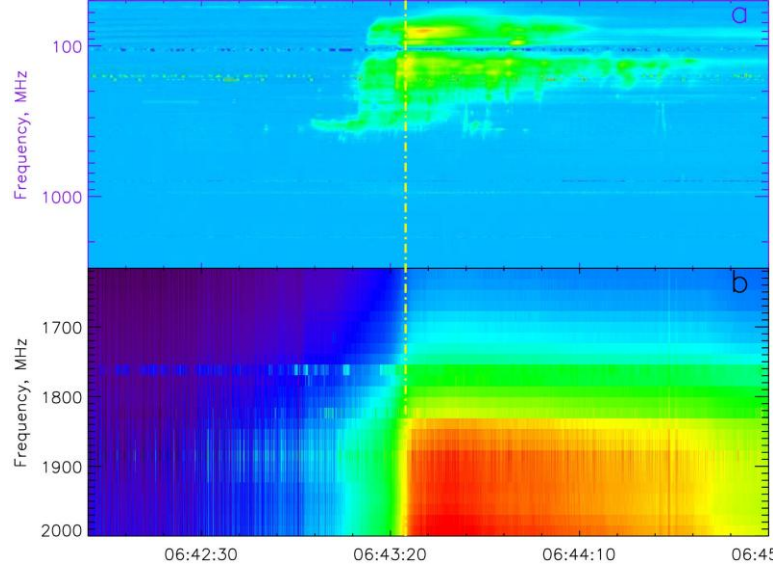
Figure 8. Dynamic spectrum: *a* — data from the 50–3000 MHz SOLARSPEL spectropolarimeter; *b* — MUSER-I data. The vertical line indicates the peak of the hard X-ray emission at 06:43:24

Black asterisks represent the integral flux spectrum from BBMS (4–8 GHz), SRH (11.6 and 15.24 GHz), NoRP (9.4 and 17 GHz), and CBS (35.25, 36.25, 39.75 GHz) data for the peak of the burst at 06:43:24. Since the duration of the peak considered is less than the time resolution of the SRH integral flux curves (3.5 s), not all SRH frequencies could be used for analysis. When constructing the spectrum from SRH data, we selected only those observation frequencies that were within the 0.5 s interval relative to a given time point, which corresponded to the time resolution of CBS data.

The spectrum shape at frequencies above 2 GHz is typical of the gyrosynchrotron spectrum. The core emission becomes dominant in the integral spectrum at frequencies above 6 GHz, and the spectrum index is $f^{1.4}$. The power-law decay index can be described as $f^{-2.5}$. On the contrary, in the remote source spectrum the SRH

frequency range covers the decreasing part of spectrum. After the flat part of the spectrum, where the flux from the remote source is comparable to the flux from the flare core, the decrease begins after 4 GHz with $f^{-1.1}$. The next feature of the remote source is a high degree of right circular polarization. In the frequency range from 4.5 to 7.5 GHz, it runs to 80 % (see Figure 7, *b*).

Measurements of the dynamic spectrum at lower frequencies were obtained with the SOLARSPEL spectropolarimeter in the receiving frequency range 50–3000 MHz (Figure 8, *a*). In its dynamic spectrum (*a*), a response to the flare was observed in the frequency range 80–350 MHz. The emission began in a narrow band of ~350 MHz at 06:43:00 and lasted in this band for ~40 s. In a wide band, the emission began at 06:43:10 with maximum intensity during the peak of hard emission. The emission gradually fades, initially at higher frequencies.

Figure 8, *b* displays the MUSER-I dynamic spectrum. The data and figure were obtained using programs developed by Chinese colleagues, including image calibration and improvement [Wang et al., 2013; Tan et al., 2015]. MUSER-I 1600–2000 MHz data shows a flare response in the emission from 1750–2000 MHz. Note that this emission was not recorded in the dynamic spectrum (*a*) due to the lower sensitivity of the 50–3000 MHz SOLARSPEL antenna in the upper part of the operating range (above 1000 MHz). The amplitude of MUSER-I signals increased sharply during the peak. The integral spectrum flux decreased rapidly with decreasing frequency and ceased at frequencies below 1850 MHz (see Figure 8, *b*). There was a slight drift toward low frequencies. Unfortunately, there is a record for this event only in the left polarization of the spectrometer; therefore, the calibrated LCP data was multiplied by two to represent it on the spectrum and compare it with microwave data (see Figure 7, *a*, green rhombs).

DISCUSSION

The data set on the dynamics and spatial structure of the flare makes it possible to define the event under study as a circular ribbon flare with a compact positive field domain in the core and a remote source at the distance of 215 arcsec. The magnetic structure was formed the day before the flare, as evidenced by the appearance of a quasi-stationary circular structure in the EUV emission around the magnetic domain [Masson et al., 2009]. The initiation of the flare impulsive phase is visible in the images of the flare core in the 1600 Å channels: first, a compact bright source appears which is located north of the positive field domain (see Figure 6). It is located at the point of approach of footpoints of two ropes, stretched sequentially in a northwesterly direction. As the flare develops, the ropes become brighter, and after the impulsive phase a long wraparound rope occurs which rises up over time. Simultaneously with the rise of this rope, plasma is seen to flow along the outer spine. A similar scheme for the initiation of a coronal mass ejection has been proposed by Uralov et al. [2002]. It was adopted in [Meshalkina et al., 2009] to explain the initiation of circular ribbon flares.

In our event, dimensions of the SRH antenna beamwidth were comparable to those of the flare core, which makes it impossible to study the interaction between the ropes in microwave emission in more detail. Recording of sources of polarized emission of different signs in the impulsive phase is consistent with the assumption about the formation of a common rope (see Figure 4). The location and brightness of the observable sources of polarized emission result from convolution of the real sources with the SRH antenna beamwidth. Hence, on radio maps the distance between the apparent brightness centers of polarized sources decreases with increasing receiving frequency, i.e. it depends on the size of the antenna bemwidth. At the highest mapping frequency of 12.2 GHz in this work, the SRH spatial resolution (10.4×18.2 arcsec) was insufficient to determine the actual location of the polarized sources.

After the impulsive phase, plasma was seen to flow along large loops oriented along the outer spine. The loops could be observed in difference images of EUV emission a few minutes after the impulsive phase. Figure 3 shows that their observable shape and the location of the remote footpoint are close to the field lines calculated in the potential approximation. It follows from the calculations that the height of the loops is in the range 50–130 Mm with a length 300–400 Mm. To fill the loops with plasma for 4 min, its flow velocity has to be several times higher than the velocity of 330 km/s in the plane of the sky. Estimates suggest that the required flow velocity can be achieved if it is of the order of the velocity of ion sound at a plasma temperature 20–30 MK in the flare core. A similar propagation mechanism with formation of a heat wave of replacement has been discussed in [Brown et al., 1979; Vlahos, Papadopoulos, 1979; Levin, Melnikov, 1993; Meshalkina, Altyntsev, 2024].

The peak of the emission from the remote source in microwaves lags behind the peak in the flare core by ~5 s. The emission spectrum of the remote source is broadband with a maximum spectrum at a frequency below 4 GHz. The accuracy of determining the delay from SRH data is ~1 s since SRH measurements in the remote source were carried out at an interval of 3.5 s. In the flare core, the accuracy of determining the peak from the 35 GHz profile was fractions of a second. With an average loop length of 350 Mm, we obtain a flight velocity of emitting electrons $\sim 7 \cdot 10^9$ cm/s. The ~17 keV kinetic energy of electrons at this velocity is insufficient to generate the microwave spectrum of the remote source. If we take into account (as is often done [Aschwanden, 2004]) the helicity of magnetic field lines and the pitch angle of propagating electrons, the estimated velocity can be multiplied by 2, then the electron energy becomes more reasonable — ~70 keV. Note that it was the only time such an estimate was obtained for a remote source of a circular flare during observations of quasi-periodic oscillations with SSRT at a high time resolution [Altyntsev et al., 2022]. In this work, we have estimated the energy of emitting electrons at >100 keV.

At sufficiently large pitch angles of electrons propagating along large loops, it is natural to expect their capture at tops of the loops. Their emission can explain the response to the flare in dynamic spectra in the range 80–350 MHz. If we assume that the emission is plasma, the plasma density at loop tops varies in a wide range from $8 \cdot 10^7$ to $1.5 \cdot 10^9$ cm^{-3}. Calculations give 10–20 G magnetic fields, i.e. the observed frequencies are within 3–6 harmonics of the cyclotron frequency of electrons. In this case, it is natural to expect that the emission will be generated at double plasma resonance [Ledenev, 1998; Zheleznyakov et al., 2016].

In the flare core and the remote source, the spectra are gyrosynchrotron with different power-law decay indices f^β. A harder spectrum with β=–1.1 was observed in the remote source. Estimated power-law index of electron energy distribution δ by the formula β=1.22–0.9δ [Dulk, Marsh, 1982] yields δ≈2.5. A feature of the microwave emission from the remote source is a high

degree of circular polarization up to 80 %. According to calculations of the gyrosynchrotron spectrum in [Fleishman, Melnikov, 2003], such a high degree of polarization indicates large pitch angles of emitting electrons. On the other hand, for large pitch angles the above estimate for isotropic electron distribution $\delta \approx 2.5$ can only be considered as a first approximation and requires refinement.

For the flare core, observations with the spectropolarimeters gave an estimate of the slope of the spectrum $\beta \approx -2.5$, from which we get $\delta \approx 4.1$. Unfortunately, SRH observations were available to the frequency of 12.2 GHz, i.e. only in the rising spectrum part. The power-law growth index $\beta \approx 1.4$ is two times lower than the calculated value of the gyrosynchrotron spectrum emitted by a homogeneous source.

Short growth and decay fronts of the hard peak of microwave and hard X-ray emissions suggest that acceleration to energies above 100 keV occurred in the open configuration of the magnetic field. Electron emission fluxes of lower-energy electrons increase after the peak, which indicates magnetic field trapping and accumulation in ropes.

CONCLUSION

Observations in microwave emission have provided important insights into morphological properties of the March 25, 2024 circular flare. The flare's hard emission was demonstrated to be associated with the interaction between magnetic flux ropes. For the first time, a microwave spectrum of electron emission from a remote source has been obtained and a connection has been found between meter-wave emission and electron acceleration in the flare core. Thus, we have demonstrated the high diagnostic potential of SRH multiwave observations for studying events with relatively small temporal and spatial scales. In-depth study of the dynamics of microwave sources and their polarization and spectral properties in this flare will be the subject of our future work.

REFERENCES

Altyntsev A., Lesovoi S., Globa M., Gubin A., Kochanov A., Grechnev V., Ivanov E., Kobets V., Meshalkina N., et al. Multiwave Siberian Radioheliograph. *Sol.-Terr. Phys.* 2020, vol. 6, iss. 2, p. 30. DOI: 10.12737/stp-62202003.

Altyntsev A.T., Meshalkina N.S., Sych R.A., Kolotkov D.Y. Double peak quasi-periodic pulsations in a circular-ribbon flare. *Astron. Astrophys.* 2022, vol. 663, id. A149, 8 p. DOI: 10.1051/0004-6361/202243144.

Aschwanden M.J. *Physics of the Solar Corona: An Introduction.* Springer-Verlag; Praxis, 2004, 842 p.

Brown J.C., Melrose D.B., Spicer, D.S. Production of a collisionless conduction front by rapid coronal heating and its role in solar hard X-ray bursts. *Astrophys. J.* 1979, part 1, vol. 228, pp. 592–597. DOI: 10.1086/156883.

Chen X., Yan Y., Tan B., Huang J., Wang W., Chen L., et al. Quasi-periodic pulsations before and during a solar flare in AR 12242. *Astrophys. J.* 2019, vol. 878, no. 2, p. 78. DOI: 10.3847/1538-4357/ab1d64.

Dulk G.A., Marsh K.A. Simplified expressions for the gyrosynchrotron radiation from mildly relativistic, nonthermal and thermal electrons. *Astrophys. J.* 1982, vol. 259, p. 350. DOI: 10.1086/160171.

Fleishman G.D., Melnikov V.F. Gyrosynchrotron emission from anisotropic electron distributions. *Astrophys. J.* 2003, vol. 587, iss. 2, pp. 823–835. DOI: 10.1086/368252.

Guidice D.A., Cliver E.W., Barron W.R., Kahler S. The Air Force RSTN System. *Bull. of the American Astronomical Society.* 1981, vol. 13, p. 553.

Kumar P., Nakariakov V.M., Cho K.S. Observation of a quasiperiodic pulsation in hard X-ray, radio, and extreme-ultraviolet wavelengths. *Astrophys. J.* 2016, vol. 822, no. 1, p. 7. DOI: 10.3847/0004-637X/822/1/7.

Ledenev V.G. Generation of electromagnetic radiation by an electron beam with a bump on the tail distribution function. *Solar Phys.* 1998, vol. 179, iss. 2, pp. 405–420. DOI: 10.1023/A:1005007026541.

Lee J., White S.M., Chen X., Chen Y., Ning H., Li Bo, Masuda S. Microwave study of a solar circular ribbon flare. *Astrophys. J. Lett.* 2020, vol. 901, p. L10. DOI: 10.3847/2041-8213/abb4dd.

Lemen J.R., Title A.M., Akin D.J., Boerner P.F, Chou C., Drake J.F., Duncan D.W., Edwards Ch.G., et al. The Atmospheric Imaging Assembly (AIA) on the Solar Dynamics Observatory (SDO). *Solar Phys.* 2012, vol. 275, no. 1-2, pp. 17–40. DOI: 10.1007/s11207-011-9776-8.

Lesovoi S.V., Altyntsev A.T., Ivanov E.F., Gubin A.V. A 96-antenna radioheliograph. *Res. Astron. Astrophys.* 2014, vol. 14, iss. 7, article id. 864–868. DOI: 10.48550/arXiv.1403.4748.

Lesovoi S.V., Kobets V. Correlation plots of the Siberian Radioheliograph. *Sol.-Terr. Phys.* 2017, vol. 3, iss. 1. pp. 19–25. DOI: 10.12737/article_58f96eeb8fa318.061 22835.

Levin B.N., Melnikov V.F. Quasi-linear model for the plasma mechanism of narrow-band microwave burst generation. *Solar Phys.* 1993, vol. 148, iss. 2, pp. 325–340. DOI: 10.1007/ BF00645093.

Masson S., Pariat E., Aulanier G., Schrijver C.J. The nature of flare ribbons in coronal null-point topology. *Astrophys. J.* 2009, vol. 700, iss.1, pp. 559–578. DOI: 10.1088/0004-637X/700/1/559.

Meegan C., Lichti G., Bhat P.N., et al. The Fermi gamma-ray burst monitor. *Astrophys. J.* 2009, vol. 702. p. 791. DOI: 10.1088/0004-637X/702/1/791.

Meshalkina N.S., Uralov A.M., Grechnev V.V., Altyntsev A.T., Kashapova L.K. Eruptions of magnetic ropes in two homologous solar events of 2002 June 1 and 2: a key to understanding an enigmatic flare. *PASJ.* 2009, vol. 61, p. 791. DOI: 10.1093/pasj/61.4.791.

Meshalkina N.S., Altyntsev A.T. Heating manifestations at the onset of the 29 June 2012 flare. *Sol.-Terr. Phys.* 2024, vol. 10, iss. 3, pp. 11–17. DOI: 10.12737/stp-103202402.

Nakajima H., Nishio M., Enome S., Shibasaki K., Takano T., Hanaoka Y., Torii C., et al. The Nobeyama Radioheliograph. *Proc. IEEE.* 1994, vol. 82, p. 705.

Pontin D.I., Priest E.R., Galsgaard K. On the nature of reconnection at a solar coronal null point above a separatrix dome. *Astrophys. J.* 2013, vol. 774, iss. 2, article id. 154, 10 p. DOI: 10.1088/0004-637X/774/2/154.

Priest E.R., Titov V.S. Magnetic reconnection at three-dimensional null points. *Philosophical Transactions of the Royal Society of London Series.* 1996, vol. A354(1721), pp. 2951–2992. DOI: 10.1098/rsta.1996.0136.

Shang Z., Xu K., Liu Y., Wu Z., Lu G., Zhang Y. Y., et al. A broadband solar radio dynamic spectrometer working in the millimeter-wave band. *Astrophys. J. Suppl. Ser.* 2022, vol. 258, p. 25. DOI: 10.3847/1538-4365/ac4257.

Shang Z., Wu Z., Liu Y., Bai Yu, Lu G., Zhang Y. Y., et al. The calibration of the 35–40 GHz solar radio spectrometer with the new moon and a noise source. *Astrophys. J. Suppl. Ser.* 2023, vol. 268, p. 45. DOI: 10.3847/1538-4365/acee00.

Sun X, Hoeksema J.T, Liu Y, Aulanier G., Su Y., Hannah I.G., Hock R.A. Hot spine loops and the nature of a late-phase solar flare. *Astrophys. J.* 2013, vol. 778, iss. 2, p. 139. DOI: 10.1088/0004-637X/778/2/139.

Tan C.M., Yan Y.H., Tan B.L., Yoshimi N., Tanaka H., Enome S. Study of calibration of solar radio spectrometers and the quiet-Sun radio emission. *Astrophys. J.* 2015, vol. 808, p. 61. DOI: 10.1088/0004-637X/808/1/61.

Torii C., Tsukiji Y., Kobayashi S., et al. Full-automatic radio-polarimeters for solar patrol at microwave frequencies. *Proc. of the Research Institute of Atmospherics.* Nagoya University, 1979, vol. 26, pp. 129–132.

Uralov A.M., Lesovoi S.V., Zandanov V.G., Grechnev V.V. Dual-filament initiation of a coronal mass ejection: observations and model. *Solar Phys* 2002, vol. 208, iss. 1, pp. 69–90. DOI: 10.1023/A:1019610614255.

Vlahos L., Papadopoulos K. On the upconversion of ion-sound to Langmuir turbulence. *Astrophys. J.* 1979, Part 2. Letters to the Editor, vol. 234, Dec. 15, 1979, pp. L217, L218. Navy-supported research. DOI: 10.1086/183143.

Yan Y., Zhang J.,Wang W., Liu F., Chen Z., Ji G. The Chinese Spectral Radioheliograph — CSRH. *Earth, Moon, and Planets.* 2009, vol. 104, iss. 1-4, pp. 97–100. DOI: 10.1007/ s11038-008-9254-y.

Yan Yihua, Chen Linjie, Yu Sijie. First radio burst imaging observation from Mingantu Ultrawide Spectral Radioheliograph. *IAUS.* 2016, vol. 320, pp. 427–435. DOI: 10.1017/ S174392131600051X.

Wang Wei, Yan Yihua, Liu D., Chen Z., Su C., Liu F., et al. Calibration and data processing for a Chinese Spectral Radioheliograph in the decimeter wave range. *Publications Astronomical Society Japan.* 2013, vol. 65, iss. SP1, id. S18. DOI: 10.1093/pasj/65.sp1.S18.

Zhang Q. Circular-ribbon flares and the related activities. *Rev. Modern Plasma Physics.* 2024, vol. 8, iss. 1, article id. 7. DOI: 10.1007/s41614-024-00144-9.

Zhdanov D.A., Zandanov V.G. Broadband microwave spectropolarimeter. *Central European Astrophysical Bulletin.* 2011, vol. 35. p. 223.

Zheleznyakov V.V., Zlotnik E.Ya., Zaitsev V.V., Shaposhnikov V.E. Double plasma resonance and its manifestations in radio astronomy. *Physics-Uspekhi.* 2016, vol. 59, no. 10. DOI: 10.3367/UFNe.2016.05.037813.

URL: https://radiomag.iszf.irk.ru/books/sibirskii-radiogeliograf/page/sintez-radioizobrazenii-s-pomoshhiu-paketa-srh-synth (accessed June 25, 2025).

URL: https://badary.iszf.irk.ru/srhCorrPlot.php (accessed June 25, 2025).

URL: https://ckp-rf.ru/catalog/usu/4138190/ (accessed June 25, 2025).

URL: http://ckp-angara.iszf.irk.ru/ (accessed June 25, 2025).

How to cite this article
Altyntsev A.T., Meshalkina N.S., Anfinogentov S.A., Zhdanov D.A., Myshyakov I.I., Ivanov E.F., Chengming Tan, Zhao Wu. Processes of acceleration and transfer of electrons in a pulse circular ribbon flare. *Sol.-Terr. Phys.* 2025, vol. 11, iss. 3, pp. 3–12. DOI: 10.12737/stp-113202501.

FEATURES OF TURBULENT CASCADE DEVELOPMENT IN THE MAGNETOSHEATH DURING ICME

L.S. Rakhmanova
Space Research Institute RAS,
Moscow, Russia, rakhlud@gmail.com

M.O. Riazantseva
Space Research Institute RAS,
Moscow, Russia, orearm@gmail.com

A.A. Khokhlachev
Space Research Institute RAS,
Moscow, Russia, aleks.xaa@yandex.ru

Yu.I. Yermolaev
Space Research Institute RAS,
Moscow, Russia, yermol@cosmos.ru

G.N. Zastenker
Space Research Institute RAS,
Moscow, Russia, gzastenk@iki.rssi.ru

Abstract. Large-scale disturbances in the interplanetary medium are the main cause of the global perturbations inside Earth's magnetosphere. Transition region called magnetosheath is known to be located in front of the magnetosphere in which plasma and magnetic field properties, as well as their variations differ significantly from those in the solar wind. Particularly, plasma passage through the magnetosheath has been demonstrated to modify substantially features of the cascade of turbulent fluctuations of the solar wind, with the pattern of the modification being different for quiet and disturbed conditions in the interplanetary medium. In this study, we examine features of turbulent cascade formation in the magnetosheath during interplanetary manifestation of coronal mass ejection (ICME), by analyzing several cases of ICME interactions with the magnetosphere. The analysis is conducted by comparing magnetic field variations measured simultaneously in the solar wind and in the dayside magnetosheath by Wind, Cluster, THEMIS, and MMS spacecraft in 2016–2017. Interaction of ICME with the magnetosphere is shown to cause the least change in the fluctuation power if there is a compression region in front of it; on the opposite, when there is no compression region, the fluctuation power increases considerably. ICMEs that caused significant changes in the *Dst* index were determined to be accompanied by the least changes in the turbulent cascade in the magnetosheath, whereas the most significant modification of the turbulence features were observed during ICMEs which did not trigger substantial geomagnetic disturbances.

Keywords: solar wind, magnetosheath, turbulence, space plasma.

INTRODUCTION

It is known that the main sources of global magnetospheric disturbances are large-scale interplanetary disturbances [Yermolaev et al., 2015; Borovsky, Denton, 2006]. At the same time, geoeffectiveness of the solar wind (SW) and the relationship of geomagnetic disturbances with interplanetary medium parameters are usually studied using measurements in the vicinity of the L1 point, located 1.5 million km from Earth's orbit [Pallocchia et al., 2006; Boynton et al., 2012; Podladchikova, Petrukovich, 2012], and ignoring the processes in boundary layers of the magnetosphere. In front of the outer boundary of the magnetosphere — the magnetopause — there is always a bow shock (BS) and a transition region formed because supersonic and super-Alfvén SW streams flow around the magnetosphere. In the transition region, or magnetosheath (MSH), plasma and magnetic field characteristics change significantly — magnetic field lines are compressed, the magnetic field changes direction, plasma is compressed, slows down, and heats, as well as the fluctuation intensity of all parameters increases greatly. Processes in MSH depend on the relative position of BS and the interplanetary magnetic field: due to

the presence of ions behind quasi-parallel BS, which are reflected from BS and then carried away by SW plasma to MSH, the amplitude of plasma parameter and magnetic field variations behind quasi-parallel BS is by an order of magnitude higher than behind quasi-perpendicular BS, and can reach the order of magnitude of the parameter itself [Greenstadt, 1972; Shevyrev, Zastenker, 2005]. Moreover, the temperature anisotropy that occurs on quasi-perpendicular BS leads to the development of a large number of instabilities and wave processes behind it [Schwartz et al., 1996; Lacombe, Belmont, 1995].

Despite the fact that there are general ideas about the global change in plasma and field characteristics behind BS, and it can, on average, be described by gas-dynamic and magnetohydrodynamic (MHD) models [Spreiter et al., 1966; Tóth et al., 2005] on scales comparable to the size of the magnetosphere ($\sim 10^5$ km), the processes on smaller scales ($\sim 10^2$–10^3 km) can only be reproduced by time-consuming hybrid and kinetic models (e.g. [Karimabadi et al., 2014; Palmroth et al., 2018]), which cannot be applied to space weather forecasting. Studies based on simultaneous measurements in front of and

behind BS show that the direction of the magnetic field directly in front of the magnetopause may differ from that recorded in SW [Šafránková et al., 2009; Pulinets et al., 2014]. In addition, recent studies indicate that during such geoeffective large-scale phenomena as Interplanetary Coronal Mass Ejections (ICMEs) there can also be mismatches between field directions in MSH and SW [Turc et al., 2017] on time scales of the order of an hour. Since IMF B_z is considered as the most important parameter of the interplanetary medium responsible for the dynamics of the magnetosphere, it is important to take into account the processes in MSH for a more correct understanding of solar-terrestrial relations.

On scales comparable to the proton gyroradius, kinetic effects play an important role in space plasma, energy dissipation begins, and the MHD description becomes inapplicable. The processes occurring on scales smaller than 10^3 km can be analyzed in terms of turbulent cascade characteristics. In recent years, a large amount of experimental data with high temporal resolution has significantly expanded the understanding of turbulence features in MSH (for example, [Zimbardo et al., 2010; Sahraoui et al., 2020; Rakhmanova et al., 2021]). For undisturbed SW plasma, the spectrum of turbulent magnetic field fluctuations has a universal form described by a power function with an exponent of –5/3 (Kolmogorov scaling) on scales larger than the ionic gyroradius (MHD scales). On scales of the order of the proton inertial length, the spectrum break and transition to kinetic scales occur on which the spectrum is also described by the power law with exponent α. According to statistical data, on average α=–(2.8÷3), whereas according to theoretical predictions α ranges from –7/3 [Schekochihin et al., 2009] to –8/3 [Boldyrev, Perez, 2012]. Most studies show that the characteristics of turbulent fluctuation spectra change at BS: Kolmogorov scaling on MHD scales is disrupted [Czaykowska et al., 2001; Huang et al., 2017; Rakhmanova et al., 2018a; Rakhmanova et al., 2024a] and the spectra can be described by the power law with an exponent of –1, typical of a set of incoherent waves or scales of energy pumping. On kinetic scales, some studies have demonstrated a significant steeping of fluctuation spectra behind BS [Rakhmanova et al., 2018b, 2024a], presumably caused by increased energy dissipation due to a large number of wave processes and instabilities characteristic of MSH.

Note also that turbulence characteristics depend on SW plasma type, determined largely by its solar source [Bruno et al., 2014; Riazantseva et al., 2019, 2020; Ervin et al., 2024]. Furthermore, it has been shown [Rakhmanova et al., 2024c; Rakhmanova et al., 2024b] that different turbulence types are characterized by different dynamics of turbulence properties behind BS, including different degrees of modification of the turbulent cascade in dayside MSH and the specific nature of its recovery during plasma propagation to MSH flanks.

Thus, the study into the features of the development of a turbulent cascade in MSH during disturbances in SW can provide insight into the processes occurring in the transition region during observation of potentially geoeffective phenomena in the interplanetary medium, and complement existing ideas about solar-terrestrial relations. In this paper, we have analyzed 15 cases of ICMEs recorded at Earth's orbit and changes in plasma turbulence characteristics when crossing BS in these periods. ICMEs are interplanetary coronal mass ejections that lead to the formation of large-scale magneto-plasma structures propagating in the interplanetary medium. If the propagation velocity of magnetoplasma structure from the Sun exceeds the velocity of surrounding SW plasma, a compression region (Sheath) can form in front of it, as in front of a piston, which features an increased plasma pressure (density and temperature) and fluctuation power. If the propagation velocity of the disturbance exceeds the local velocity of a fast MHD wave, an interplanetary shock is also formed in front of the piston. In Earth's orbit, ICME is identified by a set of plasma and magnetic field parameters [Yermolaev et al., 2009], as well as by ionic composition and energetic particle fluxes [Richardson, Cane, 2010]. ICME is characterized by an increase in the magnetic field compared to the surrounding SW, a significant decrease in temperature, an increase in velocity at the beginning of the event, and its decrease by the end of the event. Besides, there is often an increase in the relative content of alpha particles, as well as ions with large charges such as iron and oxygen. ICME is generally observed in two forms in Earth's orbit — Ejecta or magnetic cloud (MC). MC includes ICMEs that feature a quiet magnetic field of high amplitude without significant variations, with a smooth rotation of the magnetic field vector by a large angle, a significant decrease in temperature and proton density, and hence in the plasma parameter β — the ratio of thermal pressure to magnetic pressure [Burlaga, 1991]. The difference between ICMEs of these two types is probably due to different trajectories at which they are crossed by recording spacecraft (SC) [Yermolaev et al., 2009; Kilpua et al., 2017]. ICME formation, distribution, and internal structure are described in detail, for example, in the review [Kilpua et al., 2017]. For this work, we have taken events from the catalog [Yermolaev et al., 2009]; Ejecta and MC events were examined separately. Ejecta events without Sheath observed in front of ICME were considered separately from the events with Sheath, whereas Sheath was always recorded in MC. The periods corresponding directly to Sheaths were also studied independently. In addition, by analyzing the *Dst* index, we identified the Ejecta events that occurred in both SW and MSH, but without significant geomagnetic disturbances, and found characteristic changes in the turbulent cascade properties during these periods. We analyzed simultaneous measurements of turbulence characteristics in SW, using data from the Wind satellite; and in MSH, using data from any THEMIS, Cluster, MMS satellite. The analysis was carried out for 2016–2017, since this period corresponded to the descending phase of the solar cycle and to the observation of a sufficient number of geoeffective events in the interplanetary medium, and there is a large amount of available satellite data obtained in MSH.

1. DATA AND ANALYSIS METHOD

The time intervals corresponding to ICMEs have been selected from the catalog [Yermolaev et al., 2009; http://iki.rssi.ru/pub/omni/catalog/]. For all ICME observations in 2016–2017, we have determined the location of THEMIS, Cluster, and MMS satellites, as well as the availability of their measurements for the given time intervals, from [https://cdaweb.gsfc.nasa.gov/sp_phys/]. The location of a satellite inside MSH was found by analyzing the ion energy distribution, the proton density and velocity. We chose only the events during which the satellites were in the dayside MSH ($X_{GSE}>5$ R_E) and there were rapid satellite measurements of the magnetic field in MSH. We employed data from FGM instruments: on board THEMIS satellites [Auster et al., 2008] with a sampling rate of 4 vectors per second, on board Cluster satellites [Balogh et al., 2001] with a sampling rate of 5 vectors per second, on board MMS satellites with a sampling rate of 16 vectors per second (in a fast mode) [Russell et al., 2016]. With magnetic field measurements available for the selected event, we compared satellite measurements in MSH and SW. We used measurements of plasma parameters in SW with SWE [Ogilvie et al., 1995] at a temporal resolution of 92 s and of the magnetic field with MFI [Lepping et al., 1995] at a sampling rate of 11 vectors per second on board the Wind satellite in the vicinity of the libration point L1. Plasma parameters in MSH were analyzed using data from ESA/THEMIS [McFadden et al., 2008], CIS/Cluster [Rème et al., 2001] and FPI/MMS [Pollock et al., 2016]. We have selected 15 ICME events recorded in Earth's orbit.

To compare the data obtained in SW and MSH, it is necessary to correctly determine the time of plasma propagation between spacecraft. The propagation time was found from correlation analysis of time series of proton density from the Wind satellite and one of the satellites in MSH. For this purpose, density measurements were reduced to a general time grid with a resolution of 92 s, then a preliminary time shift $T_0=dX/|V_X|$ was calculated, where dX is the distance between satellites along the X_{GSE} axis; V_X is the average SW plasma velocity component along the X_{GSE} axis, measured by the Wind satellite during the event. Next, we calculated the density correlation coefficient for the time shift range $[T_0–3600$ s; T_0+3600 s]. The correlation coefficient was computed for an interval of 2 to 8 hrs, depending on the available data interval. The dT shift corresponding to the maximum of the correlation coefficient was determined, and the resulting value was selected as the time shift for the interval considered. Each dT value was manually checked against the visual coincidence between density fronts or magnetic field components on the two satellites and was adjusted if necessary. Figure 1 compares measurements from Wind SC in SW and from MMS-1 SC in MSH for the February 2–3, 2016 event. Panels *a*, *b* show proton density and velocity measurements; the left Y-axis represents the satellite in SW; the right one, the satellite in MSH. Panels *c*, *d* exhibit magnetic field magnitude and components in SW and MSH. The horizontal arrows above the top panel of the figure

indicate SW types — before 22:00 there was a Sheath in front of ICME; from 22:00, the ICME itself, which belonged to the Ejecta type. The Wind data is shifted by 4380 s. The time variation in the proton density is clearly seen to coincide on the two satellites throughout the interval, as well as there are local inconsistencies in plasma structures, which usually emerge due to differences in their propagation velocities.

To identify the geomagnetic response to the event in question, we analyzed the *Dst* index from the Kyoto Observatory [https://wdc.kugi.kyoto-u.ac.jp/dstdir/]. Figure 1, *d* presents *Dst* values with a temporal resolution of 1 hr. The arrival of ICME is seen to be accompanied by a geomagnetic storm with minimum *Dst*=–57 nT. In this paper, the events were divided into those causing a significant response from the magnetosphere if they occurred with a change in *Dst* to less than –30 nT, and those that did not cause a significant geomagnetic response if *Dst* did not fall below –30 nT after the arrival of ICME.

For further analysis of the turbulence characteristics in this event, we have selected two intervals marked in Figure 1 with a gray fill: interval 1 refers to Sheath; and interval 2, to Ejecta. The intervals are taken according to their duration (~ 1 hr), as well as from considerations that the parameters are quasi-stationary, i.e. without significant density jumps or rotations of the magnetic field vector, which generally correspond to the intersection of discontinuities of various types. For each interval, the time shift was additionally adjusted manually.
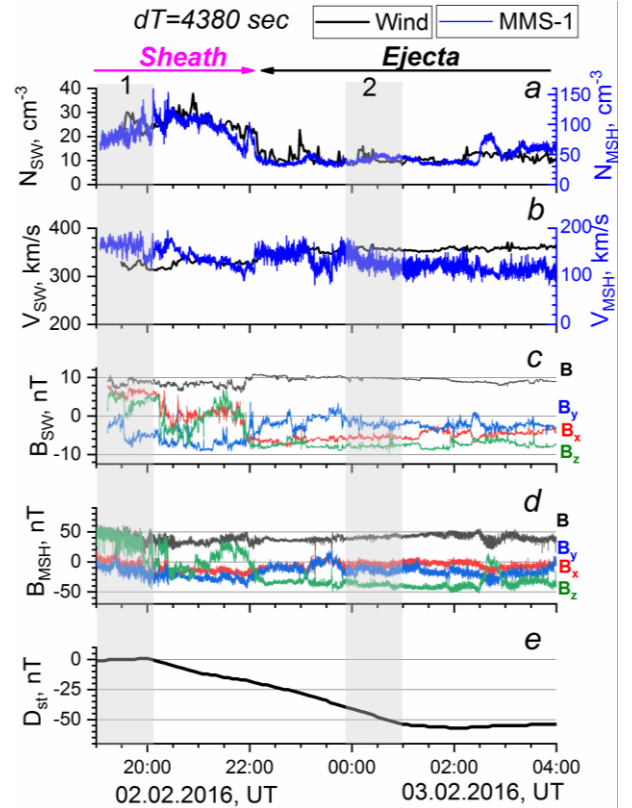

Figure 1. The February 2–3, 2016 event: proton density (*a*) and velocity (*b*) as measured by Wind in SW and by MMS-1 in MSH; magnetic field magnitude and components as measured by Wind in SW (*c*) and by MMS-1 in MSH (*d*); the *Dst* index (*e*)

For the selected intervals, turbulence characteristics in SW and MSH were found by Fourier analysis. Since the temporal resolution of magnetometers in the satellites in use varies, the intervals for calculating fluctuation spectra have different durations in SW and MSH. This difference is due to the use of Fourier analysis, which imposes a limit on the number of points in the spectrum. In this case, for the MMS-1 and Wind satellites the duration of the intervals is 68 and 50 min respectively. The intervals were chosen so that their centers coincide. Fourier spectra were computed for fluctuations of both the magnetic field vector (trace magnetic field fluctuation spectra) and the magnetic field magnitude. The magnetic field vector fluctuations are the sum of the incompressible (Alfvén) component of fluctuations, whereas magnetic field magnitude fluctuations represent the compression component. The contribution of the compression component of fluctuations to the cascade in SW is generally negligible, and turbulence is considered to be purely Alfvén [Schekochihin et al., 2009]. In MSH, the proportion of compression fluctuations becomes significant [Huang et al., 2017], which is an important feature of turbulence in this region.

Figure 2 illustrates the calculated spectra for the intervals marked in gray in Figure 1: panels *a*, *c* show interval 1 (Sheath); panels *b*, *d*, interval 2 (Ejecta). Panels *a*, *b* are spectra in SW; panels *c*, *d*, spectra in MSH. Note that on the scales in SW considered, the noise of MFI can make a significant contribution to the spectra

For the obtained spectra, two scales, separated by a break, are pronounced: MHD and kinetic. On these scales, the spectra were linearly approximated on a logarithmic scale for each range, and the exponent of the
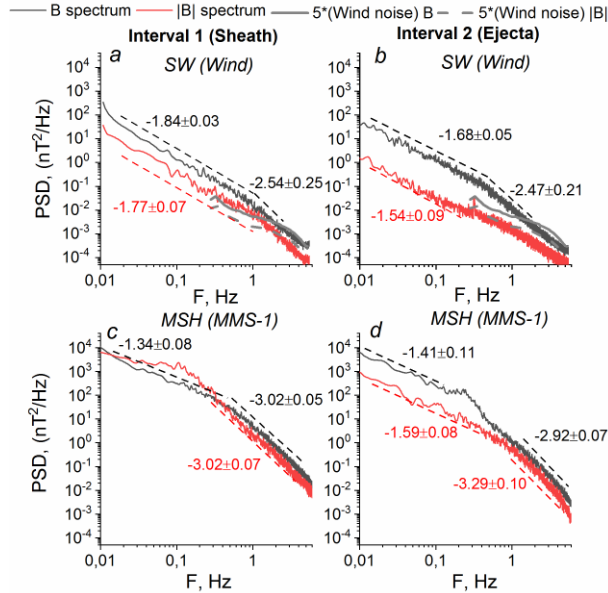

Figure 2. Spectra (solid lines) of trace magnetic field (black curves) and magnitude (red curves) fluctuations in SW (*a*, *b*) and MSH (*c*, *d*) for intervals 1 (*a*, *c*) and 2 (*b*, *d*) in Figure 1, as well as the results of approximation of the spectra (dashed lines). Gray lines in panels *a*, *b* are MFI's noise spectra multiplied by a factor of 5: solid lines are trace magnetic field fluctuation spectra; dashed lines are magnetic field magnitude fluctuation spectra.

power law (slope) of the spectrum was found. In some cases, such an approximation is impossible due to the presence of a peak in the spectrum (the fluctuation spectrum of the magnetic field magnitude in Figure 2, *c*) or because the noise level is reached (the spectrum of magnetic field magnitude fluctuations in Figure 2, *b*).

For most events in SW, analyzed both in this paper and in earlier statistical studies [Woodham et al., 2018], the spectrum breaks at frequencies above 0.1 Hz. In this work, we have chosen the frequency range 0.095–0.105 Hz to estimate the intensity of fluctuations on MHD scales. For each spectrum, we determined the intensity of magnetic field vector and magnitude fluctuations in SW and MSH.

Figure 2 indicates that in SW during the Sheath period the MHD-scale spectra are slightly steeper (~–1.8) than the Kolmogorov spectrum with a slope of –5/3. This slope is typical for Sheath regions [Riazantseva et al., 2024]. During the Ejecta period, the spectra have a slope close to the Kolmogorov one on MHD scales. For interval 1 inside Sheath, the spectrum of magnetic field magnitude fluctuations has a scaling close to that of the field vector fluctuation spectrum, while the intensity of magnetic field vector and magnitude fluctuations differs three times. SW is generally characterized by a large difference in power (by 10 or more times) due to the dominant contribution of Alfvén incompressible fluctuations, which is observed, for example, for the Ejecta period (see Figure 2, *b*) having the power of the compression component ~40 times lower. However, Sheath exhibits a high density, which causes an increase in the proportion of the compressible component of fluctuations. On kinetic scales, the fluctuation spectra have slopes close to –8/3, given in a number of theoretical descriptions of turbulence.

In MSH, the spectra are characterized by flattening on MHD scales and a deviation of scaling from the Kolmogorov scale for magnetic field vector fluctuations. At the same time, during the Sheath period there is a peak in the spectrum of field magnitude fluctuations; and during the Ejecta period, in the field vector spectrum. The frequency range in which the peak was observed was excluded from consideration. It is beyond the scope of this paper to discuss the nature of these peaks. Such peaks are typically caused by wave processes in MSH due to temperature anisotropy, and the type of process depends on external conditions [Schwartz et al., 1996; Lacombe, Belmont, 1995]. Both intervals are typified by steeping of the spectra on kinetic scales. For the Sheath interval, the intensity of magnetic field vector and magnitude fluctuations is close on both MHD and kinetic scales, which indicates a significant contribution of compression fluctuations to the cascade. For the Ejecta interval, the proportion of compression fluctuations in MSH on MHD scales, as well as in SW, is much smaller than the proportion of Alfvén fluctuations, whereas their contribution increases on kinetic scales.

The break frequency of spectra is also an important feature of turbulence since it is believed that the scale on which the break appears is related to the mechanism

of energy dissipation and plasma heating. However, identifying this scale requires significant statistics, and even if any, the scale is still not clearly defined (see, e.g., [Woodham et al., 2018]). In this paper, the statistics does not allow us to reliably determine which scale is typical of the spectrum break, so this problem was left aside.

A total of 47 intervals have been identified for 15 ICME events, divided according to the type of ICME and the intensity of geomagnetic disturbances they triggered into the following groups: 1) Ejecta ICME before which there was a compression region and after which $Dst<-30$ nT, i.e. there was a geomagnetic disturbance (GS) — Ejecta/Sh/GS; 2) Ejecta ICME before which there was a compression region and after which $Dst>-30$ nT, i.e. there was no significant geomagnetic disturbance — Ejecta/Sh/noGS; 3) Ejecta ICME before which no compression region was observed and $Dst>-30$ nT — Ejecta/noSh; 4) Sheath after which $Dst<-30$ nT — Sh; 5) ICME of MC type after which $Dst<-30$ nT — MC. The number of intervals of each type and the presence/absence of the magnetospheric response to the event, as well as averages of IMF B_z and SW plasma velocity for the selected group of events are listed in Table. According to the results of statistical studies [Rakhmanova et al., 2024a, b], the disturbed periods in SW and in particular the period of ICME passage are characterized by a significant modification of the turbulent cascade throughout the dayside MSH, regardless of the satellite location relative to the magnetopause and BS. Therefore, in this work we do not separate intervals near the boundaries and in the middle of MSH. There is also no separation according to the type of the BS behind which the measurements were made.

Using the statistics obtained, we have analyzed the changes when crossing BS: 1) the power of *PSD* fluctuations on MHD scales; 2) the degree of compression (compression coefficient) on MHD scales $CC=PSD_{|B|}/PSD_B$, where $PSD_{|B|}$ is the intensity of magnetic field magnitude spectrum fluctuations, PSD_B is the power of magnetic field vector fluctuations; 3) slopes P_1 and P_2 on MHD and kinetic scales respectively for each interval type. The results of the analysis are presented in the next section.

2. RESULTS

Figure 3 compares slopes of magnetic field vector fluctuation spectra in SW and MSH on MHD (*a*) and kinetic (*b*) scales for events of different types. Magnetic field magnitude fluctuations in SW are adversely affected by MFI noise, which hinders identification of slopes of spectra of these fluctuations for kinetic scales. Accordingly, the scaling of fluctuations was compared only for the magnetic field vector. Black dashed lines indicate the equality of the slopes of the spectra in front of and behind BS, i.e. preservation of scaling when entering into MSH. Blue dashed lines show the model slopes specific to each scale range. For the intervals related to Sheath and MC, the spectra on MHD scales in SW are close to the Kolmogorov spectra. For other SW types, there is a wide spread of slopes. In MSH, most spectra have slopes lower in magnitude than in SW and as described in theories. Note that the number of points in Figure 3 may be smaller than the number of intervals in Table since in a large number of cases wave phenomena are observed in MSH and it is impossible to approximate the spectra on MHD scales. In the fourth column of Table is the number of cases of observation of well-defined peaks in the spectra of magnetic field vector fluctuations in MSH. The most common wave phenomena are observed for Ejecta/Sh/noGS events — 10 of 13 cases, as well as for Ejecta/noSh events — 10 of 13 cases. Thus, for ICMEs that did not produce a significant magnetospheric response, intense wave activity is observed in 76 % of cases in the dayside MSH. For the events that evoked a significant magnetospheric response, wave processes in MSH occurred in 38 % of cases.

For Ejecta/Sh/GS events, slopes of spectra on MHD scales in MSH correspond to those measured in SW, both for the Kolmogorov scaling and for deviation from it in SW. For other events, there is no connection between the slopes of the spectra in the two regions.

On kinetic scales, the fluctuation spectra in MSH have, on average, a slope larger in magnitude than that in SW, which is typical of MSH plasma. The smallest slope
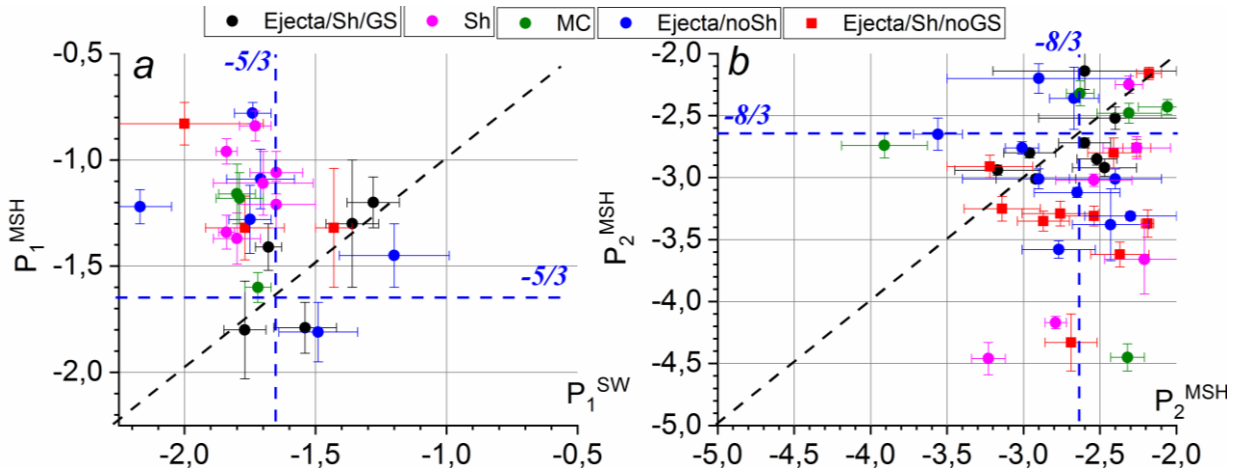

Figure 3. Slope of magnetic field vector fluctuation spectrum in MSH as function of the slope in SW on MHD scales (*a*) and on kinetic scales (*b*)

L.S. Rakhmanova, M.O. Riazantseva, A.A. Khokhlachev, Y.I. Yermolaev, G.N. Zastenker

Types of intervals considered and their characteristics

Type	Number of intervals	Magnetospheric response	Number of intervals with peak in MSH	Average B_z in SW, nT	Average V in SW, km/s
Ejecta/Sh/GS	8	+	5	−5.3±3.3	355±4
Ejecta/Sh/noGS	13	−	10	3.7±4.1	420±64
Ejecta/noSh	13	−	10	1.2±2.1	382±42
Sh	8	+	2	0.7±3.2	422±109
MC	5	+	1	−6.3±5.7	473±100

change when plasma enters into MSH is observed for Ejecta/Sh/GS events; the largest one, for Ejecta/Sh/noGS, Ejecta/noSh, and Sh events. Interestingly, for four of five MC events, there is a spread of slopes in SW, whereas in MSH the slope values are close to –8/3. Such a change may indicate that the cascade of turbulent fluctuations can collapse and form again behind BS, not only for MHD, as suggested in [Huang et al., 2017], but also for kinetic scales. Yet, it is impossible to answer this question unambiguously in the framework of this work due to the limited statistics on MC. For one of the five events, the slope on kinetic scales is close to –4.5, which is typical for observing the wave processes or local coherent structures such as Alfvén vortices [Alexandrova et al., 2008].

Figure 4 compares averages and standard deviations of changes in slopes of fluctuation spectra at BS on MHD (*a*) and kinetic (*b*) scales for the ICME types considered. The slope change is defined as $P_{1,2} = \left(P_{1,2}^{MSH} - P_{1,2}^{SW} \right) / P_{1,2}^{SW}$, where indices 1 and 2 relate to MHD and kinetic scales respectively. In the case of flatter fluctuation spectra characteristic of MSH, $\Delta P < 0$; in the case of fluctuation spectrum steeping at BS, $\Delta P > 0$. Despite the large standard deviations of the values, we can see that different ICME types have their own peculiarities in changing the scaling behind BS. The most significant difference is observed for the Ejecta events that cause and do not cause magnetospheric disturbances. In the former case, there is the smallest change in the scaling of fluctuation spectra on both MHD and kinetic scales. In the latter, most events show an increase in wave activity and energy dissipation rates in MSH.

The magnetic field vector fluctuation intensity in MSH is plotted versus the corresponding intensity in SW, measured on MHD scales, in Figure 5, *a*. Averages and standard deviations of variation in the spectral power $\log(PSD_{MSH}/ /PSD_{SW})$ are presented in Figure 4, *c*. For MC and Ejecta/Sh/GS, crossing of BS is seen to occur with an increase in the intensity of fluctuations by two orders of magnitude. Sheath and Ejecta/Sh/noGS are characterized by a less pronounced increase in fluctuations — by 1–2 orders of magnitude. The most significant enhancement of fluctuations, in some cases by more than three orders of magnitude, is recorded during Ejecta/noSh periods.

One of the main differences between MSH plasma and undisturbed SW plasma is an increase in the proportion of the compression component of fluctuations behind BS.
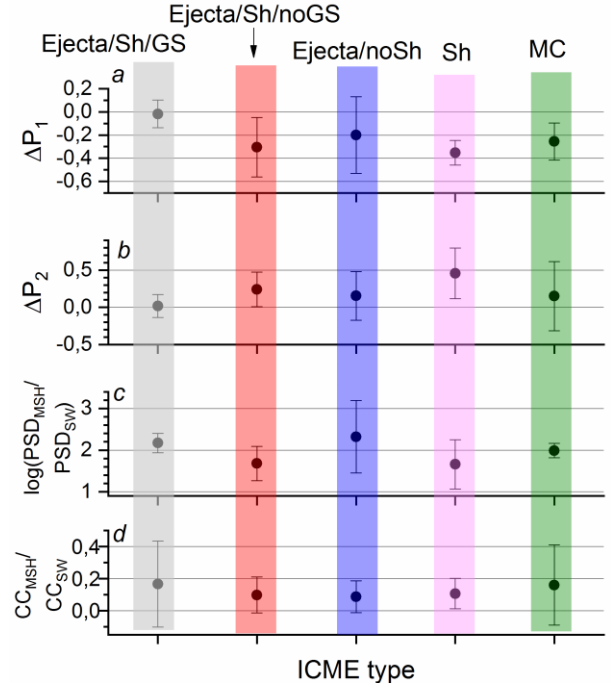
Figure 4. Average and standard deviation of changes in slopes P_1 (*a*) and P_2 (*b*), as well as changes in the spectral power of fluctuations on MHD scales (*c*) and the compression coefficient (*d*) for ICMEs of different types

Figure 5, *b* compares compression coefficients in SW and MSH for all types of intervals considered. Averages and standard deviations for ICMEs of different types are shown in Figure 4, *d*. It is clearly seen that in SW the power of the compression component of magnetic field fluctuations for most events is ten times lower than the power of the Alfvén component ($CC_{SW} < 0.1$), which is typical of SW. At the same time, the proportion of compression fluctuations is, on average, higher for Sheath regions, which is natural for regions of compressed plasma. There is no significant difference in the compression coefficient for Ejecta intervals of different types. In MSH, the CC_{MSH} coefficient is, on average, higher than in SW, and the proportion of the compressible component is usually comparable to that of the Alfvén one. There is no clear relationship between the compressibilities of fluctuations in SW and MSH: on average, the compressibility increases by one order of magnitude for all the ICME types considered. Thus, an increase in compressibility does not seem to play a role in the difference in the dynamics of the turbulent cascade behind BS for ICMEs of different types and in the difference in the geomagnetic response to them.
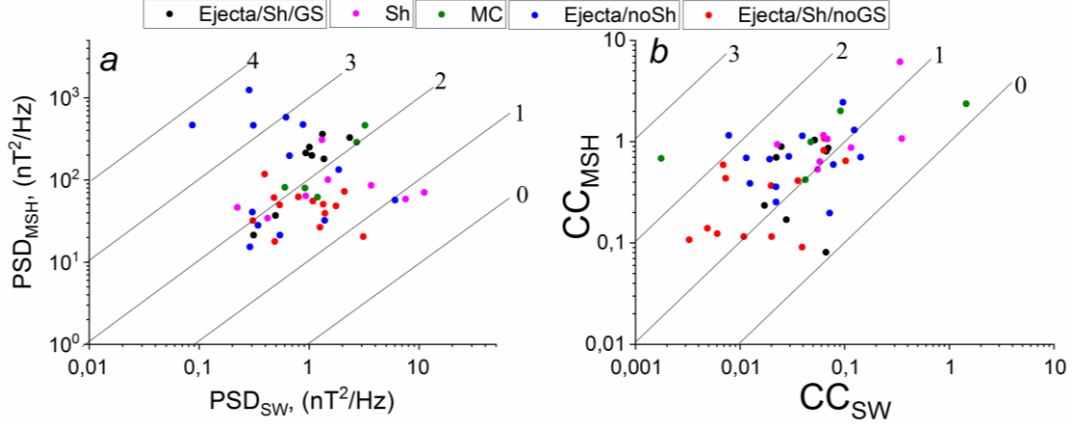
Figure 5. Intensity of magnetic field vector fluctuations in MSH as a function of corresponding intensity in SW for MHD scales (*a*); the compression coefficient in MSH versus that in SW for different ICME types (*b*); lines indicate an increase in intensity (*a*) and degree of compression (*b*) 10^n times; *n* is given near the corresponding line

3. DISCUSSION AND CONCLUSIONS

In this paper, by analyzing simultaneous measurements of turbulence characteristics in the solar wind and in the dayside magnetosheath, we have examined the difference in turbulent cascade forming behind the bow shock for 15 ICME events of various types and varying degrees of geoefficiency. The following has been shown.

1. The most pronounced change in the scaling of the turbulent cascade on both MHD and kinetic scales is observed during Ejecta ICMEs, which are not accompanied by a significant magnetospheric response (*Dst*>–30 nT); it is not important whether there is or is not a Sheath in front of ICME; during these events behind BS, wave activity on inertial scales increases considerably, and the energy dissipation rate is enhanced.

2. The least pronounced change in the scaling of the turbulent cascade on both MHD and kinetic scales is typical for Ejecta regions with Sheath in front of them, causing significant disturbances of the magnetosphere (*Dst*<–30 nT).

3. Ejecta events without Sheath occur with the greatest enhancement of MHD-scale fluctuations at BS, which can be as large as four orders of magnitude.

4. The degree of compressibility of fluctuations varies on average by one order of magnitude behind BS, regardless of ICME type and for different magnetospheric responses to ICME.

The data on the change in scaling of fluctuations upon plasma entry into MSH agrees, on average, with the data obtained earlier in statistical studies [Czaykowska et al., 2001; Huang et al., 2017; Rakhmanova et al., 2024a, b]: there is a deviation of scaling from the Kolmogorov one on MHD scales and steeping of spectra on kinetic scales. However, this paper demonstrates an important difference between events that had the same type, i.e. a solar source, but were followed by a different response from the magnetosphere.

It should be noted that geoeffectiveness of Ejecta ICME has a well-explained relationship with IMF B_z (see Table): the events that cause a significant magneto-

spheric response are characterized by a pronounced southern orientation of the interplanetary magnetic field. Nonetheless, according to statistical analysis [Rakhmanova et al., 2024a], average B_z does not clearly affect the change in turbulence characteristics at BS. In this work, we have also analyzed the relationships of changes in the turbulence parameters at BS with the SW plasma and magnetic field parameters, in particular with the plasma velocity, and have found no dependences in ICME events. A significant increase in the intensity of fluctuations on MHD scales during Ejecta events that did not have a compression region in front of them and were not followed by a significant magnetospheric response, as well as the frequent observation of pronounced wave processes during these periods suggest that the energy of fluctuations coming from SW was converted into MHD waves. An increase in dissipation (steeping of fluctuation spectra on kinetic scales) characteristic of these periods also indicates the appearance of excess energy in the cascade, which is redistributed from large scales to smaller ones through the cascade. Intensification of wave processes is also observed during Ejecta periods with Sheath, which did not lead to significant magnetospheric disturbances, despite the evidence for greater geoeffectiveness of such events [Yermolaev et al., 2015].

Such features in the formation of the turbulent cascade behind BS suggest that not only global reconnection processes at the magnetopause, which are determined by the direction of the interplanetary magnetic field and SW dynamic pressure and are often indicated as the dominant process in solar-terrestrial relations, but also energy transfer processes through the cascade (e.g., [D'Amicis et al., 2020]) and their changes near BS, which may be specific to SW streams of different types, contribute to the geoeffectiveness of various phenomena in the interplanetary medium. This contribution requires more detailed research in order to build more accurate models of solar-terrestrial relations.

REFERENCES

Alexandrova O., Lacombe C., Mangeney A. Spectra and anisotropy of magnetic fluctuations in the Earth's magnetosheath: Cluster observations. *Ann. Geophys*. 2008, vol. 26, iss. 11, pp. 3585–3596. DOI: 10.5194/angeo-26-3585-2008.

Auster H.U., Glassmeier K.H., Magnes W., Aydogar O., Baumjohann W., Constantinescu D., et al. The THEMIS Fluxgate Magnetometer. *Space Sci. Rev*. 2008, vol. 141, pp. 235–264. DOI: 10.1007/s11214-008-9365-9.

Balogh A., Carr C.M., Acuna M.H., Dunlop M.W., Beek T.J., Brown P., et al. The Cluster Magnetic Field Investigation: Overview of in-flight performance and initial results. *Ann. Geophys*. 2001, vol. 19, pp. 1207–1217. DOI: 10.5194/angeo-19-1207-2001.

Boldyrev S., Perez J.C. Spectrum of kinetic Alfven turbulence. *Astrophys. J. Lett*. 2012, vol. 758, no. 2, 5 p. DOI: 10.1088/ 2041-844 8205/758/2/L44.

Borovsky J.E., Denton M.H. The differences between CME-driven storms and CIR-driven storms. *J. Geophys. Res*. 2006, vol. 111, A07S08.

Boynton R.J., Balikhin M.A., Billings S.A., Sharma A.S., Amariutei O.A. Data derived NARMAX *Dst* model. *Ann. Geophys*. 2012, vol. 29, iss. 6, pp. 965–971. DOI: 10.5194/angeo-29-965-2011.

Bruno R., Trenchi L., Telloni D. Spectral slope variation at proton scales from fast to slow solar wind. *Astrophys. J. Lett*. 2014, vol. 793, L15.

Burlaga L.F. Magnetic clouds. *Physics of the Inner Heliosphere*: vol. 2. Eds R. Schwenn and E. Marsch. Springer-Verlag, 1991, p. 1. DOI: 10.1007/978-3-642-75364-0_1.

Czaykowska A., Bauer T.M., Treumann R.A., Baumjohann W. Magnetic field fluctuations across the Earth's bow shock. *Ann. Geophys*. 2001, vol. 19, iss. 3, pp. 275–287. DOI: 10.5194/angeo-19-275-2001.

D'Amicis R., Telloni D., Bruno R. The effect of solar-wind turbulence on magnetospheric activity. *Front. Phys*. 2020, vol. 8, 604857. DOI: 10.3389/fphy.2020.604857.

Ervin T., Jaffarove K., Badman S.T., Huang J., Rivera Ye.J., Bale S.D. Characteristics and source regions of slow Alfvénic solar wind observed by Parker Solar Probe. *Astrophys. J*. 2024, vol. 975, no. 2, 156. DOI: 10.3847/1538-4357/ad7d00.

Greenstadt E.W. Binary index for assessing local bow shock obliquity. *J. Geophys. Res*. 1972, vol. 77, pp. 5467–5479. DOI: 10.1029/JA077i028p05467.

Huang S.Y., Hadid L.Z., Sahraoui F., Yuan Z.G., Deng X.H. On the existence of the Kolmogorov inertial range in the terrestrial magnetosheath turbulence. *Astrophys. J. Lett*. 2017, vol. 836, no. 1, L10. DOI: 10.3847/2041-8213/836/1/L10.

Karimabadi H., Roytershteyn V., Vu H.X., Omelchenko Y.A., Scudder J., Daughton W., et al. The link between shocks, turbulence, and magnetic reconnection in collisionless plasmas. *Phys. Plasmas*. 2014, vol. 21, 062308. DOI: 10.1063/ 1.4882875.

Kilpua E., Koskinen H.E.J., Pulkkinen T.I. Coronal mass ejections and their sheath regions in interplanetary space. *Living Rev. Solar Phys*. 2017, vol. 14, article number 5. DOI: 10.1007/s41116-017-0009-6.

Lacombe C., Belmont G. Waves in the Earth's magnetosheath: observations and interpretations. *Adv. Space Res*. 1995, vol. 15, pp. 329–340. DOI: 10.1016/0273-1177(94)00113-F.

Lepping R.P., Acũna M.H., Burlaga L.F., Farrell W.M., Slavin J.A., Schatten K.H., et al. The WIND Magnetic Field Investigation. *Space Sci Rev*. 1995, vol. 71, pp. 207–229. DOI: 10.1007/BF00751330.

McFadden J.P., Carlson C.W., Larson D., Ludlam M., Abiad R., Elliott B., et al. The THEMIS ESA plasma instrument and in-flight calibration. *Space Sci. Rev*. 2008, vol. 141, pp. 277–302. DOI: 10.1007/s11214-008-9440-2.

Ogilvie K.W., Chornay D.J., Fritzenreiter R.J., Hunsaker F., Keller J., Lobell J., et al. SWE, a comprehensive plasma instrument for the WIND spacecraft. *Space Sci Rev*. 1995, vol. 71, pp. 55–77. DOI: 10.1007/BF00751326.

Pallocchia G., Amata E., Consolini G. Geomagnetic *Dst* index forecast based on IMF data only. *Ann. Geophys*. 2006, vol. 24, pp. 989–999. DOI: 10.5194/angeo-24-989-2006.

Palmroth M., Ganse U., Pfau-Kempf Y., Battarbee M., Turc L., Brito T., et al. Vlasov methods in space physics and astrophysics. *Living Reviews in Computational Astrophysics*. 2018, vol. 4, article number 1. DOI: 10.1007/s41115-018-0003-2.

Podladchikova T.V., Petrukovich A.A. Extended geomagnetic storm forecast ahead of available solar wind measurements. *Space Weather*. 2012, vol. 10, S07001. DOI: 10.1029/2012 SW000786.

Pollock C., Moore T., Jacques A., Burch J., Gliese U., Saito Y., et al. Fast Plasma Investigation for Magnetospheric Multiscale. *Space Sci. Rev*. 2016, vol. 199, pp. 331–406. DOI: 10.1007/s11214-016-0245-4.

Pulinets M.S., Antonova E.E., Riazantseva M.O., Znatkova S.S., Kirpichev I.P. Comparison of the magnetic field before the subsolar magnetopause with the magnetic field in the solar wind before the bow shock. *Adv. Space Res*. 2014, vol. 54, pp. 604–616. DOI: 10.1016/j.asr.2014.04.023.

Rakhmanova L.S., Riazantseva M.O., Zastenker G.N., Verigin M.I. Effect of the magnetopause and bow shock on characteristics of plasma turbulence in the Earth's magnetosheath. *Geomagnetism and Aeronomy*. 2018a, vol. 58, pp. 718–727. DOI: 10.1134/S0016793218060129.

Rakhmanova L., Riazantseva M., Zastenker G., Verigin M. Kinetic scale ion flux fluctuations behind the quasi-parallel and quasi-perpendicular bow shock. *J. Geophys. Res.: Space Phys*. 2018b, vol. 123, pp. 5300–5314. DOI: 10.1029/ 2018JA025179.

Rakhmanova L., Riazantseva M., Zastenker G. Plasma and magnetic field turbulence in the Earth's magnetosheath at ion scales. *Front. Astron. Space Sci*. 2021, vol. 7, 616635. DOI: 10.3389/fspas.2020.616635.

Rakhmanova L., Khokhlachev A., Riazantseva M., Yermolaev Y., Zastenker G. Modification of the turbulence properties at the bow shock: Statistical results. *Front. Astron. Space Sci*. 2024a, vol. 11, 1379664. DOI: 10.3389/fspas. 2024.1379664.

Rakhmanova L., Khokhlachev A., Riazantseva M., Yermolaev Y., Zastenker G. Changes in and recovery of the turbulence properties in the magnetosheath for different solar wind streams. *Universe*. 2024b, vol. 10, no. 5, 194. DOI: 10.3390/universe10050194.

Rakhmanova L., Khokhlachev A., Riazantseva M., Yermolaev Y., Zastenker G. Turbulence development behind the bow shock during disturbed and undisturbed solar wind. *Sol.-Terr. Phys*. 2024c, vol. 10, no. 2, pp. 13–25. DOI: 10.12737/ stp-102202402.

Rème H., Aoustin C., Bosqued J.M., Dandouras I., Lavraud B., Sauvaud J.A., et al. First multispacecraft ion measurements in and near the Earth's magnetosphere with the identical Cluster Ion Spectrometry (CIS) experiment. *Ann. Geophys*. 2001, vol. 19, pp. 1303–1354. DOI: 10.5194/angeo-19-1303-2001.

Riazantseva M.O., Rakhmanova L.S., Zastenker G.N., Yermolaev Yu.I., Lodkina I.G., Chesalin L.S. Small-scale plasma fluctuations in fast and slow solar wind streams. *Cosmic*

Res. 2019, vol. 57, no. 6, pp. 434–442. DOI: 10.1134/S0010952519060078.

Riazantseva M.O., Rakhmanova L.S., Yermolaev Yu.I., Lodkina I.G., Zastenker G.N., Chesalin L.S. Characteristics of turbulent solar wind flow in plasma compression regions. *Cosmic Res.*, 2020, vol. 58, no. 6, pp. 468–477. DOI: 10.1134/S001 095252006009X.

Riazantseva M.O., Treves T.V., Khabarova O., Rakhmanova L.S., Yermolaev Yu.I., Khokhlachev A.A. Linking turbulent interplanetary magnetic field fluctuations and current sheets. *Universe*. 2024, vol. 10, no. 11, 417. DOI: 10.3390/ universe10110417.

Richardson I.G., Cane H.V. Near-Earth interplanetary coronal mass ejections during solar cycle 23 (1996–2009): catalog and summary of properties. *Solar Phys.* 2010, vol. 264, pp. 189–237. DOI: 10.1007/s11207-010-9568-6.

Russell C.T., Anderson B.J., Baumjohann W., Bromund K.R., Dearborn D., Fischer D., et al. The Magnetospheric Multiscale Magnetometers. *Space Sci Rev.* 2016, vol. 199, pp. 189–256. DOI: 10.1007/s11214-014-0057-3.

Šafránková J., Hayosh M., Gutinska O., Němeček Z., Přech L. Reliability of prediction of the magnetosheath B_z component from the interplanetary magnetic field observations. *J. Geophys. Res.* 2009, vol. 114, A12213. DOI: 10.1029/ 2009A014552.

Sahraoui F., Hadid L., Huang S. Magnetohydrodynamic and kinetic scale turbulence in the near-Earth space plasmas: A (short) biased review. *Rev. Mod. Phys.* 2020, vol. 4, article number 4. DOI: 10.1007/s41614-020-0040-2.

Schekochihin A.A., Cowley S.C., Dorland W., Yermolaev Yu.I., Lodkina I.G., Chesalin L.S. Astrophysical gyrokinetics: Kinetic and fluid turbulent cascades in magnetized weakly collisional plasmas. *Astrophys. J. Suppl.* 2009, vol. 182, pp. 310–377. DOI: 10.1088/0067-0049/182/1/310.

Schwartz S.J., Burgess D., Moses J.J. Low-frequency waves in the Earth's magnetosheath: Present status. *Ann. Geophys.* 1996, vol. 14, pp. 1134–1150. DOI: 10.1007/s00585-996-1134-z.

Shevyrev N.N., Zastenker G.N. Some features of the plasma flow in the magnetosheath behind quasi-parallel and quasi-perpendicular bow shocks. *Planet. Space Sci.* 2005, vol. 53, pp. 95–102. DOI: 10.1016/j.pss.2004.09.033.

Spreiter J.R., Summers A.L., Alksne A.Y. Hydromagnetic flow around the magnetosphere. *Planet. Space Sci.* 1966, vol. 14, pp. 223–253.

Turc L., Fontaine D., Escoubet C.P., Kilpua E.K.J., Dimmock A.P. Statistical study of the alteration of the magnetic structure of magnetic clouds in the Earth's magnetosheath. *J. Geophys. Res.: Space Phys.* 2017, vol. 122, pp. 2956–2972. DOI: 10.1002/2016JA023654.

Tóth G., Sokolov I., Gombosi T., Chesney D., Clauer C.R., De Zeeuw D.L., et al. Space Weather Modeling Framework: A new tool for the space science community. *J. Geophys. Res.* 2005, vol. 110, A12226. DOI: 10.1029/2005 JA011126.

Woodham L.D., Wicks R.T., Verscharen D., Owen C.J. The role of proton cyclotron resonance as a dissipation mechanism in solar wind turbulence: A statistical study at ion-kinetic scales. *Astrophys. J.* 2018, vol. 856, no. 1, 49. DOI: 10.3847/1538-4357/aab03d.

Yermolaev Y.I., Nikolaeva N.S., Lodkina I.G., Yermolaev M.Y. Catalog of large-scale solar wind phenomena during 1976–2000. *Cosmic Res.* 2009, vol. 47, pp. 81–94. DOI: 10.1134/ S0010952509020014.

Yermolaev Y.I., Lodkina I.G., Nikolaeva N.S., Yermolaev M.Y. Dynamics of large-scale solar-wind streams obtained by the double superposed epoch analysis. *J. Geophys. Res.: Space Phys.* 2015, vol. 120, pp. 7094–7106. DOI: 10.1002/ 2015JA021274.

Zimbardo G., Greco A., Sorriso-Valvo L., Perri S., Vörös Z., Aburjania G., et al. Magnetic turbulence in the geospace environment. *Space Sci. Rev.* 2010, vol. 156, pp. 89–134. DOI: 10.1007/s11214-010-9692-5.

URL: http://iki.rssi.ru/pub/omni/catalog/ (accessed April 8, 2025).

URL: https://cdaweb.gsfc.nasa.gov/sp_phys/ (accessed April 8, 2025).

URL: https://wdc.kugi.kyoto-u.ac.jp/dstdir/ (accessed April 8, 2025).

How to cite this article
Rakhmanova L.S., Riazantseva M.O., Khokhlachev A.A., Yermolaev Y.I., Zastenker G.N. Features of turbulent cascade development in the magnetosheath during ICME. *Sol.-Terr. Phys.* 2025, vol. 11, iss. 3, pp. 13–21. DOI: 10.12737/stp-113202502.

EFFECT OF SOLAR ACTIVITY AND SOLAR WIND PARAMETERS ON PLASMA TEMPERATURE AND DENSITY IN EARTH'S PLASMASPHERE

G.A. Kotova (ID)
Space Research Institute RAS,
Moscow, Russia, kotova@cosmos.ru

D.V. Chugunin (ID)
Space Research Institute RAS,
Moscow, Russia, dimokch@cosmos.ru

V.V. Bezrukikh
Space Research Institute RAS,
Moscow, Russia, bezrukikh31@mail.ru

Abstract. Measurements from the Interball-1 and Magion-5 satellites of the Interball mission in 1995-2001 have been used to analyze the dependence of the equatorial plasmasphere characteristics on magnetic local time, as well as on solar activity, dynamic pressure, and solar wind density. The proton density at solar minimum is on average higher than at solar maximum, which is probably due to changes in plasma mass composition in the plasmasphere at solar maximum. The daytime and nighttime proton temperatures increase with increasing solar extreme ultraviolet flux, at least in the years of solar maximum. The plasmaspheric plasma density and thermal pressure rise with increasing dynamic pressure and/or density of the undisturbed solar wind, which might be associated with restructuring of the convective electric field in the magnetosphere.

Keywords: cold plasma, density, temperature, magnetic local time, solar activity, geomagnetic activity, solar wind pressure.

INTRODUCTION

Most studies analyzing the solar wind (SW) effect on the inner magnetosphere are limited to considering the outer boundary of the cold plasma region — the plasmapause.

Plasma density variations in the plasmasphere on different L shells (L is the McIlwain parameter, the distance in the magnetic equator plane to the geomagnetic field line in Earth radii R_E) during the day, year, and solar cycle were first discussed in [Park et al., 1978] based on whistler data. The plasma density, determined from the frequency and time of whistler propagation, refers to the equatorial plane of the plasmasphere. The large statistical data obtained from a ground station in California (~110° W) shows annual density variations. The plasma density on the magnetic shell $L \approx 2.5$ in December was ~1.5 times higher than in June. As solar activity decreased in the period from 1957 to 1964, the plasma density also decreased. Moreover, Park et al. [1978] with reference to previous studies emphasized that plasma dynamics in the inner plasmasphere at $L < \sim 3$ differs from plasma dynamics in the outer plasmasphere. Plasma distribution in the inner plasmasphere is little affected by geomagnetic activity and is close to the equilibrium saturation level, when downward plasma flows from the plasmasphere at night are balanced by flows from the ionosphere during the day.

Carpenter and Andersen [1992] have examined not only a change in the location of the plasmapause, but also the dynamics of the cold plasma density in the plasmasphere near the equatorial plane at $2 < L < 8$ under various conditions. Using data from ISEE wave experiments and ground-based whistler research data, an empirical formula have been derived for calculating the maximum electron density N_{eq}, recorded under prolonged quiet geomagnetic conditions,

$$
\begin{aligned}
\lg\left(N_{eq}\left(L, d, R\right)\right) &= -0.3145L + 3.9043 + \\
&+ 0.15\cos\left[2\pi\left(d+9\right)/365\right]\exp\left[-\left(L-2\right)/1.5\right] - \\
&- 0.5\cos\left[4\pi\left(d+9\right)/365\right]\exp\left[-\left(L-2\right)/1.5\right] + \\
&+ \left(0.00127R - 0.0635\right)\exp\left[-\left(L-2\right)/1.5\right],
\end{aligned}
\tag{1}
$$

where d is the ordinal number of the day in the year; R is the sunspot number averaged over 13 months. In (1), the first two terms are the main ones describing a decrease in plasma density with distance away from Earth, but the authors also take into account the increase in cold plasma density with increasing solar activity, annual (or seasonal) variations with maximum density in December, and semi-annual variations with maximum density at the equinox [Carpenter, 1962]. However, Formula (1) does not contain a dependence on the magnetic local time (MLT). To identify such a dependence, there was insufficient data obtained in the inner plasmasphere during long quiet periods.

Later, it was found that annual variations in the density of plasmaspheric plasma are not always accompanied by the observation of the December maximum. The plasma density in the plasmasphere in June may be higher than in winter. This depends on the geographic longitude of the observation area [Menk et al., 2012; Chugunin et al., 2017; Kim et al., 2018]. Yasyukevich et al. [2019] have analyzed total electron content varia-

tions in the plasmasphere (*PEC*) over Irkutsk (52°17' N, 104°18' E) during the daytime and at night for several years (2010–2013). The authors showed that in this region *PEC* values are higher in summer than in winter; increased *PEC* values were also recorded during equinoxes. Correlation with geomagnetic and solar activity indices was observed only for daytime *PEC*.

The direct dependence of the plasmaspheric plasma density on solar activity has not been confirmed either. Shim et al. [2017], indeed, point to a slight increase in *PEC* by 10–30 % at 1336–20200 km with an increase in solar activity, but at the same time they observe a decrease in the electron content near the equatorial plane with an increase in geomagnetic activity during solar maxima. Richards et al. [2000] analyze seasonal plasma density variations in the plasmasphere and indicate that the electron density anticorrelates with both geomagnetic and solar activity due to changes in the neutral hydrogen density of the ionosphere.

Variations in the inner plasmasphere parameters should be closely linked to variations in the upper ionosphere parameters. Plasma density and temperature variations with a period of 27 days (the synodic rotation period of sunspots is 27.2753 days) in the upper ionosphere according to DMSP data have been examined by Rich et al. [2003]. At solar maximum in the dusk sector, the density periodically changes by 40–50 %; and the temperature, by 5–10 %. The 27-day variations in the upper ionosphere parameters were detected at all latitudes below the polar oval. These latitudes correspond to magnetic shells of the plasmasphere. The authors naturally attribute the presence of such variations in the upper ionosphere parameters to variations in the ionizing ultraviolet radiation from the Sun. At the same time, in the lower ionospheric regions in the E or F layers, such variations in plasma parameters are subtle in the equatorial plane [Lee et al., 2012]. According to [Rich et al., 2003; Lee et al., 2012], at low altitudes the distribution of ionospheric plasma is subject to other strong dynamic processes that mask 27-day variations. Rich with co-authors suggested that similar variations in the parameters should exist in the plasmasphere.

The existence of ~27-day plasma density variations in the plasmasphere was reported only when analyzing data obtained by the Van Allen Probes satellites at *L*>4.5 [Thaller et al., 2019]. The authors found no correlation between the plasma density in the outer plasmasphere and the extreme UV flux (EUV, Extreme Ultra Violet) and attributed the observed variations to the effect of the convection electric field in the magnetosphere, i.e. to the processes of emptying and filling the plasmasphere. For the outer plasmasphere, this explanation seems to be quite reasonable.

The direct effect of SW on the plasma density in the plasmasphere was apparently first considered by Kotova et al. [Kotova et al., 2002a, b]. Data obtained by Interball-1 in July–October 1999 in the dusk (15–22 MLT) and dawn (02–10 MLT) sectors on the outer *L* shells of the plasmasphere (*L*~3.5) indicated that the plasma density in the plasmasphere increases with increasing SW dynamic (ram) pressure. A delay between measurements of SW and plasma in the plasmasphere was no longer than 6 hrs.

Jakowski and Hoque [2018] observe that the empirical model of plasmasphere density constructed for *L*<3 indicates that the cold plasma density in the inner plasmasphere is higher on the dayside than on the nightside at the same initial density values at a height of 1000 km. The authors attribute this fact to the compression of the dayside magnetosphere since it is flowed around by the SW stream.

From measurements of SW parameters (density, dynamic pressure, electric field, and the geomagnetic activity index K_p), a numerical model of the plasmasphere with machine learning has been built which can predict characteristics of this region of the magnetosphere 1–2 days in advance [Bianco et al., 2023]. This suggests that the direct effect of SW on the inner magnetosphere is significant and requires careful analysis.

Almost all studies in Earth's plasmasphere are based on measurements of the plasma density, most often the electron density, which can be obtained from various wave experiments that involve examining the low-frequency radiation in the magnetosphere. Direct measurements of plasmaspheric parameters are very rare, but only in such experiments it is possible to determine the thermal plasma temperature and energy.

In this paper, using measurements from the Interball-1 spacecraft and the Czech subsatellite Magion-5 of the Interball mission for 1995–2001, we first analyze the dependence of the equatorial plasmasphere characteristics on the distance to Earth (*L*) and on the magnetic local time, which will reduce the influence of these factors on the search for other causes of plasmaspheric plasma density and temperature variations. Then, we examine the effect of solar activity and SW parameters on the cold proton density and temperature in Earth's plasmasphere.

1. EXPERIMENTAL DATA

This work is based on data acquired by the retarding potential wide-angle cold plasma analyzer PL-48 (Faraday cup) installed on the Interball satellites.

Interball-1 was launched in August 1995 into orbit with an apogee of ~200000 km, a perigee of ~500 km, an inclination of 63.8°, and an orbital period of ~90 hrs. It crossed the plasmasphere ~1 time every 4 days at solar minimum of cycle 23 in 1995–1997 and at solar maximum of the cycle in 1999–2000. In the initial period after launch, the satellite reached the *L* shell closest to Earth L_{min}~1.4. Later, as a result of the evolution of the orbit, its perigee rose and in 1997–1998 during the ascending phase of the solar cycle the satellite only occasionally entered the plasmasphere and recorded cold plasma; from 1999 until the end of its active operation, the perigee of the orbit decreased. In each Interball-1 orbit, minimum *L* values were observed near the magnetic equator, and this made it possible to analyze the dynamics of cold plasma parameters in the magnetic equator plane as a function of *L*, eliminating the latitude dependence [Kotova, Bezrukikh, 2022]. Energy spectra of ions (0–25 eV) were measured for 2 s at different intervals from 30 s to 5 min depending on the telemetry mode.

Magion-5, whose data was also used for the analysis, was launched in August 1996 together with the main spacecraft Interball-2 into an orbit with an inclination of ~65°, a perigee of ~1.2 R_E, and an apogee of ~4 R_E. Because of various technical problems, the PL-48 device data was obtained only from August 1999 to July 2001, when the spacecraft ceased its active operation. Measurements from this spacecraft were carried out with a sufficiently high time resolution; the energy spectrum of thermal protons was measured for 0.4 s in cadence of ~8 s. The orbital period of Magion-5 was ~6 hrs, i.e. it crossed the plasmasphere four times a day. However, for various reasons, most of the data was obtained per day only on one inbound branch of the orbit; occasionally, there is data from two consecutive orbits of the satellite, but also only when it enters the plasmasphere.

Both SC were stabilized by rotating with a two-minute period around an axis directed at the Sun. When calculating plasma parameters from measured spectra, it was assumed that in the thermal region the particles are distributed by energy according to the Maxwellian law, taking into account partial shielding by the potential of the satellite with due regard to the rate of corotation of plasma with Earth and the spacecraft velocity [Kotova et al., 2014].

Databases obtained during periods of weak and moderate geomagnetic activity near the plane of Earth's magnetic equator were created to analyze the dependences of plasmaspheric plasma parameters on solar activity and SW characteristics. This excludes the influence of the magnetic latitude dependence on the data [Artemyev et al., 2014]. Interball-1 data was collected at $1.2<L<5$; and Magion-5 data, at $2.5<L<3.5$. Figure 1 illustrates radial distributions of the proton density (*a*) and temperature (*b*) in the plasmasphere in the equatorial plane according to Interball-1 data [Kotova, Bezrukikh, 2022]. The data is classified by local time; for Interball-1, it turned out that daytime crossings occurred from September to January; and nighttime crossings, from March to July. It is apparent that at $L>3.5$ the dependences, which approximate the density distribution, and the point fields coincide; yet in the inner plasmasphere the density during the day is about 1.5 times higher than at night. The general, regardless of local time and season, equatorial distribution of density N

was approximated by the dependence

$$N = 6500\,L^{-2.7}. \tag{2}$$

Kotova and Bezrukikh [2022] have shown that (2) fits well with other empirical relations derived in a smaller range of distances from Earth. By scaling $N \sim L^{-2.7}$, the data from the two satellites was reduced to $L=3$. This procedure mitigates the effect of the plasmaspheric density dependence on the distance from Earth. The local time dependence is discussed in more detail in the next section. Similarly, the proton temperature T, measured on different L shells by Interball-1 and Magion-5 was reduced to $L=3$, using the expression $T \sim L^{0.4}$, although it can be seen from Figure 1, *b* that distributions of T have a much larger range of values and differ by 15–20 % day and night.

2. MAGNETIC LOCAL TIME DEPENDENCE OF PLASMA CHARACTERISTICS IN THE PLASMASPHERE

Figure 2 shows the magnetic local time dependence of the proton density (*a*) and temperature (*b*) calculated from Magion-5 data. All Magion-5 measurements were made during solar maxima of cycle 23 over the region 50° W – 60° E. Significant changes in the plasmaspheric plasma parameters are observed within 24 hours.

According to the data, the maximum density is observed in the vicinity of noon. At noon (12:00), the proton density exceeds the night density ~2–5 times (Figure 2, *a*). The maximum temperature was recorded at ~16:00 (Figure 2, *b*), which corresponds to the maximum in the diurnal variation of ion and electron temperatures in the ionosphere in the F layer and above [Lyashenko, 2005]. The diurnal behavior of ion density and temperature is seen to be independent of season: the apparent change in the parameters measured in May–July (red dots) near the summer solstice gradually transforms to a change in the parameters measured in winter (blue dots) near the winter solstice. We can also see a slight rise in temperature during early morning hours, which coincides with diurnal temperature variations in the ionosphere.

Figure 1. Proton density (*a*) and temperature (*b*) measured by Interball-1 in the plane of the magnetic equator of the plasmasphere for two MLT intervals (daytime hours 09:00–18:00 (red dots) and night hours 21:00–06:00 (blue dots)), as function of the distance to the center of Earth. The corresponding power-law approximations are highlighted in the same colors. The black curve in panel *a* indicates general approximation (2)

Figure 2. Proton density (*a*) and temperature (*b*) measured by Magion-5 in the plane of the magnetic equator of the plasmasphere as function of the magnetic local time. Black dots mark all measurements; red dots, measurements made in May–July near the summer solstice; and blue dots, parameters measured in winter near the winter solstice.
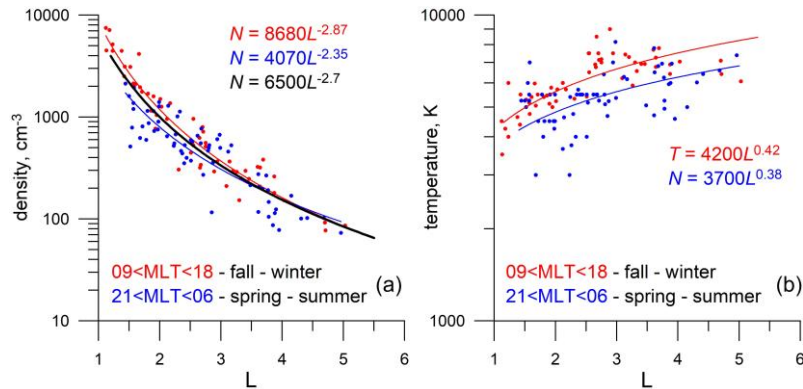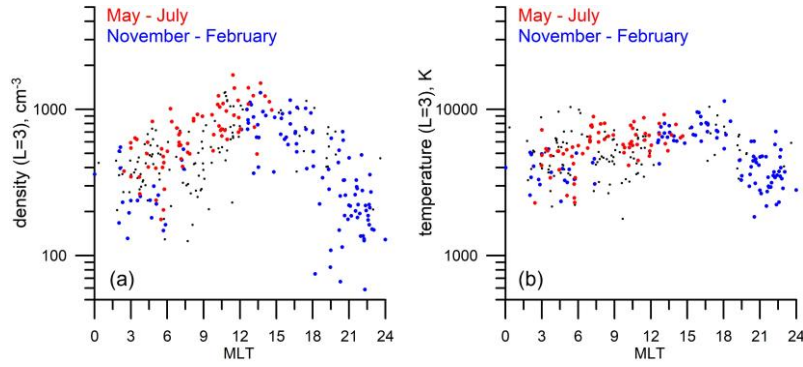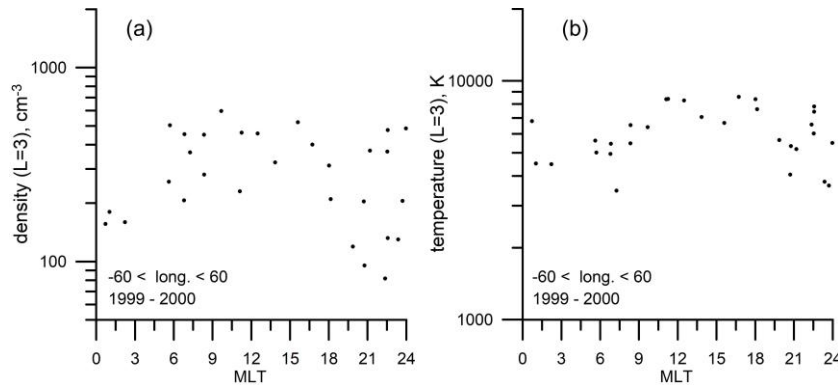

Figure 3. Magnetic local time dependences of the proton density (a) and temperature (b) measured by Interball-1 in the plane of the magnetic equator of the plasmasphere. The presented measurements were carried out in 1999–2000 in the range of geographic longitudes from –60° to 60°

Interball-1 data relates to the years of both low solar activity (1995–1997) and solar maximum (1999–2000). When presenting all the data depending on MLT, no daily change in the parameters is observed. Figure 3 illustrates variations in the proton density and temperature during the day, but measured only during solar maximum in the range 60° W — 60° E. Despite the small number of points, the diurnal behavior of the temperature and density is similar to that shown in Figure 2 according to Magion-5 data.

3. EFFECT OF SOLAR ACTIVITY ON PLASMASPHERIC PLASMA CHARACTERISTICS

As already mentioned, the Magion-5 measurements were carried out during solar maxima of cycle 23 when the parameters characterizing solar activity vary widely and this makes it possible to see the solar activity dependence of the proton density and temperature in the plasmasphere. Interball-1 measurements were made both during solar minimum (1995–1997) and solar maximum of the cycle, which allows us to compare the plasmaspheric plasma density and temperature in different periods.

Figure 4 plots the proton density (*a*, *b*) and temperature (*c*) in the plasmasphere, measured near the plane of the magnetic equator and normalized to *L*=3, as function of the sunspot number R_s (*a*) and the solar radio emission flux *F*10.7 (*b*, *c*).

The index *F*10.7 correlates well with the EUV solar flux. This flux is the main factor of ionospheric ionization from the E layer and higher [Chen et al., 2011]. Although *F*10.7 does not always correctly describe the EUV radiation flux, it is usually used to estimate its variations.

Interball-1 data (Figure 4, *a*, *b*) indicates that the proton density at solar minimum of the cycle (green dots) is on average higher than at solar maximum (purple dots). Any dependence of the proton density in the plasmasphere on these indices was failed to be identified from Magion-5 data at solar maximum when R_s changed from 40 to 350; and *F*10.7, from 120 to 325. However, both day and night proton temperatures are seen to increase with increasing solar activity (Figure 4, *c*).

4. 27-DAY AND ANNUAL VARIATIONS IN PLASMASPHERIC PARAMETERS

Figure 5 shows an attempt to detect ~27 day proton temperature and density variations in the plasmasphere. Vertical lines indicate official data on the beginning of Carrington cycles (~27.3 days) [https://www.astroleague.org/files/obsclubs/Carrington%20Rotation%20Start%20Dates.pdf]. The bottom panel depicts changes in *F* 10.7. The peak of this index in late March – early April 2001 was linked with strong X-class solar flares during this period.

Figure 4. Proton density (*a*, *b*) and temperature (*c*), measured by Interball-1 (*a*, *b*) and Magion-5 (*c*) in the plane of the magnetic equator of the plasmasphere, as function of the solar activity indices R_s (*a*) and $F10.7$ (*b*, *c*). Measurements at solar minimum (1995–1997) are highlighted in green in the left panels (*a*, *b*); measurements at solar maximum (1999–2000), in purple. In the right panel (*c*), daytime measurements (06–18 MLT) are shown in red; and nighttime measurements (18–06 MLT), in blue
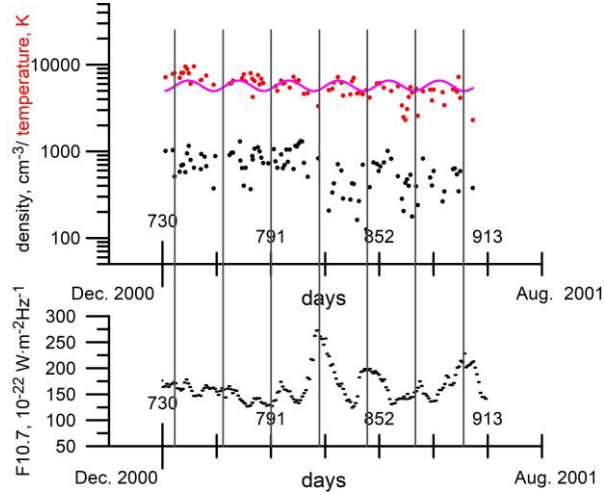
Figure 5. Proton temperature (top panel) and density (middle panel) variations measured by Magion-5 in the plane of the magnetic equator of the plasmasphere from January to June 2001. Along the X-axis are the days since 1999. The pink curve in the top panel indicates temperature data approximated by the sinusoidal dependence. Bottom panel depicts $F10.7$ variations [https://cdaweb.gsfc.nasa.gov/index.html]. Vertical lines are the beginnings of Carrington solar rotations, as observed from Earth [https://www.astroleague.org/iles/obsclubs/Carrington%20Rotation%20Start%20Dates.pdf]

Sinusoidal temperature variations from January to June 2001 with a period of ~28 days can be distinguished, but there is no noticeable correlation with $F10.7$. This is not surprising since the correlation of plasma temperature and density in the plasmasphere with $F10.7$ is poorly resolved (Figure 4, *b*, *c*).

Figure 6 illustrates the temperature (red dots) and density (blue) variations measured by Magion-5 and normalized to $L=3$ over the entire operation period of PL-48. The plot of proton temperature variations shows semi-annual variations with maxima in the vicinity of the equinox periods in spring (March 21) and autumn (September 23), but the annual period of temperature and density variations is also distinguished (highlighted by vertical dashed lines). The maximum in May–June

2000 prevails in the plot of density variations. This maximum, as in February–March 2001, is obviously a consequence of the midday density maximum (see Figure 2) since the measurements during this period were made in the daytime sector of the plasmasphere. Figure 2 shows that in the inner plasmasphere the plasma density dependence on local time is more significant than the seasonal dependence, at least in the longitude sector in which Magion-5 performed measurements (50° W – 60° E). The temperature dynamics seems to indicate the same thing. The local maximum proton temperature observed near the vernal equinox in early April 2000 (~460 days) was recorded at ~16–17 MLT. Then the temperature reaches a local maximum in the middle of August 2000 at ~6 MLT. At the same hours, temperature maxima are seen in Figure 2, *b*, although periods of these observations are close to the spring and autumn equinoxes.

Interball-1 made measurements not so frequently as Magion-5; therefore, the amount of data is insufficient to examine seasonal variations in plasmaspheric plasma parameters.

5. RELATIONSHIP OF ION DENSITY AND THERMAL PRESSURE IN THE PLASMASPHERE WITH SOLAR WIND DENSITY AND DYNAMIC PRESSURE

Despite Interball-1 crossing Earth's plasmasphere only once every four days and only at a sufficiently low perigee of the orbit, the long period of its operation makes it possible to analyze the dependence of cold plasmaspheric plasma characteristics on the parameters of the SW stream impinging upon Earth's magnetosphere.
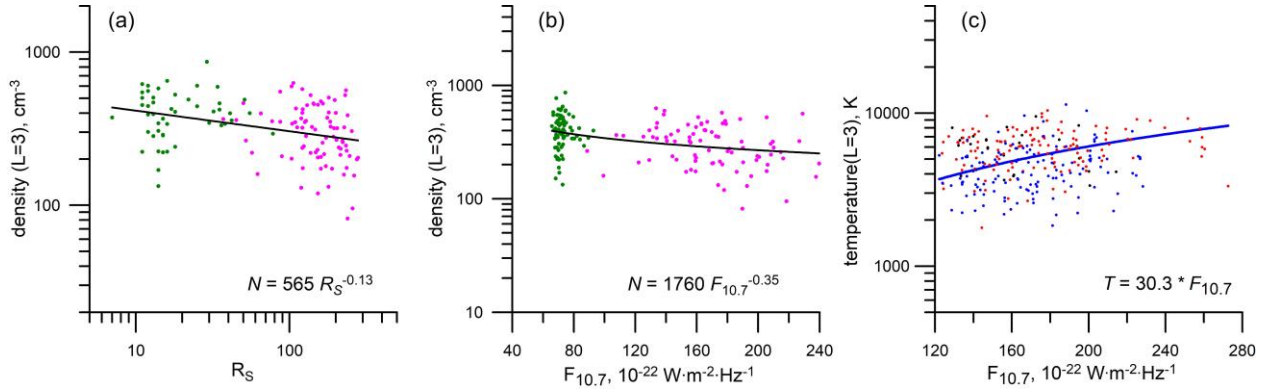
Figure 7 plots the proton density (*a*, *b*) and thermal pressure (*c*), measured by Interball-1 in the plane of the magnetic equator of the plasmasphere, as function of the SW density N_{SW} (*a*) and dynamic pressure (*b*, *c*) ρV_{SW}^2 (p is the mass density, V_W *is* the SW velocity). Straight lines represent approximating dependences; while the black color (*a*, *b*) highlights the dependences obtained
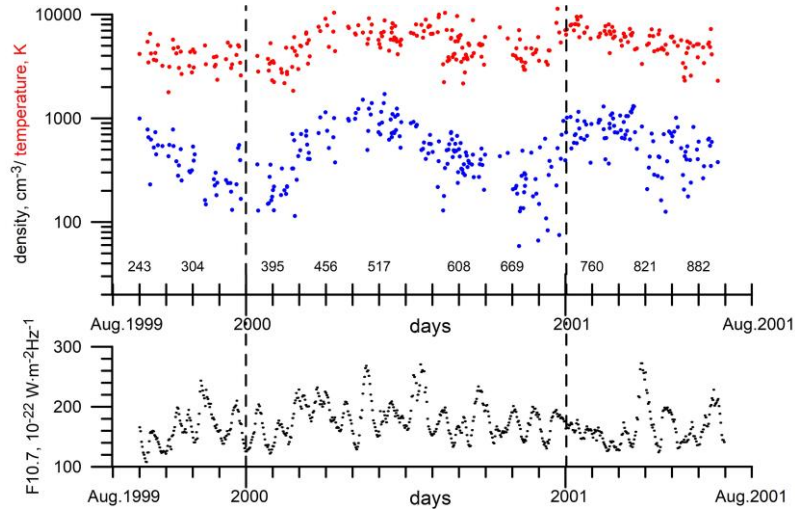
Figure 6. Proton temperature (red dots) and density (blue) variations, measured by Magion-5 in the plane of the magnetic equator of the plasmasphere, from September 1999 to June 2001. Along the X-axis are the days since 1999. The bottom panel illustrates *F*10.7 variations [https://cdaweb.gsfc.nasa.gov/index.html]. Vertical lines indicate a change of year

Figure 7. Proton density (*a*, *b*) and thermal pressure (*c*), measured by Interball-1 in the plane of the magnetic equator of the plasmasphere, as function of SW density N_{SW} (*a*) and dynamic (ram) pressure (*b*, *c*). The green color highlights measurements at solar minimum (1995–1997); purple, at solar maximum (1999–2000). Straight lines are approximating dependences

for all points (relations in black). Coefficients of determination *D* are also given for approximations of all measurements. In panel *b*, for example, the corresponding colors indicate approximations separately for measurements made during years of solar minimum and maximum. The dependences are seen to be similar. At the same time, it has been demonstrated once again that the thermal proton density in the plasmasphere during years of low solar activity is on average higher than during years of high solar activity.

The dependences shown in panels *a* and *b* are interrelated since the SW dynamic pressure depends largely on its density (Figure 8). The red line and the corresponding ratio in panel *a* are derived from the equations $N = 142.3\rho V_{SW}^2$ and $\rho V_{SW}^2 = 0.28 N_{SW}$. The calculated dependence practically coincides with the approximation obtained. Thus, it is impossible to say which dependence is the main one.

The dependence in panel *c* may be due to the dependence of the proton density in the plasmasphere on the SW dynamic pressure (*b*).
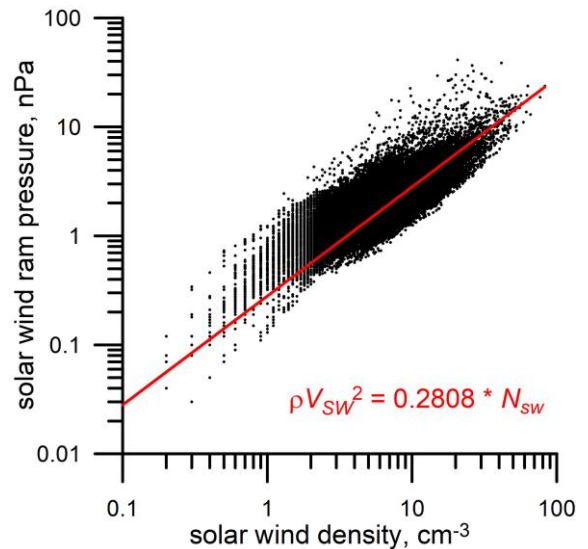
Figure 8. SW dynamic (ram) pressure as function of proton density on August 01, 1995–September 30, 2000

The Magion-5 data indicate the presence of the same relationships between the plasmaspheric plasma characteristics and the SW parameters, yet only for the dayside plasmasphere (Figure 9).

6. DISCUSSION

Using Interball data, we have tried to analyze in as much detail as possible various factors that have an effect on changes in the cold plasma density and temperature in the equatorial plane of Earth's inner plasmasphere. The main factor responsible for the distribution of cold plasmaspheric plasma density and temperature near Earth is the distance of magnetic plasma shells from Earth. To exclude the effect of the distance of the plasma measurement site from Earth, the data was scaled to the magnetic shell $L=3$. We analyzed the data obtained only inside the plasmasphere, but not near its boundary layer or in plasmaspheric plumes.

The second factor that can significantly affect the plasma distribution in the plasmasphere is the local time. The measurements carried out by Magion-5 during the years of high solar activity suggest that there is a strong dependence of the proton density on the local measurement time. The maximum density is observed at ~12 MLT; the density at night is on average 2–5 times lower.

Proton temperature variations in the inner plasmasphere as function of MLT are similar to diurnal variations in ionospheric temperature, which is confirmed by the analysis performed earlier in [Kotova et al., 2002a, 2008]. Magion-5 data has shown that the ion temperature in the plasmasphere at $L<\sim2.5$–2.8 is close to the electron temperature in the upper ionosphere at all MLT values, except for the midday-evening region (12–20 MLT), where the temperature in the plasmasphere is higher than in the ionosphere [Kotova et al., 2008]. The ratio of the ion temperature in the plasmasphere to the electron temperature in the upper ionosphere increases with L. During years of high solar activity, this temperature ratio increases faster than during years of low solar activity [Kotova, Bezrukikh, 2022].

The Interball-1 data, which relates to the period of high solar activity, confirm the diurnal proton density and temperature variations measured by Magion-5.

However, it is possible that due to the noticeable difference between Earth's magnetic and geographic axes the ion density increase during daylight hours and diurnal temperature variations also depend on the geographic longitude of the site over which measurements are made. The available data is insufficient to verify this.

In addition to the two obvious factors that determine the plasmaspheric plasma density and temperature, solar and geomagnetic activity, as well as the SW stream impinging upon Earth and forming plasma and magnetic field distribution in the magnetosphere have a significant effect on cold plasma parameters.

According to Interball-1 data obtained during solar minimum and maximum of cycle 23, the proton density of the inner plasmasphere during the years of low solar activity was on average higher than during the years of high solar activity. Interball-1 measurements during minimum and maximum of the solar cycle are evenly distributed in local time. The spread of density values is quite large (see Figure 4). This result is inconsistent with that obtained earlier [Park et al., 1978] from ground-based Whistler measurements in 1957–1964. The results received from the data on the total electron content in the plasmasphere [Shim et al., 2017] depend primarily on determination of *PEC* that may or may not include the region of the upper ionosphere with a predominance of oxygen ions. The height of the transition from oxygen to hydrogen also depends on many factors.

A more likely reason for the difference between the Interball-1 data obtained during solar minimum and maximum and the wave measurements of electron density is the difference in the mass composition of plasmaspheric plasma during these periods. From Interball-1 measurements we determine only the proton density by calculating it through Maxwellian distribution approximation of the main peak in the ion energy spectrum [Kotova et al., 2014]. Meanwhile, various data has shown that with an increase in solar activity and $F10.7$ the relative content of helium and oxygen ions in the plasmasphere increases [Craven et al., 1997; Denton et al., 2025]. Due to the quasineutrality of plasma, the electron density is equal to the sum of densities of all positive ions, so with a significant increase in the number of heavier ions the proton density may decrease.
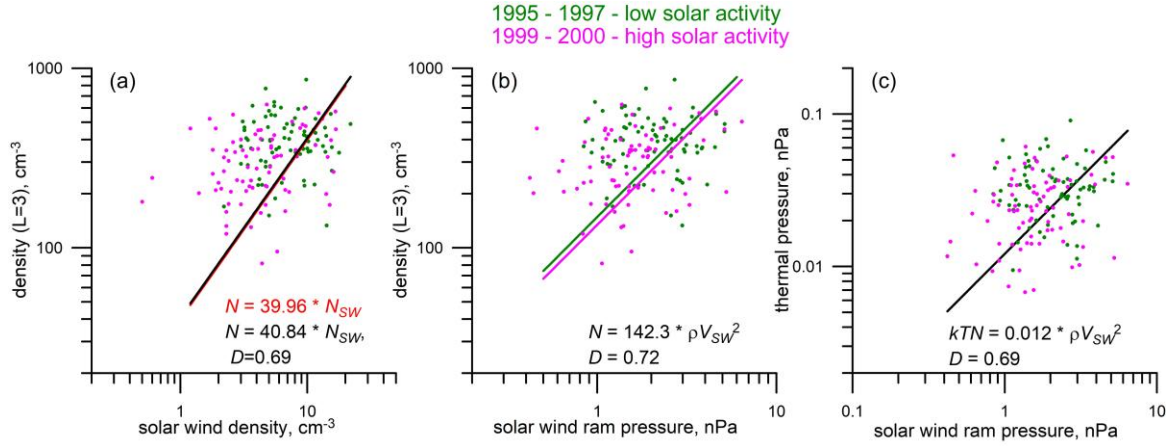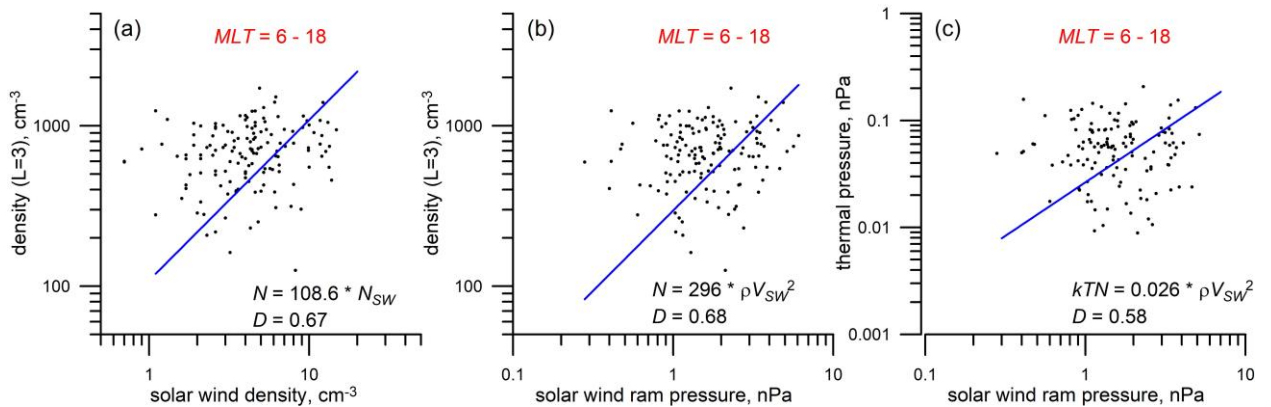

Figure 9. Proton density (*a*, *b*) and thermal pressure (*c*), measured by Magion-5 in the plane of the magnetic equator of the dayside plasmasphere, as function of solar wind density N_{SW} (*a*) and dynamic (ram) pressure ρV_{SW}^2 (*b*, *c*). Straight lines are approximating dependences

No trend was found in the proton temperature from comparison between Interball-1 measurements at solar minimum and maximum. More detailed Magion-5 data acquired during solar maximum does not indicate any dependence of ion density on solar activity, but suggests that both daytime and nighttime proton temperatures rise with increasing solar activity indices.

When analyzing the proton density and temperature variations measured by Magion-5 in the plane of the magnetic equator of the plasmasphere, it is impossible to determine seasonal variations during the years of maximum of the cycle (September 1999 – June 2001) since diurnal variations are clearly more significant, which apparently mask less significant seasonal variations in the parameters.

Sometimes we can detect 27-day temperature variations in the plasmasphere, but more data is needed for detailed analysis of such variations and their relationship with the solar EUV flux.

The data reviewed mainly relate to periods of low and moderate geomagnetic activity. Measurements performed during the main phase of magnetic storms on October 22, 1999 and January 13, 1996 with Interball-1, on October 15, 1999, June 26, 2000, August 29, 2000, March 20, 2001, and March 28, 2001 with Magion-5 (one flyby through the plasmasphere on August 13, 2000 during recovery from a strong storm (minimum Dst=–234 nT, August 12)), as well as measurements from this satellite during SSC on November 26, 2000, do not stand out from the rest of the plasmaspheric data. No dependence of the proton density or temperature of the inner plasmasphere on the geomagnetic activity indices K_p, Dst, AE was revealed. This, however, applies to the mean characteristics of the plasmasphere. In order to see changes in plasma characteristics in a single event, say, during one magnetic storm, it is necessary to measure plasma density and temperature in one region for a long time. Once in 6 hrs, such measurements were carried out by Interball-2 [Verigin et al., 2011]. It has been shown that during the main phase of magnetic storms the ion temperature of the plasmasphere generally decreases, whereas the plasma density increases or remains at the level characteristic of undisturbed conditions. We managed to explain this behavior of ion temperature, using a model of drift shell displacement from Earth caused by a decrease in the magnetic field in the inner plasmasphere during a magnetic storm.

Finally, let us turn to the dependence of the plasmaspheric characteristics on the SW parameters. Interball-1 data suggests that the plasmaspheric plasma density increases with increasing SW external (dynamic) pressure. The same dependence in the dayside plasmasphere is indicated by Magion-5 data. The SW pressure plays a major role in the interaction between the geomagnetic field and the SW stream. This interaction determines the shape of the magnetosphere, its compression from the daytime side, and the anti-sunward extended magnetotail. Nonetheless, inside the magnetosphere the cold magnetospheric plasma pressure is extremely low compared to the magnetic field pressure and cannot directly depend on the SW pressure. The formation of the plasmasphere and plasmapause is, however, significantly determined by the electric field of convection in the magnetosphere. The magnitude and distribution of this convection field in the magnetosphere depend presumably on SW pressure [Lukyanova, 2004]. It is likely in this indirect way that the SW pressure and density affect the density of cold protons. This issue requires serious theoretical analysis.

CONCLUSION

Using Interball-1 and Magion-5 data obtained in Earth's plasmasphere near the equatorial plane, we have analyzed possible causes of thermal (cold) proton density and temperature variations. The following results have been received.

The main factors responsible for cold plasma density and temperature variations in the equatorial plane of the plasmasphere include the distance of the magnetic shell from Earth and the local time. On average, proton temperature variations in the inner plasmasphere depending on MLT are similar to diurnal temperature variations in the ionosphere — maximum temperatures are observed after dawn and after noon. According to Magion-5 data, during the years of high solar activity the maximum proton density was observed at ~12 MLT.

In addition, the plasma density and temperature in the inner plasmasphere depend on the phase of the 11-year solar cycle. The proton density at solar minimum is on average higher than at solar maximum, which is likely to be due to changes in the mass composition of plasma in the plasmasphere and a decrease in the proportion of protons in the ion density during the maximum phase. Day and night proton temperatures increase with increasing solar UV flux, at least during the years of solar maximum.

The plasmaspheric plasma density and thermal pressure increase with increasing dynamic pressure and/or density of undisturbed SW, which is probably due to the restructuring of the convection electric field in the magnetosphere.

For a more complete study of the causes of variations in thermal plasmaspheric plasma characteristics, on the one hand, it is necessary to analyze data from ground-based and satellite wave measurements that allow us to determine the density of background plasma in order to assess the daily behavior of density in various longitude sectors throughout the solar cycle. Additional analysis of the behavior of plasmaspheric plasma temperature in the absence of new local plasma measurements should probably be carried out using data from previous experiments performed, for example, by the Dynamics Explorer-1, 2 (DE-1 and DE-2) satellites. On the other hand, to understand the causes of changes in the plasmasphere characteristics, it is necessary to theoretically analyze the physical relationships between processes in the magnetosphere and interplanetary medium.

REFERENCES

Artemyev A.V., Kotova G.A., Verigin M.I. Role of the field-aligned density distribution for efficiency of electron scattering by hiss waves. "Physics of Auroral Phenomena". *Proc. XXXVII Annual Seminar. Apatity*. 2014, pp. 55–58.

Bianco S., Haas B., Shprits Y. PINE-RT: An operational real-time plasmasphere model. *Front. Astron. Space Sci*. 2023, vol. 10, 1116396. DOI: 10.3389/fspas.2023.1116396.

Carpenter D.L. Electron-density variations in the magnetosphere deduced from whistler data. *J. Geophys. Res*. 1962, vol. 67, no. 9, pp. 3345–3360. DOI: 10.1029/JZ067i009p03345.

Carpenter D.L., Anderson R.R. An ISEE/whistler model of equatorial electron density in the magnetosphere. *J. Geophys. Res*. 1992, vol. 97, pp. 1097–1108. DOI: 10.1029/91JA01548.

Chen Y., Liu L., Wan W. Does the *F*10.7 index correctly describe solar EUV flux during the deep solar minimum of 2007–2009? *J. Geophys. Res*. 2011, vol. 116, A04304. DOI: 10.1029/2010JA016301.

Chugunin D.V., Kotova G.A., Klimenko M.V., Klimenko V.V. Longitudinal dependence of the H+ concentration distribution in the plasmasphere according to Interball-1 satellite data. *Cosmic Res*. 2017, vol. 55, no. 6, pp. 457–463. DOI: 10.1134/S001095251706003X.

Craven P.D., Gallagher D.L., Comfort R.H. Relative concentration of He+ in the inner magnetosphere as observed by the DE 1 retarding ion mass spectrometer. *J. Geophys. Res*. 1997, vol. 102, no. A2, pp. 2279–2289. DOI: 10.1029/96JA02176.

Denton R.E., Takahashi K., Hartley D.P. Models for plasmasphere and plasmatrough density and average ion mass including dependence on L, MLT, geomagnetic activity, and phase of the solar cycle. *Front. Astron. Space Sci*. 2025, vol. 11, 1459281. DOI: 10.3389/fspas.2024.1459281.

Jakowski N., Hoque M.M. A new electron density model of the plasmasphere for operational applications and services. *J. Space Weather Space Clim*. 2018, vol. 8, no. A16. DOI: 10.1051/swsc/2018002.

Kim E., Kim Y.H., Jee G., Ssessanga N. Reconstruction of plasmaspheric density distributions by applying a tomography technique to Jason-1 plasmaspheric TEC measurements. *Radio Sci*. 2018, vol. 53, pp. 866–873. DOI: 10.1029/2017 RS006527.

Kotova G.A., Bezrukikh V.V. The density and temperature distributions of thermal protons in the magnetic equatorial plane of the Earth's plasmasphere according to the Interball-1 spacecraft data. *Geomagnetizm and Aeronomy*. 2022, vol. 62, no. 5, pp. 546–554. DOI: 10.1134/S0016793222050061.

Kotova G., Bezrukikh V., Verigin M., Smilauer J. New aspects in plasmaspheric ion temperature variations from Interball 2 and Magion 5 measurements. *J. Atmos. Solar-Terr. Phys*. 2008, vol. 70, no. 2-4, pp. 399–406. DOI: 10.1016/j.jastp.2007. 08.054.

Kotova G., Bezrukikh V., Verigin M. The effect of the Earth's optical shadow on thermal plasma measurements in the plasmasphere. *J. Atmos. Solar-Terr. Phys*. 2014, vol. 120, pp. 9–14. DOI: 10.1016/j.jastp.2014.08.013.

Kotova G.A., Bezrukikh V.V., Verigin M.I., Lezhen L.A. Temperature and density variations in the dusk and dawn plasmasphere as observed by INTERBALL TAIL in 1999–2000. *Adv. Space Res*. 2020a, vol. 30, no. 7, pp. 1831–1834. DOI: 10.1016/S0273-1177(02)00458-1.

Kotova G.A., Bezrukikh V.V., Verigin M.I., Lezhen L.A., Barabanov N.A. Interball 1/ Alpha 3 cold plasma measurements in the evening plasmasphere: quiet and disturbed magnetic conditions. *J. Adv. Space Res*. 2002b, vol. 30, iss. 10, pp. 2313–2318. DOI: 10.1016/S0273-1177(02)80256-3.

Lee C.-K., Han S.-C., Bilitza D., Seo K-W. Global characteristics of the correlation and time lag between solar and ionospheric parameters in the 27-day period. *J. Atmos. Solar-Terr. Phys*. 2012, vol. 77, pp. 219–224. DOI: 10.1016/j.jastp.2012.01.010.

Lukianova R.Yu. Effect of abrupt changes in the solar wind dynamic pressure on the polar cap convection. *Geomagnetism and Aeronomy*. 2004, vol. 44, no. 6, pp. 691–702.

Lyashenko M.V. Variations of ionospheric plasma parameters during 23 cycle of solar activity decline. VIII Conference of Young Scientists. Section «Physics of Near-Earth Space», BSFP-2005. Proc. 2005, pp. 108–112. (In Russian). URL: http://bsfp.iszf.irk.ru/sites/default/files/school/2005/Lyashenko-108-112.pdf (accessed May 30, 2025).

Menk F.W., Ables S.T., Grew R.S., Clilverd M.A., Sandel B.R. The annual and longitudinal variations in plasmaspheric ion density. *J. Geophys. Res*. 2012, vol. 117, A03215. DOI: 10.1029/2011JA017071.

Park C.G., Carpenter D.L., Wiggin D.B. Electron density in the plasmasphere: Whistler data on solar cycle, annual, and diurnal variations. *J. Geophys. Res*. 1978, vol. 83, no. A7, pp. 3137–3144. DOI: 10.1029/JA083iA07p03137.

Rich F.J., Sultan P.J., Burke W.J. The 27-day variations of plasma densities and temperatures in the topside ionosphere. *J. Geophys. Res*. 2003, vol. 108, no. A7, 1297. DOI: 10.1029/2002JA009731.

Richards P.G., Chang T., Comfort R.H. On the causes of the annual variation in the plasmaspheric electron density. *J. Atmos. Solar-Terr. Phys*. 2000, vol. 62, pp. 935–946.

Shim J.S., Jee G., Scherliess L. Climatology of plasmaspheric total electron content obtained from Jason 1 satellite. *J. Geophys. Res*. 2017, vol. 122, pp. 1611–1623. DOI: 10.1002/ 2016JA023444.

Thaller S.A., Wygant J.R., Cattell C.A., Breneman A.W., Tyler E., Tian S., et al. Solar rotation period driven modulations of plasmaspheric density and convective electric field in the inner magnetosphere. *J. Geophys. Res*. 2019, vol. 124, pp. 1726–1737. DOI: 10.1029/2018JA026365.

Verigin M.I., Kotova G.A., Bezrukikh V.V., Bogdanov V.V., Kaisin A.V. Ion dift in the Earth's inner plasmasphere during magnetospheric disturbances and proton temperature dynamics. *Geomagnetism and Aeronomy*. 2011, vol. 51, no. 1, pp. 39–48. DOI: 10.1134/S0016793211010154.

Yasyukevich A.S., Vesnin A.M., Yasyukevich Yu.V., Padokhin F.M. Correlation between total and plasmasphere electron content and indexes of solar and geomagnetic activity. *Russian Open Conference on Radio Wave Propagation (RWP)*. Kazan. Russia. 2019, pp. 87–90. DOI: 10.1109/ RWP.2019.8810364

URL: https://www.astroleague.org/files/obsclubs/Carrington%20Rotation%20Start%20Dates.pdf (accessed May 30, 2025).

URL: https://cdaweb.gsfc.nasa.gov/index.html (accessed May 30, 2025).

INFLUENCE OF INTERPLANETARY PARAMETERS
ON THE DEGREE OF SYMMETRY OF THE RING CURRENT

G.A. Makarov (ID)
Yu.G. Shafer Institute of Cosmophysical Research
and Aeronomy SB RAS,
Yakutsk, Russia, gmakarov@ikfia.ysn.ru

Abstract. The paper studies the influence of interplanetary factors on the degree of symmetry of the magnetospheric ring current. The geomagnetic indices *SYM-H*, *ASY-H,* and interplanetary parameters for the period 1981–2015 are considered. The indicator of the degree of symmetry of the ring current is the ratio *SYM-H/ASY-H*. Analysis is based on annual averages of geomagnetic and interplanetary parameters. This approach allows us to identify large-scale patterns. The relationships are examined of the degree of symmetry of the ring current and the indices *SYM-H* and *ASY-H* with the value *B* of the interplanetary magnetic field (IMF), the IMF north-south component B_n, and the solar wind velocity *V*. It is concluded that properties of magnetospheric ring currents are described by these indices more adequately when offsets in their values are taken into account than without regard for them. It is found that when offsets in *ASY-H* are considered the symmetric ring current prevails approximately twice over the asymmetric one for average conditions in the solar wind: *V*<550 km/s, *B*<10 nT, |B_n|<2 nT. Under quiet solar wind conditions (*V*<450 km/s, *B*<5.5 nT, |B_n|<0.7 nT), the degree of symmetry of the ring current increases. It is established that with intensification of interplanetary parameters (*V*, *B*, |B_n|) the symmetric ring current index *SYM-H* grows more strongly than the asymmetric ring current index *ASY-H*.

Keywords: geomagnetic indices *SYM-H* and *ASY-H*, magnetospheric ring current, interplanetary parameters.

INTRODUCTION

The magnetospheric ring current consists of two main parts: symmetric and asymmetric. The geomagnetic indices *SYM* and *ASY* were developed to estimate the symmetric and asymmetric ring current components respectively [Iyemori et al., 1992].

Quite a lot of works have studied the influence of interplanetary parameters on the *SYM* and *ASY* indices. Shi et al. [2006] have found that when the interplanetary magnetic field (IMF) north-south component B_n is negative, an increase in the solar wind (SW) dynamic pressure additionally enhances the ring current asymmetry. Singh et al. [2013] have examined the effect of smooth and abrupt changes in IMF B_n on *ASY-H* and *ASY-D* during magnetic substorms. Haiducek et al. [2017], using the SWMF system, have modelled the forecast of the geomagnetic indices K_p, *SYM-H*, *AL* and have established that the model excels at predicting *SYM-H*. Bhaskar and Vichare [2019] with the aid of an artificial neural network have successfully predicted *SYM-H* and *ASY-H* during nine geomagnetic storms of solar cycle 24; the SW velocity and density, as well as IMF *B*, B_y, B_z were utilized as input data. During the main phase of severe storms, there are noticeable deviations of the predicted index values from the observed ones, which indicates the effect of internal factors such as magnetospheric processes. In [Makarov, 2022] based on extensive statistical data, the relationships of *SYM-H* and *ASY-H* with key interplanetary parameters have been analyzed and it has been obtained that the dependence of *ASY-H* and *SYM-H* on the IMF north-south component is determined by the IMF strength. Moreover, it has been found that *SYM-H* and *ASY-H* depend on the SW plasma parameter β: their absolute values decrease with increasing β regardless of the sign of IMF B_n [Makarov, 2024]. It is assumed that this is due to the transition of the magnetosphere to quiet state because of the increasing predominance of thermal pressure over magnetic pressure in SW and a decrease in the level of turbulence.

Correlation relationships between *ASY-H* and interplanetary medium parameters for 107 magnetic storms with *Dst*<–50 nT induced by SW streams of different types (CIR — corotating interaction regions and ICME — interplanetary coronal mass ejections) have been investigated in [Boroev, Vasiliev, 2020] and it has been found that average *ASY-H* during the magnetic storm main phase depends on the electric field and the IMF southward component regardless of the stream type; no relationship between *ASY-H* and SW velocity has been detected. Namuun et al. [2023] have examined correlation relationships between *SYM-H* and various interplanetary parameters for 131 CME-driven magnetic storms and 161 CIR-induced magnetic storms. The authors have concluded that *SYM-H* in the case of CME storms has a greater dependence on the SW velocity and the convective electric field, and in the case of CIR storms it more strongly depends on the SW electric field, the velocity of the open magnetic flux *d*φ/*dt*, and the reconnection electric field E_{KL}.

Symmetric and asymmetric ring currents have different properties [Bakhmina, Kalegaev, 2008]. The symmetric ring current is formed due to decoupled motion of magnetospheric plasma protons and electrons, trapped by the geomagnetic field along closed trajectories around Earth, and it exists constantly. The partial ring current is formed in the night and dusk sectors near the geomagnetic equator due to enhanced magnetospheric convection during disturbances. The partial ring current is thought to develop during the magnetic storm main phase and to decay immediately after its maximum [Barkhatov et al., 2008]. Although the weak longitude asymmetry of the magnetospheric magnetic field measured on Earth's surface is also present during geomagnetically quiet periods, it is not known for certain whether it is related to the existence of the partial ring current in the quiet magnetosphere [Kalegaev et al., 2008].

Weygand and McPherron [2006] have studied such a characteristic of ring currents as the degree of symmetry, defined as the *SYM-H/ASY-H* ratio. They have figured out that the ring current is always asymmetric. Examining *SYM* and *ASY* variations, the authors [Weygand, McPherron, 2006; Iyemori et al., 2010] have revealed that there are offsets of their values. According to the definition given in these papers, offset is a non-zero index value under magnetically quiet conditions. Weygand and McPherron [2006] have suggested that the offsets may be caused by the joint effect of various magnetospheric current systems. Earlier in [Alexeev et al., 1996; Maltsev et al., 1996; Tsyganenko, Sitnov, 2005], it has been shown that not only the ring current itself, but also magnetopause currents, the magnetotail, and field-aligned currents contribute to geomagnetic characteristics of the ring current.

Most works on the relationship of *SYM* and *ASY* with interplanetary parameters have been performed for storm and sub-storm conditions. The study of solar-terrestrial relations and space weather phenomena is incomplete without taking into account the large-scale properties of the ring current and its long-term dynamics. Such properties can be investigated by analyzing data with a time resolution of a day or longer. Such studies are often conducted by statistical methods using daily and annual average terrestrial, interplanetary, and solar parameters. For daily average terrestrial parameters, different phases of geomagnetic storms may overlap; therefore, the storm parameters (phase, intensity, duration, etc.) will largely be smoothed over. In this regard, it is important to study variations in annual average *SYM* and *ASY* obtained from daily average data. The purpose of the work is to examine the effect of interplanetary parameters on the degree of magnetospheric ring current symmetry.

EXPERIMENTAL DATA

The *SYM* and *ASY* indices are calculated from the *H* and *D* components of the geomagnetic field at six mid-latitude stations (the network consists of more than ten stations). These indices have a 1-min time resolution and are divided into *SYM-H*, *SYM-D*, *ASY-H*, and *ASY-D*. *SYM-H* and *SYM-D* are, in fact, averaged deviations

of the geomagnetic field *H* and *D* components from the quiet level at observation stations adjusted for geomagnetic latitude, whereas *ASY-H* and *ASY-D* are defined as the differences between maximum and minimum *H* and *D* components after subtracting the corresponding symmetric parts from the disturbance field. The *SYM-H* index is generally negative (similar to *Dst*), *SYM-D* takes values of both signs, and *ASY-H* and *ASY-D* are always positive. The method for determining the *SYM* and *ASY* indices is described in detail in [Iyemori et al., 2010].

The data is analyzed based on annual average *SYM-H* and *ASY-H* and interplanetary parameters for 1981–2015. The geomagnetic indices were taken from the website of the World Data Center for Geomagnetism [https://wdc.kugi.kyoto-u.ac.jp/index.html]; interplanetary data, from the website of NASA's Space Physics Data Facility [http://omniweb.gsfc.nasa.gov/]. The IMF components in this database are represented in the RTN coordinate system: the R-axis is directed radially from the Sun; the T- axis, toward the Sun's rotation; and the N-axis is the vector product of the R and T axes. At zero heliographic latitude, the N and T axes are parallel. The RTN and GSE coordinate systems at near-Earth distances differ in the opposite directions of the R and X axes, as well as T and Y axes respectively.

After excluding days with no data on interplanetary and geomagnetic parameters, 10759 days remained in the data array. When examining the relationship of *SYM-H* and *ASY-H* with the IMF north-south component B_n, the data was classified according to the sign of B_n: there were 5670 days with $B_n < 0$ (including 118 days when daily average B_n was zero), and 5089 days with $B_n > 0$.

RESULTS AND DISCUSSION

Figure 1 plots the index of the degree of ring current symmetry *SYM-H/ASY-H* as function of IMF *B*, SW velocity *V*, and IMF north-south component B_n (*c*). The plots yielded the corresponding linear regression equations and correlation coefficients *r*. The index of the degree of symmetry is seen to depend on *B* and *V*; the correlation coefficient between *SYM-H/ASY-H* and IMF *B* is 0.8; and between *SYM-H/ASY-H* and *V*, it does not exceed 0.5. As for the relationship between *SYM-H/ASY-H* and IMF B_n, when considering the data regardless of the sign of the IMF north-south component (panel (*c*)) it is absent: $r = 0.1$. Since the IMF north-south component is one of the main factors influencing magnetospheric processes, the index data was divided into two subarrays according to the sign of B_n. Panel (*d*) shows the relationships between *SYM-H/ASY-H* and B_n separately for southward and northward IMF. The relationship is seen to be pronounced: at $B_n \leq 0$, $r = 0.73$; at $B_n > 0$, $r = 0.50$. It can be said that as the absolute values of the interplanetary parameters increase, the value of *SYM-H/ASY-H* increases in absolute value and approaches 1.

SYM-H/ASY-H $= -1$ means that the symmetric and asymmetric components of the ring current are equated to the maximum values of the interplanetary parameters. It turns out that the asymmetric current prevails over the
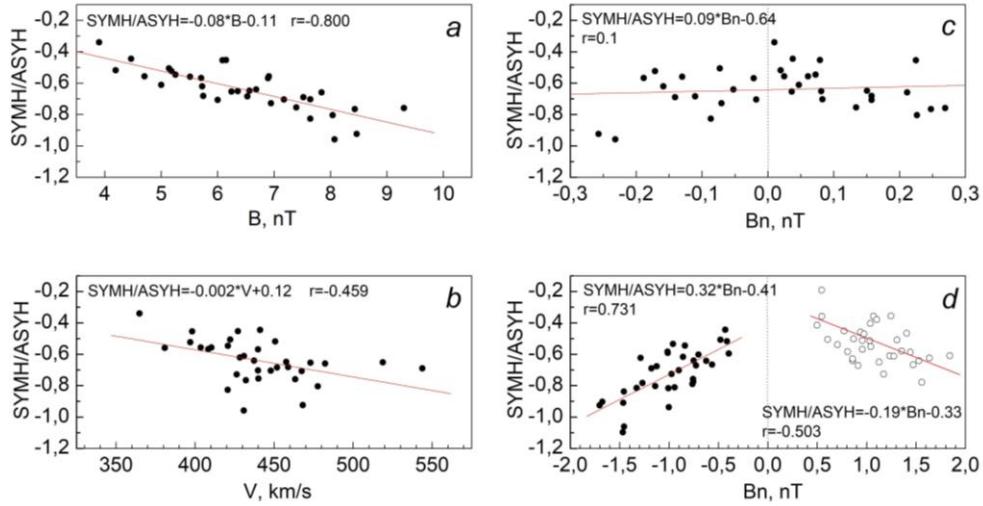
Figure 1. Index of the degree of ring current symmetry *SYM-H/ASY-H* as function of IMF *B* (*a*), solar wind velocity *V* (*b*), and IMF north-south component B_n without classifying (*c*) and by classifying (*d*) data according to the sign of B_n; panels present linear regression equations and correlation coefficients *r*

symmetric one most of the time, but this cannot be the case. With large-scale averages, it is logical to assume that the symmetric component of the ring current should dominate the asymmetric one due to the fact that in the absence of geomagnetic disturbances the symmetric ring current is constantly present in the magnetosphere [Kalegaev et al., 2008]. Such a current decays slowly during the geomagnetic storm recovery phase, which can last quite a long time [Weygand, McPherron, 2006], whereas the asymmetric ring current develops during the geomagnetic storm main phase and its decay time is much shorter [Weygand, McPherron, 2006; Bakhmina, Kalegaev, 2008].

In Introduction, offsets of *SYM* and *ASY* were discussed. Weygand and McPherron [2006] have suggested that the offset of *SYM-H* probably occurs due to the combination of three effects: Chapman—Ferraro currents under quiet conditions; ring current under quiet conditions, and the difference between the tail effect on quiet and stormy days, whereas the offset of *ASY-H* is due to the combination of two effects: the asymmetric ring current that is always present in the inner magnetosphere, and noise on local time plots, which was caused by incomplete subtraction of the quiet day variation at each station.

The presence of an offset in *Dst* values has been detected in [Takalo, Mursula, 2001; Hakkinen et al., 2003]. Takalo and Mursula [2001] have investigated the seasonal diurnal variations of the *Dst* index on quiet and all days and have found that these variations are associated with uneven distribution of stations of the *Dst* network. Analysis of diurnal and seasonal variations in *Dst* allowed Hakkinen et al. [2003] to conclude that stations of the *Dst* network had different entry levels so that average *Dst* differed by 10 nT. In [Makarov, 2020], it has been shown that the annual *Dst* variation occurs due to the uneven distribution of the network of stations involved in determining *Dst*.

In [Weygand, McPherron, 2006], the *SYM-H* index was adjusted for the contribution of SW dynamic pressure to it, and during statistical study on storm time it was estimated that the offset of *SYM-H* and *ASY* is ~18±2 nT depending on the method in use. Zhao et al. [2022], having examined the relationship of very large geomagnetic storms (Δ *SYM-H*<–200 nT) with SW parameters, came to the conclusion that the empirical formulas employed in such works estimate the intensity of storms with large statistical errors. In [Makarov, 2021] based on data on seasonal variations in the indices, as well as on the results of regression analysis of annual average indices and the level of magnetic activity for 1981–2016, it has been found that the offsets for *SYM-H* is –0.1 nT and for *ASY-H* is 13.6 nT. In this paper, it is difficult to take into account the offset during statistical study of the contribution of different sources to *SYM-H* and *ASY-H*.

Given the importance of the offsets of the indices considered, we re-estimate the relationship between the index of the degree of ring current symmetry and interplanetary parameters, using offsets obtained in [Makarov, 2021] from the results of statistical study. The offset of *SYM-H* is tiny, so it can be ignored, but in *ASY-H* it is significant. After *ASY-H* was corrected for 13.6 nT, *SYM-H/ASY-H* were calculated (for the results see Figure 2).

Comparing Figure 2 with Figure 1 shows that, firstly, there is practically no relationship between *SYM-H/ASY-H* and interplanetary parameters, except for the weak connection between the symmetry index and the IMF north-south component when the data was classified according to the sign of B_n (*d*); and, secondly, average *SYM-H/ASY-H* varies near –2. This behavior of the symmetry index may indicate the predominance of the symmetric ring current over the asymmetric one in the case of annual average data. Indeed, the symmetric ring current exists continuously, whereas the partial ring current develops during the magnetic storm main phase and decays immediately after its maximum. The ring current becomes
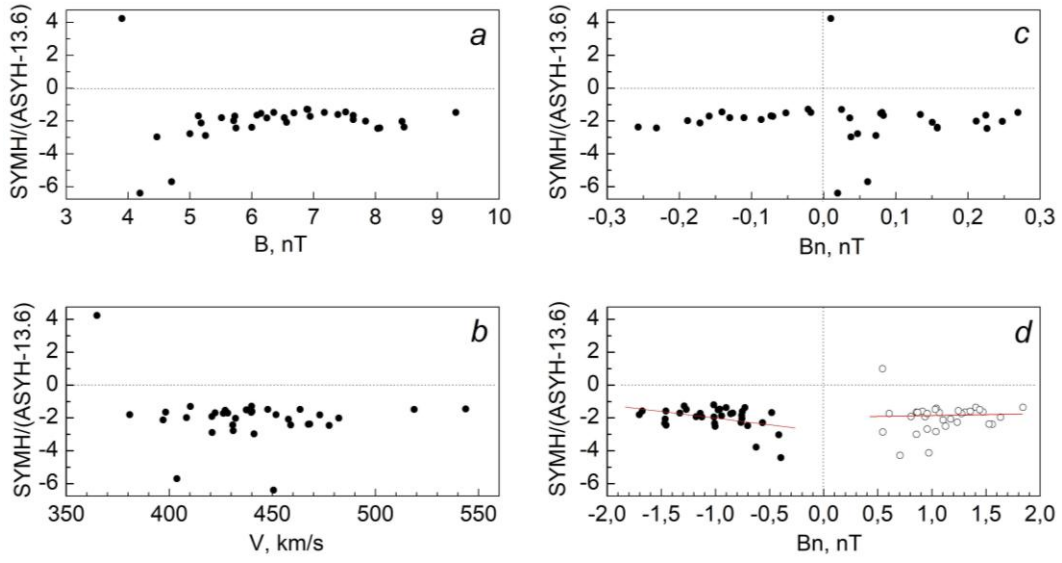
Figure 2. Index of the degree of ring current symmetry *SYM-H*/*ASY-H* as function of IMF*B* (*a*), SW *V* (*b*), and the IMF north-south component B_n (without classifying (*c*) and by classifying (*d*) data according to the sign of B_n) after considering the offset of *ASY-H*
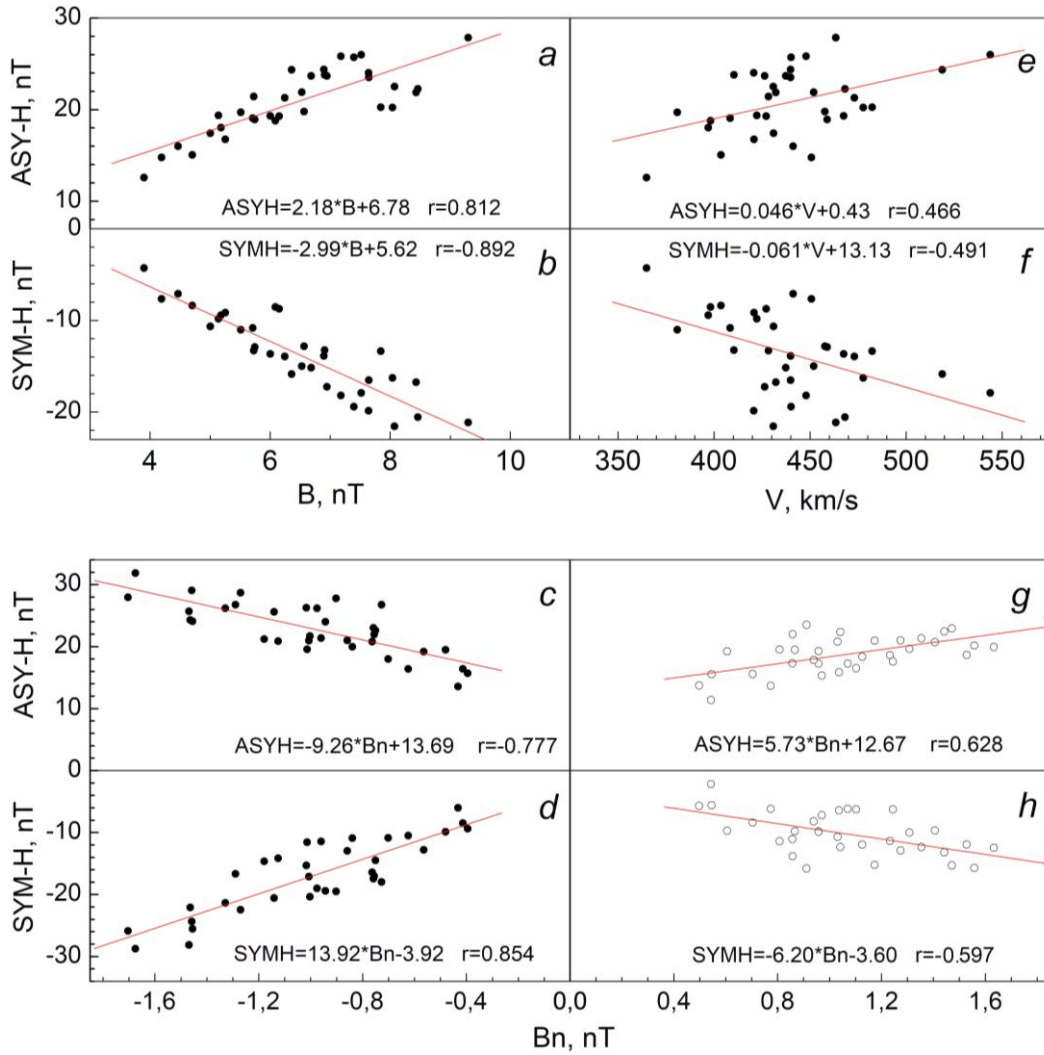
Figure 3. The *ASY-H* and *SYM-H* indices as function of IMF *B* (*a* and *b* respectively), SW velocity *V* (*e* and *f*), and the IMF north-south component B_n (*c*, *d*, *g*, *h*; data is classified according to the sign of B_n); panels show linear regression equations and correlation coefficients *r*

symmetric during the recovery phase [Kalegaev et al., 2008]. Since the storm recovery phase is much longer (about three times or more) than the main phase, the symmetric ring current persists for a longer time and at daily averaging makes a contribution to geomagnetic variations, which exceeds the contribution of the asymmetric ring current in the main phase when the intensity of this current is much higher. It is known [Weygand, McPherron, 2006], for example, that the response time for *SYM-H* (5.25 and 64.3 hr) is almost twice as long as that for *ASY-H* (2.2 and 20.9 hrs).

In Figure 2, *a*, *b*, *c*, three points can be seen when $|SYM\text{-}H/ASY\text{-}H|>4$, they correspond to small values of *B*, *V*, and $B_n>0$, i.e. to the cases when the partial ring current is minimum. The outlier with positive symmetry corresponds to positive *SYM-H*. Panel (*d*) quite clearly demonstrates the nonlinear relationship of *SYM-H/ASY-H* with B_n according to which the symmetric ring current noticeably prevails over the asymmetric current at small values of B_n. The index of the degree of ring current symmetry can be seen to increase when $V<450$ km/s, $B<5.5$ nT, $|B_n|<0.7$ nT. Such patterns are expected due to different properties of symmetric and asymmetric currents. Thus, when taking into account the offset, *ASY-H* more adequately reflects properties of magnetospheric ring currents than when ignoring it. The offsets of the indices are caused by contributions of all major magnetospheric current systems.

Figure 3 illustrates the correlation relationships of *ASY-H* and *SYM-H* with interplanetary parameters. When the relationship with B_n was examined, the data was divided into two subarrays: $B_n \le 0$ and $B_n>0$; in other cases, the sign of B_n was ignored. The relationships shown in the figure are consistent with the known ones — the geomagnetic indices increase in absolute value with increasing *B*, *V*, and $|B_n|$. Note should be made of the linear regression coefficients: in all equations related to interplanetary parameters, the coefficients for *SYM-H* are higher than for *ASY-H*, with values of both indices being comparable. This implies that *SYM-H* increases more strongly than *ASY-H* as the absolute values of SW parameters increase: 1.37 for *B*, 1.33 for *V*, 1.5 for $B_n<0$, and 1.08 for $B_n>0$. This paper is based on annual average data. With this averaging of data, storm and substorm processes are smoothed out; in addition, it is necessary to take into account time scales of ring current components — they are larger in the symmetric component [Weygand, McPherron, 2006]. The said *SYM-H* property probably also makes an additional contribution to the relationship of *SYM-H/ASY-H* with interplanetary parameters.

MAIN RESULTS

The geomagnetic index *ASY-H* has been shown to more accurately measure properties of magnetospheric ring currents when taking into account the offset of its values than when ignoring this offset. When considering the offset of *ASY-H*, the symmetric component of the ring current prevails approximately twice over the asymmetric one for average conditions in the solar wind: $V<550$ km/s, $B<10$ nT, $|B_n|<2$ nT. When the solar wind is quiet ($V<450$ km/s, $B<5.5$ nT, $|B_n|<0.7$ nT), the index of the degree of ring current symmetry increases.

From annual average *SYM-H* and *ASY-H*, it has been found that with an increase in the absolute values of interplanetary parameters (SW velocity, IMF magnitude IMF north-south component), the symmetric ring current index *SYM-H* increases more strongly than the asymmetric ring current index *ASY-H*.

REFERENCES

Alexeev I.I., Belenkaya E.S., Kalegaev V.V., Feldstein Y.I., Grafe A. Magnetic storms and magnetotail currents. *J. Geophys. Res*. 1996, vol. 101, no. A4, pp. 7737–7747. DOI: 10.1029/95JA03509.

Bakhmina K.Yu., Kalegaev V.V. Modeling the partial ring current effect in a disturbed magnetosphere. *Geomagnetism and Aeronomy*. 2008, vol. 48, no. 6, pp. 713–718.

Barkhatov N.A., Levitin A.E., Tserkovnyuk O.M. Relation of the indices characterizing the symmetric (*SYM*) and asymmetric (*ASY*) ring currents to the *AE* (*AU, AL*) indices of auroral electrojet activity. *Geomagnetism and Aeronomy*, 2008, vol. 48, no. 4, pp. 499–503.

Bhaskar A., Vichare G. Forecasting of *SYM-H* and *ASY-H* indices for geomagnetic storms of solar cycle 24 including St. Patricks day, 2015 storm using NARX neural network. *Journal of Space Weather and Space Climate.* 2019, vol. 9, no. A12. DOI: 10.1051/swsc/2019007.

Boroyev R.N., Vasiliev M.S. Relationship of the *ASY-H* index with interplanetary medium parameters and auroral activity in magnetic storm main phases during CIR and ICME events. *Sol.-Terr. Phys*. 2020, vol. 6, iss. 1, pp. 35–40. DOI: 10.12737/stp-61202004.

Haiducek J.D., Welling D.T., Ganushkina N.Y., Morley S.K., Dogacan Su Ozturk. SWMF global magnetosphere simulations of January 2005: Geomagnetic indices and cross-polar cap potential. *Space Weather.* 2017, vol. 15, pp. 1567–1587.

Hakkinen L.V.T., Pulkkinen T.I., Pirjola R.J., Nevanlinna H., Tanskanen E.I., Turner N.E. Seasonal and diurnal variation of geomagnetic activity: Revised *Dst* versus external drivers. *J. Geophys. Res*. 2003, vol. 108, no. A2, p. 1060. DOI: 10.1029/2002JA009428.

Iyemori T., Araki T., Kamei T., Takeda M. *Mid-latitude geomagnetic indices ASY and SYM (Provisional) No. 1: 1989–1990*. Data Analysis Center for Geomagnetism and Space Magnetism; Kyoto University, Japan, 1992, 240 p.

Iyemori T., Takeda M., Nose M., et al. *Mid-latitude geomagnetic indices ASY and SYM for 2009 (Provisional)*. Data Analysis Center for Geomagnetism and Space Magnetism; Kyoto University, Japan, 2010. URL: http://wdc.kugi.kyoto-u.ac.jp/aeasy/asy.pdf (accessed October 5, 2021).

Kalegaev V.V., Bakhmina K.Yu., Alexeev I.I., Belenkaya E.S., Feldstein Ya.I., Ganushkina N.V. Ring current asymmetry during a magnetic storm.*Geomagnetism and Aeronomy*. 2008, vol. 48, no. 6, pp. 747–759.

Makarov G.A. Geometric factor in seasonal variations of daily average values of the geomagnetic index *Dst*. *Sol.-Terr. Phys*. 2020, vol. 6, iss. 4, pp. 50–56. DOI: 10.12737/stp-64202008.

Makarov G.A. Offset in the geomagnetic indices of the magnetospheric ring current. *Sol.-Terr. Phys*. 2021, vol. 7, iss. 3, pp. 29–35. DOI: 10.12737/stp-73202103.

Makarov G.A. Geomagnetic indices *ASY-H* and *SYM-H* and their relation to interplanetary parameters. *Sol.-Terr. Phys*. 2022, vol. 8, iss. 4, pp. 36–43. DOI: 10.12737/stp-84202203.

Makarov G.A. Large-scale relationships of the geomagnetic indices *SYM-H* and *ASY-H* with the north-south IMF component and the solar wind beta parameter. *Sol.-Terr. Phys*. 2024, vol. 10, iss. 3, pp. 91–96. DOI: 10.12737/stp-103202411.

Maltsev Y.P., Arykov A.A., Belova E.G., Gvozdevsky B.B., Safargaleev V.V. Magnetic flux redistribution in the storm time magnetosphere. *J. Geophys. Res*. 1996, vol. 101, no. A4, pp. 7697–7704.

Namuun B., Tsegmed B., Li L.Y., Leghari G.M. Differences in the response to CME and CIR drivers of geomagnetic disturbances. *Sol.-Terr. Phys*. 2023, vol. 9, iss. 2, pp. 31–36. DOI: 10.12737/stp-92202304.

Shi Y., Zesta E., Lyons L.R., Yumoto K., Kitamura K. Statistical study of effect of solar wind dynamic pressure enhancements on dawn-to-dusk ring current asymmetry. *J. Geophys. Res*. 2006, vol. 111, A10216. DOI: 10.1029/2005JA011532.

Singh A.K., Sinha A.K., Pathan B.M., Rajaram R., Rawat R. Effect of prompt penetration on the low latitude *ASY* indices. *J. Atmos. Solar-Terr. Phys*. 2013, vol. 94, pp. 34–40.

Takalo J., Mursula K. A model for the diurnal universal time variation of the Dst index, *J. Geophys. Res*. 2001, vol. 106, no. A6, pp. 10905–10914.

Tsyganenko N.A., Sitnov M.I. Modeling the dynamics of the inner magnetosphere during strong geomagnetic storms. *J. Geophys. Res*. 2005, vol. 110, A03208. DOI: 10.1029/2004JA010798.

Weygand J.M., McPherron R.L. Dependence of ring current asymmetry on storm phase. *J. Geophys. Res*. 2006, vol. 111, A11221. DOI: 10.1029/2006JA011808.

Zhao M.X., Le G.M., Lu J.Y. Can we estimate the intensities of great geomagnetic storms ($\Delta SYM\text{-}H \leq -200$ nT) with the Burton equation or the O'Brien and McPherron equation? *Astrophys. J*. 2022, vol. 928, p. 18. DOI: 10.3847/1538-4357/ac50a8.

URL: https://wdc.kugi.kyoto-u.ac.jp/index.html (accessed March 29, 2025).

URL: http://omniweb.gsfc.nasa.gov/

How to cite this article

Makarov G.A. Influence of interplanetary parameters on the degree of symmetry of the ring current. *Sol.-Terr. Phys*. 2025, vol. 11, iss. 3, pp. 31–36. DOI: 10.12737/stp-113202504.

GEOMAGNETIC CUTOFF OF COSMIC RAYS DURING THE MARCH 23–24, 2023 MAGNETIC STORM: RELATIONSHIP WITH SOLAR WIND PARAMETERS AND GEOMAGNETIC ACTIVITY TAKING INTO ACCOUNT LATITUDINAL EFFECTS

O.A. Danilova
Pushkov Institute of Terrestrial Magnetism, Ionosphere, and Radio Wave Propagation, St. Petersburg Branch RAS, St. Petersburg, Russia, md1555@mail.ru

N.G. Ptitsyna[†]
Pushkov Institute of Terrestrial Magnetism, Ionosphere, and Radio Wave Propagation, St. Petersburg Branch RAS, St. Petersburg, Russia

V.E. Sdobnov
Institute of Solar-Terrestrial Physics SB RAS, Irkutsk, Russia, sdobnov@mail.ru

Abstract. In this paper, we calculate geomagnetic cutoff rigidities during the strong magnetic storm of March 23–24, 2023, using 1) the spectrographic global survey method based on observational data from cosmic ray recording by the global network of stations (R_{sgs}); 2) numerical trajectory calculations in a model magnetic field of the magnetosphere (R_{eff}). The geomagnetic cutoff rigidity has been determined for nine cosmic ray stations at different latitudes. We calculated the correlations of the variations in the geomagnetic cutoff rigidity ΔR_{sgs} and ΔR_{eff} with magnetic and dynamic solar wind parameters and the geomagnetic activity indices Dst and K_p. It has been found that the geomagnetic cutoff rigidity calculated by both methods correlate most strongly with Dst and the electromagnetic parameters of the solar

wind. No significant correlation with the dynamic parameters was observed. The analysis has shown that the response of ΔR_{sgs} to the controlling magnetic parameters and Dst changes with latitude of the observation station: the correlation reaches its highest values at midlatitudes and drops significantly toward the equator. The correlations of ΔR_{eff} calculated by the model do not reveal a latitudinal dependence.

Keywords: cosmic rays, geomagnetic threshold, cosmic ray cutoff rigidity, interplanetary magnetic field, geomagnetic activity.

INTRODUCTION

Under the influence of the geomagnetic field, charged particles of galactic cosmic rays (CRs) change their trajectory. Some of them with rigidity below the threshold value characteristic of the station that measures them (geomagnetic cutoff rigidity, R_c) do not reach Earth's surface. Due to the screening nature of the geomagnetic field, significantly fewer particles penetrate to the equator than to high latitudes. Variations in CR fluxes in the magnetosphere during magnetic storms are caused by changes in the CR geomagnetic cutoff rigidity/geomagnetic thresholds ΔR. The thresholds depend on the screening properties of the geomagnetic field.

During a magnetic storm, the solar wind (SW) energy is transferred to Earth's magnetosphere by coronal mass ejections (CMEs) or high-velocity corotating interaction regions (CIRs) from coronal holes. The influx of energy generated during increased solar activity and its subsequent attenuation in the magnetosphere determines the evolution of a geomagnetic storm, which is described by various geomagnetic indices. The K_p index — a planetary index characterizing the global geomagnetic disturbance within a three-hour time interval — is defined as average disturbance levels of two horizontal geomagnetic field components observed at 13 selected magnetic observatories located in the subauroral zone be-

tween 48° and 63° north and south geomagnetic latitudes. Another widely used one is the so-called disturbance storm time index Dst, which is calculated as the hourly average disturbance of the horizontal H component of the geomagnetic field at four low-latitude magnetic observatories. It is a measure of change in the magnetic field by the magnetopause current system (DCF) and the westward ring current (DR). The current system developed during a geomagnetic disturbance causes a decrease in the magnetospheric magnetic field and hence in geomagnetic screening, thereby facilitating penetration of CRs to lower latitudes. In turn, the dynamics of current systems depends on the dynamics of magnetic and time-varying parameters of near-Earth space.

Knowledge of the dependences of ΔR on SW and magnetosphere parameters can shed light on important features of the SW–magnetosphere coupling and its associated geomagnetic effects, which control CR transport through the magnetosphere and atmosphere during disturbances. Studying latitude effects of this coupling is essential for safety of the crew and passengers of space flights, as well as high-latitude and altitude flights [Burov et al., 2005; Iucci et al., 2005].

The response of geomagnetic screening to changes in the geomagnetic conditions in SW and the interplanetary magnetic field (IMF) during magnetic storms has

O.A. Danilova, N.G. Ptitsyna, V.E. Sdobnov

been examined theoretically and experimentally in [Kanekal et al., 1998; Leske et al., 2001; Shimazu, 2009; Tyssøy and Stadsnes, 2014; Adriani et al., 2016]. However, no definitive answer has been found yet to the question as to which near-space parameters control CR transport during disturbances. To answer this question, it is necessary, at least, to have a sufficiently extensive base of relevant data for geomagnetic storms of various types and intensities from different sources on the Sun and in interplanetary space, which occurred during different solar cycle phases. The data would allow us to draw generalized conclusions about changes in geomagnetic screening during interplanetary and geomagnetic disturbances of various types. Earlier in [Ptitsyna et al., 2019; Danilova et al., 2023 and references there], for one moderate and seven strong geomagnetic storms of solar cycles 23 and 24, we have calculated geomagnetic cutoff rigidities and their correlations with helio- and geosphere parameters. Most of the storms considered were recorded during descending phases and solar minima. In this paper, to further expand our data archive, we analyze the severe storm in March 2023 near the maximum of cycle 25, caused by specific stealth CME. Besides, we have added to our study the calculation and analysis of data for three additional low-latitude CR stations, bearing in mind the search for latitude effects. The purpose of this work is to identify geomagnetic thresholds, using two independent methods R_{eff} and R_{shs} during the March 23–24, 2023 severe storm, to analyze the dependence of their changes on the interplanetary medium and geomagnetosphere parameters, focusing on latitudinal effects, as well as to compare results obtained by different methods. To solve these problems, we calculated correlations of variations in geomagnetic cutoff rigidities ΔR_{sgs} and ΔR_{eff} with SW electromagnetic and dynamic parameters, Dst, and K_p.

1. METHODS AND DATA

The spectrographic global survey (SGS) method and the method of tracing trajectories of CR particles in a model magnetic field have been employed to calculate the geomagnetic cutoff rigidity during the severe magnetic storm on March 23–24, 2023.

The SGS method is based on the assumption that CR flux variations on Earth's surface are determined by the rigidity spectrum, the pitch-angle distribution of particles in interplanetary space, and the particle density gradient at the Larmor radius [Kovalev et al., 2022]. This method provides information on the distribution of primary CRs by energy and pitch angles in interplanetary space, as well as on changes in the planetary system of geomagnetic cutoff rigidities for each moment of observations (R_{sgs}), from ground-based observations of CRs made at the worldwide network of stations.

Table 1 lists standard errors in determining the IMF longitude λ and latitude Ψ angles, the differential rigidity spectrum A_0, CR pitch-angle anisotropy amplitudes A_1 and A_2, variations in the geomagnetic cutoff rigidity ΔR_c, surface ΔT_{SL} and mass average ΔT_{MA} atmospheric temperatures by the SGS method in accordance with the accuracy of measurements of CR neutron I_{nm} and charged I_{mt} components.

The statistical error in determining ΔR_{sgs} with due regard to the accuracy of measurements at CR stations does not exceed 0.05 GV in absolute value. The geomagnetic cutoff rigidity variations obtained by this method are further referred to as observed.

The second method involves trajectory calculations of R_c [Shea et al., 1965] in the model magnetic field of the magnetosphere (R_{eff}). In this paper, we employ the Tsyganenko model Ts01 ([Tsyganenko et al., 2003] and

Table 1

Standard errors in IMF, CR, Earth's magnetosphere and atmosphere parameters, determined by the SGS method in accordance with the accuracy of neutron monitor and muon telescope data [Kovalev et al., 2022]

I_{nm}, %	I_{mt}, %	λ, deg.	Ψ, deg.	A_0, %	A_1, %	A_2, %	ΔR_c, GV	T_{SL}, °C	T_{AM}, °C
±0.1	±0.1	±16.9	±21.5	±1.0	±8.8	±1.7	±0.03	±1.3	±0.3
	±0.2	±16.9	±21.5	±1.0	±8.8	±1.7	±0.03	±2.5	±1.2
±0.15	±0.1	±17.0	±21.8	±1.3	±8.8	±1.7	±0.04	±1.3	±0.3
	±0.2	±17.0	±21.8	±1.3	±8.8	±1.7	±0.04	±2.5	±1.0
±0.2	±0.1	±17.5	±22.1	±1.6	±8.9	±1.8	±0.05	±1.3	±0.3

references there) to compute the effective geomagnetic thresholds R_{eff}. At the same time, the accuracy of determining geomagnetic thresholds depends on the accuracy of the magnetospheric model adopted for calculations. According to the Ts01 model, the magnetic field inside the magnetosphere (without the main magnetic field) is the sum of contributions from the main magnetospheric current systems. In parameterizing the current systems, we have used satellite data collected during 37 geomagnetic storms with $Dst<-65$ nT [Tsyganenko et al., 2003]. The Ts01 model includes Chapman—Ferraro currents,

symmetric and partial volume circular currents, transverse tail currents, and large-scale field-aligned currents. Tyasto et al. [2012] have shown that during strong magnetic storms the Ts01 magnetospheric model describes the situation in the magnetosphere better than the Ts04 model. To calculate the magnetic field from internal sources, a representation of Earth's main magnetic field (EMMF) is utilized as expansion in terms of spherical harmonic functions up to $n=10$. The geomagnetic cutoff rigidity variations obtained by this method are further referred to as model.

Geomagnetic cutoff rigidities have been determined for nine multi-latitude CR stations, listed in Table 2. The stations were chosen in such a way that under quiet conditions they covered the main range of threshold R_c affected by the geomagnetic field.

Next, we calculated the correlation coefficients k and the standard errors s between ΔR_{eff} and ΔR_{sgs} with the following parameters: IMF's total value B and its components B_z and B_y, the azimuthal component of electric field E_y, the plasma parameter β, SW velocity V, density N, and pressure P, as well as Dst and K_p. These parameters are available in the OMNI database [https://omniweb.gsfc.nasa.gov/form/dx1.html].

Plasma β is the ratio of plasma pressure to magnetic pressure; in the OMNI database, this parameter is calculated using the formula

$$\beta = \left(4.16T/10^5 + 5.34\right)N_p/B^2 ,$$

where T is the temperature (K); N_p is the proton density (cm^{-3}); B is the total magnetic field (nT).

The electric field was calculated by the formula

$$E = -VB_z 10^{-3} ,$$

where E is the electric field (mV/m); V is the proton velocity (km/s); and B_z is the magnetic field component (nT).

Table 2

Cosmic ray stations

Station name	International code	Geographic latitude	Geographic longitude	R_c
Kingston	KGSN	42.99° S	147.29° E	1.9
Moscow	MOSC	55.47° N	37.32° E	2.08
Novosibirsk	NVBK	54.80° N	83.00° E	2.32
Irkutsk	IRKT	52.47° N	104.03° E	3.13
Jungfraujoch	JUNG	46.55° N	7.98° E	4.51
Almaty	AATB	43.25° N	76.92° E	5.21
Rome	ROME	41.90° N	12.52° E	6.11
Athens	ATHN	37.97° N	23.72° E	8.48
Emilio Segre Obs.	ESOI	33.30° N	35.80° E	10.73

2. RESULTS

2.1. Helio-, geosphere parameters and CR cutoff rigidity during the March 23–24, 2023 storm

In Figure 1 from top to bottom are electromagnetic and dynamic parameters of SW and geomagnetic activity during the March 23–24, 2023 geomagnetic storm: B, B_z, E_y, β, SW V, N, P, as well as K_p and Dst.
A peculiarity of the storm under study was that it was caused by stealth CME. Such CMEs are not associated with any visible manifestations on the Sun, so it is difficult to identify them and hence to predict their geoeffectiveness. In particular, the CME that initiated the geomagnetic storm of interest was not observed by any of the observers and was not cataloged. However, since the peak Dst index unexpectedly reached –163 nT, the storm was classified as severe [Tahir et al., 2024; Teng et al., 2024].

On March 23 at ~8:00–14:00 UT, B, N, P, and B_z are seen to gradually increase, which can be interpreted as the passage of interplanetary CME sheath (ICME sheath) or compression region before ICME near Earth.

It can be assumed that the main phase of the storm began at ~13:00 UT with a sharp compression of the magnetosphere after a jump in P to 14.8 nPa. With the

beginning of the main phase, β decreased abruptly from the background $\beta \approx 2$ before the storm to $\beta \approx 0.2$ and remained so throughout the main phase of the storm. Such a low β value may be associated with increased plasma turbulence and serve as a trigger for a magnetic storm [Kurazhkovskaya et al., 2021]. The B_z component fluctuated between southward and northward before finally turning south at ~18:00 UT. At that time, the active stage of the storm began when Dst started to decrease sharply and reached a minimum ($Dst=-163$ nT) at 02:00 UT on March 24, 2023. After that, Dst began to increase, B_z also began to grow, and the magnetic storm entered the relaxation phase.

Figure 2, $a-f$ presents calculated variations in the geomagnetic thresholds ΔR_{sgs} and ΔR_{eff} for all the stations considered. Panel g also shows Dst variations to illustrate the relationship between dynamics of the geomagnetic thresholds and evolution of the storm. The trend of the ΔR_{eff} and ΔR_{sgs} curves is seen to agree well with Dst.

There is a clear dependence of lowering the ΔR_{eff} thresholds on latitude. The value of ΔR_{eff} reached its maximum drop (≈-0.8 GV) during the main phase at the storm maximum ($Dst=-163$ nT) at the station with the lowest threshold rigidity R_c (KGSN).
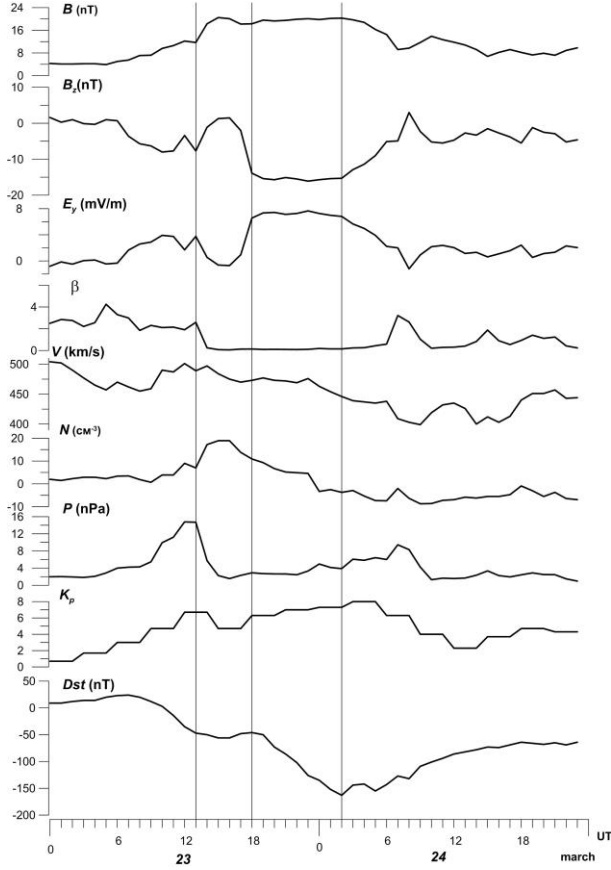
Figure 1. Parameters of SW, IMF, and geomagnetic activity during the storm on March 23–24, 2023. Vertical lines indicate the storm main phase, as well as the beginning of the active stage of the main phase at ~18:00 UT on March 23

Figure 2. Variations in geomagnetic thresholds ΔR_{sgs} (red lines) and ΔR_{eff} (blue lines) during the September 23–24, 2023 storm. From top to bottom for ROME (*a*), AATB (*b*), JUNG (*c*), IRKT (*d*), MOSC (*e*), and KGSN (*f*). Panel (*g*) is the *Dst* index. Vertical lines indicate the storm main phase and the onset of the active phase (18:00 UT on March 23)

During the storm main phase, ΔR_{sgs} decreases more slowly and to a smaller extent than ΔR_{eff}. In addition, oscillations with a period of about several hours are superimposed on the general trend of ΔR_{sgs}, which follows *Dst*. Amplitude of these oscillations during the recovery phase is of roughly the same order as the decrease in ΔR_{sgs} near the storm maximum: (for example, 2 hrs after the storm maximum at IRKT, $\Delta R_{sgs}=-0.45$ GV). Such jumps in ΔR_{sgs} are especially characteristic for the storm recovery phase at low-latitude stations. It is, therefore, impossible to determine with sufficient accuracy the maximum drop in geomagnetic cutoff rigidity during the storm. We can only note that along with the evolution of the ring current (~30 hrs for this storm), which determines ΔR_{eff}, other shorter-period (~2–3 hrs) processes seem to make a significant contribution. Figure 2 also demonstrates that the difference between the ΔR_{eff} and ΔR_{sgs} curves depends on latitude. It has a 0.44 GV maximum during minimum *Dst* for KGSN with minimum $R_c=1.90$ GV.

2.2. Correlation analysis

The time curves of Figure 2 suggest that ΔR_{eff} and ΔR_{sgs} vary with evolution of the storm and hence with changes in SW and geomagnetic activity parameters. In order to quantify the relationship between the parameters and the variations in geomagnetic thresholds, we have analyzed the correlations of ΔR with the
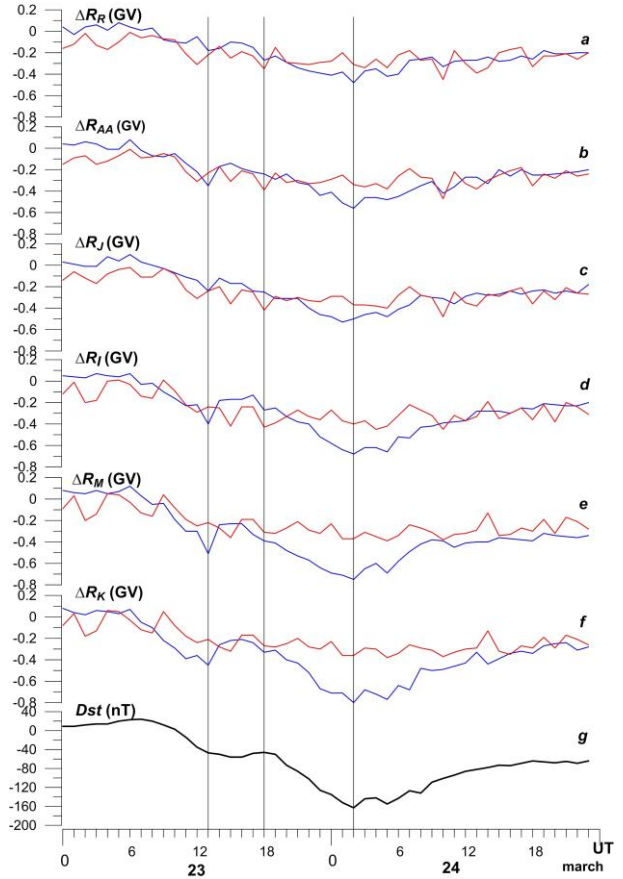
SW, IMF parameters and the geomagnetic activity indices. Correlation coefficients *k* and standard errors *s* were calculated. Figure 3 plots the correlation *k* between ΔR and the SW, IMF, and geomagnetosphere parameters during the March 23–24, 2023 storm. Panel *a* illustrates the correlation of variations in model thresholds ΔR_{eff} with interplanetary and magnetic parameters; panel *b*, the correlation between observed ΔR_{sgs}. Columns of the diagrams in different colors correspond to the results of the correlation analysis for different stations. The columns (stations) are arranged in ascending order of latitude (decreasing station threshold under quiet conditions).

Panel *a* shows that the greatest correlation is observed between ΔR_{eff} and *Dst*. For ΔR_{eff}, $k=0.96\pm0.05$ at YUNG. At other stations, *k* is almost the same. A high but somewhat lower negative correlation is also seen for K_p. For example, at MOSC $k=-0.8\pm0.14$. The correlation close to $k=-0.8$ was obtained for the relationship between the model geomagnetic thresholds and the general magnetic field *B*. At MOSC, $k=-0.74\pm0.16$; at ESOI, $k=-0.7\pm0.08$. In this case, $k<0$. A high anticorrelation was also derived for the relationship with E_y: $k=-0.68\pm0.18$ at MOSC. Similar *k* values were also found for the other stations. A fairly high correlation of about the same order ~0.65–0.7 was
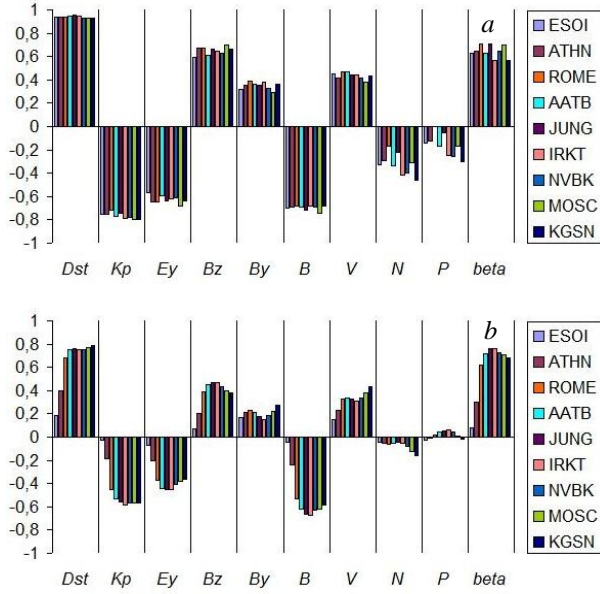
Figure 3. Correlation coefficients k between cutoff rigidities and geo- and heliosphere parameters during the March 23–24, 2023 storm: ΔR_{eff} (*a*); ΔR_{sgs} (*b*)

obtained for β and B_z. Note that the relationship of ΔR_{eff} with B_z is weaker than with the total field B. The k value is much smaller for the correlation between ΔR_{eff} and B_y. For example, $k=0.39\pm0.14$ at ROME. The k value calculated for the correlation ΔR_{eff}–V is of the same order and even smaller for the anticorrelation ΔR_{eff}–N and ΔR_{eff}–P. It can be argued that variations in geomagnetic cutoff rigidities are most closely related to variations in geomagnetic activity indices. Moreover, all electromagnetic parameters, except for B_y, contribute substantially to threshold variations. As for the SW dynamic parameters, the relationship with them is insignificant. Note that the coefficients of correlation ΔR_{eff} with all parameters cal-

culated for different stations differ very little.

A slightly different pattern is observed for the variation in threshold rigidities obtained by the SGS method (panel *b*). In general, the correlation coefficients for observed ΔR_{sgs} are lower than for model ΔR_{eff}. The closest correlation for mid-latitude stations is observed between ΔR_{sgs} and *Dst*, as well as β, reaching almost 0.8. The k value is the largest for KGSN (0.79±0.07). There is almost no correlation with *Dst* at the low-latitude stations ESOI and ATHN. The same can be said about the relationship of ΔR_{sgs} with the total magnetic field B and β. The correlation ΔR_{sgs}–β is the closest at the mid-latitude stations JUNG and IRKT ($k=0.76\pm0.08$), and for ΔR_{sgs}–B $k=-0.67\pm0.09$. For the other parameters, the correlation is much lower, and it is absent for the SW dynamic parameters N and P.

2.3. Correlations of geomagnetic thresholds with SW, IMF, and geomagnetic activity parameters

Figure 4 illustrates the relationship between variations in geomagnetic thresholds ΔR and the SW, IMF, geomagnetic activity parameters under study as function of geomagnetic cutoff rigidities R_c of stations under quiet conditions. The k values are shown for ΔR_{eff} (*a*) and ΔR_{sgs} (*b*). Colors and symbols denote the curves related to *Dst*, K_p, B_z, E_y, B_y, P, B, β, V, and N. Curves in panels *a*, *b* confirm the conclusions, obtained from the diagrams (see Figure 3, *a*, *b*), that the closest correlation is observed between ΔR_{sgs} and *Dst*, β; a slightly less close one, with B_z; and the greatest anticorrelation, with B, K_p, and E_y. Besides, panel *b* demonstrates the dependence of k on latitude and hence on R_c. The closest correlation is seen at midlatitudes for which $R_c\approx2\div6$ GV; and the maximum, at IRKT and JUNG for which $R_c=3.13$ and 4.51 respectively. With an increase in $R_c>6$ GV, k decreases significantly. For the other parameters considered, k is small, so they are not geoeffective and can be ignored.
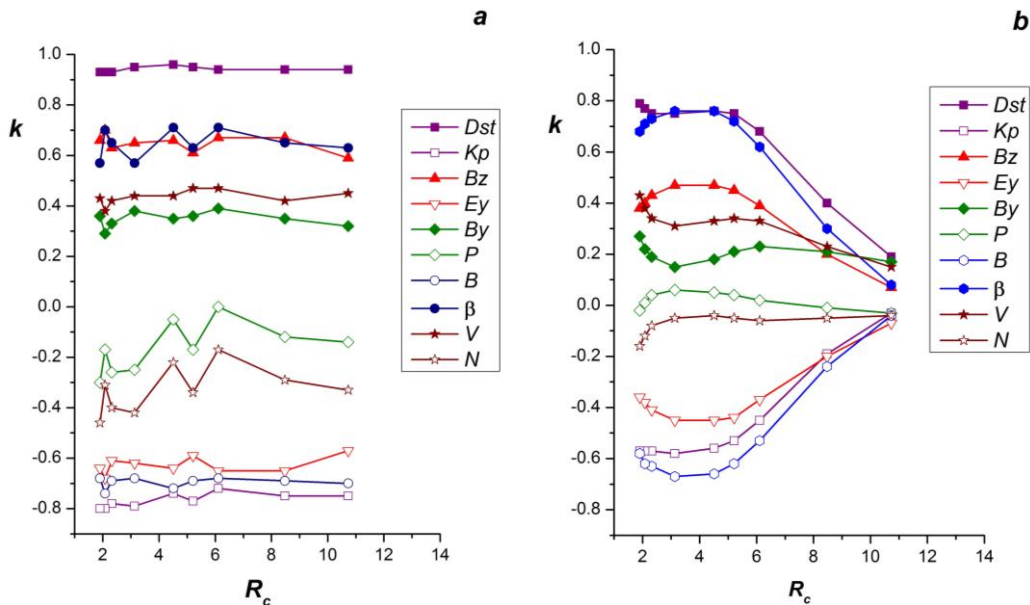

Figure 4. Correlation coefficients k between geomagnetic cutoff rigidities and geo- and heliospheric parameters depending on latitude: ΔR_{eff} (*a*); ΔR_{sgs} (*b*)

For ΔR_{eff} (*a*), the strongest correlation and anticorrelation (see Figure 3, *a*) are found for the same parameters as for ΔR_{sgs} — with *Dst*, β, B_z, K_p, *B*, and E_y. However, *k* for all parameters of the correlation ΔR_{eff} is higher than for ΔR_{sgs}. As for the latitude dependence, a weak trend similar to the latitude effect in ΔR_{sgs} can be detected only for B_z and E_y. For the other parameters under study, there is almost no dependence on latitude. Here, we also discuss only geoeffective parameters for which *k* is large enough.

2.4. Correlation between ΔR_{eff} and ΔR_{sgs}

Let us compare the results obtained by the SGS method and trajectory calculations using the Ts01 model. To do this, we calculated the correlation *k* between ΔR_{eff} and ΔR_{sgs} (Table 3).

Analysis of Figures 3, 4 shows that ΔR_{eff} and ΔR_{sgs} in general similarly describe variations in thresholds during the storm and the contribution of helio- and geosphere parameters to these variations. This is despite the fact that the drop in the model thresholds ΔR_{eff} systematically exceeds the drop in the observed ones ΔR_{sgs}. Table 2 suggests that the correlation *k* during the storm under study between observed and model thresholds for all stations, except for ESOI and ATHN, is quite high: from *k*=0.71±0.07 for ROME to the correlation maximum *k*=0.78±0.07 for JUNG. This behavior of *k* indicates a similar sensitivity to interplanetary and geomagnetic parameters of observed and model variations in geomagnetic thresholds for the stations with R_c<6.11 GV (ROME). The low correlation between ΔR_{eff} and ΔR_{sgs} at ESOI and ATHN reflects the difference in the latitude effect noticeable at low-latitude stations (see 2.3).

Table 3

Correlation coefficients *k* between ΔR_{eff} and ΔR_{sgs}

	ESOI	ATHN	ROME	AATB	JUNG	IRKT	NVBK	MOSC	KGSN
k	0.14±0.13	0.42±0.1	0.71±0.07	0.76±0.07	0.78±0.07	0.71±0.09	0.76±0.08	0.77±0.08	0.73±0.08

CONCLUSIONS

In this paper, we have examined variations in geomagnetic cutoff rigidities ΔR_{eff} and ΔR_{sgs} during the March 23–24, 2023 storm, which were calculated by two different methods, observational and model. In addition, we have analyzed the relationship of these variations with electromagnetic and dynamic parameters of solar wind and geomagnetic activity, as well as the dependence of this relationship on latitude.

It has been found that the geomagnetic thresholds calculated by both methods correlate most strongly with geomagnetic activity, especially with *Dst*, which indicates the greatest contribution to variations of ring current rigidities. Besides, there is a high correlation with electromagnetic parameters of IMF *B*, β, B_z, E_y. There is no significant correlation with the SW dynamic parameters *V*, *N*, *P*. It is believed that the development of a magnetic storm mainly depends on two parameters: the IMF southward component whose growth leads to reconnection of the SW magnetic field and Earth's magnetosphere, and on the SW pressure *P* whose rise results in the compression of the magnetosphere [Dungey, 1961; Burton et al., 1975; Akasofu, 1984]. However, the development of the storm under study and hence a decrease in geomagnetic screening during the storm and geomagnetic cutoff rigidity variations were indeed determined by B_z and, to an even greater extent, by the total magnetic field *B* and the plasma parameter β, whereas *P* and the other dynamic parameters of SW practically played no role. Note that such results were obtained for a severe storm in March 2023, i.e. on the ascending branch of solar cycle 25, one and a half years before its maximum. These results are generally consistent with the conclusions about the predominant influence of *Dst* and some electromagnetic parameters on ΔR, drawn for the March 8–11, 2012 strong storm also on the ascending branch of solar cycle 24 two years before the maximum [Danilova et al., 2023]. At the same time, for most storms, largely recorded outside solar maximum [Ptitsyna et al., 2019], along with the constant strongest correlation with *Dst* and electromagnetic parameters there is a significant relationship between geomagnetic thresholds and SW velocity. In this case, sets of other control parameters for individual storms differ. Nevertheless, we can conclude that properties of geomagnetic screening during strong disturbances depend on the phase of the solar cycle in which the event occurred. However, these conclusions need further, more detailed verification.

Analysis has shown that the response of ΔR_{sgs} to the controlling electromagnetic parameters, as well as to *Dst* and K_p, varies with the latitude of the observation station: the correlation reaches its highest values at midlatitudes ($R_c \approx 2 \div 6$ GV) and decreases significantly toward the equator. Practically no latitude dependence has been found for the correlations of ΔR_{eff} with interplanetary and geomagnetic parameters, only the correlation of ΔR_{eff} with B_z and E_y demonstrates a similar but weaker latitude effect.

Despite the difference in the magnitude and behavior of *k*, at low-latitude stations the correlation between ΔR_{eff} and ΔR_{sgs} as a whole is quite high (0.7). This suggests that both methods in use adequately describe ΔR in terms of variations in geomagnetic and interplanetary parameters at midlatitudes. The difference between the effects obtained by these methods at low-latitude stations should be investigated further.

for ΔR_{sgs} were obtained using the equipment of Shared Equipment Center "Angara" [http://ckp-rf.ru/ckp/3056/] and the Unique Research Facility "Russian National Ground-Based Network of Cosmic Ray Stations" (CRS network) [https://ckp-rf.ru/usu/433536].

REFERENCES

Adriani O., Barbarino G.C., Bazilevskaya G.N., Bellotti R., Boezio M., Bogomolov E.A., et al. PAMELA's measurements of geomagnetic cutoff variations during the 14 December 2006 storm. *Space Weather*. 2016, vol. 14, no. 3. DOI: 10.1002/2016SW001364.

Akasofu S.-I. The magnetospheric currents: An introduction. In T.A. Potemra (Ed.), Magnetospheric currents. *Geophysical Monograph Series*. 1984, vol. 28, pp. 29–48. DOI: 10.1029/GM028p0029.

Burov V.A., Meleshkov Yu.S., Ochelkov Yu.P. The technique of operational evaluation of the level of radiation danger due to the cosmic weather disturbance during air travel. *Heliogeophysical Research*. 2005, iss. 7, pp. 1–41.

Burton R.K., McPherron R.L., Russell C.T. An empirical relationship between interplanetary conditions and *Dst. J. Geophys. Res*. 1975, vol. 80, iss. 31, pp. 4204–4214. DOI: 10.1029/JA080i031p04204.

Danilova O.A., Ptitsyna N.G., Tyasto M.I., Sdobnov V.E. Variations in cosmic ray cutoff rigidities during the March 8–11, 2012 magnetic storm (CAWSES II period). *Sol.-Terr. Phys*. 2023, vol. 9, iss. 2, pp. 81–87. DOI: 10.12737/stp-92202310.

Dungey J.W. Interplanetary magnetic field and the auroral zones. *Phys Rev Lett*. 1961, vol. 6, pp. 47–48. DOI: 10.1103/ PhysRevLett.6.47.

Iucci N., Levitin A.E., Belov A.V., Eroshenko E.A., Ptitsyna N.G., Villoresi G., et al. Space weather conditions and spacecraft anomalies in different orbits. *Space Weather*. 2005, vol. 3, S01001. DOI: 10.1029/2003SW 000056.

Kanekal S., Baker D., Blake J., Klecker B., Cummings J., Mewaldt R., Mason G., Mazur J. High-latitude energetic particle boundaries and the polar cap: A statistical study. *J. Geophys. Res.: Space Phys*. 1998, vol. 103, pp. 9367–9372.

Kovalev I.I., Olemskoy S.V., Sdobnov V.E. A proposal to extend the spectrographic global survey method. *J. Atmos. Solar-Terr. Phys*. 2022, vol. 235, p. 105887. DOI: 10.1016/ j.jastp.2022.105887.

Kurazhkovskaya N.A., Zotov O.D., Klain B.I. Relationship between geomagnetic storm development and the solar wind parameter β. *Sol.-Terr. Phys*. 2021, vol. 7, no. 4, pp. 25–34. DOI: 10.12737/szf-74202104.

Leske R.A., Mewaldt R.A., Stone E.C., von Rosenvinge T.T. Observations of geomagnetic cutoff variations during solar energetic particle events and implications for the radiation environment at the space station. *J. Geophys. Res*. 2001, vol. 106, pp. 30011–30022. DOI: 10.1029/2000JA000212.

Ptitsyna N.G., Danilova O.A., Tyasto M.I., Sdobnov V.E. Influence of the solar wind and geomagnetic activity parameters on variations in the cosmic ray cutoff rigidity during strong magnetic storms. *Geomagnetism and Aeronomy*. 2019, vol. 59, no. 5, pp. 530–538. DOI: 10.1134/S001679321905 0098.

Shea M.A., Smart D.F., McCracken K.G. A study of vertical cutoff rigidities using sixth degree simulations of the geomagnetic field. *J. Geophys. Res*. 1965, vol. 70, pp. 4117–4130.

Shimazu H. Solar proton event and proton propagation in the Earth's magnetosphere. *J. National Institute of Information and Communications Technology*. 2009, vol. 1, pp. 191–199.

Tahir A., Wu F., Shah M., Amory-Mazaudier C., Jamjareegulgarn P., Verhulst T.G.W., Ayyaz Ameen M. Multi-instrument observation of the ionospheric irregularities and disturbances during the 23–24 March 2023 geomagnetic storm. *Remote Sensing*. 2024, vol. 16, no. 9, p. 1594. DOI: 10.3390/rs16091594.

Teng W., Su Y., Ji H., Zhan Q. Unexpected major geomagnetic storm caused by faint eruption of a solar transequatorial flux rope. *Nature Communications*. 2024, vol. 15, pp. 9198–9214. DOI: 10.1038/s41467-024-53538-1.

Tsyganenko N.A., Singer H.J., Kasper J.C. Storm-time distortion of the inner magnetosphere: How severe can it get? *J. Geophys. Res*. 2003, vol. 108, no. A5, p. 1209. DOI: 10.1029/ 2002JA009808.

Tyasto M.I., Danilova O.A., Sdobnov V.E. Cosmic ray geomagnetic cutoff rigidities in the magnetic field of two empirical models during a strong disturbance in November 2003: A comparison of models. *Geomagnetism and Aeronomy*. 2012, vol. 52, pp. 1087–1096. DOI: 10.1134/S0016793212080208.

Tyssøy H.N, Stadsnes J. Cutoff latitude variation during solar proton events: Causes and consequences. *J. Geophys. Res. Space*. 2014, vol. 120, pp. 553–563. DOI: 10.1002/2014JA 0200508.

URL: https://omniweb.gsfc.nasa.gov/form/dx1.html (accessed January 16, 2024).

URL: http://omniweb.gsfc.nasa.gov (accessed January 16, 2024).

URL: http://ckp-rf.ru/ckp/3056/ (accessed January 16, 2024).

URL: https://ckp-rf.ru/usu/433536 (accessed January 16, 2024).

STUDYING DYNAMICS OF ENERGY SPECTRUM OF SOLAR DIURNAL VARIATIONS IN COSMIC RAYS DURING SOLAR ACTIVITY CYCLES 20–25, USING METHOD OF CROSSED MUON TELESCOPES

P.Yu. Gololobov (iD)
*Yu.G. Shafer Institute of Cosmophysical Research
and Aeronomy SB RAS,
Yakutsk, Russia, gpeter@ikfia.ysn.ru*

V.G. Grigoryev (iD)
*Yu.G. Shafer Institute of Cosmophysical Research
and Aeronomy SB RAS,
Yakutsk, Russia, grig@ikfia.ysn.ru*

S.K. Gerasimova (iD)
*Yu.G. Shafer Institute of Cosmophysical Research
and Aeronomy SB RAS,
Yakutsk, Russia, s_k_gerasimova@ikfia.ysn.ru*

Abstract. The cosmic ray (CR) intensity recorded by ground-based detectors experiences solar diurnal variations (SDVs) associated with the existence of anisotropic angular distribution of CRs in near-Earth space. Long-term observations show that SDVs exhibit a dependence on the solar activity cycle, experiencing periodic 11- and 22-year variations. Such behavior of SDVs is linked to a change in the nature of galactic CR propagation in the heliosphere when it changes during a solar activity cycle. On the other hand, this phenomenon can be partially due to a change in the magnitude of CR drift by the geomagnetic field associated with changes in the SDV energy spectrum.

In this work, we determine the dynamics of the SDV energy spectrum in solar activity cycles. The solution to this problem presents certain difficulties associated with peculiarities of ground-based CR recording and with the sensitivity of CR detectors to changes in the state of environment. Therefore, we employ an approach using crossed muon telescopes to estimate it, which allows us to bypass the above difficulties. We analyze data from Yakutsk, Nagoya, Sao Martinho, and Hobart muon telescopes for 1972–2022. It is shown that at solar minima during periods of positive polarity of the Sun's general magnetic field, a significant softening of the spectrum is observed. The results are discussed.

Keywords: cosmic rays, solar diurnal variation, energy spectrum, muon telescope.

INTRODUCTION

Galactic cosmic rays (GCRs), which propagate in the heliosphere, are continuously exposed to the interplanetary magnetic field (IMF) and the solar wind. The result of this interaction is the anisotropy of angular distribution of GCRs, which is observed in near-Earth space. This distribution is manifested in measurement data from ground-based cosmic ray (CR) detectors as periodic 24-hr variations in recorded intensity, called solar-diurnal variations (SDVs). It is known that amplitudes of these variations are, on average, tenths of the total intensity, and the maximum of the diurnal wave occurs at 18 LT. Nevertheless, in the solar cycle SDV parameters undergo significant changes due to changes in the state of the Sun and hence in the entire heliosphere.

Since the beginning of SDV research by ground-based detectors, the main problem has been to determine the anisotropy of primary CRs in interplanetary space. It is complicated by the fact that the approach to determining the CR anisotropy is based on the need to cover a sufficiently large area of the celestial sphere by using a large number of detectors located in different parts of the planet, often heterogeneous. In addition, the sensitivity of secondary CRs to changes in atmospheric parameters is also a serious obstacle. Furthermore, ground-based CR detectors as integrated devices that detect all particles regardless of their energy have limitations in studying the energy spectrum of anisotropy. Since GCRs are charged particles, the geomagnetic field has a significant effect on them: it changes the trajectory of the particles, and for some of them it becomes an insurmountable obstacle and leads to the formation of directions unavailable for propagation. Therefore, the use of observational data by ground-based instruments requires an understanding of the interaction of CRs with the geomagnetic field and Earth's atmosphere.

One of the most developed methods for determining the spatial-angular distribution of CRs in the interplanetary medium from ground-based measurements is the so-called method of receiving vectors (also referred to as coupling coefficients) [Krymsky et al., 1966, 1967; Fujimoto et al., 1984], which is based on general ideas about the interaction of CRs with the atmosphere and the geomagnetic field. The method allows us to take into account the individual receiving characteristics of a

detector and to estimate all possible distorting factors to define the CR distribution. The only free parameter for this method is the energy spectrum of variations, which is found by analyzing a large amount of data over a long period of time.

It is also important for ground detectors to take into account the so-called temperature effect — the effect of the atmospheric temperature regime on generation and propagation of secondary CRs to the observation point. This is most evident in the muon component of CRs. Accounting for this phenomenon requires knowledge of densities of temperature coefficients [Dorman, 1957] and the atmospheric temperature profile. Densities of temperature coefficients are calculated theoretically, and the altitude variation of temperature requires constant measurements with balloon probes over the observation point. Such measurements are currently performed only twice a day, which does not allow us to consider the temperature effect with sufficient accuracy. Despite the development of modern remote sensing methods [Berkova et al., 2018] and ground-based indirect measurements of atmospheric parameters [Nikolashkin et al., 2020], it is still urgent to solve this problem. An original and reliable way to circumvent this problem is to apply the method of crossed telescopes proposed at SHICRA SB RAS sixty years ago [Skripin et al., 1965; Skripin, 1965].

Traditionally, measurements with high-, mid-, and low-latitude neutron monitors, as well as ground and underground muon telescopes, are employed to determine the SDV energy spectrum [Rao et al., 1983; Riker et al., 1989; Ahluwalia, Sabbah, 1993; Pomerantz, Dug-gal, 1971]. Implementation of this approach made it possible to identify both the type of spectrum and its dynamics in the solar activity cycle. SDVs were demonstrated to weakly depend on CR energy and to remain constant up to a certain energy (upper cutoff) that averages ~100 GeV and varies in a cycle. The amplitude of these variations varies according to different estimates: for example, Hall et al. [1997] have shown that the upper cutoff is 100±25 GeV; Ahluwalia [1992] has indicated that it varies between 50 and 200 GeV depending on IMF strength. Presumably, the difference in estimates lies in the fact that different time intervals with arrays of stations scattered around the planet and equipped with CR detectors of different types are studied. This approach has some disadvantages: insufficiently accurate consideration of atmospheric factors and individual characteristics of detectors of different types inevitably causes considerable uncertainties. In this work, the method of crossed muon telescopes is adopted which allows us to take this disadvantage into account and estimate the SDV energy spectrum most reliably.

DATA AND METHOD

We have used data from the Nagoya, Hobart, and Sao Martinho muon telescopes of the global network GMDN [Okazaki et al., 2008; https://cosray.shinshu-u.ac.jp/crest/DB/Public/main.php], as well as the muon telescope of the Yakutsk CR spectrograph located on the Earth surface [Chuprova et al., 2009; https://ysn.ru/ipm /]. The main characteristics of the detectors are shown in Table.

Basic characteristics of the muon telescopes used in this work

Station	Direction	Geographic location	Period of recording	Count rate, imp/hr (on Jan. 01, 2018)	Statistical accuracy of 1-hr recording, %
Yakutsk	N30	62° N, 129° E	1972–2023	321000	0.17
	S30			322000	0.17
Nagoya	N2	35° N, 137° E	1971–2023	1356000	0.09
	S2			1340000	0.09
Hobart	N2	43° S, 147° E	2006–2023	620000	0.12
	S2			583000	0.12
Sao Martinho	N2	29° S, 306° E	2006–2023	891000	0.11
	S2			916000	0.10

In this work, the original method of crossed telescopes was employed to determine the SDV energy spectrum [Skripin et al., 1965]. It is based on the fact that the contribution of atmospheric factors to data from a pair of telescope directions having identical directional diagrams, but spaced in azimuth, proves to be the same. Therefore, the difference between intensities recorded by a pair of crossed telescope directions contains variations exclusively of extra-atmospheric origin due to the difference in sensitivity to primary CR anisotropy.

In this paper, we propose an approach that differs somewhat from the original method of crossed telescopes, but allows us to indirectly estimate the energy spectra of CR variations. Figure 1 exemplifies asymptotic angles of particle arrival from the north and south directions, calculated using the method of inverse trajectory calculations [Dorman et al., 1971]. It is evident that in general CRs experience a drift toward the equator by the geomagnetic field, which depends both on the detector energy and geographic location. In this case, the relationship between the asymptotic angles of particle arrival and observed SDVs is as follows: the latitude of the angle of particle arrival Φ defines the amplitude of variations as $\cos\Phi$; and the longitude Ψ, the SDV phase.

Accordingly, the phase difference $\Delta\Psi(E) = \Psi_N(E) - \Psi_S(E)$ between the north and south detection directions depend on CR energy, as well as the ratio of their amplitudes $\alpha(E) = \cos\Phi_N / \cos\Phi_S$. Thus, the use of crossed telescopes makes it possible to estimate energy spectra of CR variations without employing a large number of different detectors.

To accurately estimate the energy spectrum, we take into account the individual characteristics of the detectors with the receiving vector method [Krymsky

et al., 1966, 1967], using the expression

$$z_n^m = x_n^m + iy_n^m = \frac{\int_{R_c}^{\infty} \int_0^{2\pi} \int_0^{\frac{\pi}{2}} W(E, \theta) f_n(E) N(\theta, \varphi) e^{im\Psi(E, \theta, \varphi)} P_n^m \left(\sin \Phi(E, \theta, \varphi)\right) dE d\varphi d\theta}{\int_{R_c}^{\infty} \int_0^{2\pi} \int_0^{\frac{\pi}{2}} W(E, \theta) f_n(E) N(\theta, \varphi) dE d\varphi d\theta},$$

where θ, φ are zenith and azimuth angles; E is the particle energy; $N(\theta, \varphi)$ are the detector's directional diagrams; $W(E, \theta)$ are coupling coefficients; $f_n(E)$ is the energy spectrum of the nth harmonics of CR variations.

Thus, by comparing pairs of crossed (north and south) directions of muon telescopes, we can calculate the expected values of the phase difference $\Delta\Psi$ and the phase ratios α: $\alpha = \left|z_1^1\right|_S / \left|z_1^1\right|_N$, $\Delta\Psi = \Psi_N - \Psi_S$, where

$\Psi = \arctan\left(y_1^1 / x_1^1\right)$.

When calculating $\Delta\Psi$ and α, we assume that the energy spectrum has the form $f_1(E \le E_0) = const$ and $f_1(E > E_0) = 0$, where E_0 is the upper cutoff we set. The results are presented in Figure 2.
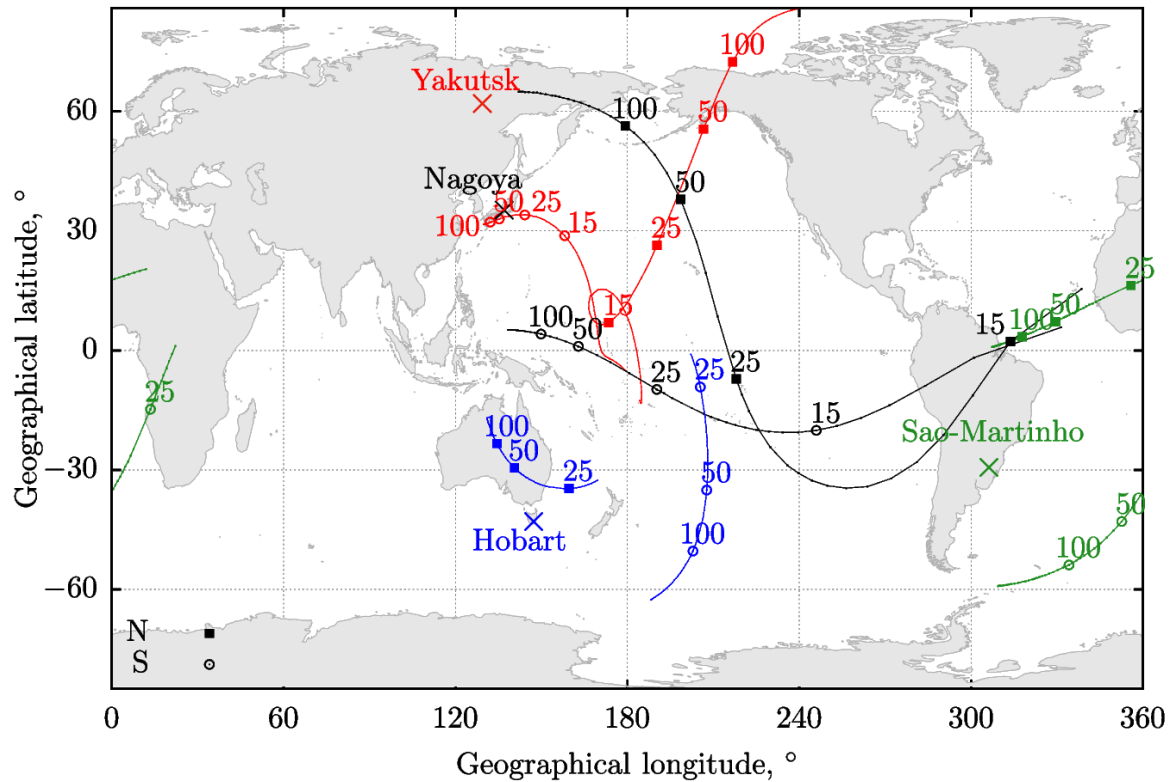

Figure 1. Asymptotic angles of particle arrival in the north and south directions at zenith angles of 30° of the muon telescopes Yakutsk, Sao Martinho, Nagoya, and Hobart. Numbers near dots denote energy (GV). Station locations are marked with crosses
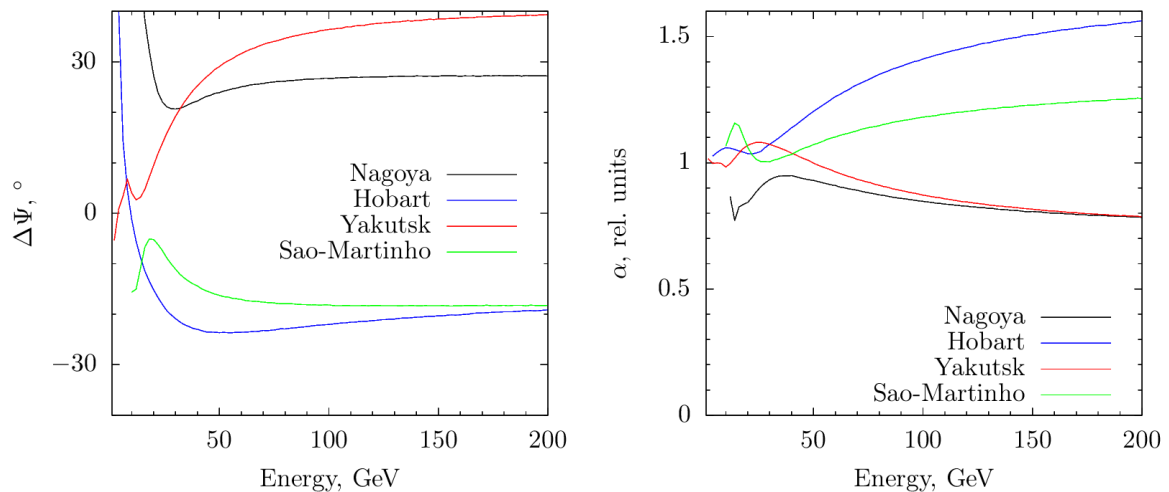

Figure 2. Results of calculation of $\Delta\Psi$ and α at different E_0 values

46

The parameters $\Delta\Psi$ and α for all stations are seen to be ambiguous in the energy range $E_0 \lesssim 50$ GeV. The north-south asymmetry of $\Delta\Psi$ and α for $E_0 \gtrsim 50$ GeV is expected and determined by the geomagnetic field structure. At energies above 150 GeV, the E_0 dependence of the parameters disappears due to an increase in the transparency of the geomagnetic field for CRs of such energies. Below, we estimate E_0 by comparing the $\Delta\Psi$ and α values we calculated with those observed using the least square method.

RESULTS AND DISCUSSION

The results of calculations of $\Delta\Psi$ and α are compared with observations by crossed muon telescopes in Figure 3. You can see that E_0 experiences 22-year variations, averaging 80 GeV and undergoing a short-term decrease to 20 GeV at solar minima during epochs of positive polarity of the Sun's general magnetic field. This behavior of E_0 is consistent with the muon telescope measurements, satisfactorily describing the $\Delta\Psi$ and α variations. High E_0 in 1980–1991 as compared to the rest of the period was obviously caused by the following reasons: when estimating E_0 before 2005, only two stations, Yakutsk and Nagoya, participated in the analysis; before 1990, the Yakutsk muon telescope had a relatively low statistical accuracy; at energies >100 GeV, the dependences of $\Delta\Psi$ and α on E_0 began to weaken, so the ambiguity in estimating E_0 increased. It is therefore fair to assume that such high E_0 values during these years are determined by these factors. Nevertheless, the same data allows us to argue that the given period was characterized by relatively high E_0.

Such a dramatic decrease in E_0 to 20 GeV is unexpectedly low, although it is consistent with the results received in [Ahluwalia, Sabbah, 1993]. With such a soft spectrum, SDVs should not be observed by CR detectors insensitive to such energies. Indeed, low-latitude neutron monitors with large geomagnetic cutoffs detect a relatively larger amplitude decrease and phase shift during these periods than high-latitude ones [Sabbah, 2013]. Moreover, underground muon telescopes should not detect SDVs during these periods. However, as shown in [Munakata et al., 2010], the muon telescope at Matsushiro station with a median energy of 0.6 TeV recorded statistically significant SDVs with ~0.04 % amplitudes, which though are associated with the generation of anisotropy by the interaction of GCRs with the heliospheric neutral sheet forming SDVs in the energy range >100 GeV [Kóta et al., 2008].

Particular attention should be given to the shape of the SDV energy spectrum. The spectrum with the upper cutoff considered in this work has no theoretical basis, yet, as shown in [Rao et al., 1983; Riker et al., 1989; Ahluwalia, Sabbah, 1993; Pomerantz, Duggal, 1971; Hall et al., 1997; Ahluwalia, 1992], it most closely corresponds to measurement data. Indeed, our calculations we carried out outside the scope of this work, using the SDV spectrum described by the power-law function, show a lower degree of agreement with observations. Nonetheless, it is impossible to exclude the possibility that the spectrum may have a different shape and change during a solar cycle.
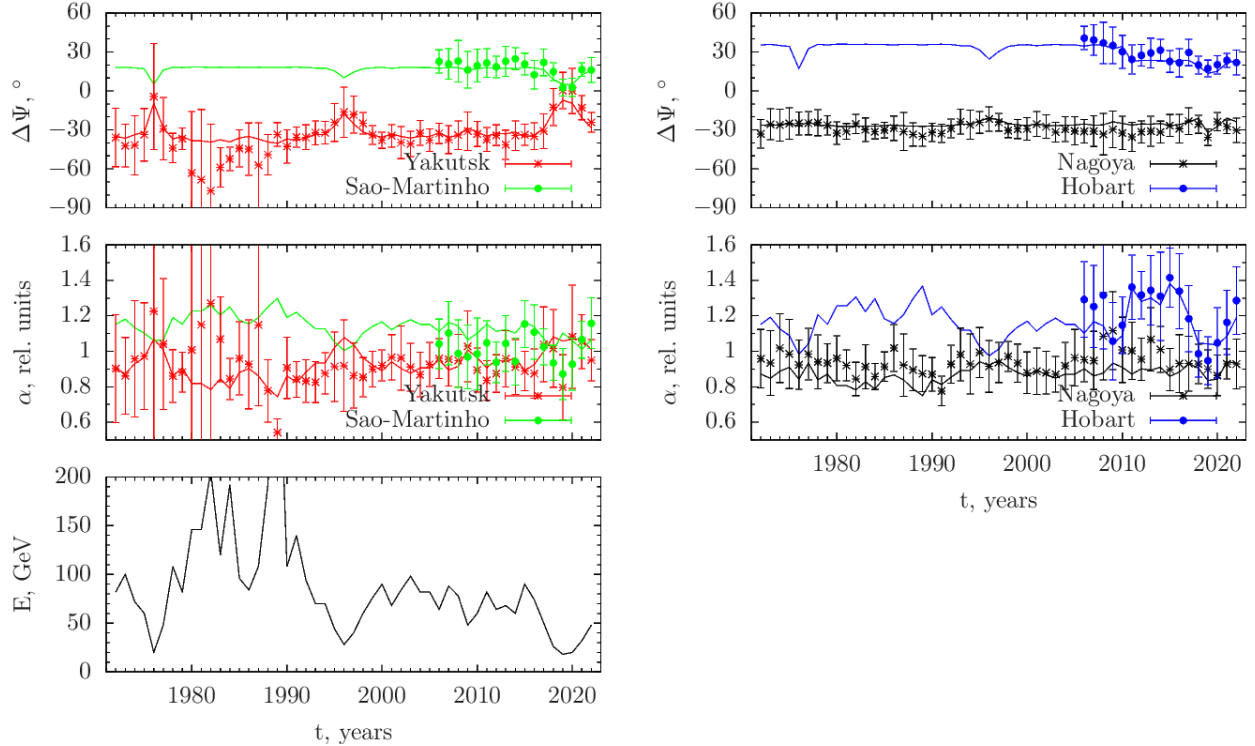

Figure 3. Comparison of calculated $\Delta\Psi$ and α with those observed by the crossed muon telescopes Yakutsk, Sao Martinho, Nagoya, and Hobart, as well as the results of estimates of the upper cutoff of E_0 for 1972–2022

As is known, the dependence of the heliospheric modulation of GCRs on the sign of the Sun's general magnetic field is due to their drift. In the epochs of positive polarity, the drift is directed from high to low solar latitudes [Gerasimova et al., 2017], and in the epochs of negative polarity; vice versa. This behavior is quite well manifested in the data on 11-year CR intensity variations [Gololobov et al., 2020]. The detected SDV energy spectrum softening during these periods may be linked to this phenomenon.

CONCLUSIONS

Using the method of crossed telescopes, we have estimated the dynamics of the SDV energy spectrum during solar cycles 20–25. It has been established that during solar minima with a positive polarity of the Sun's general magnetic field there is a significant SDV energy spectrum softening. Taking into account the sign dependence of the spectrum, we can conclude that the nature of its softening is related to the GCR drift in the heliosphere. The results can serve as an additional source of information when developing the theory of heliospheric GCR modulation.

REFERENCES

Ahluwalia H.S. A correlation between IMF and the limiting primary rigidity for cosmic ray diurnal anisotropy. *Geophys. Res. Lett.* 1992, vol. 19, iss. 6, pp. 633–636. DOI: 10.1029/92GL00525.

Ahluwalia H.S., Sabbah I.S. The limiting primary rigidity of cosmic ray diurnal anisotropy. *Planet. Space Sci.* 1993, vol. 41, iss. 2, pp. 105–112. DOI: 10.1016/0032-0633(93)90038-4.

Berkova M.D., Grigoryev V.G., Preobrazhensky M.S., Zverev A.S., Yanke V.G. Temperature effect observed for the muon component in the Yakutsk cosmic-ray spectrograph. *Physics of Atomic Nuclei.* 2018, vol. 81, no. 6, pp. 742–751. DOI: 10.1134/S1063778818050046.

Chuprova V.P., Gerasimova S.K., Grigoryev V.G., Krivoshapkin P.A., Krymsky G.F., Mamrukova V.P., et al. The brief history of experimental research of cosmic ray variations in Yakutia, *Adv. Space Res.* 2009, vol. 44, iss. 10., pp. 1200–1206. DOI: 10.1016/j.asr.2008.12.024.

Dorman L.I. Variatsii kosmicheskikh luchey [Variations of Cosmic Rays]. Moscow: Gosudarstvennoe izdatel'stvo tekhniko-teoreticheskoi literatury (State Publishing House of Technical and Theoretical Literature), 1957, 492 p. (In Russian).

Dorman L.I., Smirnov V.S., Tyasto M.I. Kosmicheskie luchi v magnitnom pole Zemli [Cosmic Rays in the Earth's Magnetic Field]. Moscow: Nauka (Science), 1971, 400 p. (In Russian).

Fujimoto K., Inoue A., Murakami K., Nagashima K. Coupling coefficients of cosmic ray daily variation for meson telescopes. Report of Cosmic-Ray Research Lab. Nagoya University. 1984, no. 9.

Gerasimova S.K., Gololobov P.Yu., Grigoryev V.G., Krivoshapkin P., Krymsky G., Starodubtsev S. Heliospheric modulation of cosmic rays: model and observation. *Sol.-Terr. Phys.* 2017, vol. 3, iss. 1, pp. 78–102. DOI: 10.12737/ article_58f970f2455545.93154609.

Gololobov P.Yu., Krivoshapkin P.A., Krymsky G.F., Gerasimova S.K. Investigating the influence of geometry of the heliospheric neutral current sheet and solar activity on modulation of galactic cosmic rays with a method of main components. *Sol.-Terr. Phys.* 2020, vol. 6, iss. 1, pp. 24–28. DOI: 10.12737/stp-61202002.

Hall D.L., Duldig M.L., Humble J.E. Cosmic-ray modulation parameters derived from the solar diurnal variation. *Astrophys. J.* 1997, vol. 482, pp. 1038–1049. DOI: 10.1086/ 304158.

Kóta J., Munakata K., Yasue S., Kato C., Mori S. The origin of solar diurnal variation of galactic cosmic rays above 100 GV. *Proc. 30th ICRC.* 2008, vol. 1, pp. 589–592.

Krymsky G.F., Kuzmin A.I., Chirkov N.P. Distribution of cosmic rays and detector response vectors. I. *Geomagnetizm i aeronomiya* [Geomagnetism and Aeronomy]. 1966, vol. 6, iss. 6, pp. 991–996. (In Russian).

Krymsky G.F., Kuzmin A.I., Chirkov N.P., et al. Distribution of cosmic rays and detector response vectors. II. *Geomagnetizm i aeronomiya* [Geomagnetism and Aeronomy]. 1967, vol. 7, iss. 1, pp. 11–15. (In Russian).

Munakata K., Mizoguchi Y., Kato C., Yasue S., Mori S., Takita M., Kóta J. Solar cycle dependence of the diurnal anisotropy of 0.6 TeV cosmic-ray intensity observed with the Matsushiro underground muon detector. *Astrophys. J.* 2010, vol. 712, pp. 1100–1106. DOI: 10.1088/0004-637X/712/2/1100.

Nikolashkin S.V., Titov S.V., Gololobov P.Yu. The effect of winter stratospheric warmings on the intensity of the muon component of secondary cosmic rays. *Proc. 26th International Symposium on Atmospheric and Ocean Optics. Atmospheric Physics.* 2020, vol. 11560. DOI: 10.1117/12.2575697.

Okazaki Y., Fushishita A., Narumi T., Kato C., Yasue S., Kuwabara T., et al. Drift effects and the cosmic ray density gradient in a solar rotation period: first observation with the Global Muon Detector Network (GMDN). *Astrophys. J.* 2008, vol. 681, pp. 693–707. DOI: 10.1086/588277.

Pomerantz M.A., Duggal S.P. The cosmic ray solar diurnal anisotropy. *Space Sci. Rev.* 1971, vol. 12, pp. 75–130. DOI: 10.1007/BF00172130.

Rao U.R., McCracken K.G., Venkatesan D. Asymptotic cones of acceptance and their use in the study of the daily variation of cosmic ray radiation. *J. Geophys. Res.* 1963, vol. 68, iss. 2, pp. 345–369. DOI: 10.1029/JZ068i002p00345.

Riker J.F., Ahluwalia H.S., Sabbah I.S. The limiting primary rigidities for the cosmic ray diurnal anisotropy during a solar magnetic cycle. *EOS: Trans. Am. Geophys. Union.* 1989, vol. 70, 1256.

Sabbah I. Solar magnetic polarity dependency of the cosmic ray diurnal variation. *J. Geophys. Res: Space Phys.* 2013, vol. 118, pp. 4739–4747. DOI: 10.1002/jgra.50431.

Skripin G.V. Issledovanie anizotropii kosmicheskikh luchey metodom skreshchennykh teleskopov [Study of the anisotropy of cosmic rays using the crossed telescopes method]. Cand. of Phys. and Math. Sci. diss. Yakutsk, 1965, 184 p. (In Russian).

Skripin G.V., Krivoshapkin P.A., Krymsky G.F., Filippov V.A. Study of cosmic ray anisotropy using the crossed telescopes method. *Geomagnetizm i aeronomiya* [Geomagnetism and Aeronomy]. 1965, vol. 5, iss. 5, pp. 817–822. (In Russian).

URL: https://cosray.shinshu-u.ac.jp/crest/DB/Public/main.php (accessed March 7, 2025).

URL: https://ysn.ru/ipm/ (accessed March 7, 2025).

URL: http://hdl.handle.net/10091/0002001448 (accessed March 7, 2025).

MHD WAVES IN THE PRE-FRONT REGION OF THE INTERPLANETARY SHOCK ON MAY 10, 2024

S.A. Starodubtsev (iD)
Yu.G. Shafer Institute of Cosmophysical Research
and Aeronomy SB RAS,
Yakutsk, Russia, starodub@ikfia.ysn.ru

Abstract. The article reports on the study of the dynamics of the IMF turbulent component from the quiet period on May 7, 2024 to the arrival of an interplanetary shock wave in the second half of May 10, 2024. To achieve the stated goal, 1-minute direct measurements of interplanetary medium parameters on the *ACE*, DSCOVR, and WIND spacecraft are involved in the analysis. Spectral analysis methods are used to study the evolution of power spectra of fluctuations in IMF modulus and MHD waves in the inertial portion of the SW turbulence spectrum at frequencies $\sim2.5\cdot10^{-4}$–$8.3\cdot10^{-3}$ Hz. The contribution of Alfvén, fast, and slow magnetosonic waves to the observed power spectrum of the IMF modulus measured by each of the three spacecraft is determined, and power spectra of MHD waves of these types are identified. It is shown that the power of the spectra of fluctuations in the IMF modulus and MHD waves increases by more than an order of magnitude as the shock wave approaches the point of its recording on the spacecraft. It is concluded that this is due to the generation of MHD waves by fluxes of energetic storm particles (ESP) — cosmic rays with energies ~1 MeV, observed in the region ahead of the interplanetary shock wave front. Analysis of all measurement data allows for the assumption that a significant increase in low-energy CR fluxes (~1 MeV) and SW turbulence levels may lead to a change in the IMF direction in the region adjacent to the IPS front.

Keywords: MHD waves, solar wind, interplanetary magnetic field, interplanetary shock.

INTRODUCTION

Nowadays, space weather forecasting is one of the most relevant areas of research in space physics. For this purpose, observations from various ground- and spaced-based instruments are used and diverse predictive models are being developed. When making a forecast, it is necessary to take into account the current state of the interplanetary medium and have an idea about the physical processes that occur in the solar wind plasma under certain conditions.

The interplanetary magnetic field (IMF) is an important component in space plasma. It plays a significant role in the generation and propagation of cosmic rays (CRs) in the heliosphere, as well as in the occurrence of geomagnetic storms and the formation of pulsations of various types in Earth's magnetosphere. In many cases, its turbulent component is also important.

Properties of turbulence in SW, in particular in the vicinity of interplanetary shock (IPS) fronts, are widely discussed in the scientific literature. Various characteristics of fluctuations in IMF magnitude and components, density, and velocity in different parts of observed SW turbulence spectrum are studied (see, e.g., [Li et al., 2005; Hu et al., 2013; Borovsky, 2020; Pitna et al., 2021; Sapunova et al., 2024; Kim, Oh, 2024; Smith, Vasquez, 2021, 2024]). In these works, in particular, it is noted that in the region ahead of IPS fronts an increase in the intensity of fluctuations in various interplanetary medium components is often observed in a wide range of frequen-

cies corresponding to the energy, inertial, and dissipative parts of the SW turbulence spectrum. At the same time, there are changes in the slopes of spectra at the corresponding inflection points of the spectra. In addition, Smith and Vasquez [2021] draw attention to the fact that, despite the constant improvement in the quality of spacecraft data, the fundamental questions of plasma physics concerning energy dissipation and observed heating of thermal plasma still remain largely unanswered. Moreover, one of the reasons for this is the insufficient number of multipoint measurements of IMF and SW parameters by SC, which are located close enough to each other to better study the three-dimensional dynamics of turbulent phenomena, which underlies many physical processes in SW plasma.

In this regard, of particular interest is to delve into the powerful heliogeophysical events that occurred in early May 2024. At that time, after a series of X-class solar flares accompanied by multiple coronal mass ejections [Ram et al., 2024; Lazzús, Salfate, 2024], significant changes in space weather and, as a consequence, various geophysical phenomena were observed in Earth's orbit. In particular, the passage of an intense IPS in the second half of May 10, 2024 caused a strong geomagnetic storm with sudden commencement (SSC) (Figure 1, *a*). It started on May 10 at 17:05 UT [https://www.obsebre.es/php/geomagnetisme/vrapides/ssc_2024_p.txt] and was the most powerful in the last two decades after the famous event on November 20, 2003, known as the Halloween Event in the scientific
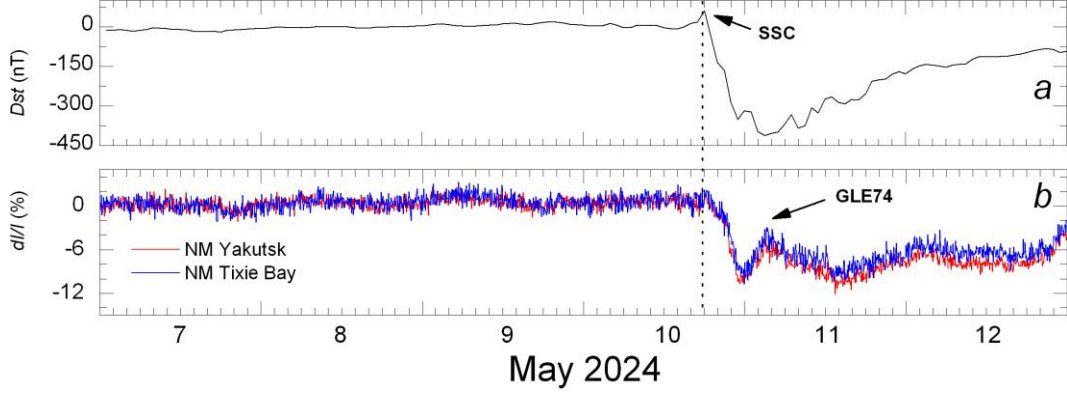
Figure 1. Geomagnetic activity index *Dst* (*a*) and CR intensity as measured by neutron monitors (NM) at the stations Yakutsk and Tixie Bay (*b*) on May 7–12, 2024. The dotted line shows the beginning of the geomagnetic storm and the Forbush effect on May 10, 2024; arrows indicate the sudden commencement (SSC) of the magnetic storm and the ground-level enhancement of CRs (GLE74)

literature. This storm was followed by a major Forbush effect (see Figure 1, *b*), powerful auroras even at low latitudes [Lazzús, Salfate, 2024], and an unusual response from the low-latitude ionosphere near the equatorial anomaly in India [Jain et al., 2025]. In addition, on May 11, 2024, the worldwide neutron monitor network recorded a ground-level enhancement of cosmic rays (GLE74) [https://www.nmdb.eu]. Thus, this extraordinary heliogeophysical event requires a comprehensive study.

This paper is a sequel to our previous work [Starodubtsev, Shadrina, 2024] and is devoted to experimental study of generation, properties, and evolution of SW MHD turbulence in the IPS pre-front region, which was recorded by a constellation of three spacecraft, located at a relatively short distance from each other in the second half of May 10, 2024, and caused a number of vivid manifestations of space weather on Earth.

1. DATA AND METHOD

The work uses one-hour data on the geomagnetic disturbance index *Dst* [https://omniweb.gsfc.nasa. gov/form/dx1.html] and one-hour pressure-corrected data on CR intensity from the stations Yakutsk and Tixie Bay [https://www.ysn.ru/ipm], as well as one-hour data on CRs recorded on board ACE SC by a detector LEMS120 during the EPAM experiment. This detector is designed to measure low-energy CR fluxes (mainly protons) in eight different differential energy channels: 0.047–0.068, 0.068–0.115, 0.115–0.195, 0.195–0.321, 0.321–0.580, 0.587–1.06, 1.06–1.90, and 1.90–4.80 MeV [https://izw1.caltech.edu/ACE/ASC/level2/index.html].

In order to study properties of the IMF turbulent component and to identify MHD waves, we have used one-minute direct measurements of IMF and SW parameters from three spacecraft: the Deep Space Climate Observatory (DSCOVR), Advanced Composition Explorer (ACE), and WIND, located near the libration point L1. Detailed information about these spacecraft and data on various interplanetary medium parameters are publicly available at [https://omniweb.gsfc.nasa.gov/ftpbrowser/

wind_min_merge.html; https://services.swpc.noaa.gov/json/rtsw/rtsw_mag_1m.json; https://services.swpc.noaa.gov/json/rtsw/rtsw_wind_1m.json]. Especially noteworthy is that SC measurements are initial, contain small gaps and failures, so they should be used with caution.

When analyzing the SC measurement data, the location of each of the spacecraft in near-Earth space was also taken into account [https://sscweb.gsfc.nasa.gov/cgi-bin/Locator.cgi].

Using the entire set of spacecraft data, IMF and MHD-wave spectral characteristics and their dynamic changes in the inertial part of the spectrum of SW turbulent fluctuations at frequencies $\sim 2.5 \cdot 10^{-4} – 8.3 \cdot 10^{-3}$ Hz were examined. Note that the first of the frequencies roughly corresponds to the boundary between the energetic and inertial parts of the spectrum of SW turbulent fluctuations, which changes little with solar cycle [Kovalenko, 1983], and the second is determined by the Nyquist frequency $\nu_N = 1/(2\Delta t)$, where $\Delta t = 60$ s is the sampling increment of the data in use. Spectral analysis methods based on the Blackman—Tukey algorithm with the Tukey correlation window were employed to gain useful information from direct measurements [Jenkins, Watts, 1971; Otnes, Enoxon, 1982]. Its application made it possible to estimate the IMF fluctuation power spectra with a 95 % confidence interval corresponding to the number of degrees of freedom equal to 66.675 [Jenkins, Watts, 1971]. All original time series of data were preliminarily subjected to the standard procedure of preparation for analysis. At this stage, observed failures and outliers were excluded from the data, with gaps in the initial series filled in with values obtained by interpolating adjacent measurements. Further, all time series of data were reduced to the zero mean, and then they were filtered by a digital bandpass filter in the frequency band indicated above [Otnes, Enokson, 1982].

Note that when studying properties of IMF fluctuations, the spectral characteristics of its magnitude and components are often examined. This is due to the fact that from the type of spectra we can draw a definite and reasonable conclusion about the presence of longitudinal or transverse waves and oscillations in SW during the time

periods of interest. In particular, it is known that for transverse Alfvén waves there are fluctuations in the field direction rather than in its magnitude. In this case, the difference between the power spectra of IMF components and strength may be as great as an order of magnitude. For the fast mode (compression waves), the power spectra of IMF components and strength are of the same order, which indicates fluctuations in both the IMF direction and magnitude [Kovalenko, 1983]. However, from these IMF fluctuation power spectra it is impossible to conclude about the contribution of MHD waves of a certain type to the spectra observed in SW. But all of them contribute to the IMF magnitude in any way. Therefore, when identifying spectral characteristics of MHD waves of different types, their known properties were taken into account. They consist in that Alfvén waves (AW) are characterized by a correlation between the IMF magnitude B and the SW velocity V; for fast magnetosonic waves (FMSW), between B and the plasma density n; and for slow magnetosonic waves (SMSW), between n and V [Neugebauer et al., 1978; Toptygin, 1983]. Nonetheless, since this work deals with spectral properties of IMF fluctuations, the coherence coefficient is used which is a generalization of the concept of correlation to the frequency domain rather than the correlation coefficient that characterizes the relationship between certain physical quantities in the time domain [Luttrell, Richter, 1986, 1987; Starodubtsev et al., 2023]. Note that, by definition, the coherence coefficient is a positive value of the square root of the coherence function. It varies from 0 to 1 and is a function of frequency. The procedure adopted in this work for estimating the spectral characteristics of fluctuations in IMF and SW plasma parameters, the corresponding coherence coefficients, as well as the method for identifying MHD waves, and their difference from oscillations are described in detail in [Starodubtsev et al., 2023].

2. RESULTS AND DISCUSSION

Figures 2–4 display the IMF magnitude B and B_z component (*a*), density n (*b*), velocity V (*c*), and temperature T (*d*) recorded by each of the three spacecraft on May 7–12, 2024. The dotted line indicates the arrival time of IPS for each spacecraft. Its arrival at DSCOVR was recorded on May 10, 2024 at 16:35 UT (see Figure 2); at ACE, at 16:37 UT (see Figure 3); at WIND, at 17:05 UT (see Figure 4). It is apparent (see Figures 2–4) that from May 7 until the arrival of the large-scale SW disturbance (coronal mass ejection accompanied by IPS) at Earth's orbit in the second half of May 10, conditions in near-Earth space were relatively quiet, and IMF and SW parameters did not experience any significant changes despite sufficiently high SW n, V, and T [Toptygin, 1983].

Figure 5, *a–c* in the GSE coordinate system shows the location of the constellation of three spacecraft relative to Earth on May 7, 2024. The distance is given in Earth radii R_E. Blue segments represent the direction of the mean IMF vector in different projections on the YX (*a*), ZX (*b*), and ZY (*c*) planes. Compared to the distance from the Sun to Earth (1 AU≈285185 R_E), all SC are located quite close to each other. Nevertheless, it can be noted that WIND is located somewhat away from Earth; and the other two SC,

at a distance of ~100 R_E (*a*, *c*). However, the direction of mean IMF during this time period is seen to be nearly the same for all spacecraft.

Let us now examine the spectral characteristics of SW turbulence, using the results of analysis of one-minute direct measurements of interplanetary medium parameters from the three spacecraft. We will begin with the quiet period of May 7, 2024. Figure 6, *a–c* presents calculated coherence coefficients $\Gamma_{BV}(\nu)$, $\Gamma_{Bn}(\nu)$, and $\Gamma_{Vn}(\nu)$ as function of frequency ν. Their values determine the contribution of MHD waves of one type to the observed power spectrum of IMF fluctuations at a certain frequency ν. The coherence values are seen to be not very high, except for $\Gamma_{Vn}(3.5\cdot10^{-3}\,\text{Hz})=0.86$ and $\Gamma_{BV}(3.4\cdot10^{-4}\,\text{Hz})=0.55$ (panel *b*), which means a significant contribution of SMSW and AW to the observed power spectrum of IMF fluctuations at these frequencies (panel *e*) during the period considered. As for the contribution of other types of MHD waves at other frequencies, it is much smaller and does not exceed 50 % as a whole. In general, in order to establish the frequency spectra of MHD waves of a certain type, it is necessary to multiply the power spectra of IMF fluctuations $P(\nu)$ by the corresponding values of the coherence coefficient $\Gamma(\nu)$, which are calculated for each SC. Panels *d–f* exhibit the observed power spectra of IMF fluctuations, their approximation by the least square method, and the corresponding power laws that describe them. Note that the corresponding powers for DSCOVR and ACE are greater than –1, whereas for WIND, on the contrary, they are much smaller than –1. From May 8 as the IPS front is approached, the spectral indices calculated from ACE and DSCOVR data gradually decrease, tending to the well-known Kolmogorov turbulence spectrum of –5/3, and for WIND they abruptly reach this value and remain almost the same up to the shock front. Perhaps this is somehow related to the location of WIND with respect to Earth and other spacecraft, from which it is at a distance of ~100 R_E along the Y-axis outside the boundary of the magnetosphere (

es 6, *d–f* also presents the established MHD wave spectra of all three types — AW, FMSW, and SMSW. As expected, they do not exceed the IMF fluctuation power spectra, and their sums within 95 % confidence intervals are comparable to the fluctuation power spectra of the IMF magnitude measured by each spacecraft. At the same time, the maximum power spectra in the frequency range considered correspond well to quiet conditions in SW [Kovalenko, 1983] and even at a low frequency $2.5\cdot10^{-4}$ Hz they do not exceed 10^2 nT^2/Hz.

Another pattern is observed just before thsee Figures 5 and 9).

Figure arrival of IPS. In Figure 7, *a–f* is the same information for the time interval before the arrival of IPS as in Figure 6, *a–f*. Values of all coherence coefficients $\Gamma(\nu)$ are seen to change; and the IMF fluctuation power spectrum, to increase by an order of magnitude, becoming steeper with powers less than –1. This also fully applies to each spectrum characterizing an MHD wave of a certain type (see Figure 7, *d–f*). Moreover, behind the IPS front in the transition turbulent region, the spectral indices on the three spacecraft drop sharply to –(2.0÷2.2) within 2–3 hrs, and then slowly tend to recover to –5/3.
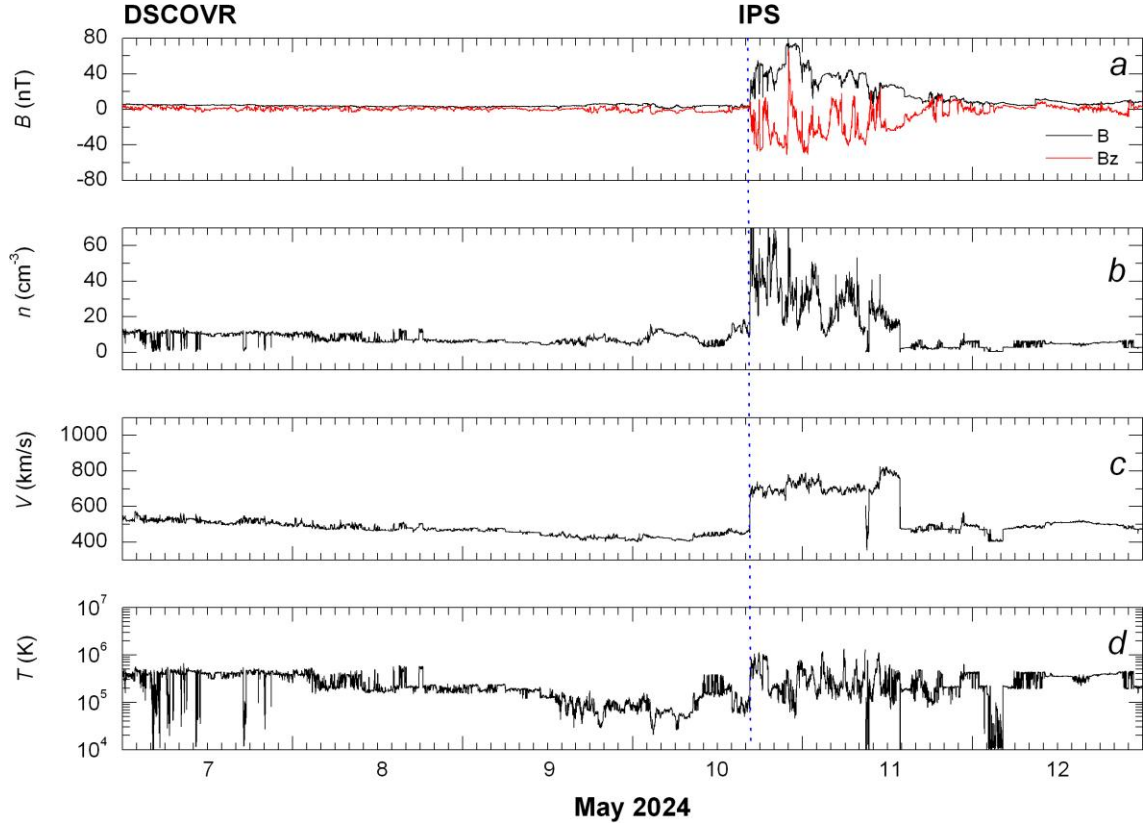
Figure 2. IMF *B* and *B$_z$(a)*, SW density *n (b)*, velocity *V (c)*, and temperature *T (d)* measured by DSCOVR on May 7–12, 2024. The dotted line is the IPS arrival time
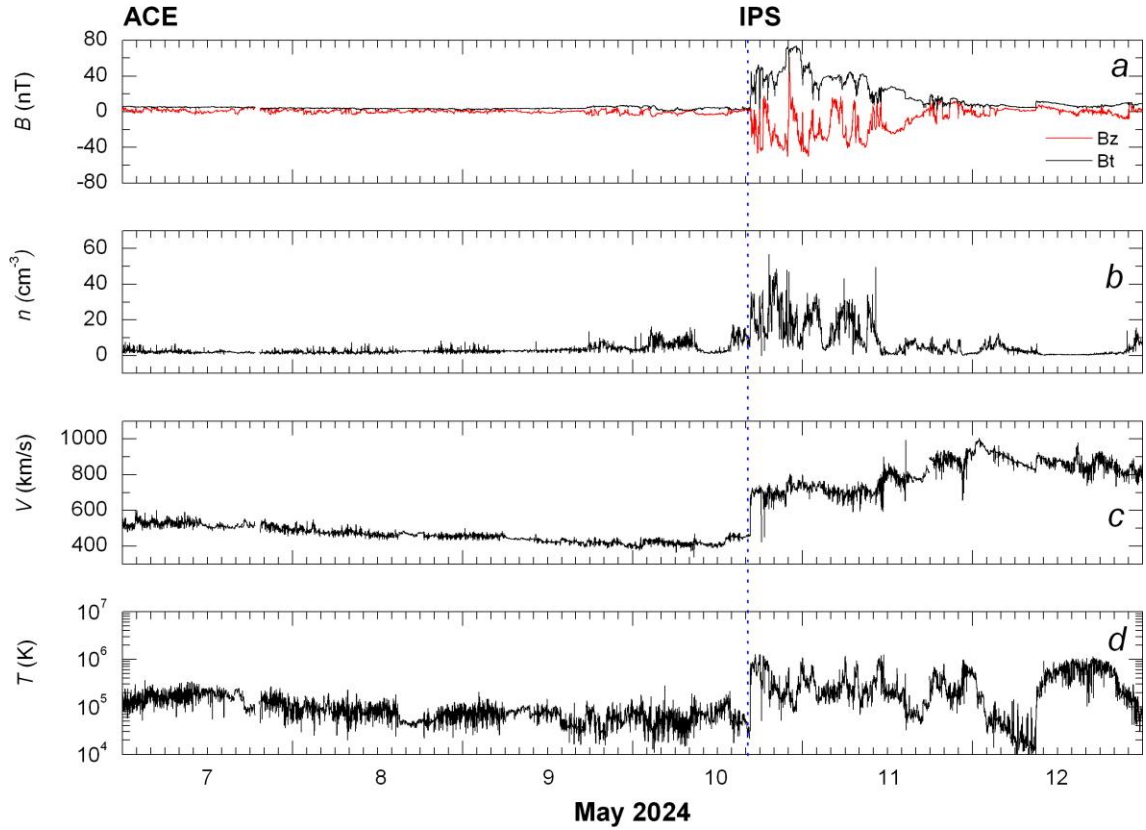
Figure 3. The same for ACE
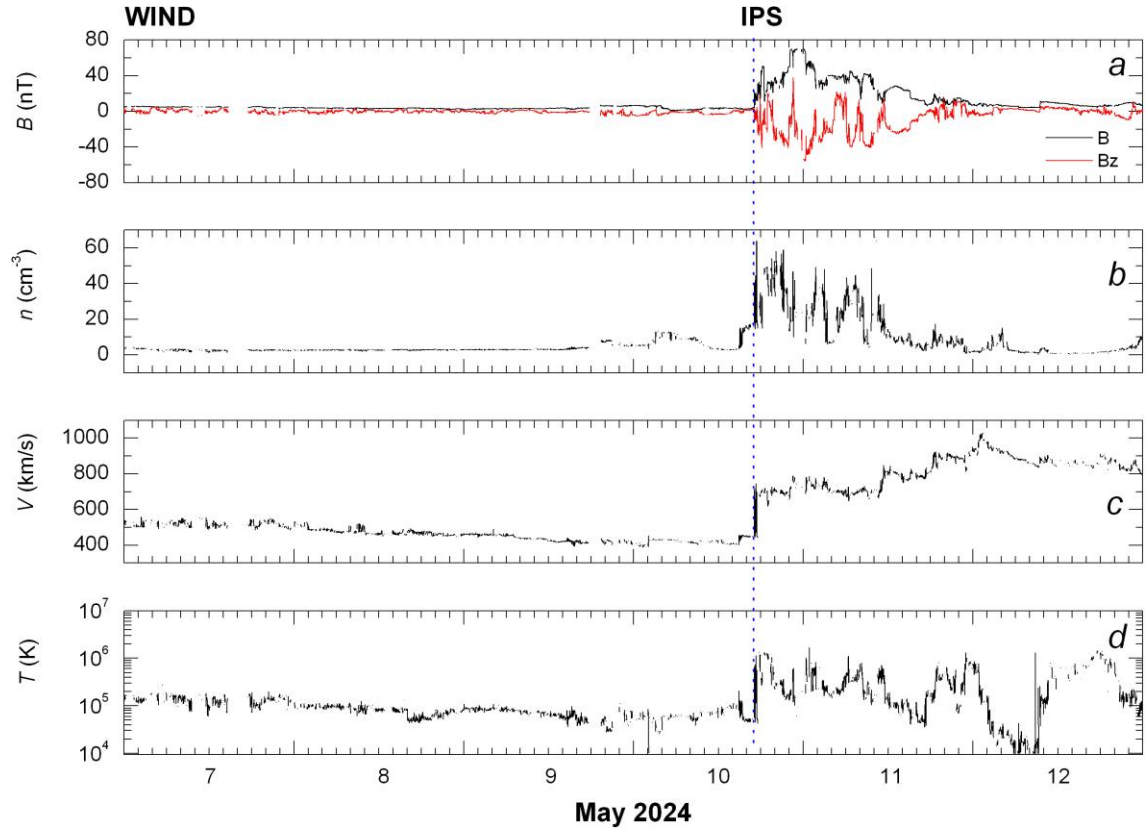
Figure 4. The same for WIND
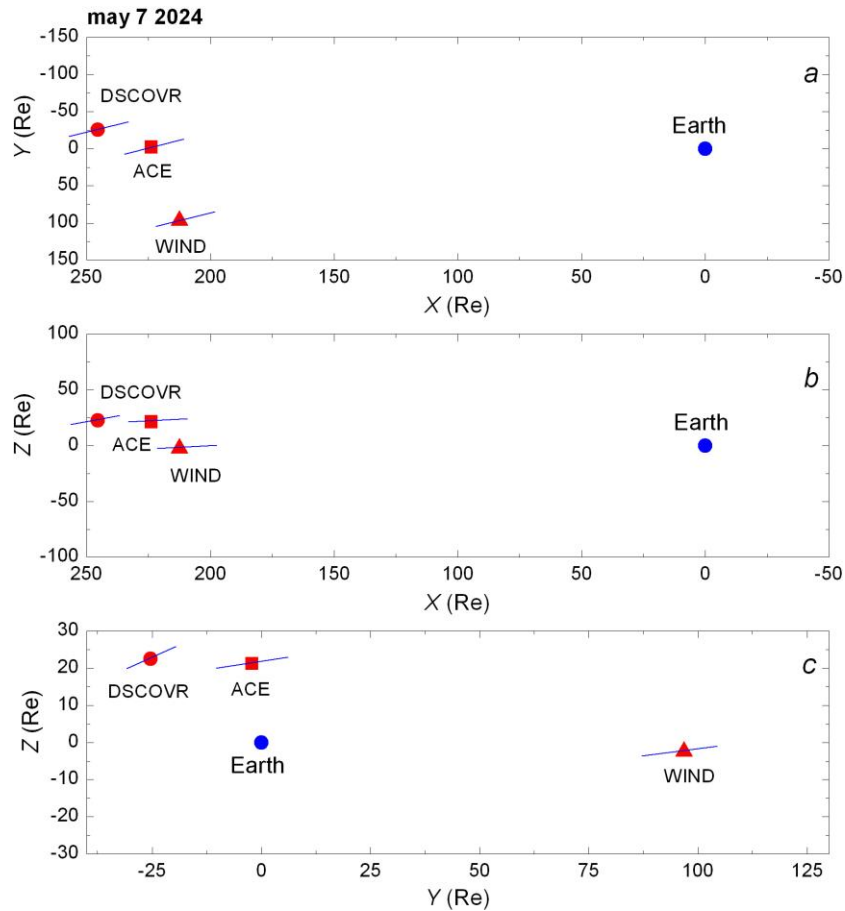
Figure 5. Location of the constellation of three spacecraft DSCOVR, ACE, and WIND during the quiet period on May 7, 2024 relative to Earth in projection on different planes in the GSE coordinate system. Blue segments represent the direction of the mean IMF in each spacecraft on that day

Figure 6. Coherence coefficients $\Gamma_{BV}(\nu)$, $\Gamma_{Bn}(\nu)$, and $\Gamma_{Vn}(\nu)$ *a–c*), as well as the power spectra of IMF fluctuations and the established power spectra of MHD waves (*d-f*) for the quiet period on May 7, 2024. The dashed line is an approximation of power spectra of IMF fluctuations; a power law describing them is given. The corresponding legends (*a*, *d*) for coherence and power spectra and 95 confidence intervals for power spectra are shown. Above each panel are names of SC

Figure 7. The same for the IPS pre-front region on May 10, 2024

Noteworthy is the shape of the IMF fluctuation power spectrum calculated from WIND data (see Figures 6, *f* and 7, *f*). In the IPS pre-front region, it also increases by an order of magnitude, but in both cases its index α<–1. This raises a certain question, but may be due to the IMF spaghetti structure in front of the IPS front or due to the wavy structure of the IPS front itself, as we have assumed earlier in [Starodubtsev, Shadrina, 2024].

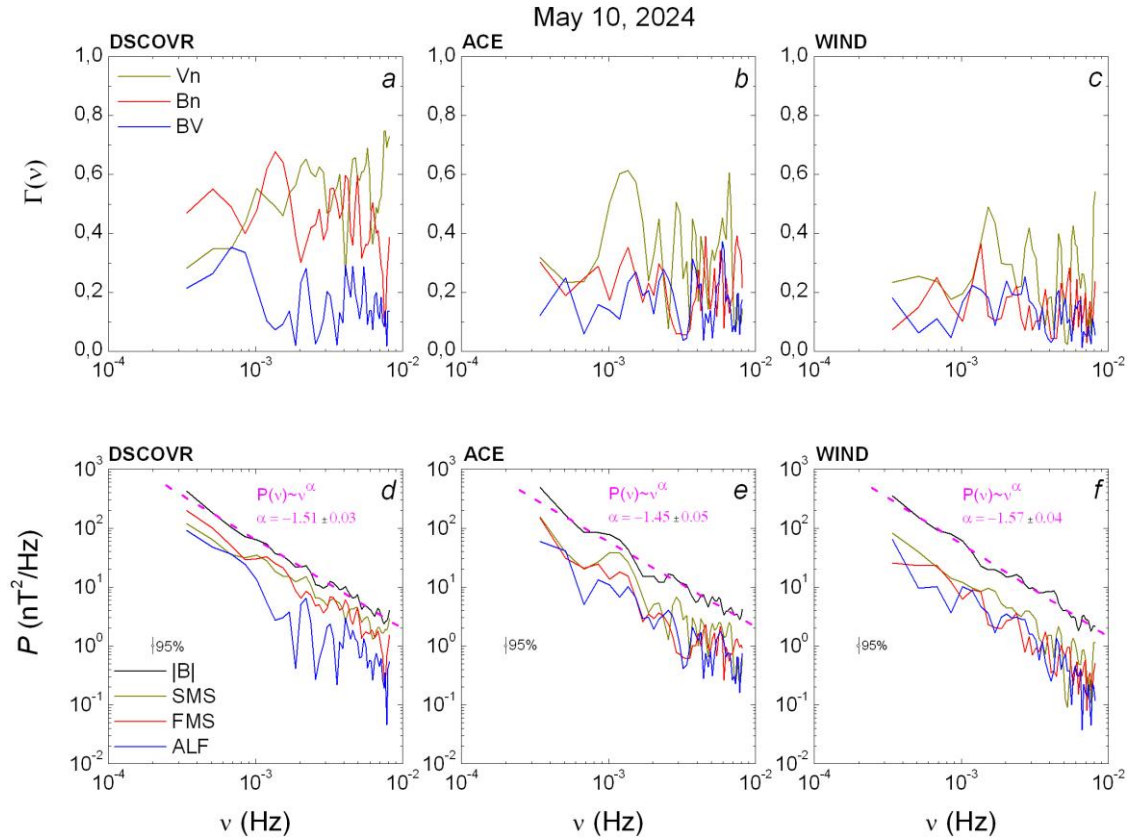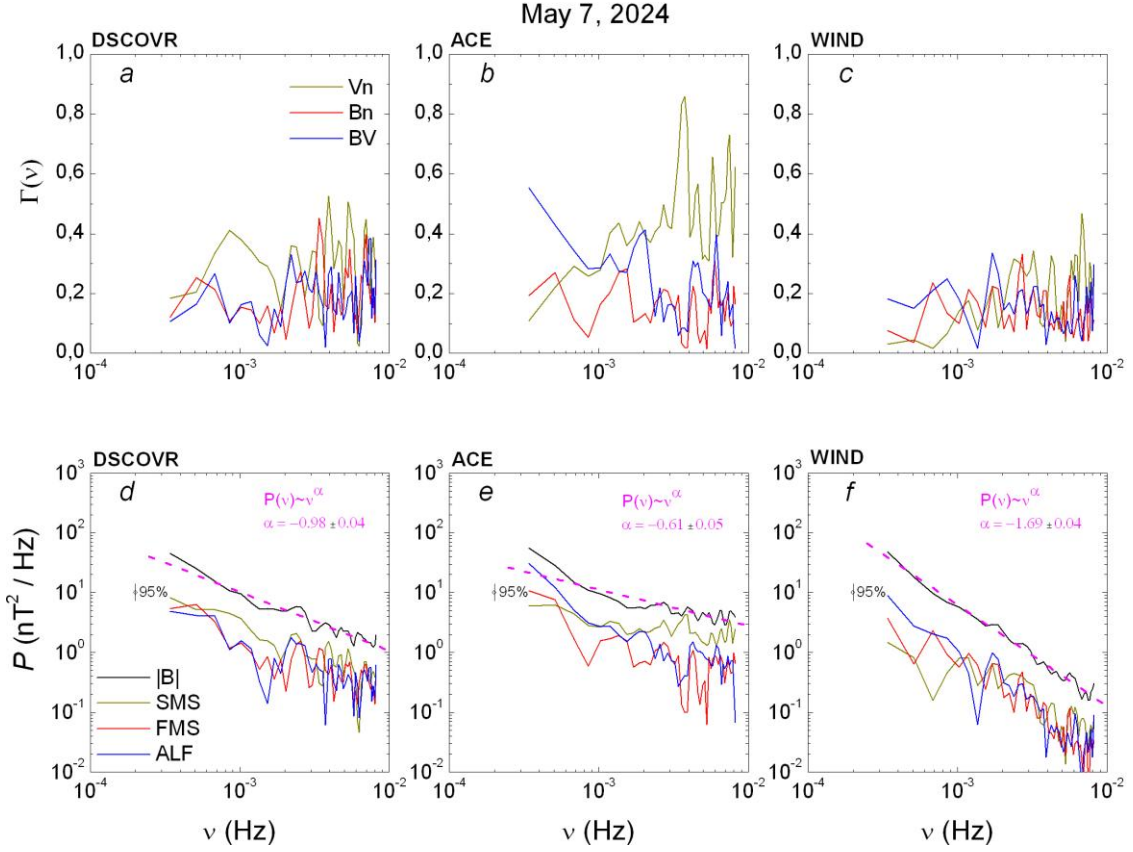More detailed analysis of the dynamics of power spectra of IMF fluctuations and MHD waves shows that as IPS approaches SC the spectra become steeper and their power increases. Why this happens can be understood by considering the theoretical works [Berezhko, 1986, 1990; Chalov, 1988; Berezhko, Starodubtsev, 1988; Reames, 1989; Vainio, 2003], which suggest that MHD waves can be generated by low-energy CR fluxes. These authors have developed mechanisms for the generation of Alfvén and magnetosonic waves due to the formation of plasma instabilities in the interplanetary medium by low-energy solar CRs (also called solar energetic particles (SEP)) or particles accelerated at IPS fronts, which are called energetic storm particles (ESP) in the scientific literature. The determining factor in these processes is the presence of low-energy (~1 MeV) CRs in the interplanetary medium, which feature large fluxes and gradients. Indeed, at the time in question there were such CR fluxes after a series of powerful solar flares in Earth's orbit. Figure 8, as Figures 2–4, shows raw data. From May 8, 2024, as ACE is approached, the low-energy CR flux,

which consists of SEP and ESP with a maximum at the IPS front and is characterized by a large spatial gradient, is seen to increase by many orders of magnitude. Taking into account the results of the above-mentioned studies, this allows us to draw a reasonable conclusion about the cause for the observed increase in the level of IMF fluctuations, which occurs due to generation of MHD waves by these particles in the IPS pre-front region on May 10, 2024.

An interesting fact is that, in contrast to the situation depicted in Figure 5, mean IMF changes direction, as observed in all three spacecraft located relatively close to each other. This is illustrated in Figure 9.

. It can be assumed that the presence of significant storm particle fluxes with an energy of ~1 MeV and a corresponding increase in the SW turbulence level cause the mean IMF to change direction in the region of space directly adjacent to the IPS front. It is, however, still too early to make certain conclusions about the reasons for this since very few statistics of observations of such events from sufficiently closely located spacecraft have been collected (only 35 cases).

CONCLUSIONS

Thus, studying the May 10, 2024 IPS event recorded by three spacecraft located near the libration point L1 allows the following conclusions to be drawn.
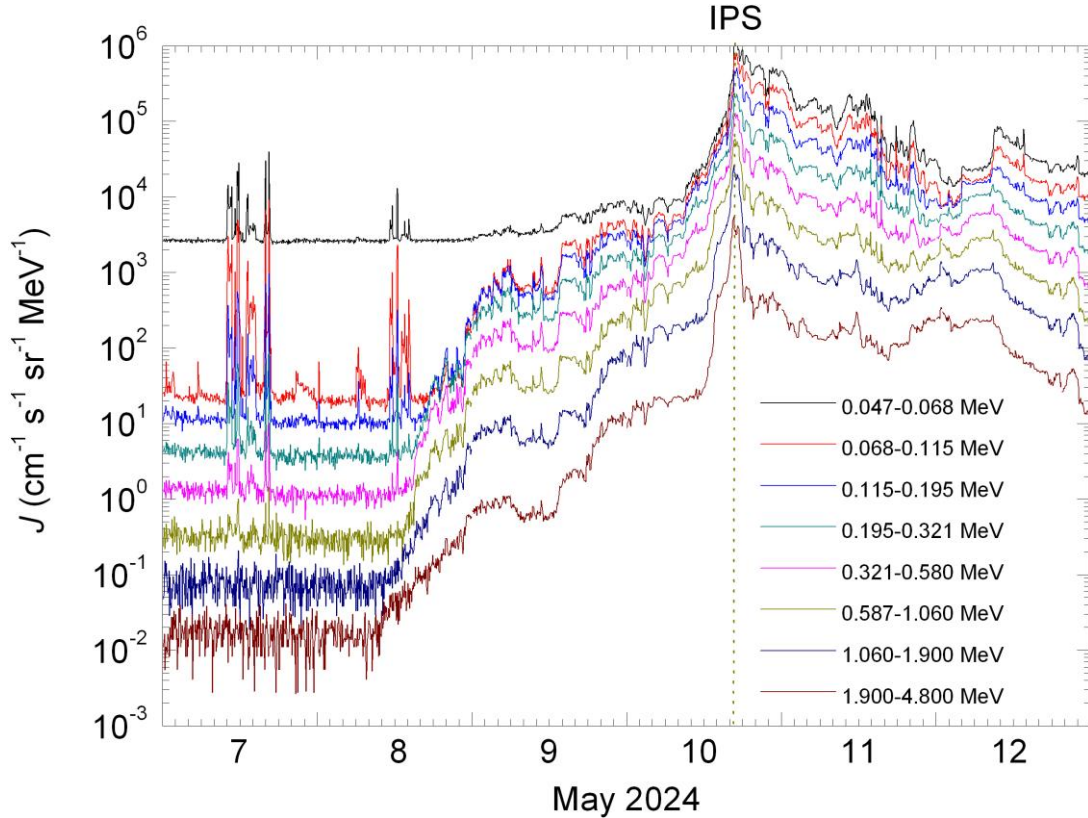

Figure 8. Low-energy CR fluxes in eight different differential channels recorded on board ACE during the EPAM experiment (LEMS120 detector) on May 7–12, 2024. A legend for the differential energy channels is shown. The dashed line is the time of IPS arrival at ACE, which coincides with the maximum CR flux of different energies
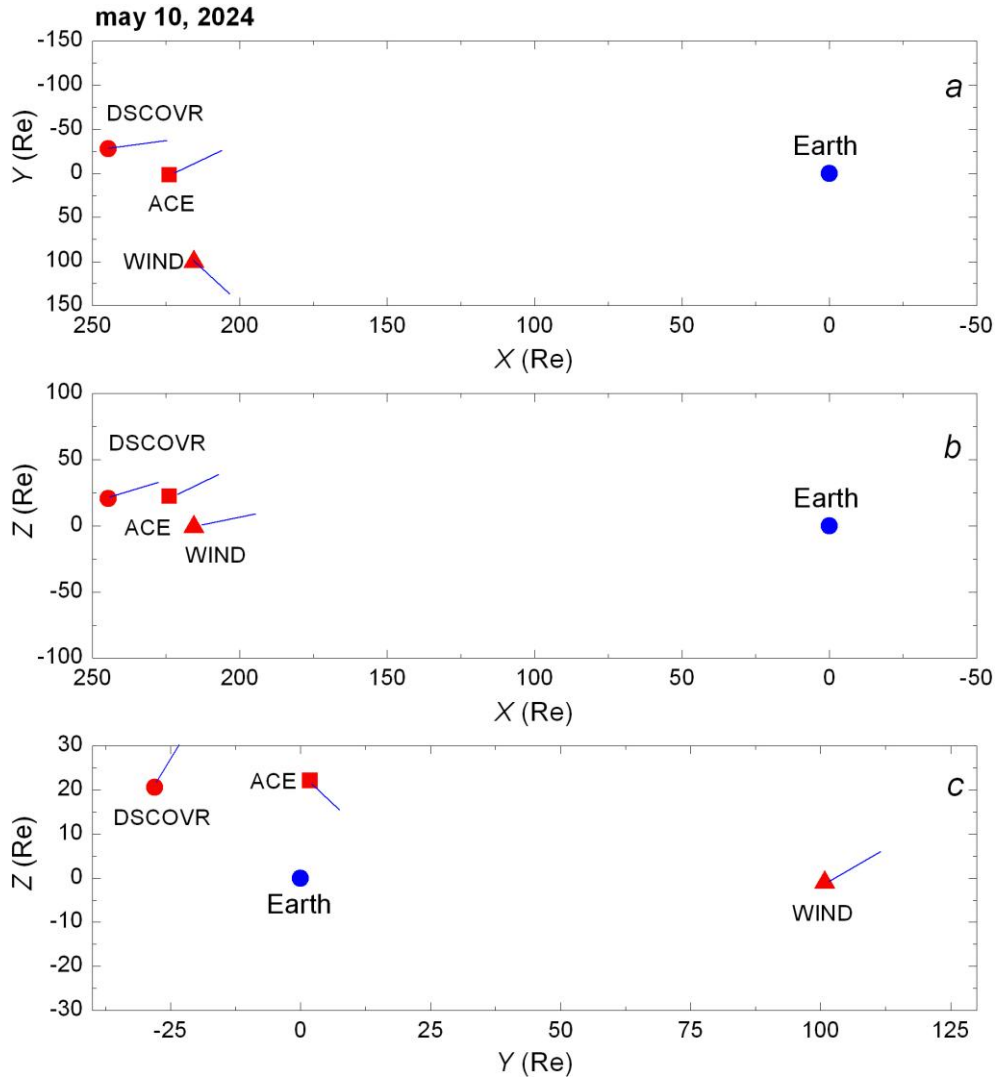
Figure 9. The same as in Figure 5 for the pre-front region of IPS recorded by three spacecraft on May 10, 2024

1. Using spectral analysis methods with direct measurements of IMF and SW plasma parameters from DSCOVR, ACE, and WIND spacecraft, we have identified MHD waves of three types: Alfvén, fast, and slow magnetosonic waves observed during the period of interest in the inertial part of the SW turbulence spectrum in the frequency range $\sim 2.5 \cdot 10^{-4}$–$8.3 \cdot 10^{-3}$ Hz.

2. It has been shown that during this event there is a significant increase, by about an order of magnitude, in the power of fluctuations in the IMF strength and MHD waves of all three established types in the IPS pre-front region.

3. The reason is low-energy CRs of solar and interplanetary origin (SEP and ESP), characterized by large fluxes and gradients whose presence in the IPS pre-front region led to the generation of MHD waves.

4. It is assumed that a significant increase in low-energy CR fluxes (~1 MeV) and the SW turbulence level can cause IMF to change direction in the region of space directly adjacent to the IPS front.

REFERENCES

Berezhko E.G. Instability in a shock wave propagating in a gas with cosmic rays. *Pis'ma v Astronomicheskii Zhurnal.* 1986, vol. 12, pp. 842–847. (In Russian).

Berezhko E.G. Generation of MHD waves in interplanetary plasma by fluxes of solar cosmic rays. *Pis'ma v Astronomicheskii Zhurnal.* 1990, vol. 16, pp. 1123–1132. (In Russian).

Berezhko E.G., Starodubtsev S.A. Nature of the dynamics of the cosmic-ray fluctuation spectrum. *Izvestiya Akademii Nauk SSSR. Ser. Fizicheskaya* [Bull. Academy of Sciences of USSR. Ser. Physics]. 1988, vol. 52, pp. 2361–2363. (In Russian).

Borovsky J.E. A statistical analysis of the fluctuations in the upstream and downstream plasmas of 109 strong-compression interplanetary shocks at 1 AU. *J. Geophys. Res.: Space Phys.* 2020, vol. 125, iss. 6, article id. e27518. DOI: 10.1029/2019JA027518.

Chalov S.V. Instability of a diffusive shock wave in a plasma with cosmic rays. *Pis'ma v Astronomicheskii Zhurnal.* 1988, vol. 14, pp. 272–276. (In Russian).

Hu Q., Zank G.P., Li G., Ao X. A Power Spectral Analysis of Turbulence Associated with Interplanetary Shock Waves. *in AIP Conf. Ser. 1539, Proc. of the Thirteenth International Solar Wind Conf.*, ed. G. P. Zank et al. 2013. 175, DOI: 10.1063/1.4811016.

Jain A., Trivedi R., Jain S., Choudhary R.K. Effects of the super intense geomagnetic storm on 10–11 May, 2024 on total electron content at Bhopal. *Adv. Space Res.* 2025, vol. 75, iss. 1, pp. 953–965. DOI: 10.1016/j.asr.2024.09.029.

Jenkins G.M., Watts D.G. *Spectral Analysis and Its Applications.* San Francisco, Cambridge, London, Amsterdam, Holden-Day, 1968, 525 p.

Kim S., Oh S. Characteristics of interplanetary shock sheath regions in the solar wind inducing the Forbush decreases. *J. Korean Astron. Soc.* 2024, vol. 57, no. 2, pp. 173–182. DOI: 10.5303/JKAS.2024.57.2.173.

Kovalenko V.A.. *Solnechy veter* [Solar Wind]. Moscow, Nauka Publ., 1983, 272 p. (In Russian).

Lazzús J.A., Salfate I. Report on the effects of the May 2024 Mother's day geomagnetic storm observed from Chile. *J. Atmospheric and Solar–Terr. Phys.* 2024, vol. 261, 106304. DOI: 10.1016/j.jastp.2024.106304.

Li G., Hu Q., Zank G.P. Upstream turbulence and the particle spectrum at CME-driven shocks. *Proc. AIP Conf. "Physics of Collisionless Shocks"*. 2005, vol. 781, pp. 233–239. DOI: 10.1063/1.2032702.

Luttrell A.H., Richter A.K. Power spectra of low frequency MHD turbulence up- and downstream of interplanetary fast shocks within 1 AU. *Ann. Geophys.* 1986, vol. 4, pp. 439–446.

Luttrell A.H., Richter A.K. Study of MHD fluctuations upstream and downstream of quasiparallel interplanetary shocks. *J. Geophys. Res.* 1987, vol. 92, pp. 2243–2252.

Neugebauer M., Wu C.S., Huba J.D. Plasma fluctuations in the solar wind. *J. Geophys. Res.* 1978, vol. 83, pp. 1027–1034.

Otnes R., Enokson L. *Prikladnoi analiz vremennykh ryadov. Osnovnye metody.* [Applied Time Series Analysis. Vol. 1. Basic Techniques.] Moscow, Mir Publ., 1982, 430 p. (In Russian).

Pitna A., Safrankova J., Nemecek Z., Durovcova T., Kis A. Turbulence upstream and downstream of interplanetary shocks. *Front. Phys.* 2021, *Frontiers in Physics.* 2021, vol. 8, id. 654. DOI: 10.3389/fphy. 2020.626768.

Ram T., Veenadhari S., Dimri B., et al. Super-intense geomagnetic storm on 10–11 May 2024: Possible mechanisms and impacts. *Space Weather.* 2024, vol. 22, iss. 12, e2024SW004126. DOI: 10.1029/2024SW004126.

Reames D.V. Wave generation in the transport of particles from large solar flares. *Astrophys. J. Lett.* 1989, vol. 342, no. 1, Part 2, pp. L51–L53.

Sapunova O.V., Borodkova N.L., Yermolaev Yu.I., Zastenker G.N. Spectra of fluctuations of solar wind plasma parameters near a shock wave. *Cosmic Res.* 2024, vol. 62, iss. 1, pp. 1–9. DOI: 10.1134/S0010952523700843.

Smith C.W., Vasquez B.J. Driving and dissipation of solar-wind turbulence: What is the evidence? *Front. Astron. Space Sci.* 2021, vol. 7, id. 114. DOI: 10.3389/fspas.2020.611909.

Smith C.W., Vasquez B.J. The unsolved problem of solar-wind turbulence. *Front. Astron. Space Sci.* 2024, vol. 11, id. 1371058. DOI: 10.3389/fspas.2024.1371058.

Starodubtsev S.A., Shadrina L.P. MHD waves at the pre-front of interplanetary shocks on September 6 and 7, 2017. *Sol.-Terr. Phys.* 2024, vol. 10, iss. 3, pp. 50–57. DOI: 10.12737/stp-103202406.

Starodubtsev S.A., Zverev A.S., Gololobov P.Yu., Grigoryev V.G. Cosmic ray fluctuations and MHD waves in the solar wind. *Sol.-Terr. Phys.* 2023, vol. 9, iss. 2, pp. 73–80. DOI: 10.12737/stp- 92202309.

Toptygin I.N. *Kosmicheskie luchi v mezhplanetnykh magnitnykh polyakh* [Cosmic rays in interplanetary magnetic fields]. Moscow, Nauka Publ., 1983, 304 p. (In Russian).

Vainio R. On the generation of Alfven waves by solar energetic particles. *Astron. Astrophys.* 2003, vol. 406, pp. 735–740.

URL: https://www.obsebre.es/php/geomagnetisme/vrapides/ssc_2024_p.txt (accessed February 27, 2025).

URL: https://www.nmdb.eu (accessed February 27, 2025).

URL: https://omniweb.gsfc.nasa.gov/form/dx1.html (accessed February 27, 2025).

URL: https://www.ysn.ru/ipm (accessed February 27, 2025).

URL: https://izw1.caltech.edu/ACE/ASC/level2/index.html (accessed February 27, 2025).

URL: https://omniweb.gsfc.nasa.gov/ftpbrowser/wind_min_merge.html (accessed February 27, 2025).

URL: https://services.swpc.noaa.gov/json/rtsw/rtsw_mag_1m.json (accessed February 27, 2025).

URL: https://services.swpc.noaa.gov/json/rtsw/rtsw_wind_1m.json (accessed February 27, 2025).

URL: https://sscweb.gsfc.nasa.gov/cgi-bin/Locator.cgi (accessed February 27, 2025).

How to cite this article
Starodubtsev S.A. MHD waves in the pre-front region of the interplanetary shock on May 10, 2024. *Sol.-Terr. Phys.* 2025, vol. 11, iss. 3, pp. 50–58. DOI: 10.12737/stp-113202507.

FEATURES OF PROPAGATION OF COMPRESSIONAL LONG-PERIOD OSCILLATIONS PENETRATING FROM THE INTERPLANETARY MEDIUM IN THE MAGNETOSPHERE — IONOSPHERE SYSTEM

A.V. Moiseev (iD)
Yu.G. Shafer Institute of Cosmophysical Research and Aeronomy SB RAS,
Yakutsk, Russia, moiseev@ikfia.ysn.ru

V.I. Popov
Yu.G. Shafer Institute of Cosmophysical Research and Aeronomy SB RAS,
Yakutsk, Russia, volts@mail.ru

V.V. Mishin
Institute of Solar-Terrestrial Physics SB RAS,
Irkutsk, Russia, vladm@iszf.irk.ru u

Yu.V. Penskikh
Institute of Solar-Terrestrial Physics SB RAS,
Irkutsk, Russia, penskikh@iszf.irk.ru

Abstract. We have studied properties of Pi3 pulsations with a period of ~30 min in the magnetosphere—ionosphere system, using satellite and ground-based observations. According to the data from ground-based magnetic stations in the pre-noon sector of the magnetosphere, propagation of pulsations was revealed in azimuth from the dayside to the nightside at a velocity 3–9 km/s in the band of corrected geomagnetic latitudes $\Phi'=76°–79°$. Along the meridian, the signal propagated poleward at a velocity 0.5–5 km/s. Analysis of signal spectra at stations located along different meridians shows three maxima: one latitude-independent maximum at a frequency of 0.55 mHz, and two latitude-dependent maxima at frequencies of 0.82 and 0.96 mHz respectively, at higher and lower latitudes. The first maximum corresponds to ULF waves penetrating from the solar wind; the other two, to magnetospheric field line resonances. The equivalent current system (ECS) during the pulsation recording was obtained by two methods: the method of spherical elementary current systems and the magnetogram inversion technique. Analysis of ECS derived by both methods has demonstrated that they match each other. The ECS during pulsations in the pre-noon sector is a large vortex consisting of smaller vortices that propagate in the ionosphere along the "sea-land" boundary line, i.e. meridional poleward propagation at velocities close to the average pulsation propagation velocities prevailed. According to the map of field-aligned current distribution in the ionosphere, the width of the maximum of the westward electrojet lies at the latitude of the ECS maximum (in the south of the large vortex) on the boundary between the regions of inflowing and outflowing field-aligned currents (regions 1 and 2), where field line resonances are observed. The obtained ECS corresponded to the DP2 current system with a predominant westward electrojet in the pre-noon and night sectors. Satellite data analysis has shown the following. In the solar wind, ULF waves in the Pi3 pulsation range propagated at a velocity of 186.4 km/s, which is significantly lower than the velocity of the medium being as high as 550 km/s. This velocity is explained by the fact that the waves propagate toward the Sun and are carried by the solar wind to Earth. In the magnetosphere, pulsations with a predominant compression component propagated from the nightside to the dayside at a velocity 90–110 km/s; from the delays in the onset of maxima of energetic electron differential fluxes, velocities 20–40 km/s were identified.

Pulsations in this event were caused by both external (oscillations in the solar wind) and internal sources (magnetospheric resonator, which could be excited, among other things, by a substorm). The dynamics of the "fine structure" of a large vortex — small vortices, in the magnetosphere as a whole coincides in propagation velocity and direction with geomagnetic pulsations.

Keywords: geomagnetic Pi3 pulsations, equivalent current vortices, azimuthal and meridional propagation, penetration of ULF waves from the interplanetary medium into the magnetosphere, field line resonance.

INTRODUCTION

It is known that Pi3 pulsations are irregular long-period oscillations in the geomagnetic field, which can be generated during a magnetospheric substorm [Saito, Matsushita, 1967]. The review [Saito, 1978] provides a classification according to which Pi3 is divided into subcategories: Ps6 and Pip. Ps6 pulsations ($T>400–600$ s) prevail in the D component of the geomagnetic field; Pip pulsations ($T<400$ s) have comparable amplitudes in all components. Sources of Pi3 and other geomagnetic pulsations are spatio-temporal variations in the intensity of three-dimensional current systems [Saito, 1969]. The Pi3 pulsations associated with a substorm are generally localized in the night sector of the magnetosphere. At the same time, the Pi3 pulsations are known to be linked with variations in interplanetary medium parameters

[Han et al., 2007]. Alimaganbetov and Streltsov [2018] have carried out a statistical analysis of wave disturbances in the solar wind (SW) during substorms and have found that wave disturbances with frequencies 0.6–0.7 mHz are often observed during substorms both in SW and on Earth. Presumably, Pi3s caused by outside forces should not only be recorded in the night sector of the magnetosphere, but also form a high-latitude current system of appropriate spatial scales.

It is known that the interaction of the diamagnetic structure (DS) with Earth's magnetosphere gives rise to phenomena similar to substorms, which can occur with Pi3 pulsations [Parkhomov et al., 2017]. These structures are in fact magnetic flux ropes filled with plasma [Eselevich, Eselevich, 2005]. A diamagnetic current flows on their surface, reducing the magnetic field inside and increasing it outside the flux tube.

An important characteristic of pulsations is their propagation whose direction may indicate their source. Moiseev et al. [2020] from ground-based geomagnetic observations have revealed azimuthal propagation of pulsations with a velocity 0.6–10.6 km/s to the east and west from midnight; along the meridian, the pulsations propagated to the equator at a velocity 0.75–7.87 km/s. Pulsation propagation can also be estimated from a shift of their current systems. In [Moiseev et al., 2024a], propagation velocities of geomagnetic pulsations localized on the dayside and designated as TCVs (traveling convection vortices) were compared with phase delays in the pulsations and based on motion of their equivalent current systems. The propagation velocities measured by these methods differ about two times (mostly in phase delays).

In this paper, we analyze the distribution of Pi3 pulsations recorded globally from ground-based and satellite observations. Field-aligned currents during pulsations are studied using the magnetogram inversion technique. As far as we know, the dynamics of global pulsations and vortices of the corresponding spatial scales have not been examined before.

The purpose of the work is to study the morphology and dynamics of large current vortices — a high-latitude current system of global Pi3 pulsations, as well as to assess the contribution of external and internal sources to the frequency spectrum of pulsations. For analysis, we have selected the September 11, 2015 event during which geomagnetic Pi3 pulsations were observed.

1. EXPERIMENTAL DATA

To examine meridional and azimuthal propagation of geomagnetic Pi3 pulsations and equivalent current vortices, we have used geomagnetic observations from the well-known SUPERMAG database [Gjerloev, 2012; https://supermag.jhuapl.edu/mag/]: coordinates of the stations are given in Tables 1 and 2. To construct equivalent current systems by the method of spherical elementary current systems (SECS), we have employed 61 SUPERMAG stations with geographic latitudes 45.14°–77.47° and longitudes 199.54°–267.89°; by the magnetogram inversion technique (MIT), 144 SUPERMAG stations in the Northern Hemisphere. Measurements from the CDAWEB database were used on satellites [http://cdawe b.gsfc.nasa.gov/]. Coordinates of the satellites are listed in Table 3. To study propagation, we rely on data from ground stations with a time resolution of 60 s since the duration of phase delays in signals ≥60 s. Satellite data had a time resolution of 3 (Themis), 60 (Geotail), 4 (Cluster), and 5 s (GOES).

2. ANALYSIS METHOD

We compared azimuthal propagation velocities obtained by two methods: from phase delays in magnetic variations at stations and from motion of vortices of equivalent ionospheric currents. The methods are described in [Moiseev et al., 2024b]. In the event of interest, there were pulsations with a well-defined shape at high latitudes, so their azimuthal propagation was studied only along corrected geomagnetic latitudes $\Phi'=76°–79°$.

Field-aligned currents (FACs) of Pi3 pulsations were examined using MIT [Bazarzhapov et al., 1979; Mishin, 1990; Penskikh, 2020]. This method can calculate key electrodynamic parameters of the ionosphere with 1-min time resolution from data on the field of geomagnetic variations from the global network of ground magnetometers. In this work, with MIT we have obtained equivalent current functions, FACs with homogeneous conductivity, as well as boundaries of FAC zones [Lunyushkin, Penskikh, 2019; Penskikh et al., 2021]. To separate Pi3 pulsations from geomagnetic data, we employed a digital bandpass filter tuned to the frequencies corresponding to these pulsations [Moiseev et al., 2024b].

3. RESULTS

Figure 1 presents measurements of plasma and interplanetary magnetic field (IMF) parameters in SW: IMF components and ion concentration (*a–d*), V_x component of ion velocity and SW dynamic pressure P_d (*e*, *f*) from THEMIS-B (ThB) data in the September 11, 2015

Table 1

Coordinates of ground stations (SMAG) employed to study azimuthal propagation of pulsations

Average latitude	Abbreviation	Geographic coordinates		Corrected geomagnetic coordinates	
		latitude	longitude	latitude	longitude
76–79	GHC	68.63	264.15	77.54	–31.68
	IGC	69.30	278.2	78.43	–5.39
	UPN	72.78	303.85	78.93	40.20
	NAL	78.92	11.95	76.57	109.96
	DMH	76.77	341.37	77.34	84.38

Table 2

Coordinates of ground magnetometric stations,
used to study meridional propagation of geomagnetic pulsations

Abbreviation	Network	Geographic coordinates		Corrected geomagnetic coordinates	
		latitude	longitude	latitude	longitude
THL	GrW	77.47	290.77	84.72	29.24
SVS		76.02	294.9	83.00	32.87
KUV		74.57	302.82	80.69	41.92
UPN		72.78	303.85	78.93	40.20
UMQ		70.68	307.87	76.38	42.58
GDH		69.25	306.47	75.25	39.39
ATU		67.93	306.43	73.99	38.19
STF		67.02	309.28	72.64	40.87
SKT		65.42	307.10	71.43	37.22
FHB		62.00	310.32	67.41	39.05
NAQ		61.16	314.56	65.75	43.19
IGC	USAE	69.30	278.20	78.43	−5.39
RPB		66.52	273.77	75.99	−13.51
CDC		64.20	283.40	73.47	3.04
T47		62.20	284.35	71.51	4.23
T53		60.82	281.85	70.39	0.08
T46		60.05	282.71	69.60	1.36
T44		58.47	281.92	68.14	−0.04
T31		56.50	280.80	66.31	−1.92
T52		53.79	282.38	63.54	0.26
T51		48.05	282.22	57.86	−0.43
OTT		45.40	284.45	54.98	2.52
RES	USAC	74.69	265.11	82.93	−35.54
GHC		68.63	264.15	77.54	−31.68
BLC		64.32	263.99	73.60	−30.06
RAN		62.82	267.89	72.45	−23.12
FCC		58.76	265.91	68.50	−25.59
GIM		56.38	265.36	66.16	−26.08
PIN		50.20	263.96	59.96	−27.43
C08		45.87	264.92	55.72	−25.69
T56		45.59	267.03	55.60	−22.65
YKC	USAW	62.48	245.52	69.42	−56.85
SMI		60.03	248.07	67.48	−52.27
FMC		56.66	248.79	64.28	−50.02
T36		54.71	246.69	61.95	−52.09
C06		53.35	247.03	60.64	−51.24
RED		52.14	246.16	59.25	−51.96
T43		50.87	245.70	57.86	−52.17
T03		50.37	247.02	57.60	−50.40
LET		49.64	247.13	56.88	−50.07

event. At the bottom in panels *g*, *h* are the *AL* and *SYMH* indices for the interval considered. From 9:00 to 11:00 UT, three ~30 min oscillations were observed in IMF B_z and P_d, which manifested themselves on Earth's surface in *AL* variations and geomagnetic Pi3 pulsations. The oscillations were preceded by a period in which IMF B_z was southward from 07:30–09:00 UT. At that time, $B_x<0$, $B_y>0$, and the SW V_x component increased from 450 to 550 km/s. The ion concentration during this period varied in antiphase with IMF, such variations in plasma concentration and magnetic field are observed in DS [Parkhomov et al., 2017], and are also typical of slow mode oscillations [Hada, Kennel, 1985]. As the geomagnetic indices show, the event was recorded during a moderate magnetic storm and when an intense substorm, whose explosive phase lasted from 08:14 to 09:40 UT, ended.

Figure 2 illustrates changes in the magnetic field recorded by satellites in the noon and dawn sectors of the magnetosphere at 9:00–11:00 UT. Observations in SW are given with a shift of 10 min to make it easier to compare the shape of oscillations in SW and in the magnetosphere.

From top to bottom are *B* and $B_{x,y,z}$. Figure 3 displays the same data after bandpass filtering: the filter is seen to cause no phase distortions in raw signals. Variations in SW recorded by ThB, ThC and in the noon sector of the magnetosphere by Geotail (GL) are similar, which means that the pattern of field variations in the noon sector is largely due to their penetration from SW.

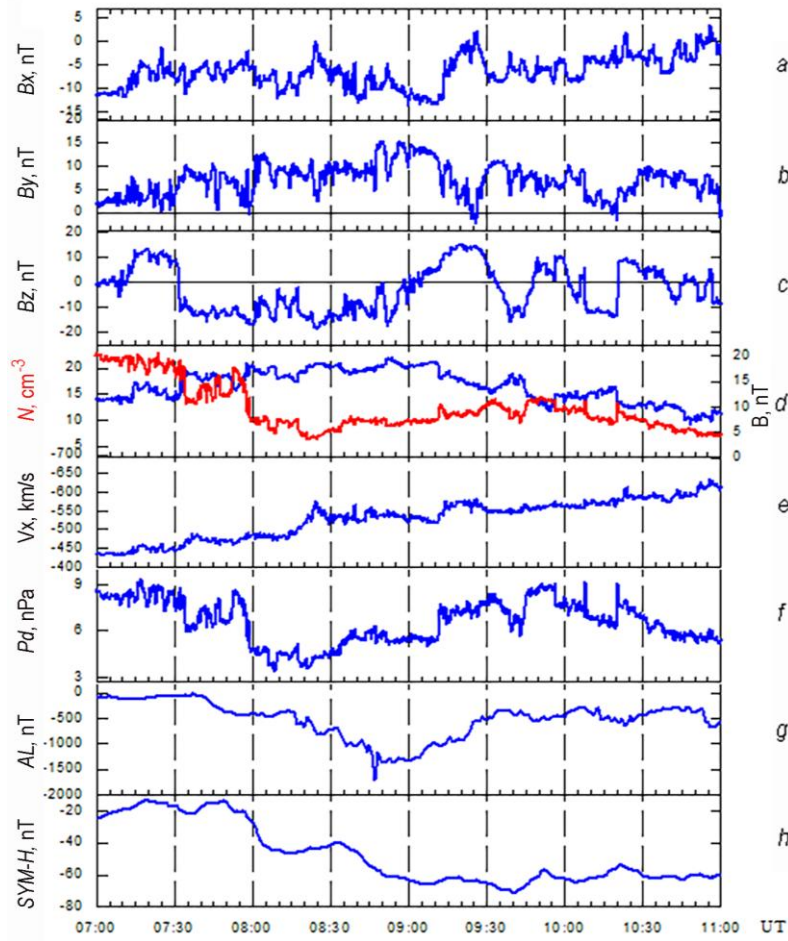The ULF wave velocity V=186.4 km/s (lower than V_{SW}=550 km/s) was found from the phase delay in vari-

A.V. Moiseev, V.I. Popov, V.V. Mishin, Yu.V. Penskikh

Figure 1. Plasma and interplanetary magnetic field parameters in SW: IMF component, its magnitude *B*, ion concentration (*a–d*), ion velocity V_x component, and SW dynamic pressure (*e, f*) according to THEMIS-B data in the September 11, 2015 event at 07:00–11:00 UT, *AL* and *SYMH* (*g, h*) for the period under study

Figure 2. Satellite measurements of the magnetic field (*B* and $B_{x,y,z}$ in SW (THEMIS-B, THEMIS-C) and in the magnetosphere (GEOTAIL and GOES-13)). Data on SW is shifted by 10 min and is given with a weighted factor
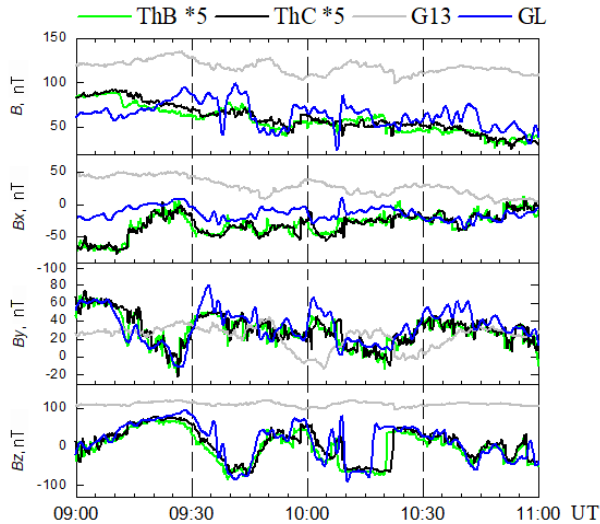

Figure 3. Satellite measurements of the magnetic field (*B* and $B_{x,y,z}$ in SW (THEMIS-B, THEMIS-C)) and in the magnetosphere (GEOTAIL and GOES-13) filtered within 1000–2400 s. Data on SW is shifted by 10 min and is given with a weighted factor

ations of |**B**| between ThC and ThB and from the distance between them. We estimated the DS normal direction whose front was detected at 09:10 UT (see Figu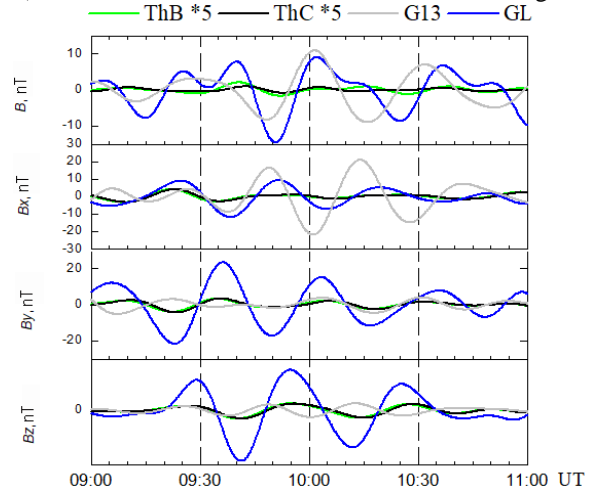re 1). Parameters of the normal were calculated using the mixed data method [Abraham-Shrauner, Yun, 1976] and the complanarity theorem [Colburn, Sonett, 1966]

$$\mathbf{n} = \pm \frac{(\mathbf{B}1 - \mathbf{B}2) \times ((\mathbf{B}1 - \mathbf{B}2) \times (\mathbf{V}1 - \mathbf{V}2))}{|(\mathbf{B}1 - \mathbf{B}2) \times ((\mathbf{B}1 - \mathbf{B}2) \times (\mathbf{V}1 - \mathbf{V}2))|} \quad (1)$$

based on which the DS velocity was determined

$$\mathbf{V}_{DS} = ((\rho 2 \mathbf{V}2 - \rho 1 \mathbf{V}1) \cdot \mathbf{n})/(\rho 2 - \rho 1) \quad (2)$$

where $\mathbf{B}1$, $\mathbf{V}1$, $\rho 1$, $\mathbf{B}2$, $\mathbf{V}2$, $\rho 2$ are magnetic field, velocity, and plasma density ahead of and behind the DS front.

The normal to the DS front is directed toward the Y component ($n = [0.095, 0.912, 0.3953]$ in the GSE coordinate system), the DS front velocity $V_{DS} = 182.8$ km/s matches well the ULF wave propagation velocity in SW, determined above from phase delays between the satellites. The observed propagation velocities can be explained by the fact that ULF waves propagate upward along the incoming stream toward the Sun and are carried away by SW to Earth.

The field variations on GOES-13 (G13), located in the dawn sector, differ in frequency from those observed in the noon sector, and it is impossible to study propagation of pulsations from phase delays on these satellites.

Figure 4 exhibits the magnetic field magnitude B, the filtered magnetic field magnitude B_f, and the field-aligned component B_0 in Mean Field Aligned coordinates on satellites located in the sector from dawn to midnight local time. Measurements are shown from satellites located at 10:00 UT in the following MLT

Table 3

Coordinates of satellites in the magnetosphere on September 11, 2015 at 10:00 UT in the GSE system

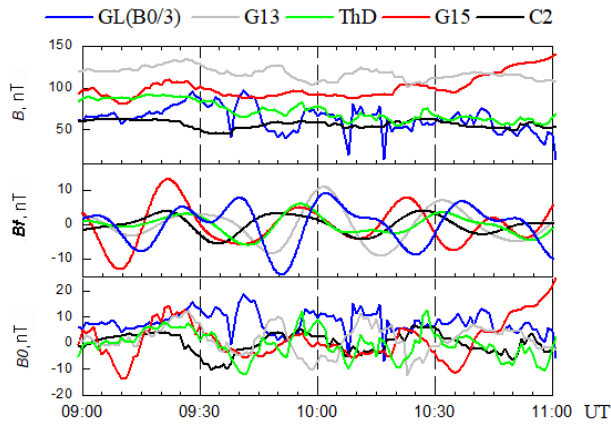| Satellites	GSE coordinates, R_e		
	X	Y	Z
THEMIS-B	61.78	−20.97	−3.26
THEMIS-C	60.27	−24.56	−3.94
GEOTAIL	8.59	3.62	−0.02
GOES-13	−1.64	−5.94	−2.39
THEMIS-D	−4.61	−9.03	−2.09
GOES-15	−6.35	−1.85	−0.19
CLUSTER-4	−8.70	−2.71	−12.05
CLUSTER-2	−10.07	−2.00	−11.39

Figure 4. From top to bottom: the magnetic field magnitude B, the magnetic field magnitude B_f filtered within 1000–2400 s, the field-aligned component B_0 in Mean Field Aligned coordinates in the magnetosphere on GEOTAIL, GOES-13, THEMIS-D, GOES-15, and CLUSTER-2 satellites

sectors: G13 (05 MLT), THEMIS-D (ThD, 04 MLT), GOES-15 (G15, 01 MLT), and CLUSTER-2 (C2, 02:30 MLT). The similarity in the waveform in the field magnitude on different satellites allows us to estimate the propagation velocity from the nightside to the dawnside: the velocity of C2-ThD is ~95 km/s; G15-G13, ~113.7 km/s. The similarity in the pulsation shape in the bottom and middle panels suggests a significant contribution of the SW compression component to geomagnetic pulsations, which is confirmed by B_0 whose maximum amplitude is observed in the noon sector; the minimum, in the midnight sector.

Figure 5 illustrates the dynamics of energetic electron fluxes in the magnetosphere $J_e = 30$–50 keV on G13 and G15, $J_e = 40$ keV on ThD, and $J_e \gg 40$ keV on Cluster-4 (C4, 3 MLT). On satellites other than ThD, rapid increases in fluxes are seen to be replaced by slower decreases. This is due to the fact that particles gradually leave the localized region, where they were injected, through magnetic drift (on ThD, rates of increase and decrease in fluxes coincide). From phase delays in variations in the fluxes (indicated by arrows), we can conclude that J_e propagate from the nightside to the dayside at velocities of 39.3 (C4-ThD) and 23.8 km/s (ThD-G13). They are close to the propagation velocities of substorm injections (24 km/s) estimated in [Reeves et al., 1996].

Figure 6, *a* illustrates filtered variations in the *H* component of magnetometers distributed in azimuth at $\Phi' = 76°$–$79°$; on the right is the LT dependence of the azimuthal propagation velocity (*b*), FAC distributions constructed using MIT for a negative half-wave on magnetograms at 09:50–10:00 UT in panel *c*, for a positive half-wave at 10:05–10:20 UT (*d*); at the bottom are distributions of equivalent ionospheric currents constructed by the SECS method at the same time points (*e*, *f*). The dynamics of vortices was analyzed by this method based on a software code written in MatLab [Vanhamäki, Juusola, 2020], available at [https://link.springer.com/chapter/10.1007/ 978-3-030-26732-2_2#Sec18]. As follows from the phase delays in magnetic pulsations (panel *a*, the maxima from which propagation was analyzed are marked with asterisks),
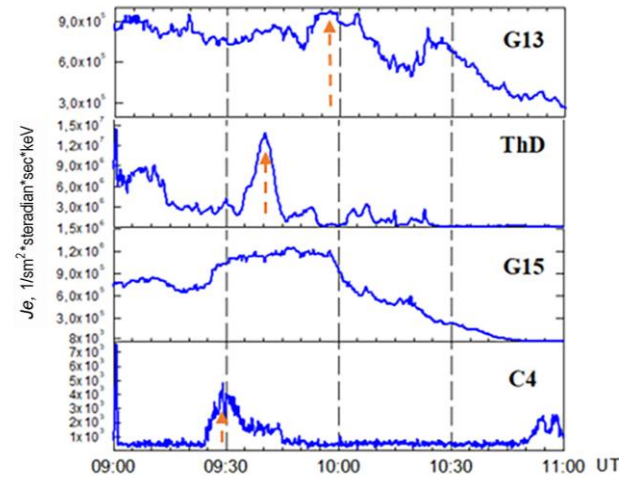

Figure 5. Fluxes of $J_e = 30$–50 keV (GOES-13), 40 keV (THEMIS-D), 30–50 keV (GOES-15), $J_e > 40$ keV (CLUSTER-4)
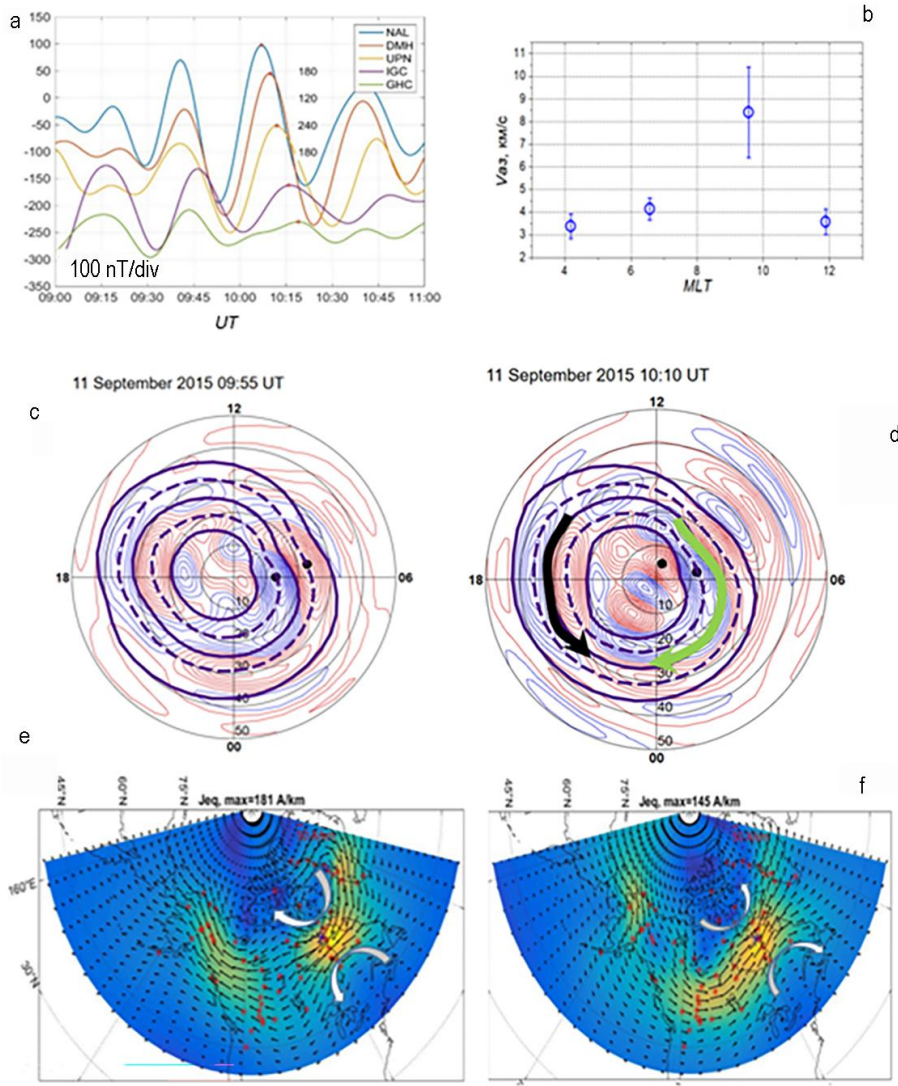
Figure 6. Geomagnetic field *H* component at azimuthally distributed stations at corrected geomagnetic latitudes 76°–79°, which was filtered within 1000–2400 s (*a*); MLT dependence of the azimuthal propagation velocity along Φ′=76°–79° (*b*); distribution of field-aligned currents with MIT (*c*, *d*); distribution of equivalent ionospheric currents with the SECS method (*e*, *f*) for a negative half-wave at 09:50–10:00 UT (*c*, *e*) and for a positive one at 10:05–10:20 UT (*d*, *f*) in geomagnetic Pi3 pulsations (panel *a*)

they propagated from the dayside to the nightside at velocities 3–9 km/s. The MIT FAC distribution maps show the inflowing (blue) and outflowing (red) FACs (panels *c*, *d*). Between sheets of opposite FACs, westward Hall currents are amplified in the dawn sector; and eastward ones, in the dusk sector (green and black arrows respectively in panel *d*). This location of the electrojets corresponds to the DP2 current system. The MIT FAC distribution maps indicate that during a positive half-wave the westward current is more extended in longitude and we can say that in addition to DP2 the DP1 current system is also amplified. SECS in panel *e* exhibits a large Hall vortex located in the dawn sector. The westward Hall current on the MIT maps corresponds to the lower part of this vortex at Φ′=70°–80°. According to the map of FAC distribution in the ionosphere, the latitudinal maximum of the westward electrojet is at the latitudes of maximum ECS (in the south of the large vortex) on the boundary between regions of

inflowing and outflowing FACs (regions 1 and 2). For negative and positive half-waves, this current differs in direction due to the opposite directions of Hall currents inside and outside the vortex (the direction is indicated by white arrows in panels *e*, *f*). Oppositely directed ECSs were also recorded during global Pc5 pulsations [Huang, 2021].

We have analyzed the dynamics of the vortices indicated by white arrows (panel *f*): trajectories of the vortices, meridional and azimuthal propagation velocities are shown in Figure 7. Displacement trajectories of high-latitude (*a*) and low-latitude (*b*) vortices are located along the sea—land boundary line. The vortices propagate along the meridian to the north at velocities 1.6–4 km/s (*c*). Opposite propagation velocities ±25 km/s (*d*) are recorded along the azimuth, from which we can conclude that the vortices do not propagate along the azimuth. Localization of vortices along the sea—land boundary line can be attributed to the so-called coastal effects.
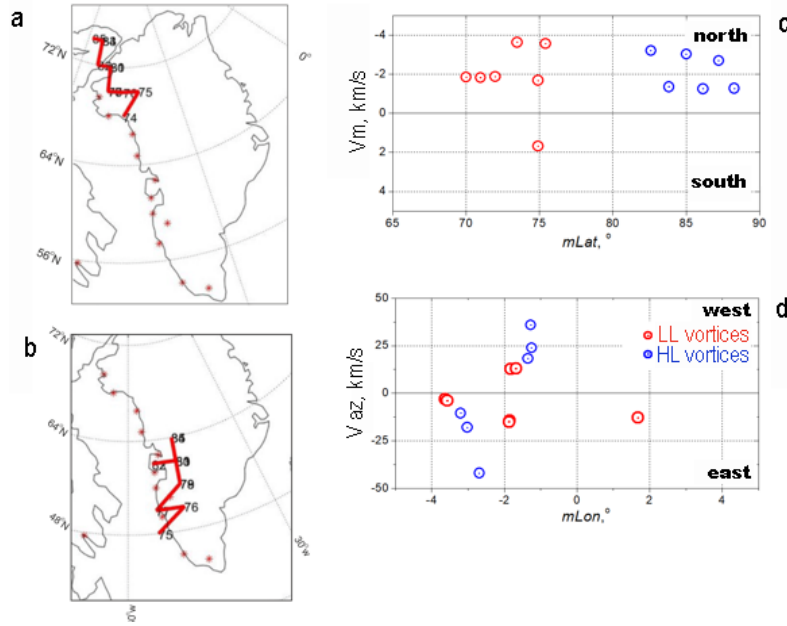
Figure 7. Vortex trajectories at higher (*a*) and lower (*b*) latitudes and velocities of meridional and azimuthal propagation along these trajectories (*c, d*) at 10:10–10:20 UT; LL, HL are low-latitude and high-latitude vortices

To study the frequency spectra of Pi3 pulsations, their dynamics in the meridional direction, as well as to identify latitudes of field line resonances, we have selected four meridional chains of ground magnetic stations whose co-ordinates are given in Table 2. Location of these chains is shown schematically in Figure 8, *c*. Panel *a* presents power spectra of ULF waves in SW, spectra of Pi3 pulsations on Earth at different latitudes, latitude dependence of the meridional velocity of pulsation propagation (*b*), and MLT dependence of westward electrojet and field line resonance latitudes (*d*). It can be seen (*a*) that the oscillation spectra in SW and on Earth have a common peak at a frequency of 0.55 mHz (designated by number 1), it shows up in all IMF components and in the SW velocity. Peaks at frequencies of 0.82 and 0.96 mHz (2.3) on spectrograms from ground stations have an explicit latitude dependence: they are observed with maximum intensity at higher and lower latitudes respectively. These peaks are also present in spectra of the interplanetary medium parameters B, B_z, and N. We determined the latitude of field line resonant oscillations Φ'_{FLR}, using the technique [Glassmeier et al., 1999], from maximum amplitude and phase difference of the oscillations along the meridional chain of stations. Φ'_{FLR} is plotted on distributions of meridional velocities of Pi3 pulsations along these meridians. It is apparent that poleward pulsation propagation along the meridian prevails to which correspond negative velocities 0.5–5 km/s; at Φ'_{FLR}, the velocities are subject to discontinuity. Locations of the westward electrojet and Φ'_{FLR} coincide (panel *d*).

4. DISCUSSION

Thus, we have studied the frequency spectrum and dynamics of global Pi3 pulsations at high latitudes and their equivalent current systems in the magnetosphere and ionosphere in the extended sector of longitudes 0–12 MLT. We have revealed that the pulsation spectrum has three peaks: at all latitudes at a frequency of 0.55 mHz, two peaks at 0.82 and 0.96 mHz at higher and lower latitudes respectively. We have found similar dynamics of small vortices, which are the fine structure of a large vortex, and pulsations in the ionosphere, but only along the meridian, as well as pulsation propagation from the dayside to the nightside in the ionosphere and in the opposite direction in the magnetosphere. The detected features are described below.

4.1. External and intramagnetospheric sources of Pi3 pulsations

In [Parkhomov et al., 1998], as in the event we deal with, two maxima were found in the spectrum of Pc5 pulsations: latitude-independent at 2.3 mHz and latitude-dependent at 4–6 mHz. The authors suggested that oscillations of the first type are associated with oscillations at the magnetopause, whereas oscillations of the second type are caused by intramagnetospheric resonances. The boundary of the FMS waveguide, the oscillations in which caused the first peak, according to their assumption, lies outside the magnetopause. In the event of interest, the latitude-independent peak of oscillations was detected at 0.55 mHz in SW, whereas ULF waves were recorded at 0.4–0.7 mHz. Latitude-dependent peaks at 0.82 and 0.96 mHz on ground-based magnetograms are present in IMF spectra and concentration. This is consistent with the conclusions drawn in [Kepko, Spence, 2003], in which when analyzing a number of geomagnetic pulsation events caused by P_d variations it has been found that discrete frequencies of intramagnetospheric resonances of 0.7, 1.3, 1.9, 2.6, and 3.4 mHz are observed in SW concentration variations and presumably reflect the existence of structures of certain sizes in the interplanetary medium. The oscillation frequencies in the event considered are close to the first harmonic of intramagnetospheric resonances, division by which is fair-
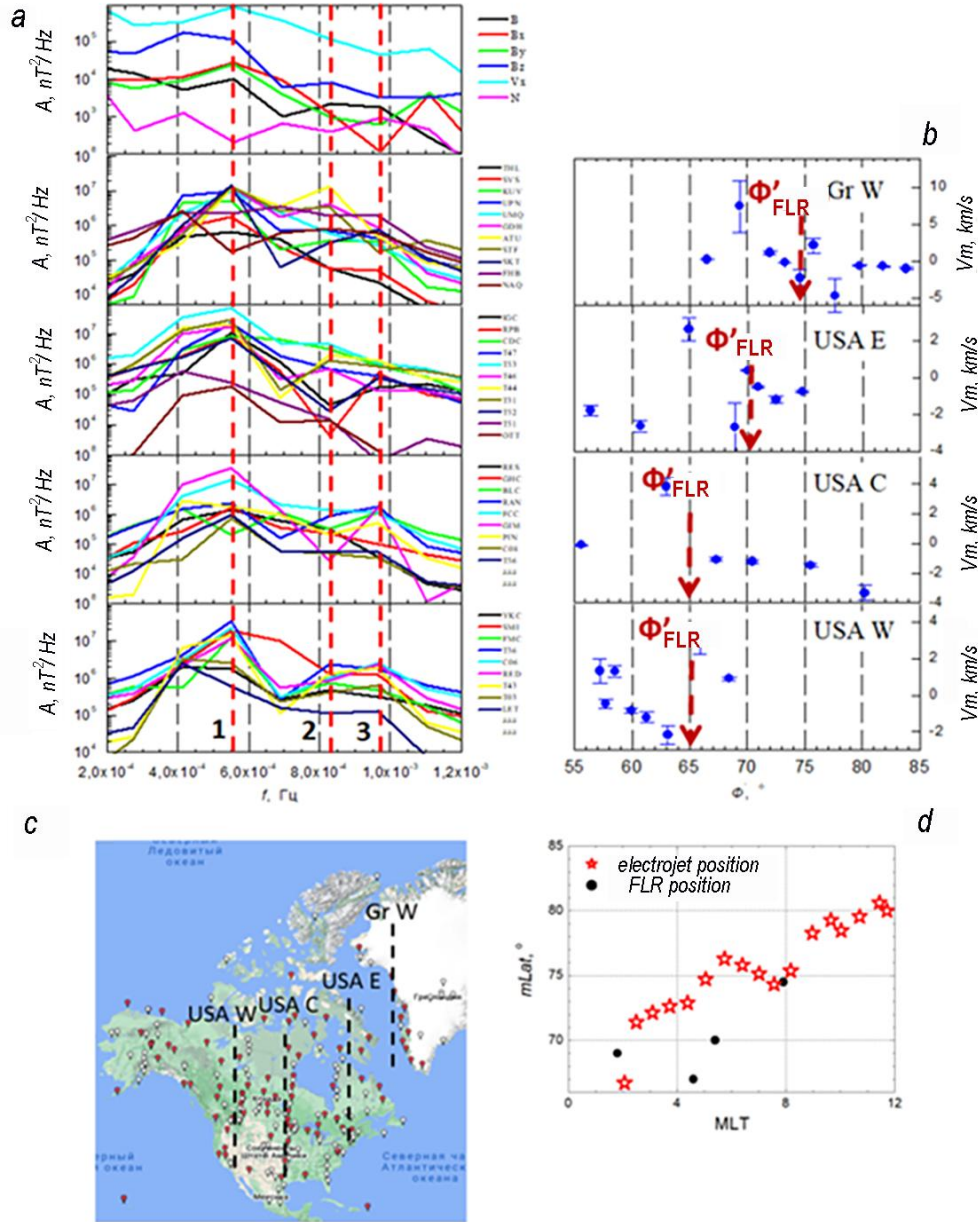
ly conventional.

Figure 8. ULF wave spectra in SW, spectra of Pi3 pulsations on Earth at different latitudes, along different meridians (*a*), pulsation propagation velocities along different meridians (*b*), a map of meridional chains of stations (*c*), MLT dependence of the geomagnetic latitude of the westward electrojet and the latitude of field line resonances (*d*)

During the event of interest, several conditions are implemented which are favorable for penetration of waves from SW and for generation of globally record-ed field variations in the magnetosphere: extreme IMF B_z, variations in P_d (ratio $\Delta P_d/P_d \sim 0.5$), and ~550 km/s SW velocity. Simultaneous variations in N and B are typ-ical of compression MHD waves: fast magnetosonic (FMS) and slow magnetosonic (SMS). For an FMS wave, these parameters change in phase, and for an SMS wave they change in antiphase [Baumjohann and Treumann, 1996], which is observed in our case in the interplanetary medium and in the magnetosphere. The Alfvén SW veloci-ty according to ThB data is ~90 km/s, which coincides by an order with the ULF wave velocity in SW (168 km/s); thus, waves in SW correspond to SMS waves. It should be

added that Alfvén waves do not pass through the tangential discontinuity, which is the magnetopause, and MS waves can partially penetrate through it [Leonovich et al., 2003].

4.2. Dynamics of geomagnetic Pi3 pulsations and equivalent current vortices

Observations show that pulsations at latitudes $\Phi'=76°$–$79°$ propagate along the azimuth from the dayside to the nightside with $V_{az}=3$–9 km/s; along the meridian, poleward with $V_m=0.5$–5 km/s. The large Hall vortex ~3500 km in diameter, observed in the dawn sector, is generally station-ary; however, there may be small vortices in it — the so-called fine structure of the large vortex 1000–1500 km in diameter. Small vortices also propagate poleward with comparable velocities 1.6–4 km/s.

Moiseev et al. [2024a, b] have examined meridional and azimuthal propagation of geomagnetic pulsations and 5–10 min small TCVs responsible for them. Comparison between propagation velocities of pulsations and vortices made in these works and in our work has shown that propagation velocities of pulsations and vortices coincide in the meridional direction, whereas in the azimuthal direction the vortices propagate faster with $V = 5$–25 km/s; in this case, TCVs do not experience a coastal effect and propagate along longitude in a sector up to 12 MLT. Both TCV and Pi3 phenomena are resonant, but if in the case of TCVs the location of their centers coincided with field line resonances (FLRs), in the case of Pi3 the location of FLR coincided with the westward electrojet, which is the lower part of the large vortex.

Huang [2021], when studying global Pc5 pulsations, has established that the pulsations did not propagate in the azimuthal direction; the author attributed the phase variation along the meridian to the evolution of the pulsation current system. The large vortex in the event considered does not propagate either, and to understand the difference in propagation of Pi3 pulsations and small vortices, we have examined azimuthal propagation at the same stations (see Figure 6, *a*) in terms of the *D* and *Z* components. Analysis of the components has revealed that no propagation was observed (not shown). Perhaps this explains the different dynamics of ECS and pulsations since all components are applied to ECS.

Coastal effects in auroras [Samsonov, Zaretsky, 1963; Nadubovich, 1967] and ionospheric currents [Shpynev et al., 1977] were actively studied from observations in the Soviet Arctic (a region in Yakutia with a center in Tixie Bay) during SibIZMIR and ICRA SB AS USSR expeditions in the winter of 1968–1969. These effects are naturally associated with the well-known Senko—Mansurov coastal effect [Senko, 1959; Mansurov, 1959], which implies that induced currents in the sea or land areas with increased conductivity are displaced to the shores or edges of these land areas due to the skin effect. Ionospheric effects involved an increase in the density of ionospheric currents in the coastline area, as well as the formation of regular vortex structures in ionospheric currents. Ionospheric projection of these phenomena was located on land at ~100–200 km from the boundary line. The SECS method allowed us to examine the evolution of small ionospheric vortices over time with 1-min resolution and to conclude that the location of the vortices at a distance of ~200 km from the coastline is consistent with the results obtained from the study of coastal ionospheric effects. Shpynev et al. [1977] state that local irregularities with spatial scales ~100–300 km are manifested in ionospheric coastal effects, which allows us to assume that small vortices 1000–1500 km in diameter (according to the SECS method) actually exist.

4.3. Comparison between satellite and ground-based measurements

Moiseev et al. [2020] have investigated the event of Pi3 pulsations whose sources were IMF B_z variations. In the magnetosphere in the range of Pi3 pulsa-

tions, propagation from the nightside to the dayside was found from phase delays in energetic electron fluxes and on Earth from phase delays in bay-like disturbances in riometric absorption. In this work, satellite and ground-based observations show the opposite propagation direction, and below we explore possible reasons for this.

To compare pulsation propagation observed on Earth and in the magnetosphere, ground stations located along latitudes $\Phi' = 76°$–79° were projected into the equatorial plane of the magnetosphere by the Tsyganenko model Ts04 [Tsyganenko, Sitnov, 2005]. The projection of the ground stations and the location of the satellites in the equatorial plane of the magnetosphere on September 11, 2015 at 10:00 UT are shown in Figure 9. The minimum distance between field line projections corresponding to the ground stations and locations of the satellites are seen to be ~5 R_e. Thus, ground-based and satellite observations can cover different regions of the magnetosphere; therefore, the nature of pulsation propagation differs.

It is also possible that the propagation pattern we have recorded reflects the plasma convection direction: from the dayside to the nightside according to observations at high latitudes and in the opposite direction in the equatorial plane of the magnetosphere. This may be supported by the fact that the pulsation period of ~30 min makes it possible to classify them as Ps6 pulsations that are accompanied by auroras having a shape corresponding to the letter Ω [Akasofu, Kimball, 1964]. In the region of these auroras, convection is sunward in the equatorial plane and antisunward at high latitudes. Unfortunately, the lack of ground-based and satellite observations of auroras during this event does not allow us to draw definitive conclusions.

Using ThD observations, we have estimated the electric drift velocity (convection velocity) at 75 km/s, comparable to propagation velocities estimated from phase delays in both the magnetic field and energetic electron fluxes.

Using the Ts04 model, distances in the XY plane were estimated between projections of stations in the equatorial plane of the magnetosphere; and propagation velocities
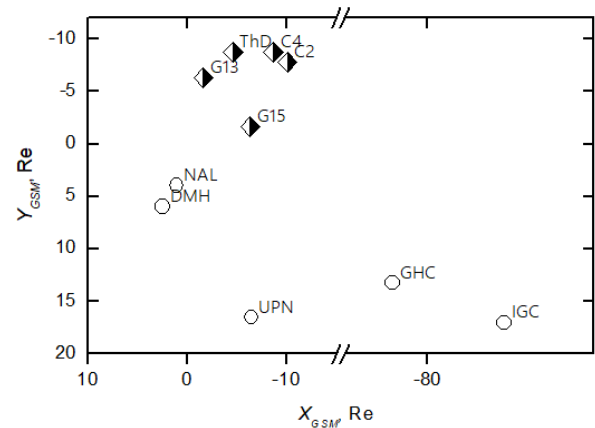

Figure 9. Projection of ground stations located along corrected geomagnetic latitudes 76°–79° (circles) and location of satellites (rhombs) in the equatorial plane of the magnetosphere on September 11, 2015 at 10:00 UT

$V_{\text{NAL\_DMH}}$=86, $V_{\text{DMH\_UPN}}$=734.2, $V_{\text{UPN\_IGC}}$=2074.7, $V_{\text{IGC\_GHC}}$=272.9 km/s, from ground-based time delays; the indices indicate the stations between which the velocities were measured. The minimum value of these velocities is in the order of the convection velocity, and the maximum value is close to the Alfvén velocity of 2225 km/s according to ThD data.

CONCLUSION

From the analysis we can draw the following conclusions. Propagation of Pi3 pulsations and small vortices coincides in magnitude and direction along the meridian. In the azimuthal direction, the vortices show the presence of a coastal effect. Propagation as observed on satellites and on Earth has the same direction as plasma convection: from the dayside to the nightside according to observations at high latitudes and in the opposite direction in the equatorial plane of the magnetosphere. ULF waves penetrating from SW and magnetospheric resonances also contribute to the frequency spectrum of pulsations.

Thus, we can conclude that pulsations in this event were caused by both external (oscillations in SW) and internal sources (the magnetospheric resonator that might have been excited by a substorm). The dynamics of the fine structure of a large vortex (small vortices) in the magnetosphere generally coincides in propagation velocity and direction with geomagnetic pulsations.

REFERENCES

Abraham-Shrauner B., Yun S.H. Interplanetary shocks seen by AMES plasma probe on Pioneer 6 and 7. *J. Geophys. Res.* 1976, vol. 81, pp. 2097–2102.

Akasofu S.I., Kimball D.S. The dynamics of the aurora: I. Instabilities of the aurora. *J. Atmos Terr. Phys.* 1964, vol. 26, pp. 205–211.

Alimaganbetov M., Streltsov A.V. ULF waves observed during substorms in the solar wind and on the ground. *J. Atmos. Solar-Terr. Phys.* 2018, vol. 181, pp. 10–18.

Baumjohann W., Treumann R.A. *Basic Space Plasma Physics.* Imperial College Press, London, 1996.

Bazarzhapov A.D., Matveev M.I., Mishin V.M. Geomagnetic variations and storms. Novosibirsk: Nauka, 1979, 248 p. (In Russian).

Colburn D.S., Sonett C.P. Discontinuities in the solar wind. *Space Sci. Rev.* 1966, vol. 5, pp. 439–506. DOI: 10.1007/BF0024 0575.

Eselevich M.V., Eselevich V.G. Fractal structure of the heliospheric plasma sheet in the Earth's orbit. *Geomagnetism and Aeronomy.* 2005, vol. 45, no. 3, pp. 326–336.

Gjerloev J.W. The SuperMAG data processing technique. *J. Geophys. Res.* 2012, vol. 117, no. A09213. DOI: 10.1029/ 2012JA017683.

Glassmeier K.-H., Othmer C., Gramm R., Stellmacher M., Engebretson M. Magnetospheric field-line resonances: A comparative planetology approach. *Earth Environment Sci.* 1999, vol. 20, pp. 61–109.

Hada T., Kennel C.F. Nonlinear evolution of slow waves in the solar wind. *J. Geophys. Res.* 1985, vol. 90, p. 531.

Han D.-S., Yang H.-G., Chen Z.-T., et al. Coupling of perturbations in the solar wind density to global Pi3 pulsations: A case study. *J. Geophys. Res.* 2007, vol. 112, A05217. DOI: 10.1029/2006JA011675.

Huang C.-S. Global Pc5 pulsations from the polar cap to the equator: Wave characteristics, phase variations, disturbance current system, and signal transmission. *J. Geophys. Res.* 2021, vol. 126, e2020JA029093. DOI: 10.1029/2020JA029093.

Kepko L., Spence H.E. Observations of discrete, global magnetospheric oscillations directly driven by solar wind density variations. *J. Geophys. Res.* 2003, vol. 108, p. 1257. DOI: 10.1029/2002JA009676.

Leonovich A.S., Mishin V.V., Cao J.B. Penetration of magnetosonic waves into the magnetosphere: Influence of a transition layer. *Ann. Geophys.* 2003, vol. 21, pp. 1083–1093.

Lunyushkin S.B., Penskikh Y.V. Diagnostics of auroral oval boundaries on the basis of the magnetogram inversion technique. *Sol.-Terr. Phys.* 2019, vol. 5, no. 2, pp. 97–113. DOI: 10.12737/stp-52201913.

Mansurov S.M. *Magnetic disturbances.* Moscow: Publ. House of the USSR Academy of Sciences, 1959, no. 1, pp. 64–71. (In Russian).

Mishin V.M. The magnetogram inversion technique and some applications. *Space Sci. Rev.* 1990, vol. 53, no. 1-2, pp. 83–163. DOI: 10.1007/bf00217429.

Moiseev A.V., Starodubtsev S.A., Mishin V.V. Features of excitation and azimuthal and meridional propagation of long-period Pi3 oscillations of the geomagnetic field on December 8, 2017. *Sol.-Terr. Phys.* 2020, vol. 6, no. 3, pp. 56–72. DOI: 10.12737/stp-63202007.

Moiseev A.V., Popov V.I., Starodubtsev S.A. Comparative analysis of the propagation of magnetic variations and equivalent current vortices of geomagnetic Pc5 pulsations along the meridian and azimuth. *Geomagnetism and Aeronomy.* 2024a, vol. 64, no. 4, pp. 548–566. DOI: 10.31857/ S0016794024040093.

Moiseev A.V., Popov V.I., Starodubtsev S.A. Investigating azimuthal propagation of Pc5 geomagnetic pulsations and their equivalent current vortices from ground-based and satellite data. *Sol.-Terr. Phys.* 2024b, vol. 10, no. 3, pp. 104–115. DOI: 10.12737/stp-103202412.

Nadubovich Yu.A. Collection of articles. Results of research on international geophysical projects. Polar aurora. Moscow: Nauka, 1967, no. 14, p. 77.

Parkhomov V.A., Mishin V.V., Borovik L.V. Long-period geomagnetic pulsations caused by the solar wind negative pressure impulse on March 22, 1979 (CDAW-6). *Ann. Geophys.* 1998, vol. 16, pp. 134–139.

Parhomov V.A., Borodkova N.L., Eselevich V.G., Eselevich M.V., Dmitriev A.V., Chilikin V.E. Features of the impact of the solar wind diamagnetic structure on Earth's magnetosphere. *Sol.-Terr. Phys.* 2017, vol. 3, no. 4, pp. 47–62. DOI: 10.12737/stp-34201705.

Penskikh Yu.V. Applying the method of maximum contributions to the magnetogram inversion technique. *Sol.-Terr. Phys.* 2020, vol. 6, no. 4, pp. 67–76. DOI: 10.12737/stp-64202009.

Penskikh Yu.V., Lunushkin S.B., Kapustin V.E. Geomagnetic method for automatic diagnostics of auroral oval boundaries in two hemispheres of Earth. *Sol.-Terr. Phys.* 2021, vol. 7, no. 2, pp. 57–69. DOI: 10.12737/stp-72202106.

Reeves G.D., Henderson M.G., McLachlan P.S., Belian R.D., Friedel R.H.W., Korth A. Radial propagation of substorm injections. *Proc. the Third International Conference on Substorms*. Eur. Space Agency Spec. Publ. 1996, ESA SP-389. p. 579.

Saito T. Geomagnetic pulsations. *Space Sci. Rev*. 1969, vol. 10, iss. 3, pp. 319–412.

Saito T. Long-period irregular magnetic pulsation Pi3. *Space Sci. Rev.* 1978, vol. 21, pp. 427–467. DOI: 10.1007/BF00173068.

Saito T., Matsushita S. Geomagnetic pulsations associated with sudden commencements and sudden impulses. *Planetary Space Sci*. 1967, vol. 15, pp. 573–587.

Samsonov V.P., Zaretsky N.S. Azimuthal and geographical distribution of auroral rays. *Geomagnetism and Aeronomy*. 1963, vol. 3, no. 2, p. 246.

Senko P.K. *Coastal effect in magnetic variations*. M.: 1959, 61 p.

Shpynev G.B., Mishin V.M., Mishin E.V. Research on geomagnetism, aeronomy and physics of the Sun. M.: Nauka, 1977, vol. 43, pp. 3–13.

Tsyganenko N.A., Sitnov M.I. Modeling the dynamics of the inner magnetosphere during strong geomagnetic storms. *J. Geophys. Res*. 2005, vol. 110, A03208. DOI: 10.1029/ 2004JA010798.

Vanhamäki H., Juusola L. Introduction to spherical elementary current systems. *Ionospheric Multi-Spacecraft Analysis Tools*. 2020, vol. 17, pp. 5–33. DOI: 10.1007/978-3-030-26732-2_13.

URL: https://supermag.jhuapl.edu/mag/ (accessed March 7, 2024).

URL: http://cdaweb.gsfc.nasa.gov/ (accessed March 7, 2024).

URL: https://link.springer.com/chapter/10.1007/978-3-030-26732-2_2#Sec18 (accessed March 7, 2024).

How to cite this article
Moiseev A.V., Popov V.I., Mishin V.V., Penskikh Yu.V. Features of propagation of compressional long-period oscillations penetrating from the interplanetary medium in the magnetosphere — ionosphere system. *Sol.-Terr.Phys*. 2025, vol. 11, iss. 3, pp. 59–69. DOI: 10.12737/stp-113202508.

PREDICTION OF ELECTRON FLUXES IN A CIRCULAR POLAR ORBIT: SELECTION OF PREDICTORS

A.O. Belova
Lomonosov Moscow State University,
Moscow, Russia, belova.ao20@physics.msu.ru

I.N. Myagkova
Lomonosov Moscow State University,
Skobeltsyn Institute of Nuclear Physics,
Moscow, Russia, irina@srd.sinp.msu.ru

Abstract. We have investigated the relationship of variations in >0.7 and >2 MeV electron fluxes of Earth's outer radiation belt in a circular polar orbit with solar wind and interplanetary magnetic field parameters, as well as with geomagnetic indices and the logarithmic electron flux in the geostationary orbit in order to explore the possibility of predicting them. We have selected the optimal input features for predicting electron fluxes in low polar orbits, which is important for ensuring the radiation safety of future space missions.

We have examined integral and maximum electron fluxes of these energies over the span of a day. We have obtained forecasts with a horizon of 1 and 2 days for an interval of 2 months in 2020 for daily maximum and integral fluxes based on linear regression.

Keywords: Earth's radiation belts, relativistic electron fluxes, forecasting, machine learning, circular polar orbit.

INTRODUCTION

Radiation conditions in near-Earth space are largely determined by charged particle fluxes in Earth's radiation belts (ERB). The contribution of ERB particles is especially significant during solar minimum when there are practically no solar cosmic ray fluxes. While particle fluxes of inner ERB are relatively stable and there are generally accepted models that can be used to reliably predict particle fluxes in it, Earth's outer radiation belt (EORB) is very unstable: its electron fluxes can vary by several orders of magnitude within 24 hours. EORB electrons were first detected a long time ago — during the second space flight in the history of mankind, using scientific equipment of SINP MSU [Vernov et al., 1958]. Since then, a large number of experiments on recording EORB electrons by Russian and foreign spacecraft (SC) have been carried out [Williams et al., 1968; Li et al., 2001; Kataoka, Miyoshi, 2008; Kuznetsov et al., 2007; Li, Hudson, 2019; Osedlo et al., 2022; Stepanova et al., 2024]. Nonetheless, the problem of reliably predicting the state of EORB through modeling has not yet been solved. This is due to the fact that to date there is no generally accepted theory of acceleration and scattering of EORB electrons which could explain the available set of experimental data.

Monitoring and prediction of EORB electrons is also of practical interest since the influence of high fluxes of relativistic and sub-relativistic EORB electrons can negatively affect the electronic equipment installed on board SC because Single Event Upsets (SEU), both reversible and irreversible, can occur when the electrons penetrate into integrated circuits [Cole, 2003; Belov et al., 2004; Romanova et al., 2005; Iucci et al., 2005; Pilipenko et al., 2006; Kudela, 2013] (in English literature, they are also called killer electrons), SC can be electrified as well [Novikov, Voronina, 2021].

On the one hand, it is impossible to predict with sufficient accuracy variations in EORB electron fluxes through theoretical calculations; on the other hand, there is a practical need to predict them to ensure radiation safety with modern machine learning methods that help identify the relationships between analyzed variables by approximating empirical dependences.

Satellite measurements made in Earth's inner magnetosphere are employed not only to describe the EORB dynamics, but also to develop forecasting models based on machine learning. Data from GOES satellites having a long time series of experimental measurements is most often applied for these purposes because GOES SC have been launched since the 1970s (see, e.g., [Wei et al., 2018; Myagkova et al., 2019; Sun et al., 2021; Landis et al., 2022; Son et al., 2022]). Currently, one of the most widely used methods for predicting the total relativistic electron flux over the span of a day (fluence) in EORB is the forecast presented on the portal of the Space Weather Prediction Center [http://www.swpc.noaa.gov/]. This model, known as REFM (Relativistic Electron Forecast Model), was developed based on research evidence [Baker et al., 1990]. The forecast uses the fact that daily fluences of >2 MeV electrons, measured in geostationary orbit, can be predicted a day ahead with the aid of a linear filter, which utilizes the SW velocity or the geomagnetic indices K_p and AE as input data. Studies have shown the presence of characteristic temporal dynamics in the behavior of electron fluxes in geostationary orbit. A significant increase in the electron flux is observed two days after the SW velocity reaches its maximum and three days after recording peak values of the geomagnetic indices. This time delay is due to the structural features of SW streams, including the region of the increased interplanetary magnetic

field (IMF) preceding the SW velocity peak. The IMF peak initiates geomagnetic activity leading to an increase in K_p. Thus, there is a significant delay between the geomagnetic indices (K_p, AE) and an increase in the electron flux as compared to direct measurements of SW parameters. It is worth mentioning the model for predicting >2 MeV relativistic electron fluxes in geostationary orbit, which is based on solving a system of continuity equations, provided that particle acceleration is affected not only by the SW velocity, but also by geomagnetic activity, and losses are influenced by the SW density. Taking into account additional factors having an effect on electron acceleration and losses in ERB made it possible to improve the accuracy and stability of forecasts [Lyatsky, Khazanov, 2008]. For low energies (1 eV – 40 keV), there is also a forecasting model with a 1-hr horizon based on IMF and SW velocity [Denton et al., 2016]. In addition to solving the continuity equations, there are other methods for predicting electron fluxes. For example, Potapov et al. [2016] employed the multiple regression method with a sliding window to predict the >1÷2 MeV relativistic electron flux. Particularly noteworthy is the NARMAX model (nonlinear autoregression with running mean with external input signals) [Balikhin et al., 2011]. One of the stages of the algorithm involves analyzing the Error Reduction Ratio *ERR*, which makes it possible to rank the parameters affecting fluxes in ERB. It was this analysis that led the authors to the conclusion that the SW density, rather than its velocity, has the greatest effect on electron fluxes in ERB. Given a fixed density, the fluxes increase as the velocity reaches a certain saturation level decreasing with increasing SW density. There is also an approach to predicting charged particle fluxes in ERB by the BAS Global Dynamic Radiation Belt Model [Glauert et al., 2014], based on solving the 3D Fokker-Planck equation. The developed model relies on a comprehensive approach to describing the dynamics of charged particles and includes the following physical processes: radial diffusion of particles in Earth's magnetosphere, particle—wave interaction, and collisional processes responsible for particle losses from radiation belts.

A separate problem is to predict fluxes of relativistic and sub-relativistic electrons detected in circular polar orbits, where the satellite crosses EORB four times during one orbital period — twice in the Southern Hemisphere and twice in the Northern Hemisphere. For circular polar orbits, we can solve the problem of predicting the daily maximum electron flux and/or the total flux (fluence), which is accumulated over the span of a day at all satellite crossings of EORB.

This study focuses on EORB and variations in electron fluxes in the circular polar orbit similar to the orbit considered in [Botek et al., 2023]. The authors have predicted electron fluxes with energies 500–600 keV and 1–2.4 MeV for the circular polar orbit, using data from PROBA-V SC and the long short-term memory (LSTM) model, for which data on the satellite's position and the geomagnetic index *SYM* was taken as input parameters. An array of measurements for 2015–2018 was used as initial da-

ta. For EORB, the Root Mean Square Error (RMSE) was 0.153 for 500–600 keV with a horizon of 1 day.

The relevance of this study stems from the fact that a similar low polar orbit is planned to be employed in the Russian Orbital Station (ROS) project. In this regard, the development of methods for predicting radiation conditions at such orbits is of considerable practical interest for ensuring the safety of SC and crews.

The purpose of this study is to develop methods for predicting variations in >0.7 and >2 MeV EORB relativistic and sub-relativistic electron fluxes in the circular polar orbit, utilizing SW, IMF parameters, geomagnetic indices, and electron flux in geostationary orbit as input features, as well as to assess the effectiveness of such forecasting.

1. FORECASTING METHOD

Spacecraft data processing, machine learning model training, and forecasting have been carried out with a program developed using Python.

In this paper, we address the problem of predicting time series, where the target variable is y_{t+h}, with h being the forecast horizon (the number of days for which the forecast is made), and features are formed based on the lags (delays) of the series:

$$X_t = \left\{ y_{t-1}, y_{t-2}, ..., y_{t-p}, F_{t-1}, F_{t-2}, ..., F_{t-p} \right\},$$

where F_t is a time series of additional features, such as SW parameters, etc., and p is the number of lags. The prediction formula in the general form is

$$y_{t+h} = f(X_t),$$

where f is a prediction function.

We have employed a machine learning model (linear regression) to predict electron fluxes in the circular polar orbit. Linear regression is a regression model used in statistics for the dependence of one (explicable) variable $\vec{y}$ on another or several other variables $\vec{X}$ with a linear dependence function.

$$y_i = a_1 X_{1i} + a_2 X_{2i} + ... + a_m X_{mi} + a_0,$$

where i is the observation number; $a_0, a_1, ..., a_m$ are the parameters to be estimated (for more detail, see [Demidenko, 1981]).

In order to compare the quality of forecasts, made using linear regression in the future, we produced a forecast with a naive model. The naive forecasting model is a model whose value at a forecast point is equal to the last known value of the predicted variable.

2. INPUT DATA

We have selected the following features as input data for forecasting.

1. SW parameters at the Lagrange point L1 between Earth and the Sun: SW velocity and density obtained by SWEPAM (Solar Wind Electron Proton Alpha Monitor) during the experiment on ACE SC.

2. IMF parameters: the field vector magnitude B_t and B_z obtained by the ACE MAG magnetometer.

3. Geomagnetic indices: *Dst* and K_p from the World Data Center for Geomagnetism (Kyoto).

4. Logarithm of maximum and integral electron fluxes over the span of a day in EORB (>0.8, >2 MeV) from GOES measurement data.

We have used three-hour K_p, hourly *Dst*, and other features averaged over 1 min. The maximum flux was defined as the largest 1-min average for each parameter for each specific day.

The data was acquired from open sources, namely from the SINP MSU Space Weather Data Analysis Center [https://swx.sinp.msu.ru/].

Data from the first three stations was converted to daily values by calculating the mean and the maximum magnitude per day. After such conversions, the number of features doubled. Later, we analyzed the significance of each of these features, and left only one of two similar variants for each of them.

The choice of the first three stations is based on the experience of forecasting the daily average flux in geostationary orbit in [Koons, Gorney, 1991; Ling et al., 2010], as well as in recent works by the SINP MSU research team [Myagkova et al., 2021; Kalegaev et al., 2019, 2023].

Time series forecasting models are usually trained on the τ previous values of the series. τ is called the window width. We have adopted a window width of a multidimensional time series equal to 26 days. Lags equal to 1 (only for the forecast for 1 day in advance), 2, 3, 4, 5, 6, 7, 13, and 26 days were taken from this window. The lags corresponding to one week are applied to the model to effectively use the current available information about the features; the lags equal to 13 and 26 days are linked to the 25–27 day solar rotation period. As shown below, the recurrent fluxes associated with solar rotation can have a significant effect on IMF and SW parameters, thereby considerably altering charged particle fluxes in radiation belts.

Our work relies on a 9-month data array from June 1, 2019 to March 1, 2020, which was divided into training and test datasets as 7:2. The data from June 01, 2019 to December 31, 2019 inclusive was used for the training dataset. The data from January 01, 2020 to March 01, 2020 was utilized as the test dataset — independent data employed to assess the forecast quality.

In the study, we selected a limited time interval corresponding to the period of minimum geomagnetic activity. This approach provided the most stable conditions for conducting a comparative analysis whose main purpose was to compare the temporal dynamics of daily integral and maximum electron fluxes in EORB at low altitudes with the similar dynamics of electron fluxes recorded in geostationary orbit.

This study was carried out taking into account the fact that forecasting models of electron fluxes in geostationary orbit based on machine learning methods have been developed and successfully operate.

The training was done on the basis of data on EORB electron fluxes, measured by Meteor-M2 (launched on July 08, 2014). The forecast was made for daily maximum and integral electron fluxes in EORB (>0.7, >2 MeV). The Meteor-M2 orbit is circular and sun-synchronous, with an altitude at the ascending node h=832 km, an inclination i≈98.85°, and an orbital period T=101.3 min. Thus, during one orbital period the satellite crossed EORB four times (Figure 1).

From the data collected during each orbital period, we identified intervals where the McIlwain parameter *L* varied from 3 to 6. Integral fluxes were calculated for these intervals, using the trapezoid formula; the daily integral flux was obtained by summing integral fluxes for each such interval. The daily maximum flux was computed as the largest flux recorded on these intervals.

Note that instead of the fluxes we employed their decimal logarithms for both the target variable and the features, namely electron fluxes in geostationary orbit. This is due to the fact that the fluxes have a wide dynamic range occupying several orders of magnitude.
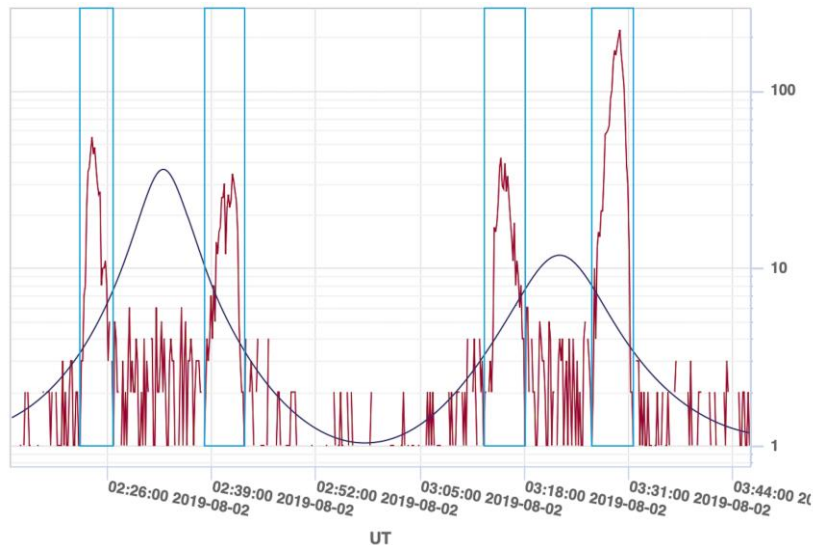

Figure 1. Electron fluxes in a circular polar orbit according to Meteor-M2 data (>0.7 MeV) and the McIlwain parameter *L*

3.   INPUT DATA ANALYSIS

During the study, we have analyzed daily integral (Figures 2, 3) and maximum (Figures 4, 5) electron fluxes from Meteor-M2 and GOES data for >2 and >0.7 MeV (>0.8 MeV for GOES since there is no channel with the required energy threshold in the device). It has been found that there is a noticeable correlation between these fluxes, the moment of increase on both satellites coincides, whereas the decrease in the polar orbit is slower and smoother compared to the geostationary one.

In addition, we have analyzed daily average Dst, K_p, SW density and velocity, and IMF vector modulus (Figures 6–8). During the period considered, average Dst did not fall below –40 nT, which indicates the absence of strong geomagnetic storms during this period. However, the SW velocity periodically increased to 600–700 km/s with a period of ~26 days, which suggests the arrival of high-speed recurrent SW streams causing significant changes in near-Earth space and an increase in charged particle fluxes in radiation belts.

4.   SELECTION OF INPUT FEATURES

The number of features obtained for the specified lookback window size is 126. This number may lead to overfitting of linear regression on the time interval in use, so it is necessary to reduce the number of features. It is believed that the number of parameters in the machine learning model should be at least an order of magnitude smaller than the learning sample size [Alwosheel et al., 2018]. The corresponding calculation for our case (seven months, daily forecast) gives an estimate 10–20 for the maximum number of features.

The selection is based on the correlation coefficient of the feature considered with the target variable. The features with maximum (absolute) correlation are used for further forecasting.

The correlation coefficients for the integral electron flux with energies >2 and >0.7 MeV are shown in Figures 9 and 10 respectively. The maximum correlation of the >2 MeV integral electron flux is expected to be observed with the GOES integral flux, exceeding all others more than three times. This suggests that it is this flux which will make the main contribution to the forecast. The next most important are also expected to be the SW velocity, K_p, and Dst, which is consistent with existing concepts.
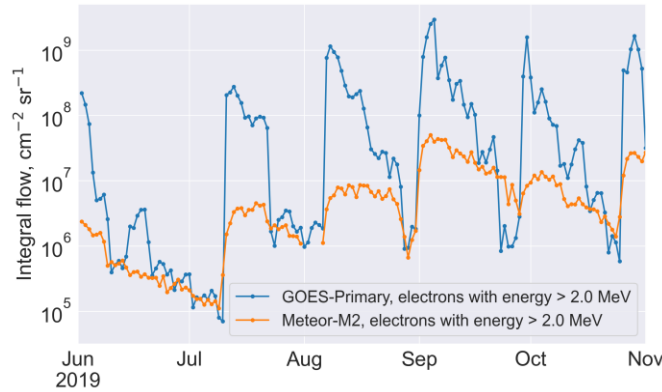

Figure 2. Total integral electron fluxes >2.0 MeV over the span of a day according to Meteor-M2 and GOES-Primary data
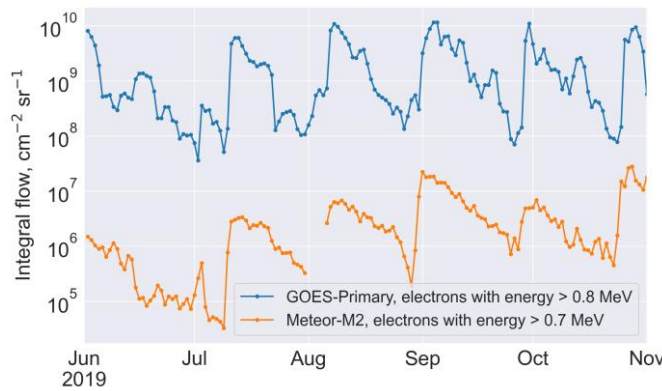

Figure 3. Total integral electron fluxes >0.7 and >0.8 MeV over the span of a day according to data from Meteor-M2 and GOES-Primary respectively
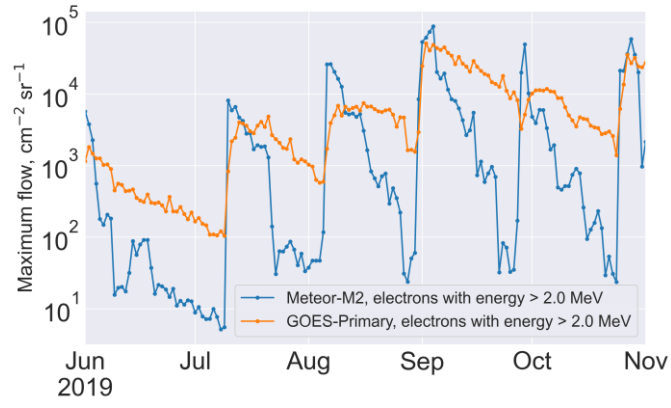
Figure 4. Daily maximum electron fluxes >2.0 MeV according to Meteor-M2 and GOES-Primary data
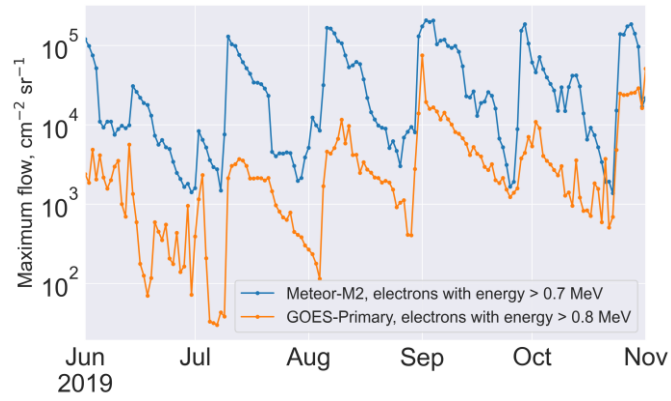

Figure 5. Daily maximum electron fluxes >0.7 and >0.8 MeV according to data from Meteor-M2 and GOES-Primary respectively
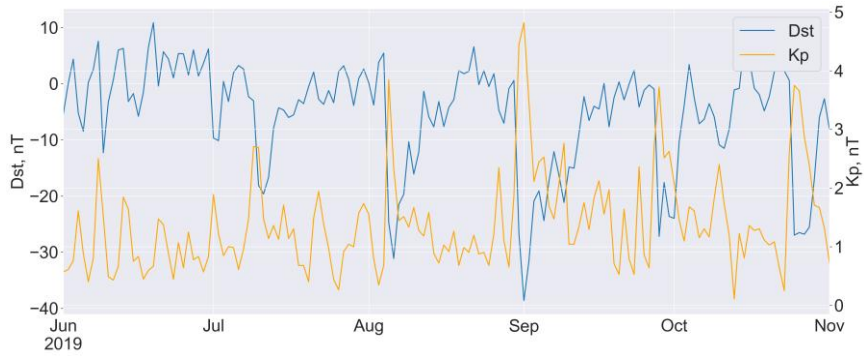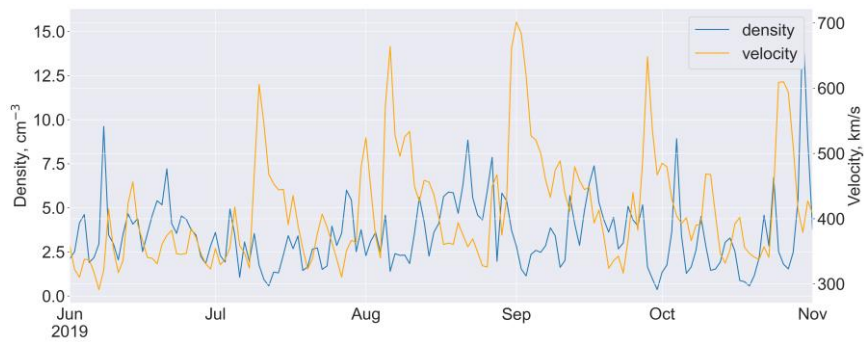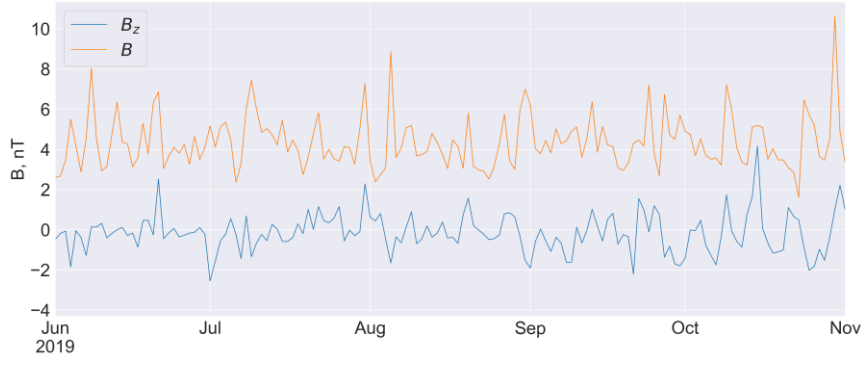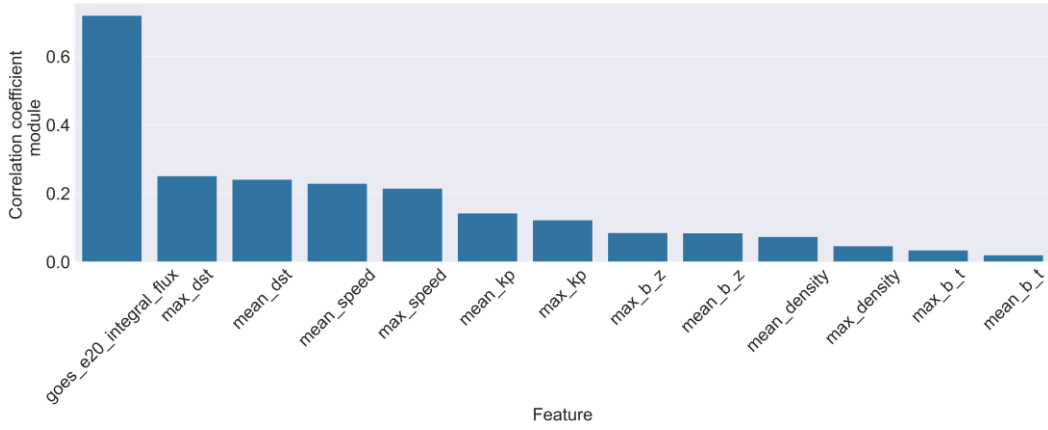

Figure 6. Daily average *Dst* and K_p
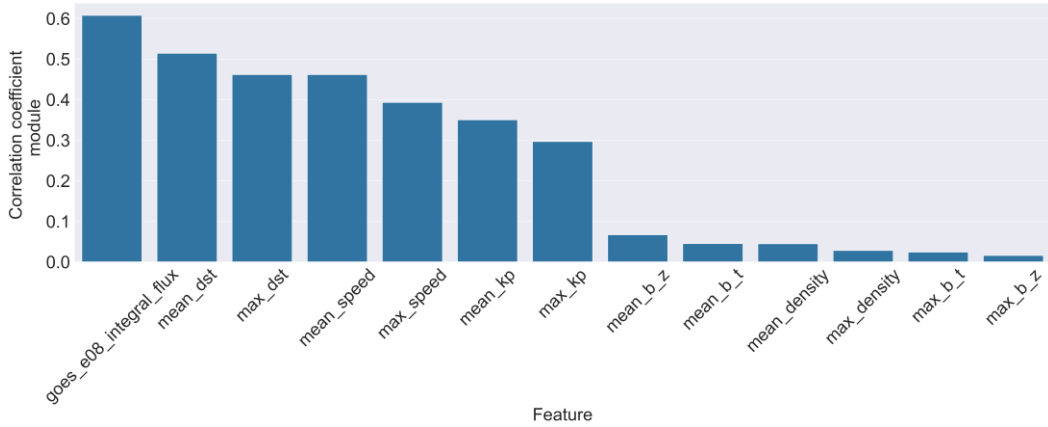

Figure 7. Daily average SW velocity and density

Figure 8. Daily average B_z and B_t

Figure 9. Modulus of the correlation coefficient of >2 MeV daily integral electron flux

Figure 10. Modulus of the correlation coefficient of >0.7 MeV daily integral electron flux

For an energy of 0.7 MeV, the maximum correlation coefficient also belongs to the GOES integral flux, yet in this case it slightly exceeds the other coefficients, which indicates a higher variability in sub-relativistic electron fluxes compared to relativistic ones.

Note that the daily averages show a higher (absolute) correlation than the maximum values, which confirms the need to use them for forecasting.

5.   FORECAST RESULTS

Daily forecasts for integral and maximum electron fluxes, made using linear regression and the naive model, are shown in Figures 11–18 (k is the number of features employed to make this forecast).

The results of prediction of >2 MeV electron fluxes appeared to be much better, which is probably due to their higher quasi-stationarity. Maximum fluxes are predicted less accurately than integral ones since they have a large spread of values over the span of several days.

To assess the quantitative measure of the forecast quality, we calculated the multiple determination coefficient R^2 and the root mean square error. The calculation was made with the test dataset, i.e. the data that was not used for training the model.

To analyze the quality of the model for solving this problem, we made a forecast with the aid of the naive model and calculated its characteristics. The values are presented in Table. The best indicators for each of the

forecast horizons and for a given energy are highlighted in blue. It can be seen that in all cases the naive forecast shows worse results than that made with linear regression. It has also been found that for *E*>0.7 MeV the forecast of integral fluxes is better; and for *E*>2 MeV, the forecast of maximum fluxes. With an increase in the forecast horizon, a significant deterioration in the quality of forecasts for both energy ranges is expected.

Metrics of machine learning models
used in the problem of forecasting >0.7 and >2 MeV electron fluxes

	Forecast for 1 day		Forecast for 2 days	
Forecast of >0.7 MeV daily integral electron fluxes				
Model\Metrics	R^2	RMSE	R^2	RMSE
Naive forecast	0.663	0.325	0.382	0.439
Linear regression	0.696	0.308	0.550	0.375
Forecast of >0.7 MeV daily maximum electron fluxes				
Model\Metrics	R^2	RMSE	R^2	RMSE
Naive forecast	0.372	0.471	–0.046	0.608
Linear regression	0.558	0.395	0.316	0.492
Forecast of >2 MeV daily integral electron fluxes				
Model\Metrics	R^2	RMSE	R^2	RMSE
Naive forecast	0.819	0.156	0.603	0.232
Linear regression	0.825	0.154	0.708	0.199
Forecast of >2 MeV daily maximum electron fluxes				
Model\Metrics	R^2	RMSE	R^2	RMSE
Naive forecast	0.852	0.144	0.721	0.198
Linear regression	0.888	0.125	0.776	0.177

Figure 11. Forecast of >0.7 MeV daily maximum electron fluxes for 1 day

Figure 12. Forecast of >0.7 MeV daily maximum electron fluxes for 2 days

Figure 13. Forecast of >0.7 MeV daily integral electron fluxes for 1 day

Figure 14. Forecast of >0.7 MeV daily integral electron fluxes for 2 days
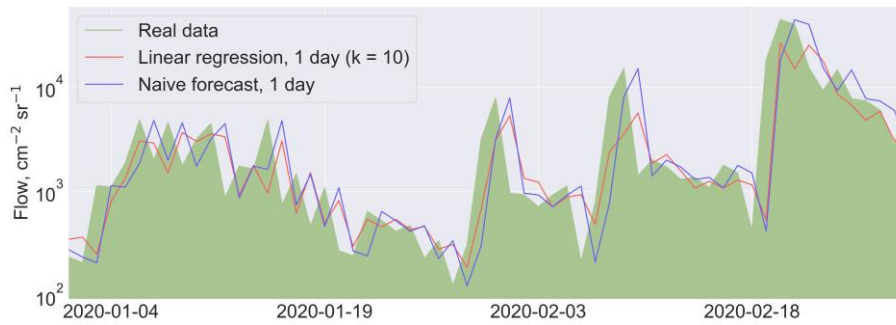

Figure 15. Forecast of >2 MeV daily maximum electron fluxes for 1 day
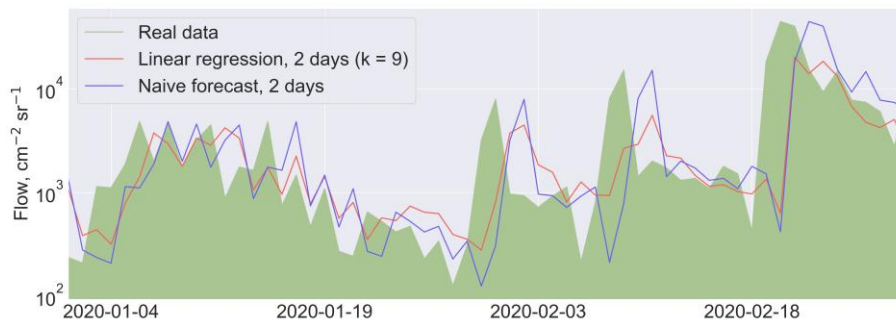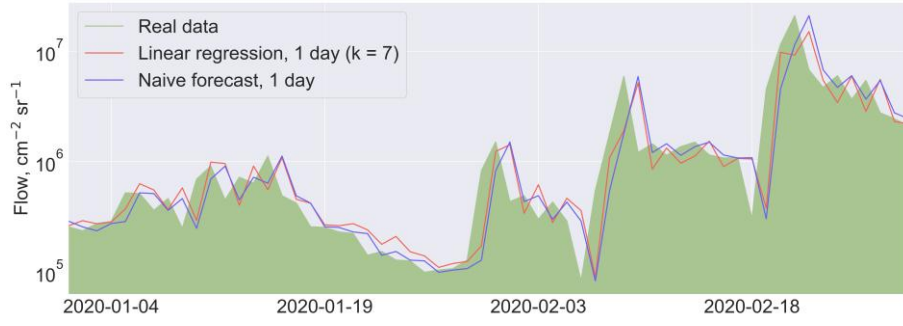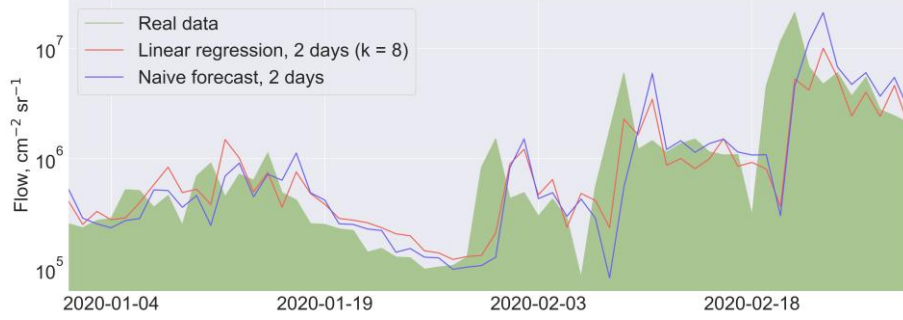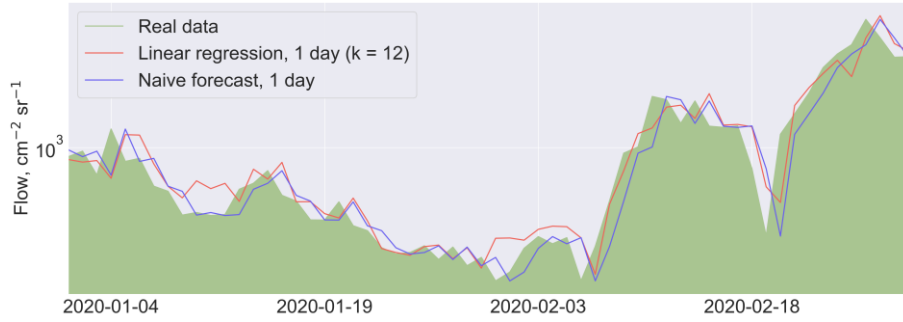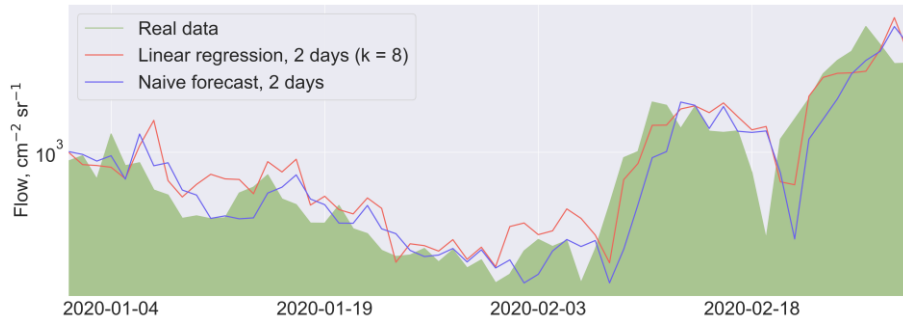

Figure 16. Forecast of >2 MeV daily maximum electron fluxes for 2 days

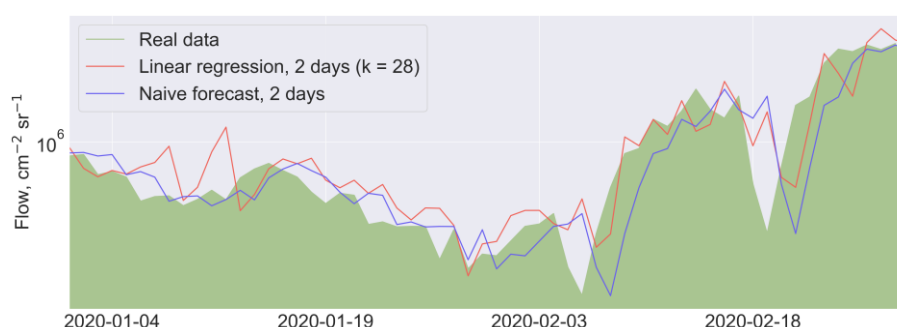*Figure 17*. Forecast of >2 MeV daily integral electron fluxes for 1 day

Figure 18. Forecast of >2 MeV daily integral electron fluxes for 2 days

CONCLUSION

The paper presents the results of the study of the possibility of predicting variations in >0.7 and >2 MeV electron fluxes (with the logarithm of flux) from Earth's outer radiation belt, measured in a circular polar orbit. The forecast was made using machine learning, where the solar wind and interplanetary magnetic field parameters, as well as geomagnetic indices and the logarithm of EORB electron flux in geostationary orbit were used as input features. We have selected optimal input features for predicting the electron flux in a low polar orbit. It has been found that in the polar orbit the maximum correlation of the >2 MeV integral electron flux in EORB is observed with the integral flux in geostationary orbit (GOES). In combination with the available results of prediction of electron fluxes in geostationary orbit for several days in advance [Myagkova et al., 2021; Kalegaev et al., 2023], the formulation of the problem of predicting electron fluxes in polar orbits can be considered promising.

From the results received during the study we can assume that in order to develop more accurate forecasting models the next possible step should be to expand the time series of experimental data in use, as well as to examine more complex machine learning models within this problem, such as artificial neural networks and gradient boosting.

REFERENCES

Alwosheel A., van Cranenburgh S., Chorus C.G. Is your dataset big enough? Sample size requirements when using artificial neural networks for discrete choice analysis. *J. Choice Modelling*. 2018, vol. 28, pp. 167–182. DOI: 10.1016/j.jocm.2018.07.002.

Baker D.N., McPherron R.L., Cayton T.E., Klebesadel R.W. Linear prediction filter analysis of relativistic electron properties at 6.6 RE. *J. Geophys. Res.* 1990, vol. 95, iss. A9, pp. 15133–15140. DOI: 10.1029/JA095iA09p15133.

Belov A.V., Villoresi J., Dorman L.I., et al. The influence of the space environment on the functioning of artificial Earth satellites. *Geomagnetism and Aeronomy.* 2004, vol. 44, iss. 4, pp. 502–510.

Balikhin M.A., Boynton R.J., Walker S.N., et al. Using the NARMAX approach to model the evolution of energetic electrons fluxes at geostationary orbit. *Geophys. Res. Lett.* 2011, vol. 38, iss. 18. DOI: 10.1029/2011GL048980.

Botek E., Pierrard V., Winant A. Prediction of radiation belts electron fluxes at a Low Earth Orbit using neural networks with PROBA-V/EPT data. *Space Weather.* 2023, vol. 21, iss. 7, e2023SW003466. DOI: 10.1029/2023SW003466.

Cole D.G. Space weather: Its effects and predictability. *Space Sci. Rev.* 2003, vol. 107, pp. 295–302. DOI: 10.1023/A:1025500513499.

Demidenko E.Z. *Linear and nonlinear regression.* Moscow: Finance and Statistics, 1981, 302 p

Denton M.H., Henderson M.G., Jordanova V.K., et al. An improved empirical model of electron and ion fluxes at geosynchronous orbit based on upstream solar wind conditions. *Space Weather.* 2016, vol. 14, iss. 7, pp. 511–523. DOI: 10.1002/2016SW001409.

Glauert S.A., Horne R.B., Meredith N.P. Three-dimensional electron radiation belt simulations using the BAS Radiation Belt Model with new diffusion models for chorus, plasmaspheric hiss, and lightning-generated whistlers. *J. Geophys. Res.: Space Phys.* 2014, vol. 119, iss. 1, pp. 268–289. DOI: 10.1002/2013JA019281.

Iucci N., Levitin A., Belov E., et al. Space weather conditions and spacecraft anomalies in different orbits. *Space Weather.* 2005, vol. 3, iss. 1. DOI: 10.1029/2003SW000056.

Kalegaev V., Panasyuk M., Myagkova I., et al. Monitoring, analysis and post-casting of the Earth's particle radiation environment during February 14 – March 5, 2014. *Space Weather Space Climate.* 2019, vol. 9, iss. A29. DOI: 10.1051/swsc/2019029.

Kalegaev V., Kaportseva K., Myagkova I., et al. Medium-term prediction of the fluence of relativistic electrons in geostationary orbit using solar wind streams forecast based on solar observations. *Adv. Space Res.* 2023, vol. 72, iss. 12, pp. 5376–5390. DOI: 10.1016/j.asr.2022.08.033.

Kataoka R., Miyoshi Y. Average profiles of the solar wind and outer radiation belt during the extreme flux enhancement of relativistic electrons at geosynchronous orbit. *Ann. Geophys.* 2008, vol. 26, iss. 6, pp. 1335–1339. DOI: 10.5194/angeo-26-1335-2008.

Koons H.C., Gorney D.J. A neural network model of the relativistic electron flux at geosynchronous orbit. *J. Geophys. Res.* 1991, vol. 96, iss. A4, pp. 5549–5556. DOI: 10.1029/90JA02380.

Kudela K. Space weather near Earth and energetic particles: Selected results. *J. Physics Conf. Ser.* 2013, vol. 409, iss. 1. DOI: 10.1088/1742-6596/409/1/012017.

Kuznetsov S.N., Myagkova I.N., Yushkov B.Yu., et al. Dynamics of the Earth's radiation belts during strong magnetic storms according to data from the CORONAS-F satellite. *Astronomical Bulletin. Studies of the Solar System.* 2007, vol. 41, iss. 4, pp. 369–378.

Landis D.A., Saikin A.A., Zhelavskaya I., et al. NARX neural network derivations of the outer boundary radiation belt

electron flux. *Space Weather.* 2022, vol. 20, iss. 5, e2021SW002774.
DOI: 10.1029/2021SW002774.

Li W., Hudson M.K. Earth's Van Allen radiation belts: From discovery to the Van Allen Probes era. *J. Geophys. Res.: Space Phys.* 2019, vol. 124, iss. 11, pp. 8319–8351. DOI: 10.1029/2018JA025940.

Li X., Baker D.N., Kanekal S.G., et al. Long term measurements of radiation belts by SAMPEX and their variations. *Geophys. Res. Lett.* 2001, vol. 28, iss. 20, pp. 3827–3830. DOI: 10.1029/2001gl013586.

Ling A.G., Ginet G.P., Hilmer R.V., Perry K.L. A neural network-based geosynchronous relativistic electron flux forecasting model. *Space Weather.* 2010, vol. 8, iss. 9. DOI: 10.1029/2010SW000576.

Lyatsky W., Khazanov G.V. A predictive model for relativistic electrons at geostationary orbit. *Geophys. Res. Lett.* 2008, vol. 35, iss. 15, L15108. DOI: 10.1029/2008GL034688.

Myagkova I., Efitorov A., Shiroky V., Dolenko S.A. Quality of prediction of daily relativistic electrons flux at geostationary orbit by machine learning methods. *Artificial Neural Networks and Machine Learning – ICANN 2019: Text and Time Series.* 2019, pp. 556–565. DOI: 10.1007/978-3-030-30490-4_45.

Myagkova I.N., Shirokiy V.R., Shugai Yu.S., et al. Short- and medium-term forecasting of relativistic electron fluxes in the Earth's outer radiation belt using machine learning methods. *Meteorology and Hydrology.* 2021, iss. 3, pp. 47–57. DOI: 10.52002/0130-2906-2021-3-47-57.

Novikov L.S., Voronina E.N. *Interaction of Spacecraft with the Environment.* Moscow: KDU, 2021, 560 p.

Osedlo V.I., Kalegaev V.V., Rubinshtein I.A., et al. Monitoring the radiation state of the near-Earth space on the Arktika-M No. 1 Satellite. *Cosmic Res.* 2022, vol. 60, iss. 6, pp. 406–419. DOI: 1134/S0010952522060089.

Pilipenko V., Yagova N., Romanova N., Allen J. Statistical relationships between the satellite anomalies at geostationary orbits and high-energy particles. *Adv. Space Res.* 2006, vol. 37, iss. 6, pp. 1192–1205. DOI: 10.1016/j.asr.2005.03.152.

Potapov A., Ryzhakova L., Tsegmed B. A new approach to predict and estimate enhancements of "killer" electron flux at geosynchronous orbit. *Acta Astronaut.* 2016, vol. 126, pp. 47–51. DOI: 10.1016/j.actaastro.2016.04.017.

Romanova N.V., Pilipenko V.A., Yadova N.V., Belov A.V. Statistical relationship of the frequency of failures on geostationary satellites with the fluxes of energetic electrons and protons. *Space Res.* 2005, vol. 43, iss. 3, pp. 186–193.

Son J., Moon Y.-J., Shin S. 72-hour time series forecasting of hourly relativistic electron fluxes at geostationary orbit by deep learning. *Space Weather.* 2022, vol. 20, iss. 10, e2022SW003153. DOI: 10.1029/2022sw003153.

Stepanova M., Pinto V., Antonova E. Regarding the relativistic electron dynamics in the outer radiation belt: a historical view. *Rev. Modern Plasma Physics.* 2024, vol. 8, iss. 25. DOI: 10.1007/s41614-024-00165-4.

Sun X., Lin R., Liu S., et al. Modeling the relationship of ≥2 MeV electron fluxes at different longitudes in geostationary orbit by the machine learning method. *Remote Sensing.* 2021, vol. 13, iss. 17, p. 3347. DOI: 10.3390/rs13173347.

Vernov S.N., Grigorov N.L., Logachev Yu.I., Chudakov A.E. Measurements of cosmic radiation on an artificial Earth satellite. *Reports of the Academy of Sciences.* 1958, vol. 120, iss. 6, pp. 1231–1233.

Wei L., Zhong Q., Lin R., et al. Quantitative prediction of high-energy electron integral flux at geostationary orbit based on deep learning. *Space Weather.* 2018, vol. 16, iss.

7, pp. 903–916. DOI: 10.1029/2018SW001829.

Williams D.J., Arens J.F., Lanzerotti L.J. Observations of trapped electrons at low and high altitudes. *J. Geophys. Res.* 1968, vol. 73, iss. 17, pp. 5673–5696. DOI: 10.1029/ja073i017p05673.

URL: https://swx.sinp.msu.ru/ (accessed September 10, 2024).
URL: http://www.swpc.noaa.gov/ (accessed September 10, 2024).
URL: https://rscf.ru/project/22-62-00048/ (accessed September 10, 2024)

IONOSPHERE RESPONSE TO THE IMPACT OF AN EXTRAORDINARY RADIO WAVE WHEN LOCATED AT A FREQUENCY CLOSE TO THE HEATING FREQUENCY

N.V. Bakhmetieva
Radiophysical Research Institute,
Lobachevsky State University,
Nizhniy Novgorod, Russia, nv_bakhm@nirfi.unn.ru

G.I. Grigoriev
Radiophysical Research Institute,
Lobachevsky State University,
Nizhniy Novgorod, Russia, grig19@list.ru

I.N. Zhemyakov
Radiophysical Research Institute,
Lobachevsky State University,
Nizhniy Novgorod, Russia, ilia.zhem@yandex.ru

E.E. Kalinina
Radiophysical Research Institute,
Lobachevsky State University,
Nizhniy Novgorod, Russia, kalinina@nirfi.unn.ru

A.A. Lisov
Radiophysical Research Institute,
Lobachevsky State University,
Nizhniy Novgorod, Russia, lisov@nirfi.unn.ru

Abstract. The paper presents the results of experiments on the impact of powerful high-frequency radio emission from the SURA mid-latitude heating facility (56.1° N, 46.1° E) on Earth's ionosphere. The disturbance in the ionosphere was created by a radio wave of extraordinary polarization under conditions when the ordinary component of the powerful wave was not reflected by the ionosphere. The probing of the disturbed region was carried out with a probe radio wave of the same polarization at a frequency higher than the heating frequency by 228–400 kHz. During the impact on the ionosphere, a weak scattered signal with an amplitude 40–60 dB lower than the amplitude of the specular reflection signal from the F-region was received from the height of reflection of the powerful radio wave. This means that the artificial disturbance of the plasma density occurred in the region of reflection of the powerful radio wave of extraordinary polarization. Possible causes of the disturbance are discussed.

Keywords: ionosphere, plasma, high-frequency heating, sounding with a probe radio wave, artificial periodic irregularities, SURA heating facility.

INTRODUCTION

Studies of the ionosphere exposed to powerful HF radio emission from heating facilities, which began in the 1960s, have revealed many phenomena both theoretically predicted and justified, and somewhat unexpected. Extensive literature is devoted to the results of these studies, including monographs and tens of hundreds of scientific publications. Among them are monographs [Gurevich, Schwarzburg, 1973; Mityakov et al., 1989; Blagoveshchenskaya, 2001; Frolov, 2017; Kelley, 2009], reviews [Ginzburg, Gurevich, 1960; Utlaut, Cohen, 1971; Stubbe, Hagfors, 1997; Leyser, 2001; Gurevich, 2007; Gurevich, 1999; Grach et al., 2016; Streltsov et al., 2018; Belikovich et al., 2007; Frolov et al., 2007; Blagoveshchenskaya, 2010, 2020; Blagoveshchenskaya et al., 2020, 2022; Kuo, 2021], which provide extensive references to theoretical and experimental studies on artificial ionospheric disturbance by powerful radio emission. A wide range of phenomena was investigated in experiments with the heating facilities Arecibo, HAARP, EISCAT, Zimenki, and SURA on the impact of powerful radio waves of ordinary polarization on the ionosphere. One of them was the occurrence of artificial turbulence in ionospheric plasma due to the development of plasma instabilities of various types near the upper hybrid resonance, i.e. the height of the resonant interaction between the high-power wave field and ionospheric electrons [Gurevich, 2007; Vas'kov, Gurevich, 1973, 1975a, b, 1979]. A detailed review of the results of numerous experiments on the impact of powerful radio emission on the ionosphere is given in the monograph [Frolov, 2017], in [Streltsov et al., 2018; Rietveld et al., 1993, 2016; Blagoveshchenskaya, 2020; Kuo, 2021]. An important condition for enhancing the heating effects was emission of a powerful radio wave by transmitters of the facility toward the magnetic zenith [Gurevich et al., 2002; Pedersen et al., 2003].

For a long time, ionospheric disturbances during radio heating were associated with a complex of nonlinear processes developing in the field of a powerful ordinary wave and causing the formation of a developed structure of plasma inhomogeneities strongly elongated along the geomagnetic field. Radio waves of extraordinary polarization were emitted to study the ionosphere and the neutral atmosphere by the method of creating artificial periodic inhomogeneities (APIs) of ionospheric plasma, first implemented at the Zimenki heating facility and subsequently developed at the SURA facility [Belikovich et al., 1975, 1999; Belikovich et al., 2002; Bakhmetieva,

Grigoriev, 2022]. The monograph [Frolov, 2017] describes in detail and discusses the results of experiments on ionospheric disturbance by an extraordinary radio wave, during which it was found that small-scale inhomogeneities with a scale transverse to the geomagnetic field $l_\perp \approx$ 10–20 m were not excited; decameter small-scale inhomogeneities with 50–200 m transverse scale and medium-scale ones with $l_\perp \approx$ 3 km were excited only in the evening and at night, whereas large-scale inhomogeneities with $l_\perp \approx$ 10–20 km or larger were excited during the same hours, provided that the heating frequency was close to the F-layer critical frequency for the extraordinary wave [Frolov et al., 2014; Frolov, 2015]. The best result was achieved by emitting a powerful radio wave in the direction of the magnetic zenith.

A large amount of research on nonlinear phenomena in plasma disturbed by a powerful radio wave of extraordinary polarization has been carried out by an international team at the EISCAT high-latitude heating facility [Blagoveshchenskaya et al., 2018; Blagoveshchenskaya et al., 2020; Blagoveshchenskaya et al., 2019, 2020, 2022; Kalishin et al., 2021; Borisova et al., 2023]. These experiments have shown that in the quiet high-latitude ionosphere the powerful radio wave of extraordinary polarization, emitted in the direction of the magnetic zenith, can affect the F-region of the ionosphere more effectively and cause a stronger disturbance of ionospheric plasma than the radio wave of ordinary polarization.

Based on the experience we have gained due to many years of research of the ionosphere by the method of resonant scattering of radio waves by APIs, a new cycle of experiments was launched at the SURA mid-latitude facility in 2006 to explore the disturbed region of the ionosphere formed during the impact of powerful radio waves of extraordinary polarization on the ionosphere. Sounding of the disturbed region with probe radio waves of the same polarization at a frequency close to the heating frequency was carried out at a partial reflection facility. Probe radio waves from the region disturbed by the radio wave of extraordinary polarization were scattered irregularly, under certain conditions. The purpose of this paper is to discuss the results of these experiments.

1. CREATING AN ARTIFICIAL DISTURBANCE IN THE IONOSPHERE AND ITS DETECTION BY PROBE RADIO WAVES

The measurements were made on October 10–11, 2006, September 1–2 and October 8, 2014, May 18, 2016, and September 24–25, 2024 in the evening hours, sometimes under conditions of strong F-layer diffusivity. In the text, we use Moscow Time (MSK) at which the SURA heating facility and the diagnostic complex operate, indicating Universal Time Coordinated (UTC) in parentheses.

October 10–11, 2006

The experiment was conducted from 19:00 to 22:00 MSK (UTC+4). The ionosphere was affected in phase

by three transmitters with radiated power P_1=210 kW, P_2=220 kW, and P_3=190 kW at a frequency of 4.3 MHz. A powerful radio wave of extraordinary polarization was emitted to the zenith.

The disturbed region was also detected by an extraordinary radio wave at a frequency f_{probe}=4.7 MHz (i.e. higher than the heating frequency by 400 kHz) with the transmitter Poisk of the partial reflection facility. In the ionospheric heating mode, SURA continuously emitted powerful radio waves for 30 s with a 60-s pause. The experiment was carried out under conditions when the F2-layer critical frequency f_oF2 was lower than the heating frequency and ordinary waves were not reflected by the ionosphere. Ionospheric conditions were monitored by the ionosonde Basis. During the experiment, natural F-spread occurred in which specular wave reflection from the F layer became blurred [Brunelli, Namgaladze, 1988]. During heating and the pause in operation of the facility, impulse sounding of the perturbed region of the ionosphere was performed. To record characteristics of amplitudes and phases of signals reflected and scattered by the ionosphere, we employed dedicated equipment designed for studying the ionosphere by the partial reflection technique, which is also used to explore the ionosphere and the neutral atmosphere by the API method [Belikovich et al., 2003]. The transmitter of the partial reflection facility radiated linearly polarized radio waves to the zenith in a pulsed mode with a pulse length of 25 (50) μs and a repetition frequency of 25 (50) Hz. The transceiver antenna system of the facility has 12 vibrators for each of the two mutually orthogonal polarizations. When received, a wave corresponding to the extraordinary component was generally identified. The received signals were amplified by a receiver with a 40 (80) kHz band, and their quadrature components were recorded digitally in increments 0.7–1.4 km in the virtual altitude range 0–700 km. The experiment has shown that, when an extraordinary radio wave had an impact on the ionosphere, a weak scattered signal appeared in the virtual altitude range 30–40 km below the specularly reflected signal, which disappeared after the end of heating.

September 1–2, 2014

The experiment took place from 21:25 to 07:10 MSK (UTC+4). The ionosphere was heated by two transmitters with P_1=150 kW and P_2=160 kW at a frequency f_{heat}=4.3 MHz. Probe waves were emitted, as in 2006, at a frequency f_{probe}=4.7 MHz. After 00:16 MSK, the ordinary component of a probe wave stopped reflecting from the ionosphere. In general, the conditions of the 2006 experiment were met, yet without F-spread. Scattered signals during the impact on the ionosphere were not recorded. After 02:45 MSK, the heating wave stopped reflecting from the ionosphere.

October 8, 2014

The experiment was carried out from 22:30 to 24:00 MSK (UTC+4). Three transmitters with P_1=170 kW, P_2=150 kW, and P_3=150 kW at f_{heat}=4.3 MHz were used for heating. The probe wave diagnostic transmitter and the frequency of probe radio waves were the same

as in September 2014. Scattered signals during the impact on the ionosphere were not recorded.

May 18, 2016

The experiment was conducted from 18:25 to 20:00 MSK (UTC+3). Heating was performed at a frequency of 5.750 MHz by two transmitters with P_1=200 kW and P_2=120 kW, the frequency of probe waves was changed from 5.600 to 5.900 MHz. By the end of the work, the F-layer critical frequency (x component) had decreased to 5.5 MHz, i.e. during this experiment, ionospheric sounding with the partial reflection facility was sometimes performed at a frequency lower than the heating frequency. Scattered signals during the impact on the ionosphere were not recorded.

September 24–25, 2024

The experiment was performed from 21:30 to 23:15 MSK (UTC+3) on September 24 and from 05:30 to 07:15 MSK (UTC+3) on September 25. The ionosphere was continuously heated by two SURA transmitters with P_1=220 kW and P_2=200 kW at a frequency of 5.227 MHz. Probe radio waves at a frequency of 5.455 MHz, i.e. higher than the heating frequency by 228 kHz, were emitted by the third transmitter with P_3=170 kW with a pulse length of 50 μs and a repetition frequency of 50 Hz.

To receive and record all the reflected and scattered ionospheric signals, an antenna system of the partial reflection facility and a receiving complex based on a 14-bit board (National Instruments) were exploited. The reception bandwidth was 850 kHz.

2. IONOSPHERE RESPONSE TO THE IMPACT OF A POWERFUL RADIO WAVE

Here are the main results of each measurement cycle.

2.1. Scattered signal characteristics on October 10–11, 2006

As mentioned above, during the impact of an extraordinary wave on the ionosphere, a weak scattered signal appeared at virtual altitudes, mainly 30–40 km below the height of the specular reflection of the signal from the F-region. The scattered signal was recorded from 19:40 to 21:00 MSK on October 10, 2006 and from 20:45 to 21:57 MSK on October 11, 2006. The effect was so pronounced that the appearance and development of the scattered signal during heating of the ionosphere were observed in real time without additional processing. Figure 1 gives a fragment of real-time recording of the amplitude of the signal, which appeared during the impact on the ionosphere, in virtual altitude —time coordinates. The amplitude of the scattered signal was by 40–50 dB lower than the amplitude of the specular reflection of the probe radio wave from the ionospheric F layer and changed rapidly with altitude and time. The signal developed for ~1 s, and the relaxation time was about a fraction of a second. The signal was noise-like: the correlation time interval did not exceed 0.2 s.

Above 340–350 km, there are diffuse specular reflections of the probe wave from the F-region. At ~105 km, the sporadic E (E_s) layer is observed with f_oE_s=2.5–3.1 MHz. The corresponding ionograms obtained by the ionosonde Basis are presented in Figure 2. Under these conditions, an ordinary radio wave with a frequency of 4.3 MHz was not reflected from the ionosphere.

Figure 3 displays amplitudes of scattered and specularly reflected signals for a series of heatings after 21:30 MSK in the same coordinates. Above 310 km, there is a diffuse specular signal at the probe wave frequency. In Figure 3, above 270 km under the altitude of the specular reflection of the probe wave (~310–320 km), there is a 4.7 MHz scattered signal, whose development correlates with the moments when the heating is switched on. In the middle of the fifth heating session after 21.71 MSK (the time is given in fractions of an hour), the power emitted by transmitters of the heating facility decreased. The amplitude of the scattered signal is seen to noticeably decrease as well, which means that it directly depends on the heating power. By the end of the seventh heating session after 21.75 MSK, the receiving voltage was turned down (20 dB attenuation was manually turned on in the receiver), which caused the amplitude of the received signal to decrease. The sporadic E layer was observed at an altitude 100–105 km during the entire measurement period.
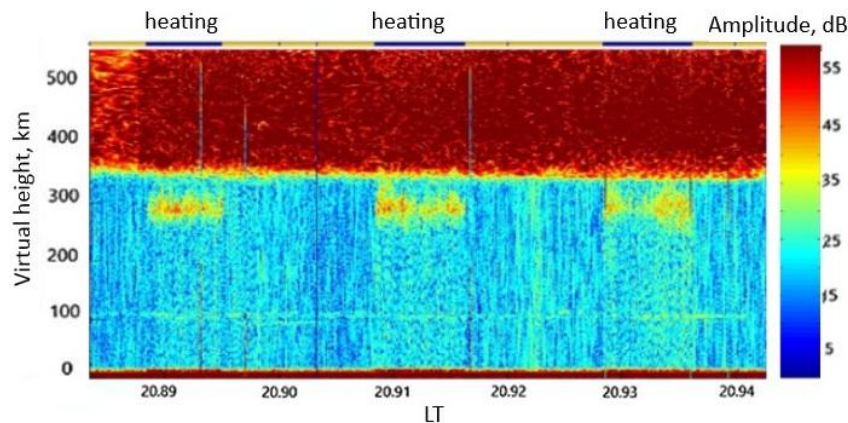
Figure 1. Fragment of real-time recording of the amplitude of a signal that appeared during the impact on the ionosphere in three heating sessions. Separate white or black vertical lines indicate incorrect scans due to failures in receiving equipment. Heating intervals are marked with dark stripes at the top. Time is given in fractions of an hour

N.V. Bakhmetieva, G.I. Grigoriev, I.N. Zhemyakov, E.E. Kalinina, A.A. Lisov
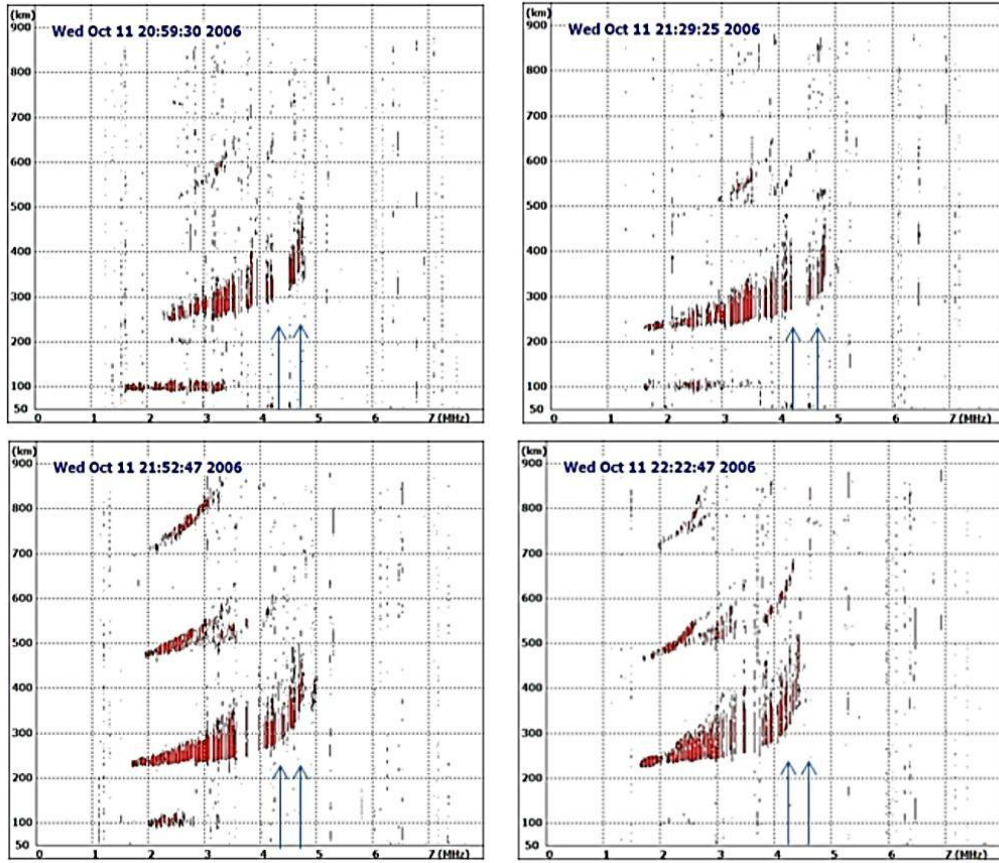
Figure 2. Ionograms obtained by the ionosonde Basis on October 11, 2006 during the experiment. Time on the ionograms is in MSK (UTC+4). Arrows indicate frequencies of heating and probe radio waves. Intense F-spread is seen to occur during the experiment
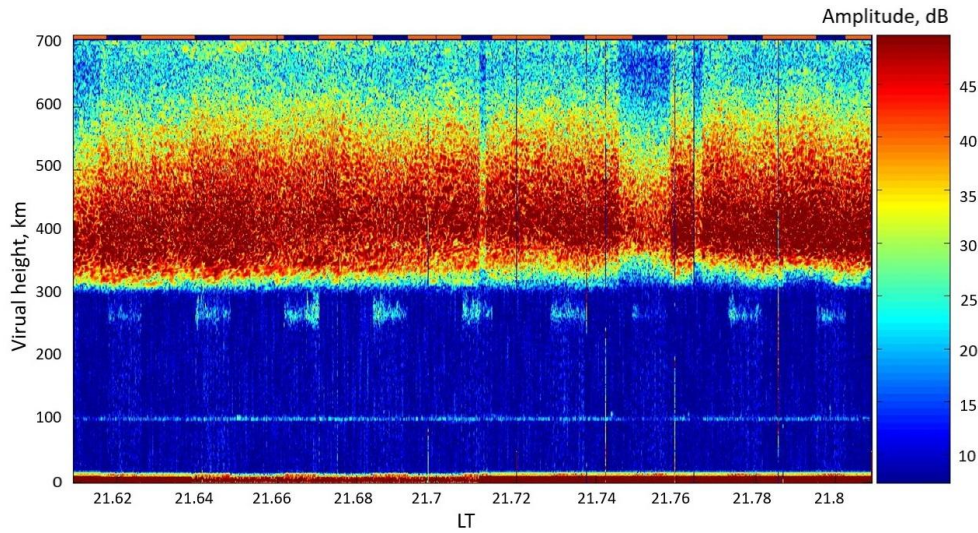
Figure 3. Fragment of real-time recording of the amplitude of a signal, which appeared during the impact on the ionosphere, for nine heating sessions after 21:30 MSK. Heating intervals are indicated by dark stripes at the top

From the analysis of the altitude electron density profiles recovered from vertical sounding ionograms it follows that the 4.7 MHz probe radio wave was reflected at altitudes close to that of reflection of the 4.3 MHz heating wave. Recall that here we are dealing with extraordinary components of heating and probe radio waves.

During heating, the F-layer diffusivity changed and hence the specular signal reflected from the F layer ac-

quired a finer height and time structure. This is clearly seen in Figure 4, which illustrates the development of a scattered signal in the session starting at 20:55:03 MSK (h:min:s). It follows from Figures 3 and 4 that the amplitude of the scattered signal changed irregularly with height and time. Within each individual heating session, scattered signals occupied a virtual altitude range from 20 to 100 km. There are 5–10 s quasiperiodic amplitude changes.

The receiving part of the partial reflection facility was designed in such a way that the ordinary and extraordinary probe wave modes could be received alternately (every other sounding pulse). Note that there was no scattered signal in the ordinary component. This is illustrated in Figure 5 which presents the result of alternating (every other sounding pulse) reception of both probe wave components during the session at 21:21:54 MSK.

The scattered signal is clearly seen to appear during heating only in the extraordinary probe wave (Figure 5, *a*), and it was absent in the ordinary one (Figure 5, *b*). Since at that time the 4.7 MHz ordinary wave was not reflected by the ionosphere (the F-layer critical frequency was lower than the probe wave frequency), the signal above 320 km in Figure 5, *b* is a probe wave signal of extraordinary polarization, attenuated due to insufficient decoupling of the magnetoionic components in the reception path of the partial reflection facility.

Notice that the results of the October 10–11, 2006 experiment were not published or reported at conferences in due course. The authors were faced with the problem of repeating the experiment, re-obtaining the observed effect, and uncovering the reason for the appearance of a scattered signal when the ionosphere is heated by a radio wave of extraordinary polarization and the disturbed region is sounded with a probe radio wave of the same polarization, but at a frequency several hundred kilo-

hertz higher than the heating frequency. Several such experiments were carried out later, and their results are presented below. As far as we know, such experiments have not been conducted before.

2.2. Results of the 2014 and 2016 experiments

September 1–2, 2014 (evening, night, morning)
After 0:16 MSK, the ordinary component of the probe wave stopped reflecting from the ionosphere and the conditions of the 2006 experiment were met, but no F-spread was observed. Scattered signals similar to those recorded in 2006 were not observed either. Probably, the transmitter power (two transmitters of 150 and 160 kW worked) turned out to be insufficient. After 02:45 MSK, the heating wave stopped reflecting from the ionosphere.

October 8, 2014
Under seemingly suitable experimental conditions, there were no scattered signals during heating. The heating was performed by three transmitters of 170, 150, and 150 kW with natural diffusivity of the F layer without intense F-spread. Figure 6 shows the amplitude of the specular reflection of the extraordinary component of the 4.7 MHz probe wave. The wave of ordinary polarization was not reflected by the ionosphere.
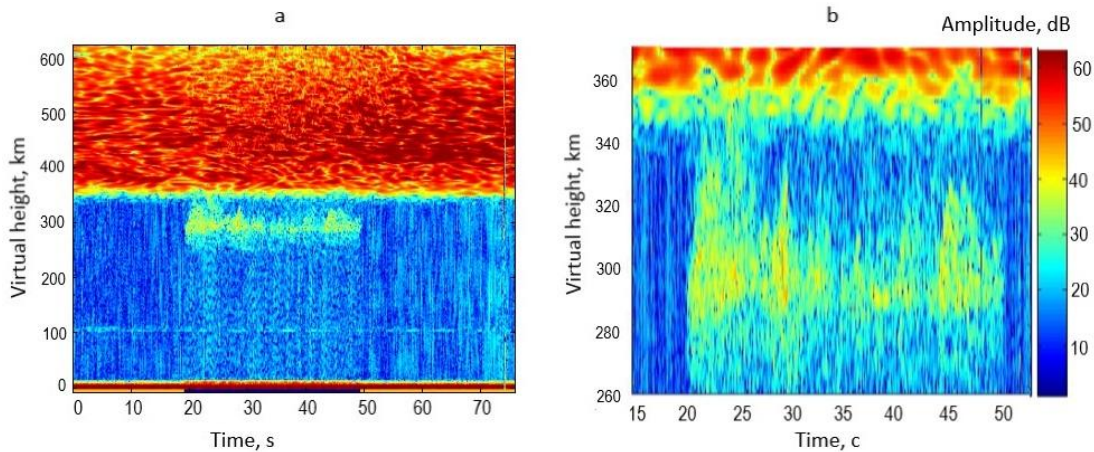

Figure 4. Development of a scattered signal in the heating session starting at 20:55:03 MSK: in a virtual altitude range 0–700 km (*a*); in a narrower altitude range 260–360 km (*b*)
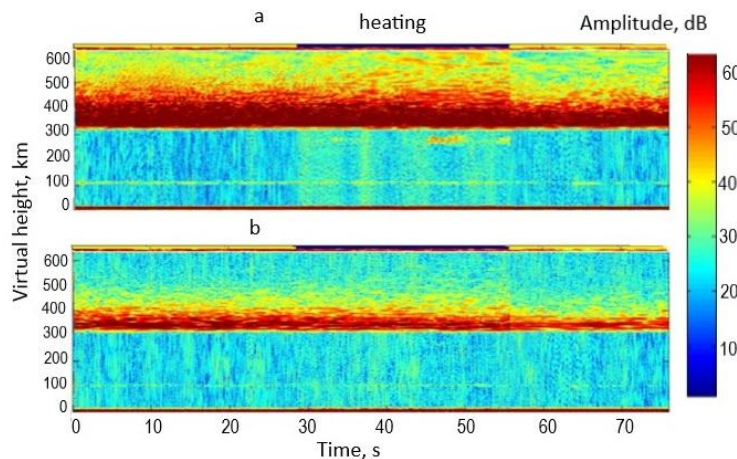

Figure 5. Example of recording of a scattered signal of extraordinary (*a*) and ordinary (*b*) polarization of a probe wave in the session at 21:21:54 MSK (h:min:s)

May 18, 2016

Two transmitters with P_1=200 kW and P_2=120 kW at a frequency of 5.750 MHz operated for heating, probe waves were transmitted in the range 5.6–5.9 MHz. At the beginning of observations, the probe wave frequency was lower than the heating wave frequency, then it was increased, and the difference between them was 150 kHz. A result similar to that presented in Figure 6 for October 8, 2014 was obtained, i.e. scattered signals were not recorded during heating.

2.3. Characteristics of the scattered signal on September 24–25, 2024

As noted above, in the next experiment in September 2024 ionospheric signals were received by the antenna system of the partial reflection facility, and a probe signal was emitted by one of the three transmitters of the SURA heating facility. The signals were recorded digitally, using a 14-bit NI board with a vertical data sampling step of 150 m. The difference between the heating frequency f_{heat}=5.227 MHz and the probe frequency f_{probe}=5.455 MHz of radio waves was 228 kHz. Due to the fact that the receiver's bandwidth was wider, during subsequent processing the received signals were filtered by a sixth-order Bessel filter with a 40 kHz bandwidth, which made it possible to almost completely eliminate the heating frequency signal from the data. The work schedule was designed to include dusk (night) hours in conditions of diffuse ionospheric F layer and early dawn hours in conditions of more regular ionosphere. Figure 7 displays fragments of recording of ionospheric signals during 30 s heating and 60 s pause in operation of the heating transmitters.
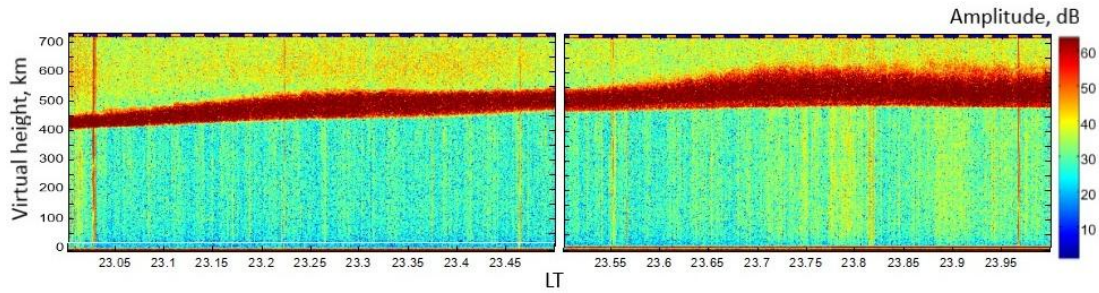
Figure 6. Specular reflection of a probe wave from the F layer on October 8, 2014, heating intervals are marked with light stripes on the top axis
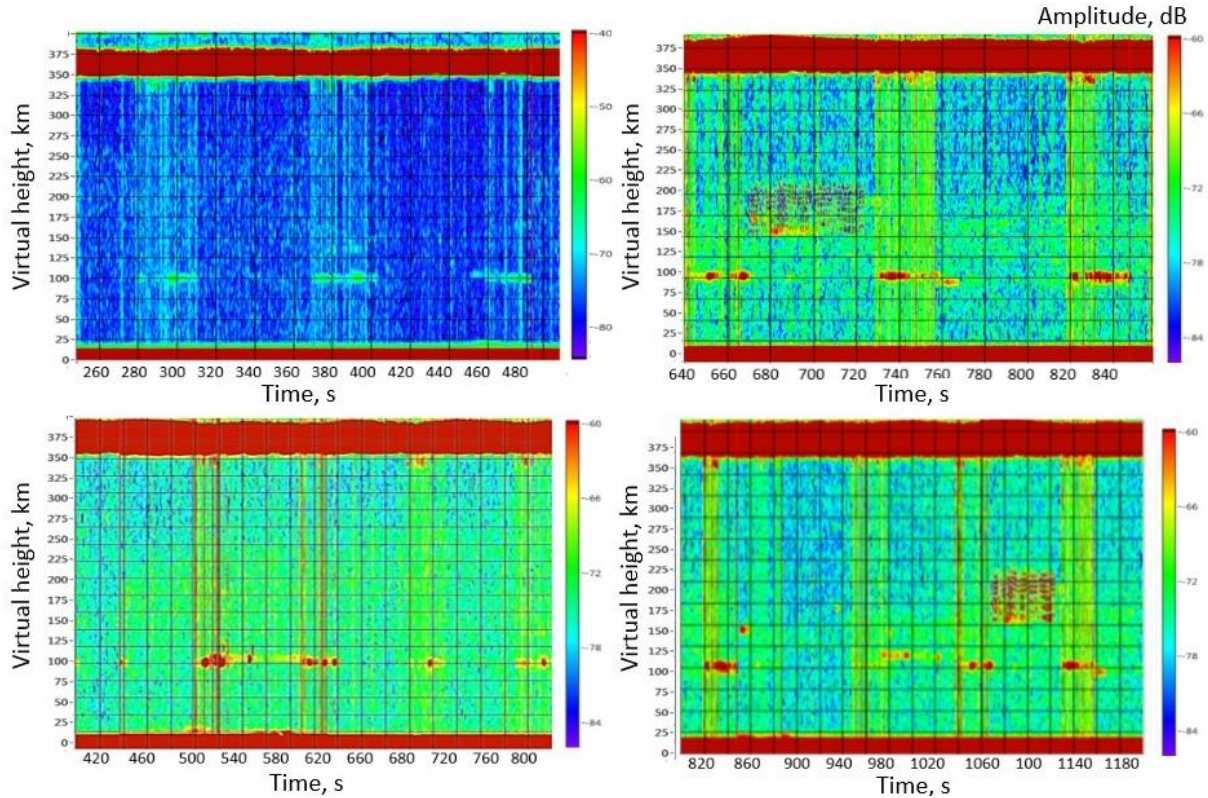
Figure 7. Appearance of scattered signals below the virtual altitude of 350 km under the altitude of the specular reflection of a probe wave and E-region signals at an altitude of 100 km during the impact on the ionosphere: in the session starting at 21:45:50 (top); in the session starting at 21:15:50 (bottom). Heating periods are well identified by vertical stripes, which indicate an incompletely filtered powerful signal at the heating frequency

Probe waves of extraordinary polarization with a frequency of 5.455 MHz were reflected above 350 km, and F-layer diffusivity was observed. During heating, scattered signals appeared below the reflection altitude of the probe radio wave. The scattered signal was by 60–70 dB weaker than the specular signal and occupied the virtual altitude range 20–25 km, being directly adjacent to the altitudes of the specular signal reflection (in contrast to the 2006 experiment). The signal developed for ~1 s and disappeared for a shorter time, as in 2006. In addition, signals from the E-region appeared (intensified) during heating. At this time, a semi-transparent sporadic E layer with 2.5–3.1 MHz critical frequency was occasionally observed on ionograms at 100–105 km. At the same time, a weakening of the scattered signal in the F layer was detected when the amplitude of the reflected signal from the E_s layer increased during ionosphere heating sessions.

During the morning hours at sunrise and after sunrise under conditions of a rapid increase in critical frequencies, a decrease in the height of the F layer, and pronounced ionospheric dynamics, there was no scattered signal at the 5.455 MHz probe wave frequency during the impact of the 5.227 MHz extraordinary wave on the ionosphere. Figure 8 exhibits a fragment of recording of ionospheric signals for 12 min in the session starting at 06:30:50. Both probe wave components are shown. Multiple off-angle reflections are seen below the virtual altitude of 200 km, oblique reflections near 150 km, and radio reflections from meteor trails near 100 km.

Thus, the scattered signal at a frequency differing by 228–400 kHz from the heating frequency was observed only in two of the five experiments we conducted during different years on the impact of a powerful radio wave of extraordinary polarization on the ionosphere and on sounding of the perturbed region by probe radio waves of the same polarization.

3. DISCUSSION

Analysis of altitude electron density profiles obtained from vertical sounding ionograms on October 10–11, 2006 has shown that the region of appearance of scattered signals practically coincided with the reflection level of the powerful wave at a true altitude of 223.4 km. This means that the artificial plasma density disturbance occurred in the region of reflection of the powerful radio wave of extraordinary polarization. There are two possible explanations for the observed effect.

3.1. Hypothesis 1 — Plasma wave excitation and induced ion scattering

The October 10–11, 2006 experiment has revealed that a powerful radio wave of extraordinary polarization causes a plasma density disturbance in the region of its reflection from the ionosphere. The question about the nature of the disturbance in the ionosphere when it is heated by a powerful radio wave of extraordinary polarization is considered in detail in [Vas'kov, Ryabova, 1997]. This disturbance can be created either directly by the electric field of a radio wave or by the field of excited plasma oscillations. In the case of large wave vectors, such oscillations can propagate below the reflection level of an extraordinary radio wave of close frequency and can be excited by a powerful radio wave due to the development of various striction instabilities. The cause for this is the excitation of high-frequency plasma oscillations as a result of induced ion scattering of an extraordinary radio wave, for which, as shown in [Vas'kov, Ryabova, 1997], the threshold field value turns out to be relatively small. Calculations based on this work have shown that under conditions of October 10–11, 2006 experiments at the frequency of the heating wave of extraordinary polarization f_{heat}=4.3 MHz and its effective radiation power ~100–120 MW, we would expect a sufficiently strong excitation of plasma waves in the order of 10^{-4} s. However, the experiment has revealed that the excitation of plasma waves by the field of the extraordinary radio wave, if it did occur, was strongly suppressed. This is evidenced by the low intensity of the scattered signal and its location near the level of reflection of the powerful wave from the ionosphere, where its electric field increases due to focusing. In the absence (or with strong suppression) of plasma waves, artificial inhomogeneities must be created directly by the field of a powerful radio wave. As a result, the amplitude
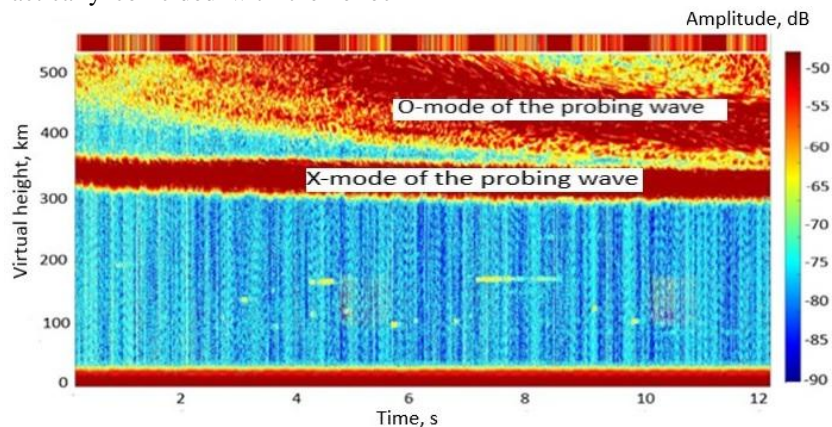

Figure 8. Fragment of recording of ionospheric signals for 12 min in the session starting at 06:30:50. The 30 s heating intervals are indicated by dark red stripes on the top axis

of a scattered signal should increase in direct proportion to the intensity of the powerful wave. The experiment with a step-by-step increase in heating power was planned, yet was not carried out for technical reasons.

3.2. Hypothesis 2 — Scattering of probe radio waves by artificial periodic inhomogeneities of ionospheric plasma

As is known, APIs in the field of a powerful wave are most effectively created by an extraordinary radio wave (X-mode) [Belikovich et al., 1999; Belikovich et al., 2002; Bakhmetieva, Grigoriev, 2022]. They exist throughout the ionosphere in the D-, E-, and F-regions, and the interlayer E–F depression. Near the specular reflection point in the F-region, APIs increase due to the "swelling" of the field of the powerful wave and an increase in its length [Ginzburg, 1967]. Under quiet conditions, APIs replicate the structure of the standing wave field described by the Airy function [Ginzburg, 1967] and scatter only probe radio waves of the same polarization as the heating wave if frequencies of heating and probe radio waves coincide, i.e. the condition of spatial synchronism is fulfilled [Belikovich et al., 1999; Belikovich et al., 2002]. We determined the synchronism frequency band during the July 16, 2006 experiment [Bakhmetyeva, Belikovich, 2007, 2008], which was aimed at studying the effect of the E_s layer on APIs. To identify the synchronism frequency band when APIs were detected for receiving scattered signals, we sequentially selected frequencies spaced away from the 4.785 MHz heating frequency by 30, 35, and 20 kHz to the 4.700 MHz frequency. It appeared that with sequential detuning from the frequency of API creation, the amplitudes of signals scattered by periodic inhomogeneities decreased; and with detuning at 85 kHz (the 4.700 MHz receiving frequency), the signals from APIs disappeared completely, only specular reflections from the F layer, E-region, and E_s layer were recorded. The synchronism frequency band, we have experimentally determined [Bakhmetyeva, Belikovich, 2007, 2008], under these conditions did not exceed 85 kHz (complete disappearance of the scattered signal from APIs) with a probe pulse duration of 30 ms and a receiver bandwidth of 40 kHz.

According to the synchronism frequency band found under quiet conditions with the 228–400 kHz frequency difference between the heating and probe radio waves, the scattered API signal should not have been observed. Nonetheless, during the October 10–11, 2006 experiment there was intense F-spread apparently caused by natural ionospheric disturbance (natural plasma inhomogeneities). This disturbance might have distorted the ordered structure of quasi-periodic inhomogeneities and led to a broadening of the angular and frequency spectrum of a signal scattered by APIs. This was probably responsible for the appearance of the scattered signal during heating in a certain altitude region near the altitude of reflection of the lower-frequency powerful wave. We believed that a test of this hypothesis could be to conduct such an experiment under quiet conditions

and in the presence of F-spread, which, to a certain extent, was an objective of the October 24–25, 2024 experiment. The experiment has confirmed that the scattered signal during heating was observed in the evening under conditions of F-layer diffusivity and was not recorded in the early morning under conditions of a rapid increase in critical frequencies, a decrease in the F-layer height, and pronounced dynamics of the ionosphere.

What could cause the natural disturbance of the F layer? It is known that in the F layer there are plasma streams directed upward during the day and downward at night from the magnetosphere or the conjugate hemisphere [Brunelli, Namgaladze, 1988]. If we assume that F-spread is created by similar streams with velocities of 20 m/s or higher, the periodic structure (API), which is formed in such a moving medium, will be distorted and shifted downward in altitude in the evening. Then a vertical velocity gradient will appear, the periodic structure will be compressed, and the synchronism condition will be met at a higher frequency due to a decrease in the altitude API period [Belikovich et al., 1999; Belikovich et al., 2002]. We can assume that in this case under conditions of strong natural disturbance, the synchronism frequency band may exceed the previously found 85 kHz and APIs will scatter probe signals in a wider frequency band.

There was no E-region on the ionograms at that time, and the semi-transparent E_s layer with $f_oE_s = 2.5$–3.1 MHz was occasionally observed at 100–105 km. As noted above, during the ionosphere heating sessions with an increase in the amplitude of the signal reflected at the altitude of 100 km, the scattered signal in the F layer generally weakened, which is clearly seen in Figure 7. This can be explained by an increase in the reflection coefficient of the probe wave from the E layer due to an increase in the electron density in it during heating. In [Gershman, Ignatiev, 1997; Ignatiev, 1975], the question about perturbation of the ionospheric E-region, including the E_s layer, when exposed to powerful radio emission, is examined in detail. When the ionosphere heats up in the E-region, the effective recombination coefficient decreases with increasing electron temperature [Gurevich, Shvartsburg, 1973], thereby causing the electron density to rise under the influence of powerful radio emission. As a result, the reflection coefficient of the powerful wave in the lower ionosphere increases, which leads to a decrease in the impact on the F layer and hence to a decrease in the intensity of probe wave scattering in the F layer. The semi-transparent E_s layer has the same effect if it is formed by the redistribution of atmospheric NO^+ and O_2^+ ions rather than metal ions, which is possible in the evening and night hours [Gershman, Ignatiev, 1997; Ignatiev, 1975]. Note also that during the night hours the electron density in the E-region decreases markedly, but does not disappear completely [Danilov, Vlasov, 1973; Brunelli, Namgaladze, 1988]. Studies of the ionosphere at sunset and sunrise, we have carried out using the method of resonant scattering of radio waves by APIs in different years, have shown that sufficient ionization in the E-region can per-

sist all night [Belikovich et al., 2002; Bakhmetieva et al., 2005, 2024]. Measurements performed by the API method on September 23–24, 2024 have shown that at least until 23 MSK, i.e. after sunset in the ionosphere, signals scattered by APIs were reliably recorded in the altitude range 90–130 km. Note that the method based on resonant scattering of radio waves by APIs allows us to detect ionospheric regular and sporadic layers with low ionization, undetectable by ionosondes [Belikovich et al., 1999; Belikovich et al., 2002; Bakhmet'eva, Belikovich, 2007, 2008].

4. BASIC REQUIREMENTS FOR DESIGNING AN EXPERIMENT

After analyzing the conditions and results of experiments in different years, we made the following conclusions on the optimal organization of such an experiment on the impact of emission of a powerful radio wave of extraordinary polarization to the zenith on the ionosphere at the SURA heating facility.

The experiments have shown that stable, preferably maximum heating power is required. Unfortunately, the capabilities of the SURA facility are limited in this regard. The power of the diagnostic transmitter is not so important, as can be seen from the results of the experiments in 2006 and 2024 when using a low-power transmitter of the partial reflection facility as a source of probe waves; a distinct scattered signal was recorded in real time. Thus, the intensity of the scattering effect largely depends on the heating power and to a much lesser extent on the diagnostic transmitter power.

The optimal situation is when the heating frequency is higher than the F2-layer critical frequency for the ordinary component and lower than the F2-layer critical frequency for the extraordinary one; in this case, only the powerful wave of extraordinary polarization is reflected by the ionosphere. In our opinion, the 228–400 kHz frequency difference between the heating and probe waves was large, it probably should be smaller. At the same time, a narrow reception band of the probe signal is desirable in order to adjust to the heating frequency. Finally, we should take into account the strong dependence of the result on the state of the ionosphere: in our conditions, a more pronounced effect was observed during intense F-spread or diffusivity of the ionosphere and was not observed in their absence.

Unlike the experiments on the impact on the ionosphere performed at the EISCAT heating facility [Blagoveshchenskaya, 2010; Blagoveshchenskaya, 2020; Borisova et al., 2023], in the experiments from 2006 to 2024 at the SURA facility the effects of ionospheric disturbance by a powerful radio wave of extraordinary polarization when detected by probe radio waves of the same polarization, but of a different frequency, were observed irregularly and were rather weak. Obviously, the power of the heating wave was of crucial importance. The emission power comparable to that of the EISCAT high-latitude facility is unattainable at SURA. Moreover, the powerful radio wave was emitted to the zenith, rather than to the magnetic zenith, which might have enhanced the observed effect.

CONCLUSION

During the impact of a powerful radio wave of extraordinary polarization on the ionosphere and when sounding the disturbed ionosphere with probe radio waves of the same polarization at a frequency close to the heating frequency, but differing by 228–400 kHz, a scattered signal appeared at virtual altitudes below the altitude of specular probe wave reflection. In October 2006, the scattered signal amplitude was 40–50 dB lower than the specular signal amplitude, and it occupied a range of virtual altitudes 30–40 km lower than the altitude of the signal mirrored from the F layer. The development time of the scattered signal was ~1 s, and the relaxation time was by an order of magnitude shorter. The signal was noise-like, and its amplitude changed rapidly with height and time. The effect was observed in the evening under conditions of strong F-layer diffusivity (F-spread phenomenon). In September 2024, in the late evening, a scattered signal with an amplitude 50–60 lower than the amplitude of the signal mirrored from the F layer appeared directly below it and occupied a virtual altitude range 15–25 km. During 30 s heating sessions, a signal from the E-region or sporadic E layer appeared (intensified) for 1 s or less. When a scattered signal appeared in the E-region, a scattered signal in the F layer generally weakened.

Analysis of vertical electron density profiles has shown that a probe wave of extraordinary polarization with a frequency by 228–400 kHz higher than the frequency of the heating wave of the same polarization was reflected almost at the altitude of reflection of the latter and a scattered signal appeared near this altitude. This implies that the powerful radio wave of extraordinary polarization caused a disturbance in the plasma density in the region of its reflection from the ionosphere. During the morning hours after sunrise under conditions of a rapid increase in critical frequencies of the ionosphere, such a scattered signal was not observed during the impact on the ionosphere.

We have proposed two explanations of the observed phenomenon. At present, it seems preferable to suppose that probe radio waves are scattered by artificial periodic inhomogeneities of ionospheric plasma, which arise in the field of a powerful radio wave. Scattering of radio waves by APIs when the polarization of heating and probe radio waves coincide, and a scattered signal appears at a frequency other than the heating one, may be due to a change in synchronism conditions and an expansion of the band of observed frequencies during scattering by APIs under conditions of intense F-spread. This is confirmed by the absence of a scattered signal in a more regular ionosphere in the morning after sunrise. Nevertheless, it has to be stated and the experiments carried out have convincingly shown that the question about the mechanisms of formation of plasma inhomogeneities in the field of a powerful radio wave of extraordinary polarization remains theoretically open.

REFERENCES

Bakhmet'eva N.V., Belikovich V.V. Results of studying the sporadic E layer by the method of resonant scattering of radio waves by artificial periodic inhomogeneities of the ionospheric plasma. *Radiophysics and Quantum Electronics.* 2008, vol. 51, no. 11, pp. 862–873. DOI: 10.1007/s11141-009-9092-4.

Bakhmetieva N.V., Grigoriev G.I. Study of the mesosphere and lower thermosphere by the method of creating artificial periodic irregularities of the ionospheric plasma. *Atmosphere.* 2022, vol. 13, no. 9, p. 1346. DOI: 10.3390/atmos13091346.

Bakhmet'eva N.V., Belikovich V.V., Kagan L.M., Ponyatov A.A. Sunset-sunrise characteristics of sporadic layers of ionization in the lower ionosphere observed by the method of resonance scattering of radio waves from artificial periodic inhomogeneities of the ionospheric plasma. *Radiophysics and Quantum Electronics.* 2005, vol. 48, no. 1, pp. 14–28.

Bakhmet'eva N.V., Belikovich V.V. Modification of the Earth's ionosphere by high-power HF radio emission: Artificial periodic inhomogeneities and the sporadic E layer. *Radiophysics and Quantum Electronics.* 2007, vol. 50, no. 8, pp. 633–644. DOI: 10.1007/s11141-007-0055-3.

Bakhmetieva N.V., Grigoriev G.I., Zhemyakov I.N., Kalinina E.E., Lisov A.A. Features of Earth's lower ionosphere during solar eclipse and sunset and sunrise hours according to measurements by the API method near Nizhny Novgorod. *Sol.-Terr. Phys.* 2024, vol. 10, iss. 3, pp. 121–136. DOI: 10.12737/stp-103202414.

Belikovich V.V., Benediktov E.A., Getmantsev G.G., Ignat'ev Yu.A., Komrakov G.P. Scattering of radio waves from the artificially perturbed F region of the ionosphere. *JETF Letters*. 1975, vol. 22, iss. 10, pp. 497–499.

Belikovich V.V., Benediktov E.A., Tolmacheva A.V., Bakhmet'eva N.V. *Issledovanie ionosfery s pomoshch'yu iskusstvennykh periodicheskikh neodnorodnostei* [Research of the ionosphere by means of artificial periodic irregularities]. Nizhny Novgorod, Institute of Applied Physics RAS Publ., 1999, 155 p. (In Russian).

Belikovich V.V., Benediktov E.A., Tolmacheva A.V., Bakhmet'eva N.V. *Ionospheric Research by Means of Artificial Periodic Irregularities.* Katlenburg-Lindau, Copernicus GmbH, 2002, 160 p.

Belikovich V.V., Vyakhirev V.D., Kalinina E.E., Tereshshenko V.D., Ogloblina O.F., Tereshshenko V.A. Study of the ionospheric D layer using partial reflections at the middle latitudes and in the auroral zone. *Radiophysics and Quantum Electronic.* 2003, vol. 46, no. 3, pp. 162–171. DOI: 10.1023/ A:1024464016629.

Belikovich V.V., Grach S.M., Karashtin A.N., Kotik D.S., Tokarev Yu.V. The "Sura" facility: Study of the atmosphere and space (a review). *Radiophysics and Quantum Electronic.* 2007, vol. 50, no. 7, pp. 497–526. DOI: 10.1007/ s11141-007-0046-4.

Blagoveshchenskaya N.F. *Geofizicheskie effekty aktivnykh vozdeistvii v okolozemnom kosmicheskom prostranstve* [Geophysical effects of active influences in near-Earth space]. St. Petersburg, Gidrometeoizdat, 2001, 287 p. (In Russian).

Blagoveshchenskaya N.F. Multi-instrumental studies of phenomena in the high latitudinal ionosphere initiated by powerful HF radio waves: Results and outlook. *Problemy Arktiki i Antarktiki* [Problems of the Arctic and Antarctic]. 2010, vol. 84, no. 1, pp. 81–98. (In Russian).

Blagoveshchenskaya N.F. Perturbing the high-latitude upper ionosphere (F region) with powerful HF radio waves: A 25-year collaboration with EISCAT. *URSI Radio Science Bulletin.* 2020, vol. 373, pp. 40–55.
DOI: 10.23919/URSIRSB. 2020.9318436.

Blagoveshchenskaya N.F., Borisova T.D., Kalishin A.S., Kayatkin V.N., Yeoman T.K. Comparison of the effects induced by the ordinary (O-mode) and extraordinary (X-mode) polarized powerful HF radio waves in the high-latitude ionospheric F region. *Cosmic Res.* 2018, vol. 56, pp. 11–25. DOI: 10.7868/S002342061801003X.

Blagoveshchenskaya N.F., Borisova T.D., Kalishin A.S., Yeoman T.K., Schmelev Y.A., Leonenko E.E. Characterization of artificial, small-scale, ionospheric irregularities in the high-latitude F region induced by high-power, high-frequency radio waves of extraordinary polarization. *Geomagnetism and Aeronomy.* 2019, vol. 59, no. 6, pp. 759–773. DOI: 10.1134/s0016793219060045.

Blagoveshchenskaya N.F., Borisova T.D., Kalishin A.S., Yeoman T.K., Häggström I. Distinctive features of Langmuir and ion-acoustic turbulences induced by O- and X-mode HF pumping at EISCAT. *J. Geophys. Res.: Space Phys.* 2020, vol. 125, no. 7, e2020JA028203. DOI: 10.1029/ 2020JA028203.

Blagoveshchenskaya N.F., Borisova T.D., Kalishin A.S., Egorov I.M., Zagorskiy G.A. Disturbances of electron density in the high latitude upper (F-region) ionosphere induced by X-mode HF pump waves from EISCAT UHF radar observations. *Arctic and Antarctic Research*. 2022, vol. 68, no. 3, pp. 248–257.
DOI: 10.30758/0555-2648-2022-68-3-248-257.

Borisova T.D., Blagoveshchenskaya N.F., Kalishin A.S. Features of artificial ionosphere turbulence induced by the O- and X-mode HF heating near the F2-layer critical frequency. *Sol.-Terr. Phys*. 2023, vol. 9, no. 1, pp. 21–30. DOI: 10.12737/stp-91202303.

Brunelli B.E., Namgaladze A.A. *Fizika ionosfery* [Physics of the ionosphere]. Moscow, Nauka Publ., 1988, 528 p. (In Russian).

Danilov A.D., Vlasov M.N. *Fotokhimiya ionizovannykh i vozbuzhdennykh chastits v nizhnei ionosfere* [Photochemistry of ionized and excited particles in the lower ionosphere]. Leningrad, Gidrometeoizdat, 1973, 190 p. (In Russian).

Frolov V.L. Spatial structure of plasma density perturbations, induced in the ionosphere modified by powerful HF radio waves: Review of experimental results. *Sol.-Terr. Phys.* 2015, vol. 1, no. 2, pp. 22–48. DOI: 10.12737/10383.

Frolov V.L. *Iskusstvennaya turbulentnost' sredneshirotnoi ionosfery* [Artificial turbulence of the mid-latitude ionosphere]. Nizhny Novgorod, Nizhny Novgorod University Publ., 2017, 468 p. (In Russian).

Frolov V.L., Bakhmet'eva N.V., Belikovich V.V., Vertogradov G.G., Vertogradov V.G., Komrakov G.P., Kotik D.S., et al. Modification of the Earth's ionosphere by high-power high-frequency radio waves. *Physics-Uspekhi.* 2007, vol. 50, iss. 3, pp. 315–324.
DOI: 10.1070/PU2007v050n03ABEH006282.

Frolov V.L., Bolotin I.A., Komrakov G.P., Pershin A.V., Vertogradov G.G., Vertogradov V.G., Vertogradov E.G., et al. Generation of artificial ionospheric irregularities in the Earth's midlatitude ionosphere affected by high-power high-frequency X-mode radio waves. *Radiophysics and Quantum Electronic.* 2014, vol. 57, no. 6, pp. 437–463. DOI: 10.1007/s11141-014-9523-8.

Gershman B.N., Ignatiev Yu.A. Theory of formation of sporadic E layer and irregularities arising in it. *Ionosfernye issledovaniya* [Ionospheric Research]. 1997, no. 50, pp. 7–28. (In Russian).

Ginzburg V.L. *Rasprostranenie elektromagnitnykh voln v plazme* [*Propagation of electromagnetic waves in plasma*]. Moscow, Nauka Publ., 1967, 683 p. (In Russian).

Ginzburg V.L., Gurevich A.V. Nonlinear phenomena in plasma. *Physics–Uspekhi.* 1960, vol. 3, iss. 1, pp. 115–146. DOI: 10.1070/PU1960v003n01ABEH003261.

Grach S.M., Sergeev E.N., Mishin E.V., Shindin A.V. Dynamic properties of ionospheric plasma turbulence driven by high-power high-frequency radiowaves. *Physics-Uspekhi.* 2016, vol. 59, no. 11, pp. 1091–1128. DOI: 10.3367/UFNe.2016.07.037868.

Gurevich A.V. Modern problems of ionospheric modification. *Radiophysics and Quantum Electronic.* 1999, vol. 42, no. 7, pp. 599–606. DOI: 10.1007/BF02677558.

Gurevich A.V. Nonlinear effects in the ionosphere. *Physics-Uspekhi.* 2007, vol. 50, pp. 1091–1121. DOI: 10.1070/ pu2007v050n11abeh006212.

Gurevich A.V., Shvartsburg A.B. *Nelineinaya teoriya rasprostraneniya radiovoln v ionosfere* [Nonlinear theory of radio wave propagation in the ionosphere]. Moscow, Nauka Publ., 1973, 272 p. (In Russian).

Gurevich A.V., Zybin K.P., Carlson H.C., Pedersen T. Magnetic zenith effect in ionospheric modifications. *Phys. Lett.* A. 2002, vol. 305, no. 5, pp. 264–274. DOI: 10.1016/S0375-9601(02)01450-0.

Ignatiev Yu.A. Influence of heating of the ionosphere by high-power radio emission on the sporadic E layer. *Radiophysics and Quantum Electronic.* 1975, vol. 18, no. 9, pp. 1010–1013. DOI: 10.1007/BF01038198.

Mityakov N.A., Grach S.M., Mityakov S.N. Disturbance of the ionosphere by powerful radio waves. *Itogi nauki i tekkhniki. Seriya "Geomagnetizm i vysokie sloi atmosfery"* [Results of Science and Technology. Series "Geomagnetism and High Atmosphere Layers"]. Moscow, Russian Institute for Scientific and Technical Information RAS, 1989, vol. 9, 138 p. (In Russian).

Kalishin A.S., Blagoveshchenskaya N.F., Borisova T.D., Yeoman T.K. Ion gyro-harmonic structures in stimulated emission excited by X-mode high power HF radio waves at EISCAT. *J. Geophys. Res.: Space Phys.* 2021, vol. 126, no. 8, e2020JA028989. DOI: 10.1029/2020JA028989.

Kelley M. C. *The Earth's Ionosphere: Plasma Physics and Electrodynamics*. Academic Press is an imprint of Elsevier, 2009, 556 p.

Kuo S. Linear and nonlinear plasma processes in ionospheric HF heating. *Plasma.* 2021, vol. 4, no. 1, pp. 108–144. DOI: 10.3390/plasma4010008.

Leyser T.B. Stimulated electromagnetic emissions by high-frequency electromagnetic pumping of the ionospheric plasma. *Space Sci. Rev.* 2001, vol. 98, no. 3-4, pp. 223–328. DOI: 10.1023/A:1013875603938.

Pedersen T.R., McCarrick M., Selcher E., Selcher C., Sentman D., Carlson H., Gurevich A. Magnetic zenith enhancement of HF radio-induced airglow production at HAARP. *Geophys. Res. Lett.* 2003, vol. 30, no. 4, 1169. DOI: 10.1029/2002GL016096.

Rietveld M.T., Kohl H., Kopka H., Stubbe P. Introduction to ionospheric heating at Tromso. I. Experimental overview. *J. Atmos. Terr. Phys.* 1993, vol. 55, no. 4/5, pp. 577–599. DOI: 10.1016/0021-9169(93)90007-L.

Rietveld M.T., Senior A., Markkanen J., Westman A. New capabilities of the upgraded EISCAT high-power HF facility. *Radio Sci.* 2016, vol. 51, no. 9, pp. 1533–1546. DOI: 10.1002/ 2016RS006093.

Streltsov A.V., Berthelier J.-J., Chernyshov A.A., Frolov V.L., Honary F., Kosch M.J., McCoy R.P., et al. Past, present and future of active radio frequency experiments in space. *Space Sci. Rev.* 2018, vol. 214, 118. DOI: 10.1007/s11214-018-0549-7.

Stubbe P., Hagfors T. The Earth's ionosphere: A wall-less plasma laboratory. *Surveys in Geophysics.* 1997, vol. 18, no. 1, pp. 57–127. DOI: 10.1023/A:1006583101811.

Vas'kov V.V., Gurevich A.V. Parametric excitation of langmuir oscillations in the ionosphere in a field of powerful radio waves. *Radiophysics and Quantum Electronic.* 1973, vol. 16, no. 2, pp. 138–145. DOI: 10.1007/BF01033319.

Vas'kov V.V., Gurevich A.V. Nonlinear resonant instability of a plasma in the field of an ordinary electromagnetic wave. *JETP.* 1975a, vol. 42, No. 1, pp. 91-97.

Vas'kov V.V., Gurevich A.V. Plasma stratification in the ionospheric region of strong radio-wave reflection. *Radiophysics and Quantum Electronic.* 1975b, vol. 18, no. 9, pp. 929–938. DOI: 10.1007/BF01038187.

Vas'kov V.V., Gurevich A.V. Self-focusing and resonance instabilities in the F-region of the ionosphere. *Teplovye nelineinye yavleniya v plazme* [Thermal nonlinear phenomena in plasma]. Gorky, IAP USSR Academy of Sciences, 1979, pp. 81–138. (In Russian).

Vas'kov V.V., Ryabova N.A. Excitation of short-wave oscillations in the ionospheric plasma by the field of a high-power radio wave with extraordinary polarization due to induced scattering by ions. *Radiophysics and Quantum Electronic.* 1997, vol. 40, no. 5, pp. 357–370. DOI: 10.1007/BF 02676200.

Utlaut W.F., Cohen R. Modifying the ionosphere with intense radio waves. *Science.* 1971, vol. 245, pp. 245–254. DOI: 10.1126/science.174.4006.245.

How to cite this article
Bakhmetieva N.V., Grigoriev G.I., Zhemyakov I.N., Kalinina E.E., Lisov A.A. Ionosphere response to the impact of an extraordinary radio wave when located at a frequency close to the heating frequency. *Sol.-Terr. Phys.* 2025, vol. 11, No. 3, pp. 80–90. DOI: 10.12737/stp-113202510.

METEOROLOGICAL RESPONSE TO CHANGES
IN IONOSPHERIC ELECTRIC POTENTIAL CAUSED BY DISTURBED SOLAR WIND

A.A. Karakhanyan
Institute of Solar-Terrestrial Physics SB RAS,
Irkutsk, Russia, asha@iszf.irk.ru

S.I. Molodykh
Institute of Solar-Terrestrial Physics SB RAS,
Irkutsk, Russia, sim@iszf.irk.ru

Abstract. The ionospheric electric potential (EP) is utilized as a characteristic of the solar forcing to determine the tropospheric response during strong disturbances. We compare EP calculations carried out using the 2001 and 2005 versions of the Weimer model. Differences in the spatial distribution of EP during geomagnetic superstorms have been revealed for the models considered. The behavior of EP anomalies and contrast averaged over high latitudes is shown. The EP contrast is the difference between EP anomalies averaged over regions of the same sign. It has been found that changes in EP anomalies differ in different versions of the model, whereas EP contrast variations, calculated by both versions, behave synchronously during disturbances. Correlation analysis of variations in the averaged EP contrast with variations in the *PC* geomagnetic index has shown that both can be used as indicators of solar activity to study individual geomagnetic superstorms. An increase in the EP contrast is accompanied by an increase in the contrast of the meteorological parameters, in particular in the contrast of high clouds during disturbances.

Keywords: ionospheric electric potential, geomagnetic superstorm, geomagnetic index, outgoing longwave radiation, cloud, water vapor, climate.

INTRODUCTION

The second wave of climate warming over the instrumental observation period, which began in the 1970s and intensified in the 1990s, is currently manifested as a sharp increase in the number of dangerous phenomena on the planet [Mokhov, 2023; https://www.ipcc.ch/report/ar6/syr/]. One of the possible causes of the climate changes is the effect of solar activity on Earth's atmosphere. The absence of a direct mechanism of the effect of solar activity on the lower atmosphere led to the search for an indirect mechanism of the influence of solar processes on the incoming radiation budget. Sources of solar influence include short-wave and UV radiation and corpuscular fluxes (GCRs, solar proton precipitation, high-energy particles). Their effects change the state of the ozone layer and the global electrical circuit, as well as strato-tropospheric circulation and cloud microphysics [Mironova et al., 2015; Krivolutsky et al., 2017; Harrison, Lockwood, 2020; Veretenenko et al., 2023a]. The physical model developed at ISTP SB RAS describes the electromagnetic interaction between the components of the magnetosphere—ionosphere—troposphere system. In contrast to the Tinsley model [Tinsley, 2008], in this model a change in the optical properties of water vapor in the IR range, namely, a change in the absorption of radiation by water dimers in the water vapor lines and continuum, results in an increase in the greenhouse effect, which causes dynamic changes in the troposphere. Since water vapor is unevenly distributed in space, an inhomogeneous tropospheric response is observed, in particular as formation or redistribution of clouds in height, which re-

duces the outgoing longwave radiation (OLR), thereby changing the radiation budget of the troposphere [Molodykh et al., 2020].

Let us take a closer look at the description of IR radiation absorption by water vapor. The infrared spectrum of water vapor absorption is known to consist of separate spectral lines and atmospheric windows located between them. In these windows, the absorption is weakly selective, or continuous, and the absorption spectrum is a water vapor continuum. Absorption by water dimers (complexes of two molecules) is the dominant factor in the absorption of self-continuum, i.e. water vapor absorption in a clear atmosphere.

Since the discovery of continuous absorption of radiation by water vapor, a large number of studies have been conducted, mainly in the atmospheric windows of near-IR and visible ranges. It has been experimentally established that the continuous absorption in the 8–12 µm atmospheric window is proportional to the square of the partial pressure of water vapor and decreases exponentially with increasing temperature [Ptashnik, 2015].

The features of the continuum make it possible to distinguish it spectrally against the background of a stronger intensity of water absorption lines, as a result the restoration of the continuum in atmospheric microwindows between water vapor absorption bands worked out. The mechanism based on the absorption of radiation by water dimers well explains the main temperature and spectral dependences of the water vapor continuum in the absorption bands. Properties of water dimers (dissociation energy and lifetime) allow them to be classified as stable (bound), or s-dimers, and meta-

stable (quasibound), or m-dimers, having different spectral characteristics. Absorption of stable or metastable dimers prevails in the continuum of water absorption, depending on thermodynamic conditions: s-dimers are common at lower temperatures; and m-dimers, at higher temperatures. The transition temperature in one direction or another depends on the intermolecular potential and varies for different molecular pairs, for example, for water dimers it is close to room temperature. Accordingly, the proportion of stable and metastable dimers in water vapor is approximately the same for atmospheric conditions. Model calculations have shown that the semi-empirical model of water dimer absorption better reproduces the experimental in-band self-continuum in the near IR range. Due to its spectral length (the atmospheric window in the mid-IR range and the contribution of spectral sections of water absorption lines), continuous absorption of water vapor can lead to a decrease in OLR, thereby affecting the radiation budget of the climate system [Simonova et al., 2022]. Based on the above ideas, in this paper we analyze the relationship of variations in the electric potential (EP) of the ionosphere with meteorological parameters (OLR, radiation absorption by water vapor in the 8–12 µm atmospheric window, upper cloudiness) for disturbed conditions in interplanetary space.

DATA AND ANALYSIS METHOD

The observed climatic changes, especially at high latitudes, require a more detailed study of the influence of physical processes occurring in near-Earth space on the lower atmosphere. This is necessary to parameterize them in order to include them in numerical climate models. We have previously used the *PC* geomagnetic activity index, which describes geomagnetic disturbances in the polar cap [Troshichev et al., 1988; https://pcindex.org /], as a solar activity proxy to study solar-tropospheric relations. This geomagnetic index reflects the expected physical processes, yet their parameterization results in the following disadvantages: 1) the integral characteristic of solar activity at the boundary of the magnetosphere; 2) the need to include a model of the magnetosphere; 3) the integral characteristic of solar activity in the ionosphere. These disadvantages complicate the use of the *PC* index due to the irregularity in the tropospheric response to solar influence. In this regard, we have taken EP as the optimal characteristic of solar influence on the troposphere. This heliogeophysical parameter describes the expected physical processes, and applying the Weimer model to its calculation allows us to parameterize processes in the magnetosphere and to obtain a spatial distribution of EP in the ionosphere.

A few words about the Weimer model, which we use to calculate EP. We have employed the 2001 version in our research before; in this work, calculations are performed with the latest version of the model, i.e. the 2005 version [Weimer, 2001, 2005]. Let us focus on the main modifications made to the model to improve it:

1. More accurate field values and more precise location of the low-latitude boundary of the convection electric field.

2. Spherical harmonic functions are used only within a small region at the pole. At lower latitudes, potentials are constructed from several functions of the Fourier series of longitude with discrete latitude steps, i.e. the calculation is made in a circle with a radius that varies depending on interplanetary magnetic field (IMF) and solar wind parameters with a constant shift of 4.2 °.

3. Nonlinear effects of saturation of the relationship between the solar wind and the magnetosphere are better reproduced for normal IMF conditions, but it is necessary to control the results of applying the model to cases with strong IMF.

Figure 1 illustrates the spatial distribution of EP calculated for the events on November 20, 2003 (left) and July 15, 2000 (right). As a quiet period, we have taken 2009. The top panel presents calculations with the 2001 model; the bottom panel, with the 2005 model.

The spatial distribution of EP for the quiet period according to the 2005 model differs from that obtained by the 2001 model by a slight increase in positive and negative potentials. Significant differences in the EP structure are observed during disturbance maximum: in the 2005 model, there is an increase in both the region and the magnitude of the negative potential, whereas in the 2001 model, the positive potential increases more considerably. The detected differences are related to the shift in the convection zone to the nightside due to improvements made to the 2005 model.

For further analysis, the spatial contrast of EP was utilized as a characteristic of solar influence. This parameter was obtained as follows. In the first step, the 2005 Weimer model [https://zenodo.org/records/2530324] was employed to calculate the spatial distribution of EP anomalies whose structure consists of two regions (of negative and positive sign). The EP anomalies were calculated from the formula

$$EP_i = EP_i - \langle EP \rangle, \tag{1}$$

where i is the hour number; $\langle EP \rangle$ is the average over seven preceding days.

In the second step, the spatial distribution of the EP contrast was constructed according to the formula

$$\Delta EP_i = \langle EP_i^+ \rangle - \langle EP_i^- \rangle, \tag{2}$$

where i is the hour number; $\langle EP_i \rangle$ is the average over the region of one sign.

Changes in the EP anomalies and contrast averaged over latitudes above 60° N were analyzed using the November 20, 2003 and April 23, 2023 events (see Table), triggered by a classical coronal mass ejection, as an example. The selected magnetic superstorms are similar in conditions of development of interplanetary disturbances, which caused the storms [Grechnev et al., 2014; Abunina et al., 2024]. The choice of the magnetic storms in different seasons also allowed us to additionally take into account seasonal variations of geomagnetic activity with a maximum in spring and autumn, which can manifest themselves in variations of meteorological parameters during disturbances [Karakhanyan, Molodykh, 2025].
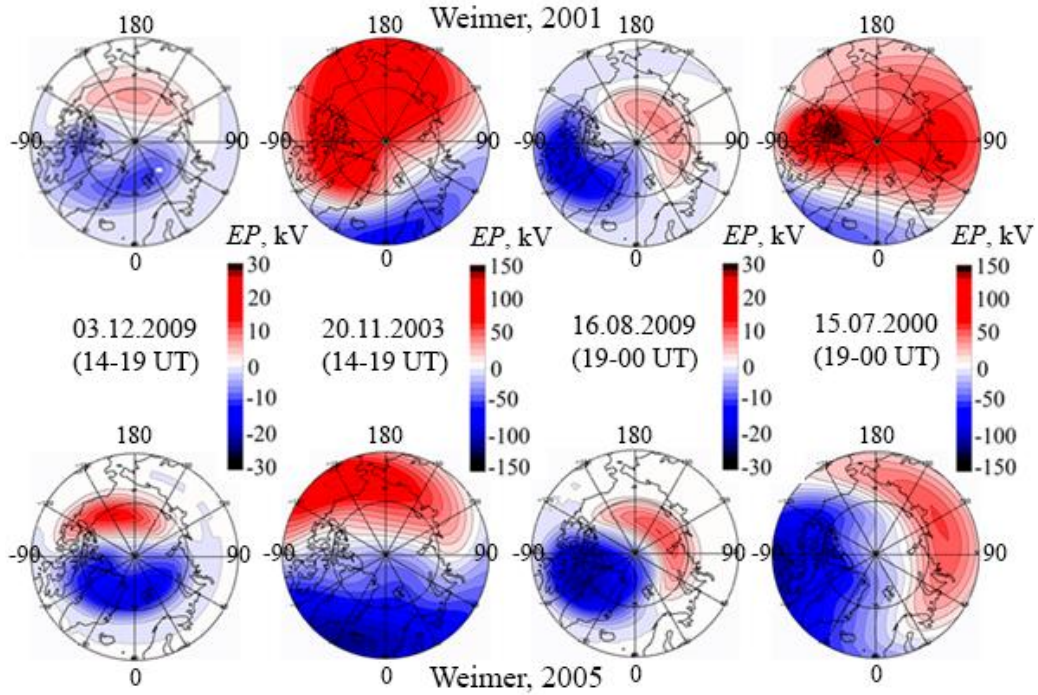
Figure 1. Spatial distributions of EP calculated using two Weimer model versions for quiet conditions in 2009 and powerful geomagnetic storms on November 20, 2003 and July 15, 2000

Interplanetary medium parameters during magnetic superstorms

Event date	V_{max}, km/s	n, cm^{-3}	$B_{z_{max}}$, nT	B_y, nT	AL, nT	Date and value of Dst, nT
Nov. 20–21, 2003	703	7.6	−50.9	22.5	−1790	Nov. 20, 2003, $Dst=-422$ nT
Apr. 23–24, 2023	711[*]	10.2[*]	−32.4[*]	−2.5[*]	−1015[*]	Apr. 24, 2023, $Dst=-213$[*] nT

*Preliminary data [https://omniweb.gsfc.nasa.gov/html/ow_data.html; https://wdc.kugi .kyoto-u.ac.jp/wdc/Sec3.html]

Ionospheric EP was calculated by the Weimer model from hourly data on the solar wind and IMF parameters obtained from the OMNI database [https://omniweb.gsfc.nasa.gov/html/ow_data.html].

The method of calculating the EP contrast was also employed to compute the contrast of meteorological parameters in order to conduct a comparative analysis of EP with meteorological parameters during disturbances. We used hourly meteorological values in a 1.0°×1.0° grid from the dataset [Wielicki et al., 1996; https://ceres-tool.larc.nasa.gov/ord-tool/jsp/SYN1degEd 41Selection.jsp/]. Note that in the troposphere there is a natural synoptic period (NSP) — a period during which cyclones/anticyclones continue to move and the location of their centers in a certain region of Earth or in the entire hemisphere (NSP ~7 days) remains unchanged. To minimize the influence of synoptic processes, weather parameter anomalies were calculated relative to the average over seven days before the event. OLR is represented by the broadband heat flux observed by CERES at the upper boundary of the troposphere (h~20 km); radiation absorption by water vapor in the 8–12 μm atmospheric window, by the radiated heat flux (h~20 km) of the CERES infrared atmospheric

window (8–12 μm). The upper cloudiness is characterized by the number of high-level clouds (from 300 hPa to the tropopause) as a percentage of sky cover.

RESULTS

Spatial distributions of EP during disturbances (see Figure 1), obtained by the 2001 and 2005 versions of the Weimer model, differ significantly.

Let us analyze the dynamics of EP variations averaged over latitudes above 60° N during November 20, 2003 and April 23, 2023 geomagnetic superstorms. Figure 2 illustrates variations in EP anomalies (top panels) and EP contrast (bottom panels), calculated by the two Weimer model versions. Comparative analysis has shown that during the magnetic superstorms the contribution of negative EP values to the overall variability in EP anomalies is greater in the 2005 model than in the 2001 model. This difference is related to the above modifications made to the 2005 model. Variations in EP contrast during disturbances, calculated by the 2001 model, correlate well with those obtained by the 2005 model. The EP contrast behavior in the two Weimer model versions agrees better than the dynamics of EP anomalies for the high-latitude region.
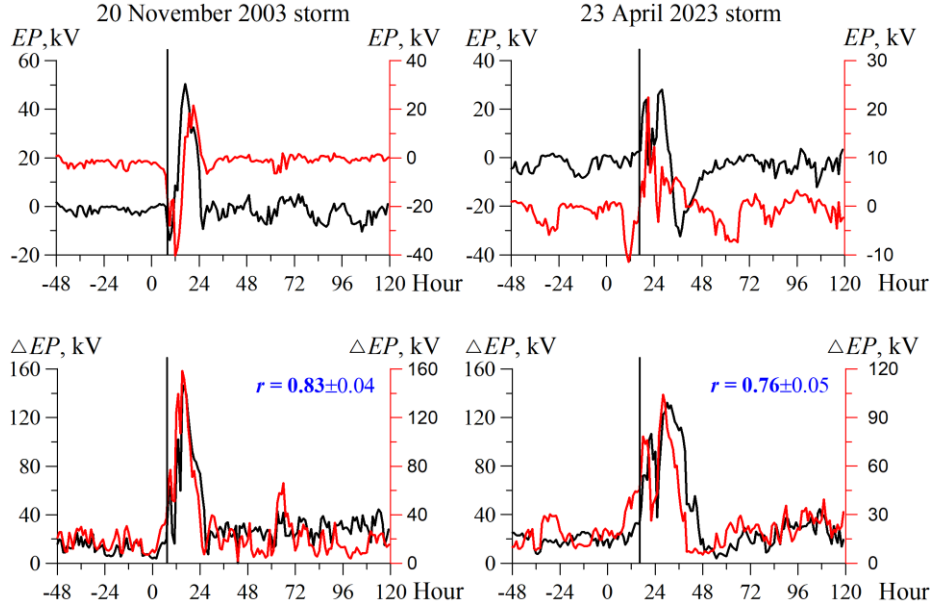
Figure 2. Variations in EP anomalies (top) and EP contrast (bottom), averaged over latitudes above 60° N, during magnetic superstorms: the 2001 Weimer model (black line), the 2005 Weimer model (red line); onset of the geomagnetic storm (vertical line); zero on the X-axis is 00 UT of the day when the geomagnetic storm began
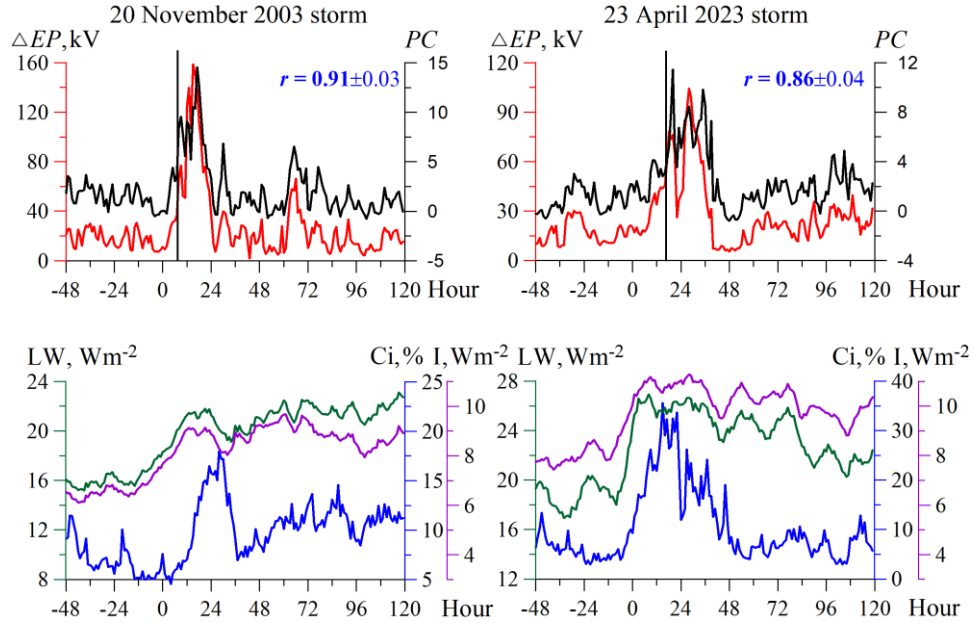

Figure 3. Variations in EP contrast (top panels, red line) and contrast of meteorological parameters (bottom panels) averaged over latitudes above 60° N: OLR (green line); radiation absorption by water vapor in the 8–12 μm atmospheric window (*I*, purple line); upper cloudiness (*Ci*, blue line), as well as variations in the *PC* geomagnetic index (top panels, black line) during magnetic superstorms. The vertical line indicates the onset of the geomagnetic storm; zero on the X-axis is 00 UT of the day when the geomagnetic storm began

Let us examine the linear relationship of variations in the EP contrast, averaged over latitudes above 60° N, with variations in the *PC* geomagnetic index during the November 20, 2003 and April 23, 2023 magnetic superstorms. The correlation is 0.71±0.5 between variations in the EP contrast, calculated by the 2001 Weimer model, and variations in the *PC* index for the cases considered.

The EP contrast variations calculated by the 2005 model correlate better with the *PC* index variations for the geomagnetic storms under study (Figure 3, top panels). The high correlation coefficient between the pa-

rameters allows us to say that the *PC* index can be used as an indicator of solar activity during isolated magnetic superstorms.

To determine the tropospheric response to changes in the potential during the magnetic storms, we use the EP contrast calculated by the 2005 Weimer model (see Figure 3, at the top). During the November 20, 2003 magnetic superstorm, an increase in the EP contrast was accompanied by an increase in the contrast of meteorological parameters, especially in the contrast of upper cloudiness. The maximum contrast of meteorological

parameters was observed within the first 12 hrs relative to the maximum contrast of EP. For the April 23, 2023 geomagnetic storm, the noted features in the change in the parameters considered are less pronounced, possibly due to the influence of substorm activity observed before the onset of the magnetic storm and resulting from amplification of field-aligned currents caused by the electric field of magnetospheric convection, which occurs when the solar wind and IMF interact with the magnetosphere.

Variations in upper cloudiness anomalies have a unidirectional trend with the dynamics of EP anomalies at high latitudes during geomagnetic superstorms (Figure 4). The features characteristic of the dynamics of the contrast of the parameters under study persist in the behavior of their anomalies. However, the amplitude of the response of positive upper cloudiness anomalies to a change in positive EP is by an order of magnitude higher than the amplitude of the response of negative upper cloudiness anomalies to a change in negative EP. Look at the maps of EP anomalies and the spatial distribution of upper cloudiness anomalies (Figure 5) during the April 23, 2023 magnetic storm. Under quiet conditions at latitudes above 60° N, upper cloudiness anomalies are uniformly distributed and amount to few percent. The greatest increase in upper cloudiness is observed in the region of increased positive potential, which has a non-linear effect on properties of water vapor, in this case coming from midlatitudes with cyclones that occur near the eastern coast of Eurasia and, moving to the north-east, reach their maximum near the Aleutian Islands.

DISCUSSION

Our planet as an open system is affected by changes in the solar wind due to active processes on the Sun. Rapid climate changes on Earth sustain the discussion about the magnitude and nature of solar influence on the lower atmosphere. The spatial inhomogeneity of the tropospheric response to solar influence may show up to a greater extent in the regional climate variability due to changes in the optical properties of water vapor in the troposphere during geomagnetic disturbances [Karakhanyan, Molodykh, 2025]. Local climate changes (high latitudes, inland regions) under the influence of solar processes can be examined in detail on the basis of data obtained from the ISTP SB RAS instrumentation, in particular from the Unique Research Facility "Optical Instruments" [https://iszf.irk.ru/usu-optical-instruments/].

In our study, we have used the contrast in EP variations, which is a proxy of solar activity. This enabled us to minimize the differences between its calculations for different Weimer model versions (see Figure 2). A high correlation is shown between variations in the EP contrast averaged over the high-latitude region and variations in the *PC* geomagnetic index (see Figure 3). This finding allows us to recommend both characteristics as an indicator of solar activity when studying magnetic superstorms. The spectrum of meteorological parameters consists of high-frequency (daily, seasonal, annual, and 2–5-year variations) and low-frequency components. The latter contains variations close to heliogeophysical periods, in particular a ~22-year variation similar to the Hale magnetic cycle on the Sun was found in the variability in trajectories of extratropical cyclones in the North Atlantic [Veretenenko et al., 2023b]. Since the solar signal present in the meteorological parameters has an amplitude lower than the amplitude of their daily and seasonal variations, we study variations not in the value itself, but in the anomalies or deviations of the meteorological parameters from their mean during disturbance. By the example of geomagnetic superstorms of
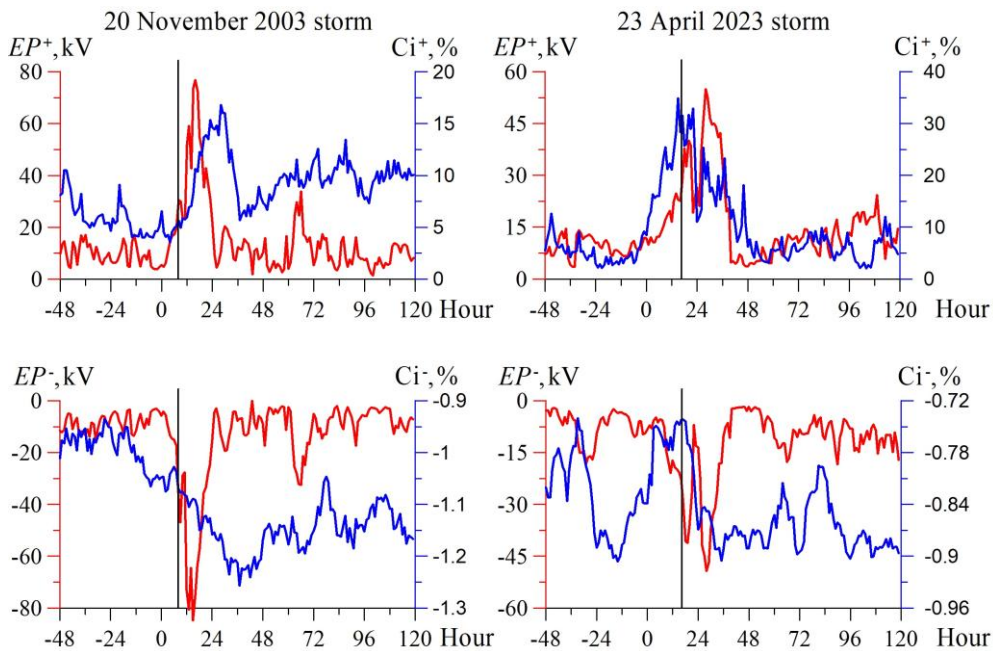

Figure 4. Variations in positive (top) and negative (bottom) EP anomalies (red curves) and upper cloudiness anomalies (blue curves), averaged over latitudes above 60° N, during magnetic superstorms. The vertical line indicates the onset of the geomagnetic storm; zero on the X-axis is 00 UT of the day when the geomagnetic storm began
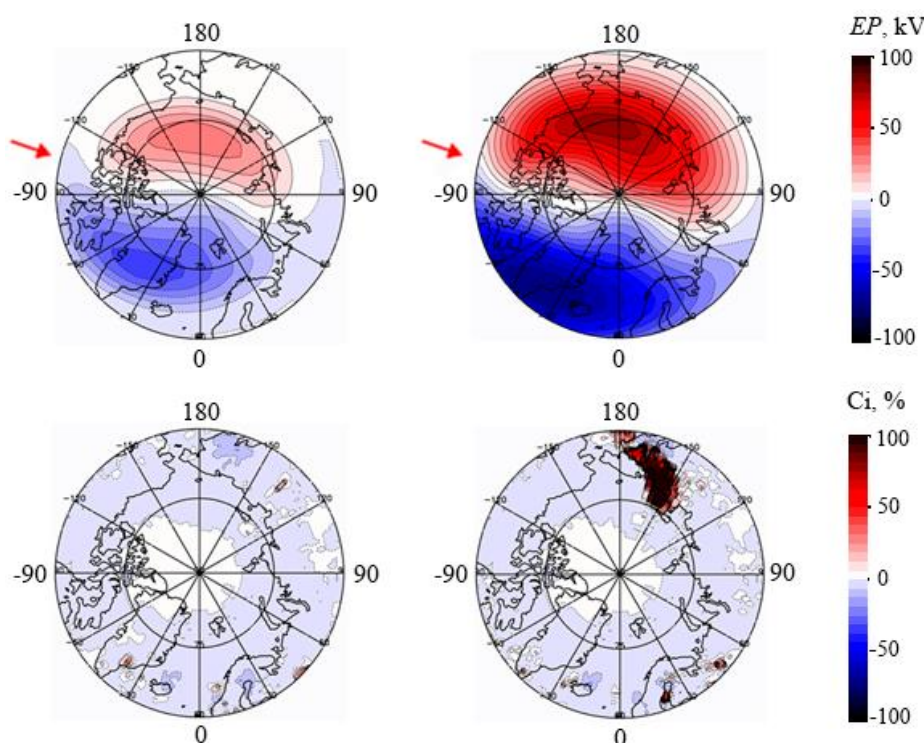
Figure 5. Spatial distributions of EP anomalies (top) and upper cloudiness (bottom) during the quiet period (left) and during their maximum (right) for an average of 3 hrs from 18 UT to 20 UT for latitudes above 60° N during the April 23, 2023 geomagnetic superstorm. The midday meridian is indicated by arrows

solar cycles 23 and 25, which are moderate and the second components of the 22-year magnetic activity cycle [Ishkov, 2010, 2024], we have shown that during individual severe disturbances an increase in the EP contrast is accompanied by an increase in the contrast of meteorological parameters, especially in the contrast of upper cloudiness (see Figure 3). For meteorological parameters, the contrast was utilized as an integral characteristic to illustrate the amplitude of variations in the meteorological response to solar influence due to the inhomogeneous structure of the tropospheric response in space. The results of the study have been obtained using the model of the mechanism of indirect influence of solar processes on the radiation budget of the climate system, developed at ISTP SB RAS. They will help to parameterize physical processes in the troposphere in accordance with the proposed scenario and hence to include solar activity, along with the solar constant, in climate models.

CONCLUSIONS

Analysis of the relationship of EP variations with variations in meteorological parameters during magnetic superstorms allowed us to obtain the following results.

Spatial distributions of EP obtained using the 2001 and 2005 Weimer model versions differ most considerably during the maximum of the disturbance.

Variations in EP anomalies averaged over latitudes above 60° N differ significantly in the Weimer model versions considered. However, variations in the average EP contrast calculated by the 2001 and 2005 versions occur synchronously during severe disturbances.

Correlation analysis of variations in the average EP contrast with variations in the *PC* geomagnetic index has shown that both characteristics can be used as a proxy of solar activity to study isolated severe disturbances.

During the disturbances, an increase in the EP contrast is accompanied by an increase in the contrast of meteorological parameters, especially in the contrast of upper cloudiness.

REFERENCES

Abunina M.A., Shlyk N.S., Belov S.M., et al. On the most interesting events in the solar wind and cosmic rays in 2023–2024. *Mezhdunarodnaya Baikal'skaya molodezhnaya nauchnaya shkola po fundamental'noi fizike. Trudy XVIII Konferentsii molodykh uchenykh «Vzaimodeistvie polei i izlucheniya s veshchestvom»* [The Baikal Young Scientists' International School on Fundamental Physics. Proc. XVIII Young Scientists' Conference "Interaction of Fields and Radiation with Matter"]. Irkutsk, 2024, pp. 5–7. (In Russian).

Grechnev V.V., Uralov A.M., Chertok I.M., et al. A challenging solar eruptive event of 18 November 2003 and the causes of the 20 November geomagnetic superstorm. IV. Unusual magnetic cloud and overall scenario. *Solar Phys.* 2014, vol. 289, iss. 12, pp. 4653–4673. DOI: 10.1007/s11207-014-0596-5.

Harrison R.G., Lockwood M. Rapid indirect solar responses observed in the lower atmosphere. *Proc. Roy. Soc. A.* 2020, vol. 476, iss. 2241, 20200164. DOI: 10.1098/rspa.2020.0164.

Ishkov V.N. Properties and surprises of solar activity XXIII cycle. *Sun and Geosphere*. 2010, vol. 5, iss. 2, pp. 43–46.

Ishkov V.N. Current solar cycle 25 on the eve of the maximum phase. *Geomagnetism and Aeronomy*. 2024, vol. 64, iss. 7, pp. 1167–1175. DOI: 10.1134/S0016793224700257.

Karakhanyan A.A., Molodykh S.I. A decline of linear relation between outgoing longwave radiation and temperature during geomagnetic disturbances. *JASTP*. 2025, vol. 270, iss. 5, 106503. DOI: 10.1016/j.jastp.2025.106503.

Krivolutsky A.A., Vyushkova T.Y., Mironova I.A. Changes in the chemical composition of the atmosphere in the polar regions of the Earth after solar proton flares (3D modeling). *Geomagnetism and Aeronomy*. 2017, vol. 57, iss. 2, pp. 156–176.
DOI: 10.1134/ S0016793217020074.

Mironova I.A., Aplin K.L., Arnold F., et al. Energetic particle influence on the Earth's atmosphere. *Space Sci. Rev.* 2015, vol. 194, iss. 1-4, pp. 1–96.
DOI: 10.1007/s11214-015-0185-4.

Mokhov I.I. Russian climate research in 2019–2022. *Izvestiya RAN. Fizika atmosfery i okeana* [Izvestiya, Atmospheric and Oceanic Physics]. 2023, vol. 59, iss. 7, pp. 830–851. (In Russian).

Molodykh S.I., Zherebtsov G.A., Karakhanyan A.A. Estimation of solar activity impact on the outgoing infrared-radiation flux. *Geomagnetism and Aeronomy*. 2020, vol. 60, iss. 2, pp. 205–211. DOI: 10.1134/ S0016793220020103.

Ptashnik I.V. Water vapour continuum absorption: short prehistory and current status. *Optika atmosfery i okeana* [Atmospheric and Oceanic Optics]. 2015, vol. 28, iss. 5, pp. 443–459. (In Russian).

Simonova A.A., Ptashnik I.V., Elsey J., et al. Water vapour self-continuum in near-visible IR absorption bands: Measurements and semiempirical model of water dimer absorption. *J. Quantitative Spectroscopy and Radiative Transfer*. 2022, vol. 277, iss. 1, 107957. DOI: 10.1016/j.jqsrt.2021.107957.

Tinsley B.A. The global atmospheric electric circuit and its effects on cloud microphysics. *Rep. on Progress in Physics*. 2008, vol. 71, iss. 6, 066801.
DOI: 10.1088/0034-4885/71/6/066801.

Troshichev O.A., Andrezen V.G., Vennerstrom S., Friis-Christensen E. Magnetic activity in the polar cap – A new index. *Planet. Space Sci.* 1988, vol. 36, iss. 11, pp. 1095–1102. DOI: 10.1016/0032-0633(88)90063-3.

Veretenenko S.V., Dmitriev P.B., Dergachev V.A. Long-term effects of solar activity on cyclone tracks in the North Atlantic. *St. Petersburg State Polytechnical University J.: Physics and Mathematics*. 2023a, vol. 16, iss. 1.2, pp. 454–460. DOI: 10.18721/JPM.161.269.

Veretenenko S.V., Dmitriev P.B., Dergachev V.A. Long-term changes main trajectories of extratropical cyclones in the North Atlantic and their possible association with solar activity. *Geomagnetism and Aeronomy*. 2023b, vol. 63, iss. 7, pp. 953–965. DOI: 10.1134/s0016793223070265.

Weimer D.R. An improved model of ionospheric electric potentials including substorm perturbations and application to the Geospace Environment Modeling November 24, 1996, event. *J. Geophys. Res.: Space Phys.* 2001, vol. 106, iss. A1, pp. 407–416. DOI: 10.1029/2000JA000604.

Weimer D.R. Improved ionospheric electrodynamic models and application to calculating Joule heating rates. *J. Geophys. Res.* 2005, vol. 110, iss. A5, A05306.
DOI: 10.1029/2004 JA010884.

Wielicki B.A., Barkstrom B.R., Harrison E.F., et al. Clouds and the Earth's Radiant Energy System (CERES): An Earth observing system experiment. *Bull. American Meteorological Society*. 1996, vol. 77, iss. 5, pp. 853–868.
DOI:
10.1175/1520-0477(1996)077<0853:CATERE>2.0.CO;2.

URL: https://zenodo.org/records/2530324 (accessed April 4, 2025).

URL: https://omniweb.gsfc.nasa.gov/html/ow_data.html (accessed April 4, 2025).

URL: https://iszf.irk.ru/usu-optical-instruments/ (accessed April 4, 2025).

URL: https://ceres-tool.larc.nasa.gov/ord-tool/jsp/SYN1degEd41Selection.jsp (accessed April 4, 2025).

URL: https://www.ipcc.ch/report/ar6/syr/ (accessed April 4, 2025).

URL: https://wdc.kugi.kyoto-u.ac.jp/wdc/Sec3.html (accessed April 4, 2025).

URL: https://pcindex.org/ (accessed April 4, 2025).

How to cite this article
Karakhanyan A.A., Molodykh S.I. Meteorological response to changes in ionospheric electric potential caused by disturbed solar wind. *Sol.-Terr. Phys.* 2025, vol. 11, iss. 3, pp. 91–97.
DOI: 10.12737/stp-113202511.

CHINESE-RUSSIAN JOINT RESEARCH CENTER ON SPACE WEATHER: RESULTS AND PROSPECTS

A.V. Medvedev (iD)
Institute of Solar-Terrestrial Physics SB RAS,
Irkutsk, Russia, medvedev@iszf.irk.ru

G.A. Zherebtsov (iD)
Institute of Solar-Terrestrial Physics SB RAS,
Irkutsk, Russia, gaz@iszf.irk.ru

N.P. Perevalova (iD)
Institute of Solar-Terrestrial Physics SB RAS,
Irkutsk, Russia, pereval@iszf.irk.ru

Abstract. We present an overview of the history, the main scientific results and prospects of the Chinese-Russian Joint Research Center on Space Weather. The Chinese-Russian Joint Research Center was established by the Institute of Solar-Terrestrial Physics SB RAS (ISTP SB RAS) and National Space Science Center CAS (NSSC CAS) in 2000. The center deals with fundamental issues in modern solar-terrestrial physics, such as quantitative description of the processes in complex interconnected system Sun — interplanetary medium — magnetosphere — ionosphere — atmosphere, assessment of capabilities of predicting interactions within this system, development of effective models for forecasting the state of the atmosphere and near-Earth space. Over the 24-year period, the Joint Research Center has united more than 10 scientific institutes in Russia and China; about 60 scientific projects have been implemented, and more than 400 joint scientific articles have been pub-lished. Joint efforts of Russian and Chinese researchers allowed obtaining important results in study of physical processes in near-Earth space. The Chinese-Russian Joint Research Center has proven its usefulness and continues studying the Sun, solar-terrestrial relations, and near-Earth space.

The future work of the Joint Research Center will be closely linked to the implementation of major unique projects in China and Russia: the International Meridian Circle Program (IMCP) led by NSSC CAS, and the National Heliogeophysical Complex of the Russian Academy of Sciences (NHC RAS) led by ISTP SB RAS. We describe these projects in this paper.

Keywords: Chinese-Russian Joint Research Center, space weather, international cooperation, International Meridian Circle Program, National Heliogeophysical Complex of the Russian Academy of Sciences.

INTRODUCTION

In the new millennium, near-Earth space has become an area of intense practical activity. The rapid development of technosphere and its growing expansion to space lead to the fact that the processes occurring on the Sun and in near-Earth space (known as space weather) significantly affect space-borne and ground-based technological systems, such as spacecraft, television, communication, navigation, electric power grids, and pipelines. Space weather factors can also pose a threat to human health and life. It is therefore essential to have complete information about these processes, to be able to diagnose and predict space weather, and to assess the potential consequences. Thus, space weather monitoring and forecasting are major scientific challenges for the scientific community of the XXI century. To provide an adequate response to these major challenges, many countries have established special National Space Weather programs. These programs identify priorities in near-Earth space research: development of diagnostic tool networks, advancement of fundamental knowledge about processes in near-Earth space, development and improvement of empirical and theoretical models.

However, physical processes in all regions of near-Earth space are closely interrelated. The system Sun — interplanetary medium — magnetosphere — ionosphere — atmosphere should be studied as a whole. New tools and methods are required to solve this complex problem. International cooperation is also essential, as the processes under study are global in scale. The Chinese-Russian Joint Research Center on Space Weather is focused on solving these problems. The main research areas of the Joint Research Center include:

- solar activity related to solar disturbances;
- propagation of solar disturbances through the solar corona and interplanetary space;
- dynamic processes of various spatial and temporal scales associated with the near-Earth space disturbances;
- propagation of disturbances from high to middle and low latitudes of Earth's ionosphere and atmosphere;
- diagnostics of near-Earth space and forecasting techniques; interaction between near-Earth space and Earth's atmosphere;
- global space weather system and its response to external influences.

MILESTONES

The Chinese-Russian Joint Research Center on Space Weather was established by the Institute of Solar-Terrestrial Physics of Siberian Branch of the Russian Academy of Sciences (ISTP SB RAS) and the National

Space Science Center of the Chinese Academy of Sciences (NSSC CAS, until 2010 known as the Center for Space Science and Applied Research CAS, CSSAR CAS).

Agreement for Scientific Cooperation between the Russian Academy of Sciences and the Chinese Academy of Sciences signed on December 18, 1992 and Agreement for Scientific Cooperation between the Chinese Academy of Sciences and Siberian Branch of the Russian Academy of Sciences signed on October 13, 1999 served as the basis for creating the Joint Research Center. Within the framework of these agreements, Director of CSSAR CAS Professor Gu Yidong and Director of ISTP SB RAS Academician Geliy A. Zherebtsov signed the Agreement for Joint Studies on Solar-Terrestrial Physics and Its Applications in Beijing on November 2, 2000. In December 2000, the first joint workshop was held in Irkutsk. Representatives of CSSAR CAS and ISTP SB RAS took decision to establish the Joint Research Center on Space Weather, and signed its Charter. The first co-directors of the Joint Research Center were Academician Geliy A. Zherebtsov and Professor Wu Ji. Since 2018, co-director of the Joint Research Center from the Chinese side is the Director General of NSSC CAS Academician Wang Chi. In 2012–2017, co-director of the Joint Research Center from the Russian side was the Director of ISTP SB RAS, Corresponding Member of RAS Aleksandr P. Potekhin. Today, co-director of the Joint Research Center is the Director of ISTP SB RAS Corresponding Member of RAS Andrey V. Medvedev.

In accordance with the Charter of the Joint Research Center on Space Weather, workshops are held alternately in Russia and China on a regular basis. At workshops researchers present their scientific results and discuss the prospects for further joint research. The first workshop took place in Irkutsk in 2000. The 10th Anniversary Meeting was held in Beijing in 2010. In 2024, ISTP SB RAS hosted the 15th Anniversary Workshop in Irkutsk (Figure 1).

At the 15th Russian-Chinese Workshop, special attention was given to the International Meridian Circle Program (IMCP) that is led by NSSC CAS and aims to study atmospheric and near-Earth space phenomena and processes using ground-based scientific instruments located along the 120° E and 60° W meridians. China and Russia play a special role in this program since a significant part of the 120° E meridian passes through their territories. New opportunities for IMCP can be provided by the National Heliogeophysical Complex of the Russian Academy of Sciences (NHC RAS), which is being created by ISTP SB RAS. The development of cooperation within IMCP was discussed during the 15th Russian-Chinese Workshop. In the following sections, we address some of the issues related to this cooperation.

The Joint Research Center promotes expanding multilateral cooperation. Many Russian and Chinese institutions have joined our investigations: National Astronomical Observatories of China CAS (NAOC CAS), Institute of Geology and Geophysics CAS (IGG CAS), Peking University (PKU), Yunnan Astronomical Observatory CAS (YNAO CAS), China Research Institute of Radiowave Propagation (CRIRP), Shandong University (SDU), Yu.G. Shafer Institute of Cosmophysical Research and Aeronomy SB RAS (SICRA SB RAS), Space Research Institute RAS (IKI RAS), Pushkov Institute of Earth Magnetism, Ionosphere and Radio Wave Propagation RAS (IZMIRAN), Central Astronomical Observatory of RAS at Pulkovo (GAO RAS), Institute of Cosmophysical Research and Radio Wave Propagation FEB RAS (IKIR FEB RAS), Polar Geophysical Institute RAS (PGI RAS).

Over the 24-year period, approximately 60 scientific projects have been implemented, around 200 exchange visits took place, and more than 230 joint scientific reports have been presented at workshops and conferences. Additionally, over 400 joint scientific articles and two monographs have been published.

MAIN SCIENTIFIC RESULTS

Joint efforts of Russian and Chinese researchers allowed obtaining important results in study of physical processes in near-Earth space. The most interesting scientific results obtained during our cooperation are presented in this Section.

Figure 1. The 15th Russian-Chinese Workshop on Space Weather, Irkutsk, September 2024

First observations of a microwave zebra pattern (ISTP SB RAS, NAOC CAS)

In 2003, researchers from the Institute of Solar-Terrestrial Physics and the National Astronomical Observatories of China first detected a zebra pattern in the microwave range [Altyntsev et al., 2005a, 2005b]. Zebra patterns are intriguing fine spectral structures that look as a number of parallel bright and dark stripes in the dynamic spectra of the solar radio emission. To date, there is no definite conclusion about the formation mechanism of zebra patterns, with more than a dozen of different models proposed. Zebra patterns are generally observed in the metric and decimetric wavelength ranges. In the microwave range, the radio burst was first recorded simultaneously with the Siberian Solar Radio Telescope (at frequencies of 5.70, 5.72, and 5.76 GHz) and the spectropolarimeter of the Huairou Solar Observing Station (in the 5.2–7.6 GHz range). This combination has allowed us to determine not only spectral, but also spatial characteristics of the event. The radio burst consisted of three (possibly, four) parallel equidistant bright stripes with a synchronous temporal evolution. The frequency interval between the stripes was ~160 MHz. The emission had 100 % circular polarization corresponding to the extraordinary mode. The sources of different zebra stripes were found to coincide spatially. It was concluded that the most probable generation mechanism of the zebra pattern considered was nonlinear interaction between harmonics of plasma waves known as Bernstein modes. In this case, the magnetic field in the emission source, as determined by the frequency separation of the zebra stripes, was ~60 G.

Fine wave dynamics in umbral flash sources (ISTP SB RAS, YNAO CAS)

For the first time, information has been obtained on the dynamics of wave processes occurring in small angular solar magnetic structures associated with the Umbral Flashes (Us) [Sych and Wang, 2018]. Fast periodic disturbances related to wave activity in the sunspot umbra were observed over a three-hour period. These disturbances align with the continuous diffuse brightening of specific wave fronts described by Yuan et al. [2014]. Additionally, short-term emergences of small local sources, known as UFs, were identified. The observed umbral brightening can be categorized into two types. The first type consists of background UFs, which exhibit random brightening of separated parts of wave fronts during propagation. These UFs are constantly observed in the umbra and lack stable shapes and spatial localization. The second type consists of local UFs, which are associated with increased wave activity near the footpoints of magnetic loops. These sources demonstrate pronounced wave dynamics and do not change spatial position over time. Different spatial shapes were observed for the local UF sources. Point sources are located at the footpoints of large magnetic loops and display activity with rare low-power pulses. Extended sources are related to the footpoints of low magnetic loops with large inclinations, exhibiting series of recurrent UF pulses. The emergence of the main UF maximum coincides with the peak power of three-minute oscillation trains in separated loops. This wave dynamics follows previously described background UFs by a number of authors, but it is localized within magnetic loops. A correlation exists between UF emergence in the photosphere and increased power of three-minute wave trains in the corona. The observed UF parameters are primarily influenced by the wave cut-off frequency. Further research will focus on investigating the relationship between the shape of local UF sources and the inclination of magnetic loops near their footpoints.

The origin of the helicity hemispheric sign rule reversals in the mean-field solar-type dynamo (NAOC CAS, ISTP SB RAS, IZMIRAN)

Observations at Huairou Solar Observatory of proxies of magnetic felicity in the Sun over the past two solar cycles have revealed reversals of the helicity hemispheric sign rule (negative in the Northern Hemisphere and positive in the Southern one). The mean-field solar dynamo model was used to study changes in the sign of the magnetic helicity for the dynamo, which operate in the bulk of the solar convection zone. The reversal of the sign of the small-scale magnetic helicity was found to follow the dynamo wave propagating inside the convection zone. Thus, the spatial configuration of the magnetic helicity reversals reflects the processes that contribute to the generation and evolution of large-scale magnetic fields. On the surface, the patterns of the helicity rule reversals are determined by the magnetic helicity boundary conditions at the top of the convection zone. The obtained results suggest that the magnetic helicity of a large-scale axisymmetric field can be treated as an additional observational tracer for the solar dynamo and it probably can be used for the solar activity forecast [Pipin et al., 2013].

Improvement of full-disk measurements of solar longitudinal magnetic fields at the Huairou observatory (NAOC CAS, ISTP SB RAS)

Magnetograms of the full solar disk are a necessary element of space weather forecasting algorithms. The Solar Magnetism and Activity Telescope (SMAT) of the Huairou Solar Observatory is one of the few instruments in the world capable of receiving full-disk magnetograms. As a result of joint Russian-Chinese studies of the instrumental characteristics of SMAT, some problems were identified that impede high-precision measurements of weak background magnetic fields of the Sun. Nonetheless, methods to improve the quality of SMAT measurements were proposed, resulting in a significant increase in data reliability [Demidov et al., 2018]. These techniques will allow us to utilize SMART measurements to address a wide range of solar physics issues related to studies of global solar magnetism and space weather.

Saturation of the magnetosphere and the polar cap during superstorms (ISTP SB RAS, NSSC CAS)

Using data from more than 110 ground-based geomagnetic observatories and the magnetogram inversion

method developed at ISTP SB RAS, new patterns of the magnetosphere saturation process have been obtained: stopping the growth of the electromagnetic energy flux through the magnetosphere boundary and the polar cap from the solar wind (SW) with its unusual intensification during superstorms [Mishin et al., 2016]. Saturation was shown to be caused not only by an increase in the southern component of the interplanetary magnetic field, but also by an increase in the solar wind dynamic pressure (Figure 2, *a*). Saturation was explained by the magnetosphere finite compressibility (during the increasing SW, the compression of the magnetopause — a decrease in the radius of its subsolar point — stops quickly due to the geomagnetic field pressure increasing earthward (Figure 2, *b*)), which also causes a stop in the growth of the polar cap and the flow of energy into the ionosphere through it. This result was confirmed by numerical simulation using a global MHD model and the Piecewise Parabolic Method with a Lagrangian Remap (PPMLR) [Hu et al., 2009; Wang et al., 2014] (Figure 2, *a*, *c*).

Figure 2. Saturation during an increase in the SW dynamic pressure P_d in the November 20, 2003 storm: electromagnetic energy flux Q_{el} (*a*), subsolar magnetopause radius L_{mp} (*b*, *c*)

Estimated peak density of atomic oxygen between 2000 and 2004 at 52ºN (NSSC CAS, ISTP SB RAS)

A method for deriving the peak density of atomic oxygen in the Mesosphere and Low Thermosphere (MLT) region from atomic oxygen [OI] 557.7 nm nightglow intensity has been developed. The method is based on the photochemical model for [OI] 557.7 nm emission and an approximate expression for the altitude distribution of the atomic oxygen density in the MLT region. This method was used to derive the peak density of atomic oxygen from the 557.7 nm airglow data obtained at the ISTP SB RAS Geophysical observatory in 2000–2004 [Hong Gao et al., 2009]. Nighttime and seasonal variations in the [OI] 557.7 nm intensity and the derived peak density of atomic oxygen were analyzed. The results show that the nighttime variations
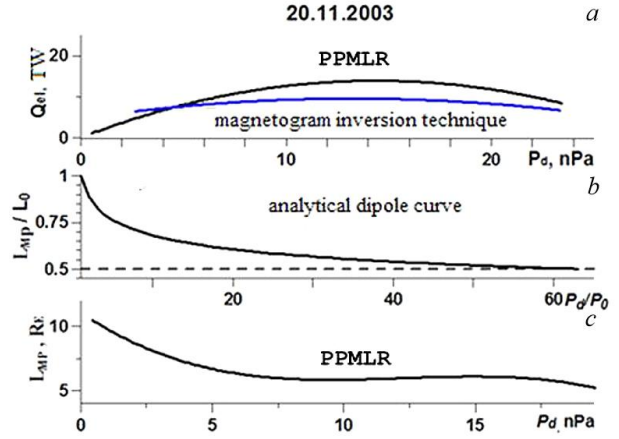
in the 557.7 nm emission intensity depend on season. The monthly mean 557.7 nm airglow intensity changes with month, showing peaks in March, June, and October, and larger values in winter months. Nocturnal and seasonal variations in the peak density of atomic oxygen are generally similar to those in the 557.7 nm airglow intensity.

Local empirical models of regular ionospheric variations (ISTP SB RAS, NSSC CAS)

Based on long-term ionospheric measurements with vertical sounding ionosondes located at Irkutsk, Norilsk, and Hainan, local empirical models of regular ionospheric variations were worked out (Figure 3) [Ratovsky et al., 2014]. Using the models, common properties and regional features were identified. A common property of the high-, mid- and low latitude ionosphere is the semi-annual daytime anomaly of the peak electron density N_mF2
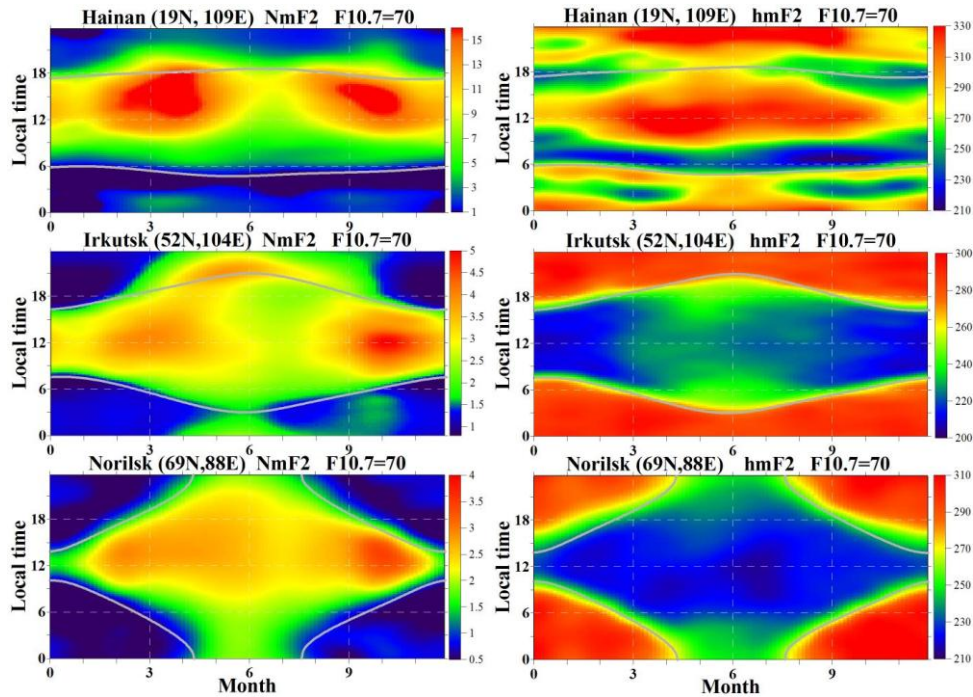

Figure 3. Diurnal-seasonal variations in N_mF2 [10^5 cm^{-3}] (left) and h_mF2 [km] (right) under low solar activity

under low solar activity and the intensification of the winter anomaly with increasing solar activity. The generality is a consequence of the global thermospheric circulation in which all regions of the ionosphere are involved. A distinctive feature of the low-latitude ionosphere is the semi-annual nighttime anomaly of N_{m}F2 under low solar activity and the highest growth rate of N_{m}F2 with an increase in F10.7 in the evening and night time. A regional feature of the ionosphere over Hainan (not reproduced by the IRI model) is the multi-peak diurnal variation in the peak height h_{m}F2 over Hainan. A distinctive feature of the mid-latitude ionosphere is the greatest intensification of the winter anomaly with increase in F10.7 and the evening anomaly in the summer diurnal variation in N_{m}F2. A regional feature of the ionosphere over Irkutsk (not reproduced by the IRI model) is the morning-evening asymmetry in the summer diurnal variation of N_{m}F2 at high solar activity. A distinctive feature of the high-latitude ionosphere is the absence of diurnal anomalies in any season and the absence of a winter anomaly at low solar activity. A regional feature of the ionosphere over Norilsk (not reproduced by the IRI model) is the "polar day effect" under low solar activity (no nighttime rise in the peak height h_{m}F2 in the summer).

Ionospheric response to geomagnetic storms at the meridional chain of ionosondes in the East Asian region (ISTP SB RAS, NSSC CAS)

In 2000–2017, coordinated studies of ionospheric effects of geomagnetic storms were carried out at the meridional chain of ionospheric stations located in the East Asian sector (90°–160° E) in Russia and China (Figure 4) [Pirog et al., 2010; Shi et al., 2011]. For some storms, these studies were supplemented with measurements in the European and American sectors. The following has been revealed: (1) Medium-latitude ionosphere shows properties of high-latitude ionosphere during superstorms. (2) There are differences in the East Asian ionospheric response to geomagnetic storms under high and low solar activity. (3) Three groups of anomalous ionospheric disturbances caused by geomagnetic storms and observed at low solar activity have been identified:
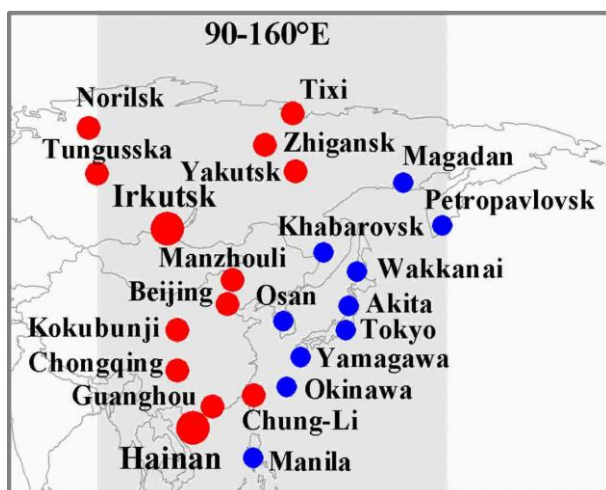

Figure 4. Meridional chains of ionosondes in East Asia

a special type of large-scale traveling ionospheric disturbances, quasi-two-day Wave Like Disturbances (WLDs), oscillations of Short Duration (OSD). (4) Longitudinal alternation of positive and negative ionospheric response during the recovery phase of some storms is observed. Longitude variations of storm ionospheric disturbances are determined by the local time of the storm sudden commencement. (5) A comparative analysis of the behavior of F-scattering in equatorial and high latitudes was performed [Shi et al., 2011].

FROM MERIDIONAL CHAINS TO THE INTERNATIONAL MERIDIAN CIRCLE PROGRAM (IMCP)

Ground-based chains of geophysical instruments are a powerful tool for studying and monitoring the effects of space weather in Earth's ionosphere and magnetosphere. Due to the latitudinal difference in solar radiation and the bounding of charged particles by the geomagnetic field, space weather disturbances are usually manifested along the meridians. As a result, observing along a specific meridian line has a great deal of advantages. The effectiveness of observations at the meridional chains has been confirmed by a rich history of such observations.

Observations at the Norilsk and Yakutsk meridional chains of stations in Russia: 1969–1983

To study geophysical phenomena in the upper atmosphere of high latitudes, ISTP SB RAS and SHICRA SB RAS organized synchronous observations at the Norilsk and Yakutsk meridional chains of stations (Figure 5). The observations were conducted as part of the International Magnetospheric Study (IMS) program (1976–1979). From 1969 to 1983, a total of 6 measurements campaigns (expeditions) were organized: 1969 — at the Yakutsk meridian; 1973 — at the Norilsk meridian; 1976 — Siberia-IMS-76, start of synchronous observations at the Yakutsk and Norilmk meridians; 1979 — Siberia-IMS-79; 1982 and 1983 — Taimyr-82. Each expedition had its own scientific program. The observation stations were fitted with the same type of equipment, and the observations were carried out according to a unified coordinated program. The standard set of equipment included magnetovariation station, all-sky camera, zenith photometer, scanning photometer, and ionosonde. The Khatanga station, located to the east of the Norilsk meridian, was used to link observations with data from the Yakutsk meridian chain.

As a result of this observations, we have first of all formulated the principles for organizing meridional chains of stations [Rakhmatullin, 2010, and references therein]:

- stations along the meridian should be positioned with the least scatter in longitude to minimize errors related to longitudinal effects;

- two or three meridional chains are necessary to study longitudinal effects and control the geophysical conditions;

- stations of the chain should be equipped with geophysical instruments of various types, such as magnetometers, ionosondes, photometers, to not only record processes in different geospheres, but also to study their interaction and identify physical mechanisms.
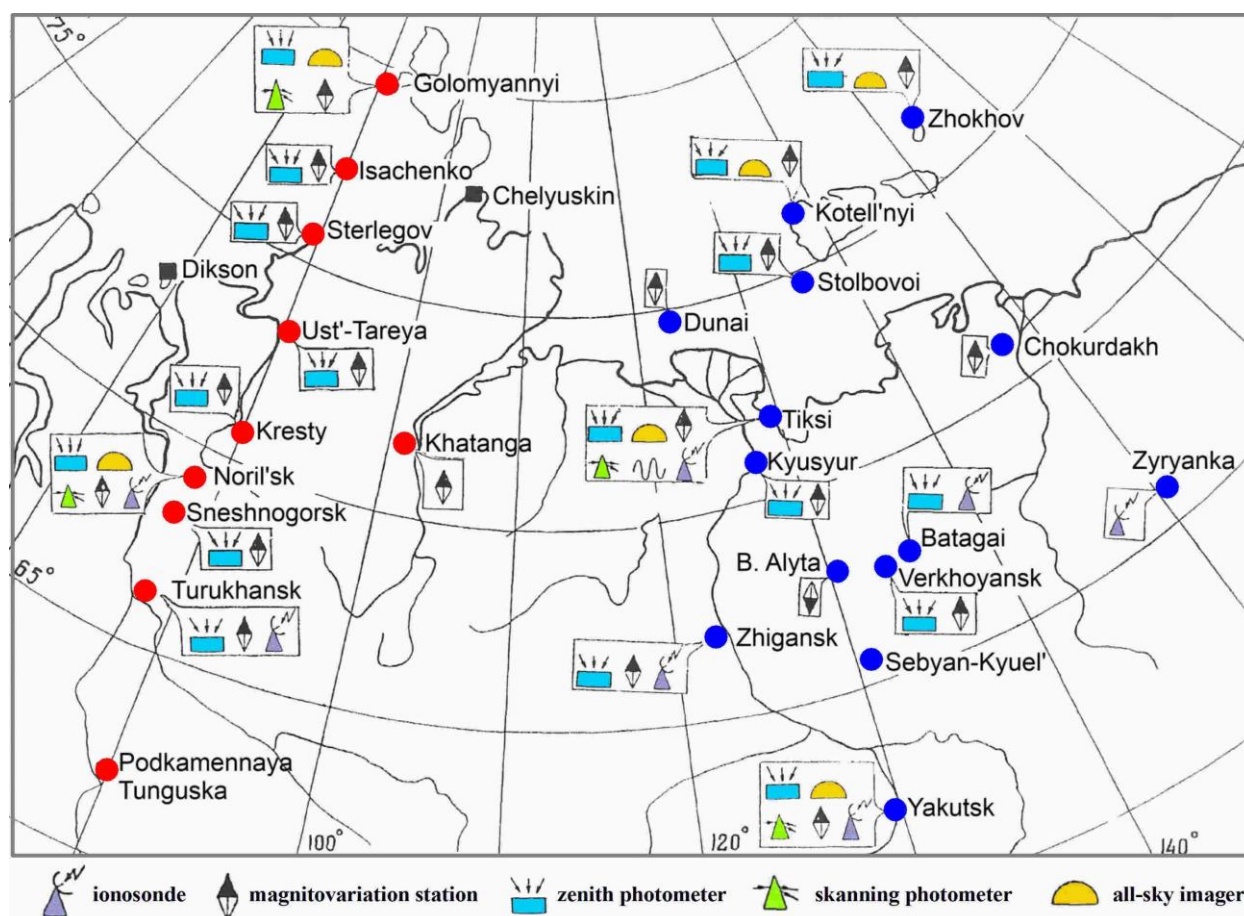
Figure 5. Norilsk and Yakutsk meridional chains of stations. Based on the materials of [Rakhmatullin, 2010]

Substorm in geomagnetic pulsations

Observations at meridional chains were essential for understanding the mechanism of a magnetospheric substorm [Rakhmatullin, 2010]. The development of geomagnetic pulsations during substorms was studied in detail. This work was pioneering for that time. And the resultant pattern of the magnetospheric substorm in geomagnetic pulsations has not changed significantly so far. For the first time, the longitudinal and latitudinal dimensions of the sources of Pi2 and Pi1B pulsations were determined, their relation to auroras was shown, and generalized schemes of drifts of pulsation sources were created. Fundamental differences in generation of Pi2 pulsations at auroral and mid-latitudes were found. It was shown that the amplitude and spectral composition of the mid-latitude Pi2 pulsations are controlled by the state of the ionospheric F2 layer.

A method was developed to determine the longitude of substorm development in the auroral zone from parameters of mid-latitude Pi2 pulsations (Figure 6). After the onset, the substorm propagates as a series of successive amplifications of magnetic activity; each occurs northwest of the previous one and is accompanied by Pi2 generation. The main axis of the Pi2 polarization ellipse is always directed toward the source. With the motion of the substorm disturbance, the polarization axis rotates counterclockwise. Thus, the longitude of the substorm can be determined from the direction of the polarization axis.
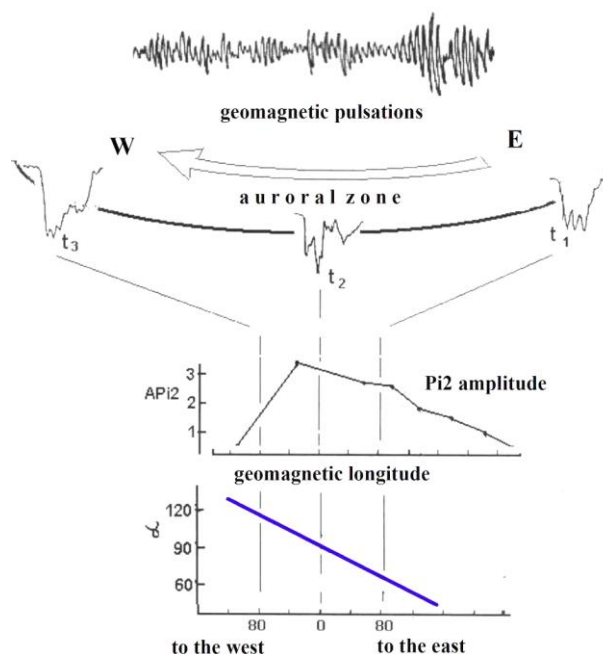

Figure 6. Scheme of substorm development in the auroral zone and in midlatitudes. Based on the materials of [Rakhmatullin, 2010]

Model of ionospheric substorm

According to the data from the Norilsk meridian, a morphological description of the processes in the high-

latitude ionosphere was made [Zherebtsov et al., 1986; Pirog et al., 1997]. Statistical schemes of ionospheric substorm development north of the MIT in LT–K_p coordinates at different latitudes were constructed, and the effect of solar activity was revealed. In addition, a regional model of critical frequencies of E and F regions for the Norilsk meridian was developed. Complex processing of data from meridional chains made it possible to obtain an equation describing the position of the Main Ionospheric Through (MIT) under different magnetic activity: $\Phi = 150.6 - 5t - 25(0.1K_p^2 - 1.3t + 12.7)^{1/2}$, where Φ is invariant latitude, t is the time counted from midnight, K_p is the geomagnetic activity index.

The extensive experimental material obtained during complex high-latitude expeditions became the basis for further research. Nowadays, we are turning to the expedition archives to confirm this or that experimental fact. The archives also serve as an experimental base for studying long-term trends. The results obtained confirm the effectiveness of meridional chains of geophysical instruments in studying the magnetosphere-ionosphere interactions.

Chinese Meridian Project (CMP)

In China, the concept of the national Meridian Project was proposed in the early 1990s [http://imcp.ac.cn/en/about/planning/; https://www.meridianproject.ac.cn/mcmp/]. Development of the Chinese Meridian Project (CMP) began in 2005 [Wang Chi et al., 2020, 2022; https://www.meridianproject.ac.cn/en/]. The project rolled into realization stage in 2008 upon being approved by the government as one of the major scientific structures. The Chinese Meridian Project is a ground-based space environment monitoring network. It is a joint effort of more than 10 research institutions and universities in China, led by NSSC CAS. The Project aims to study the propagation processes of disturbances caused by solar activities, from the Sun to the interplanetary space, magnetosphere, ionosphere, until mid-to-upper atmosphere; coupling mechanisms of different space spheres and layers, namely solar atmosphere, interplanetary space, magnetosphere, ionosphere, and mid-to-upper atmosphere; regional characteristics of the space environment above China's territory, and its rela-

tionship with global variations [Wang Chi et al., 2020]. CMP was built in two stages (Figure 7). The Phase I construction began in 2008 and was completed in 2012. Since 2012, Phase I has been in operation. Phase II started in 2019 and was successfully completed in 2024 [Wang Chi et al., 2020, 2022, 2024]. CMP Phase I consists of 15 ground-based observatories located along 120° E and 30° N (Figure 7, *a*). Each observatory is equipped with multiple instruments including magnetometers, radars, optical equipment, and sounding rockets to monitor parameters of solar wind, geomagnetic field, middle and upper atmosphere, ionosphere. CMP Phase II has added 16 new stations to Phase I, and thus created a monitoring network of 31 stations and nearly 300 instruments along 100° E and 120° E, and 30° N and 40° N (Figure 7, *c*). In addition to the usual instruments, Phase II comprises several large and advanced devices including a radio heliograph, an interplanetary scintillation telescope, an MST radar, a new generation tristatic incoherent scatter radar, etc.

CMP and Chinese-Russian Joint Research Center

Within the framework of the Chinese-Russian Joint Research Center, Russian stations have joined the chain of Chinese observatories since 2005 (Figures 4, 7, *b*). A significant number of joint studies on the ionospheric morphology over the East-Asian region under different levels of solar and magnetic activity have been conducted. Many interesting results have been obtained, some of them are described in the Section "Main scientific results". Comprehensive analysis of data from Chinese-Russian chains allowed clarifying mechanisms of interplanetary, magnetospheric, and thermospheric factors' impact on the ionospheric dynamics. It also allowed evaluating the possibility to use the existing theoretic models for reproducing the spatio-temporal dynamics of the ionosphere and to identify the possible ways of correcting models in order to improve their diagnostic and, in a long run, predictive features. The results are summarized in a collective monograph "Ionospheric disturbances in East-Asian region" [Zherebtsov et al., 2021].
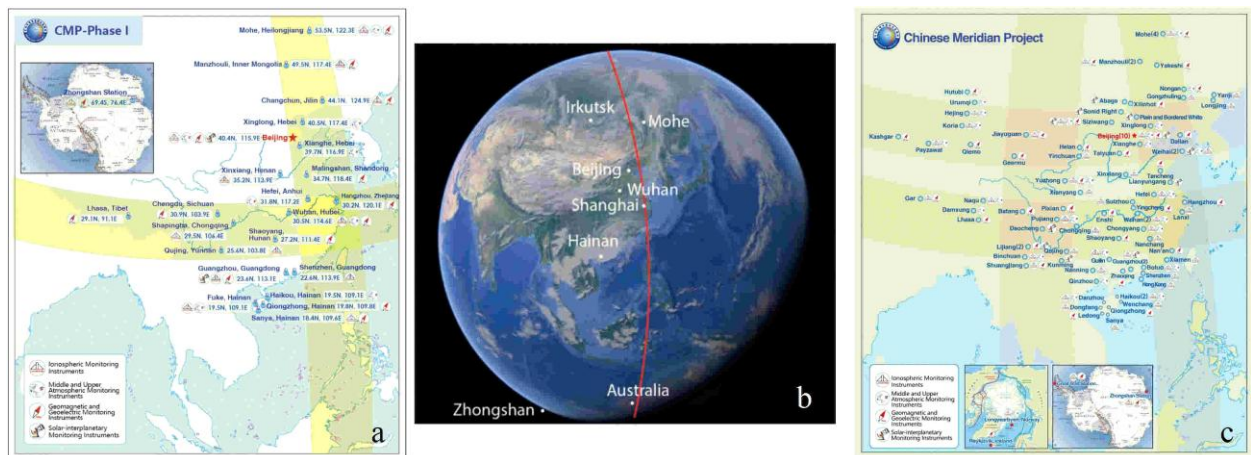

Figure 7. Chinese Meridian Project: Phase I (*a*) and Phase II (*c*) [https://www.meridianproject.ac.cn/bi/]. Observatories along 120° E making part of the Meridian Space Weather Monitoring Project in 2005 (*b*) [The 20th Anniversary, 2021]

INTERNATIONAL MERIDIAN CIRCLE PROGRAM (IMCP)

The International Meridian Circle Program (IMCP) became an excellent development of the CMP concept [Liu et al., 2020, 2022; Blanc et al., 2020; Wang Chi et al., 2024; http://imcp.ac.cn/en/]. This large and unique project of NSSC CAS was proposed to bring together more than 1000 instrumentation from over 10 countries along the 120° E and 60° W meridians to create a global monitoring network (Figure 8) [http://imcp.ac.cn/en/about/objectives/]. The Great Meridian Circle crosses China, Russia, Southeast Asia, Australia, Antarctica, Latin America, the United States, Canada. IMCP aims to conduct all-latitude, all-weather observations of the system formed by near-Earth space, the atmosphere, the Earth surface. It is designed to track propagation of space weather events from the Sun to Earth as well as to monitor various disturbances generated within the Earth system that impact near-Earth space [Liu et al., 2022; Wang Chi et al., 2024].

The instruments deployed along Great Meridian Circle can provide a complete cross-sectional scan of near-Earth space from the ground level up to approximately 3000 km, including density, temperature, magnetic and electric fields, wind fields, planetary waves, and distribution of minor species involved in Global Change [http://imcp.ac.cn/en/about/sw/]. Due to Earth's rotation, this network can give a complete three-dimensional representation of these key near-Earth space parameters every 12 hours. Accumulated over years and decades, this dataset will provide valuable insight on how climate and long-term atmospheric change are influenced by solar and terrestrial energy input. By detecting and tracking short-term anomalies, the network can warn about space weather and terrestrial disasters.

Currently, significant progress has been made on IMCP [Wang Chi et al., 2024]. The IMCP scientific program committee has been formed, and the China-Brazil joint laboratory for space weather has also been established. Networks in the North Pole and Southeast Asia are under construction. IMCP is supported by an array of Chinese and foreign research institutions, as well as international scientific associations such as the European Incoherent Scatter Radar Scientific Association (EISCAT), the Scientific Committee on Solar-Terrestrial Physics (SCOSTEP), and the Super Dual Auroral Radar Network (SuperDARN) [http://imcp.ac.cn/en/about/objectives/].

Moving forward, in addition to the 120° E – 60° W meridian circle, IMCP also plans to establish network along the 30° E – 150° W meridian circle in collaboration with the International Space Weather Initiative (ISWI) [Wang Chi et al., 2024; Blanc, 2023]. Thousands of IMCP instruments will create a three-dimensional information grid covering five continents. This grid will provide real-time data on near-Earth space, helping to protect our planet from natural and human-made hazards.

NATIONAL HELIOGEOPHYSICAL COMPLEX OF THE RUSSIAN ACADEMY OF SCIENCES (NHC RAS)

The National Heliogeophysical Complex of the Russian Academy of Sciences (NHC RAS) [Zherebtsov, 2020; http://ngkran.ru/] can make a significant contribution to IMCP for mid- and high-latitude observations at 120° E meridian. NHC RAS has been developed and is being created by ISTP SB RAS which has a long history of expertise and operation of large heliogeophysical instruments. In 2014, NHC RAS received the support from the President of the Russian Federation and the Government of the Russian Federation. The complex should provide solutions to the most important problems of solar-terrestrial physics considering the Sun — Earth system as a uniform and interrelated one. The National Heliogeophysical Complex has been developed on the basis of new technical solutions with the use of modern technologies. It integrates unique facilities, instruments, and devices.

The objectives of the National Heliogeophysical Complex RAS are: to get to a new level of development of experimental (ground-based) research in solar-terrestrial physics; to solve urgent fundamental and applied problems

Figure 8. International Meridian Circle Program (IMCP) [http://imcp.ac.cn/en/about/objectives/]

in the interest of development of new space technologies. Fundamental research involves studying solar activity (magnetic fields, flares, plasma ejections, etc.) and its effect on space weather; studying the magnetosphere-ionosphere-atmosphere system and effects imposed on it by solar factors and meteorological and lithospheric processes. Applied research involves studying the effects of space factors on operation of spacecraft and various engineering systems (radio communications, radar, GPS-GLONASS and others); monitoring of near-Earth space, spacecraft and space debris; developing methods for solar activity and near-Earth space monitoring and prediction to the benefit of different consumers.

The NHC RAS includes five large, new generation experimental instruments for research in the field of solar physics and near-Earth space physics [Zherebtsov, 2020; http://ngkran.ru/]: Large Solar Telescope-Coronagraph, Multiwave Radioheliograph, Radiophysical Complex for Atmospheric and Ionospheric Research, Network of Coherent Ionospheric Radars, Lidar Optical Complex (Figure 9). Collection, real-time processing, and storage of information from NHC RAS instruments will be performed at the Data Center which will be established in Irkutsk (ISTP SB RAS). At present, the first NHC RAS instruments (Radioheliograph and Optical tools) have commenced their functioning. The development and construction of the Large Solar Telescope and a Radiophysical Complex are underway.

The Large Solar Telescope-Coronagraph (LST-3)

One of the most pressing issues in contemporary solar physics is the observation of the small-scale structure in the solar atmosphere at various heights (including the chromosphere and corona). These observations can only be conducted using large solar telescopes. The Large Solar Telescope-Coronagraph with a mirror 3 m in diameter (LST-3) is designed for observing the solar atmosphere and corona with previously unattainable spatial, temporal, and spectral resolution [Grigoryev et al., 2020]. Missions of LST-3 include studies of energy release in flares and other dynamic phenomena, heating processes in the corona, the origin of solar magnetism and cyclicity. Operation of LST-3 in coronagraphic mode will allow us to observe space objects such as asteroids and comets near the Sun including hazardous ones in the daytime. The telescope will be installed at the Sayan Solar Observatory, located at an altitude over 2000 m (Figure 10). The choice was made in favor of the classic axisymmetric Gregory optical layout on an alt-azimuth mount. The scientific equipment of LST-3 will consist of several systems of narrow-band tunable filters and spectrographs for various wave ranges. The equipment will be placed both in the main coudé focus on a rotating platform and in the Nasmyth focus. To achieve a diffraction resolution, high-order adaptive optics will be used. It is assumed that with a certain modification of the optical configuration, LST-3 will work as a 0.7 m mirror coronagraph in near infrared lines and can also be used for observing astrophysical objects in the nighttime. The development of LST-3 should make a decisive contribution to our understanding of solar activity, which drives space weather phenomena.

The Multiwave Siberian Radioheliograph

The Multiwave Siberian Radioheliograph (MSRH) performs all-weather monitoring of processes in the solar atmosphere (in the range from meter to millimeter waves, including measurements of the solar activity index at 2.8 GHz) [Altyntsev et al., 2020; http://badary.iszf.irk.ru]. This is essential for predicting and diagnosing geoeffective solar activity phenomena. The fundamental

Figure 9. NHC RAS instruments in Eastern Siberia: 1— Large Solar Telescope-Coronagraph; 2 — Multiwave Siberian Radioheliograph; 3 — Complex of Passive Optical Instruments; 4 — Heating Facility; 5 — Data Center; 6 — IS-MST Radar; 7 — Mesostratospheric Lidar
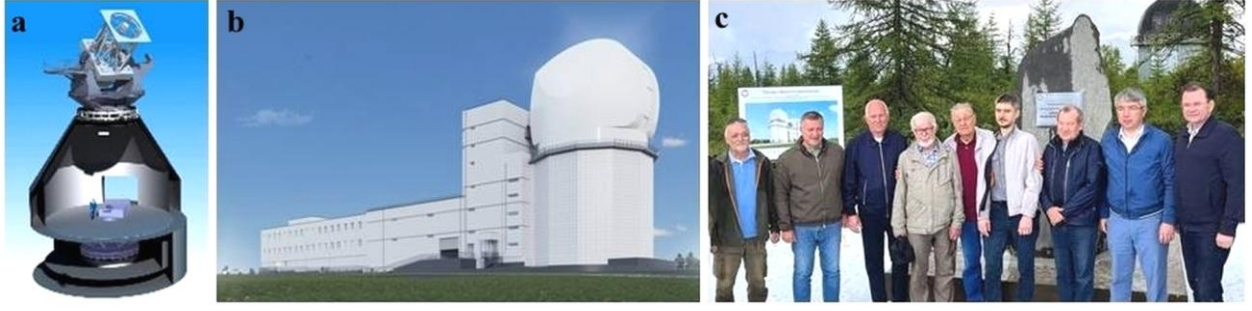
Figure 10. NHC RAS: Large Solar Telescope-Coronagraph. General view of LST-3 (*a*) and LST-3 building (*b*). Groundbreaking ceremony of LST-3 on August 5, 2023 (*c*)

research that may be implemented with the radioheliograph includes: topology of coronal magnetic fields during the active and quiet Sun; wave processes and shock waves in the solar atmosphere; evolution of large-scale structures in the solar atmosphere during the 11-year solar cycle; regular measurements of radio emission at a wavelength of 10.7 cm; assessment of geoeffectiveness of solar flare parameters; short-term prediction of powerful solar flares with a lead time of 2 to 3 days. MSRH is located at the ISTP SB RAS Radio Astrophysical Observatory (Figure 11, *a*). This allows us to carry out observations using MSRH in conjunction with the existing instruments. MSRH is an interferometer that produces solar images in the 3–24 GHz frequency range in both circularly-polarized components [Altyntsev et al., 2020]. It consists of three separate antenna arrays, each designed for one frequency band: 3–6 GHz, 6–12 GHz, and 12–24 GHz. The antenna diameters for these bands are 3, 1.8, and 1 m respectively. The numbers of antennas in the arrays are 129, 192, 207. Radioheliograph data is necessary to develop and implement methods of short-term forecast of solar flares, measurements of kinematics and characteristics of coronal mass ejection plasma, forecast of characteristics of fast solar wind streams. All-weather monitoring of explosive processes on the Sun will enable us to solve an important applied problem — to assess their impact on the operation of space facilities, as well as ground-based communication, navigation, radar, and other technological systems. MSRH is already in operation. Figure 11, *b–c* show solar images obtained with MSRH at three frequencies on September 19, 2023.

The Radiophysical Complex

The Radiophysical Complex (RPhC) for ionospheric and atmospheric research is the largest complex and multifunctional information system in the National Heliogeophysical Complex [Zherebtsov, 2020; Medvedev et al., 2020; Vasilyev et al., 2020a]. RPhC includes the most powerful and promising research instruments: a radio wave incoherent scatter (IS) radar for ionospheric sounding; a mesospheric-stratospheric-tropospheric (MST) radar for sounding the neutral atmosphere; a heating facility for modifying the ionosphere with powerful HF radio waves. This cluster of large tools will be supplemented with a system of small problem-oriented instruments and a meridional chain of stations Norilsk — Irkutsk (ionosondes, magnetometers, photometers, etc.). The IS-MST Radar, which combines capabilities of IS and MST measurements, will be able to cover layers from the troposphere to the plasmasphere (altitude range 10–1500 km) and to study processes of energy transfer from the lower and middle atmosphere to the ionosphere as well as the interaction of the magnetosphere with the upper atmosphere. Apart from atmospheric research, the radar will allow us to track spacecraft and space debris, determining precise coordinate characteristics. The antenna system is also suitable for radio astronomical observations.

RPhC will be located near Lake Baikal in Tazheran steppes [Medvedev et al., 2020]. The RPhC location is unique since the complex will provide important geophysical data and monitor near-Earth space in the center of Russia, significantly complementing observational data acquired by geophysical centers in the USA, Europe, and Japan in studying global distributions of environmental parameters.

The main focus of RPhC studies is on the upper atmosphere (80–1500 km) as one of the most important parts
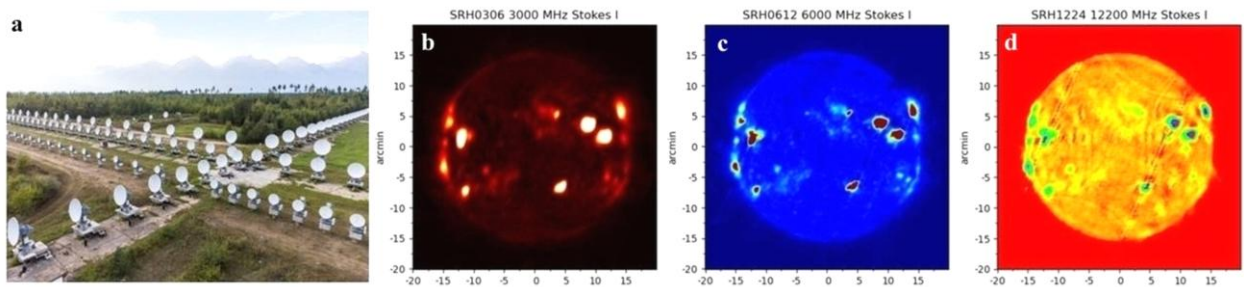

Figure 11. NHC RAS: Multiwave Siberian Radioheliograph. MSRH antenna arrays (*a*). Solar images at 3.0, 6.0, 12.2 GHz obtained by Ragioheliograph on September 19, 2023 (*b–d*)

of the Sun — Earth system. The results of the ionospheric and upper atmospheric research with RPhC are important for various fields of science and technology: space and terrestrial radio communications, radar, and navigation; near-Earth space monitoring, including problems of comet and asteroid impact hazards and space debris.

The IS-MST Radar

The IS-MST Radar includes two phased arrays spaced by 100 m and have a tilt of 20° in opposite directions so as to cover as large area as possible (Figure 12) [Medvedev et al., 2020]. The radar operating frequency band is 154–162 MHz, and the peak transmitted power of each array is 1 MW.

Figure 13 shows the main operating modes of RPhC [Medvedev et al., 2020]. The MST mode (Figure 13, *a*) will be used for diagnostics of dynamics (the neutral wind parameters) in the lower and middle atmosphere. For ionospheric research, we will utilize two operating modes corresponding to two height ranges (below 500 and above 500 km): mode IS-1 for studying interactions in the atmosphere-ionosphere system and multiparameter diagnostics of the ionospheric plasma (Figure 13, *b*); mode IS-2 for studying interactions within the ionosphere — plasmasphere system as well as measuring variations in the ion composition and tracks of plasma fluxes (Figure 13, *c*). The SO monitoring mode will provide monitoring of space objects (SO) such as spacecraft and space debris (Figure 13, *d*). In the cooperative observation mode (Figure 13, *e*), an ionospheric region, irradiated by the heater, will be scanned by the IS-MST Radar, optical tools, HF and GNSS receivers; this will ensure comprehensive diagnostics of phenomena occurring upon powerful high-frequency impact on the ionosphere. The passive mode (Figure 13, *f*), where the radar does not transmit, but detects space signals from various directions, will be useful for radioastronomy observations of radiation from the Sun and space radio sources, as well as for studying radio storms and radio signal scintillations.

The heating facility IKAR-AI

Developed with NHC RAS, the new heating facility IKAR-AI (Irkutsk short-wave antenna array with active transmitters) takes into account the extensive experience in heating in Russia and abroad [Vasilyev et al., 2020a].
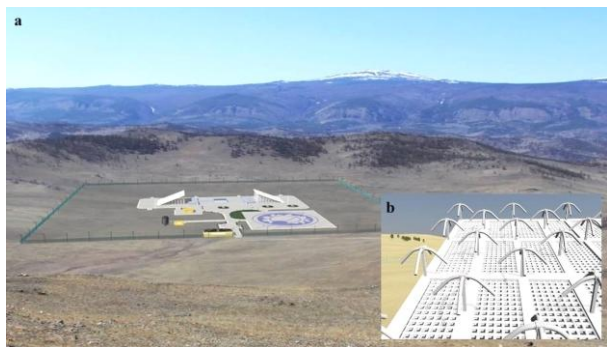

Figure 12. NHC RAS: IS-MST Radar. General view near Lake Baikal (*a*), antenna of IS-MST Radar (*b*)

The heating facility is a complex of 60 antennas on an area of 700×700 m (Figure 14, *a*). IKAR-AI will radiate in a frequency range 2.5–6.0 MHz with an effective power of several hundred megawatts. The proposed frequency band is the best to undertake new research at IKAR-AI. The transfer of shortwave radiation energy to a charged particles in the upper atmosphere is the most effective in the lower band 2.5–3.5 MHz, where the second electron gyrofrequency harmonic is located and where the most intense artificial ionospheric turbulences and optical airglow occur. The upper band part (the 4–6 MHz) allows for the efficient operation of the heating facility periods of higher solar activity, as well as for the use of IKAR-AI as a short-wave radar for ionospheric diagnostics. It is important that the heater will be surrounded by such multifunctional instruments as the incoherent scatter radar, mesostratospheric lidar, optical and radiophisical observational systems that can enable us to diagnose artificial plasma disturbances and artificial airglow structures (Figure 14, *b*).

Network of Coherent Ionospheric Radars (SECIRA)

Under the NHC RAS project, ISTP SB RAS is deploying the Russian network of coherent ionospheric radars analogous to SuperDARN [Berngardt et al., 2020; Zherebtsov, 2020]. The Russian radars can make observations over almost the entire territory of the Russian Federation (Figure 15, *a*) and are capable of studying the magnetosphere-ionosphere coupling, including effects of magnetospheric substorms and geomagnetic storms in mid-latitude and subauroral regions. The project of SECIRA radars has been developed at ISTP SB RAS. The radar is based on fully digital generation and receiving of signals, which is currently the major approach in developing new radars [Berngardt et al., 2020].

Unlike SuperDARN radars, SECIRA radars will have T-shaped phased antenna arrays (PAA) (Figure 15, *b*). Each PAA consists of 16 transmitting/receiving and 8 receiving antennas arranged in two perpendicular linear phased arrays. The distance between antennas (~15 m) coincides with distances in SuperDARN PAA. The maximum radiation power of each antenna is 1 kW. The SECIRA PAA geometry allows us to minimize the problems associated with the phase uncertainty of the received signal, as well as to consistently identify signals coming from the back lobe. The Russian system of coherent radars provides studies in several major areas: solar wind interaction with the magnetosphere and ionosphere; internal atmospheric waves; scattering by meteors and mesospheric winds; natural and artificial plasma irregularities. The Russian SECIRA network will also provide the solution to the following applied problems: continuous monitoring of ionospheric disturbances in sub-polar regions affecting the various technological systems; monitoring of the auroral oval boundary for efficient prediction of blackouts in high-frequency radio channels and optimal operating frequencies under different geophysical conditions; near real-time diagnostics of wave ionospheric disturbances as most unpredictable factor of disturbances for communication and navigation systems.
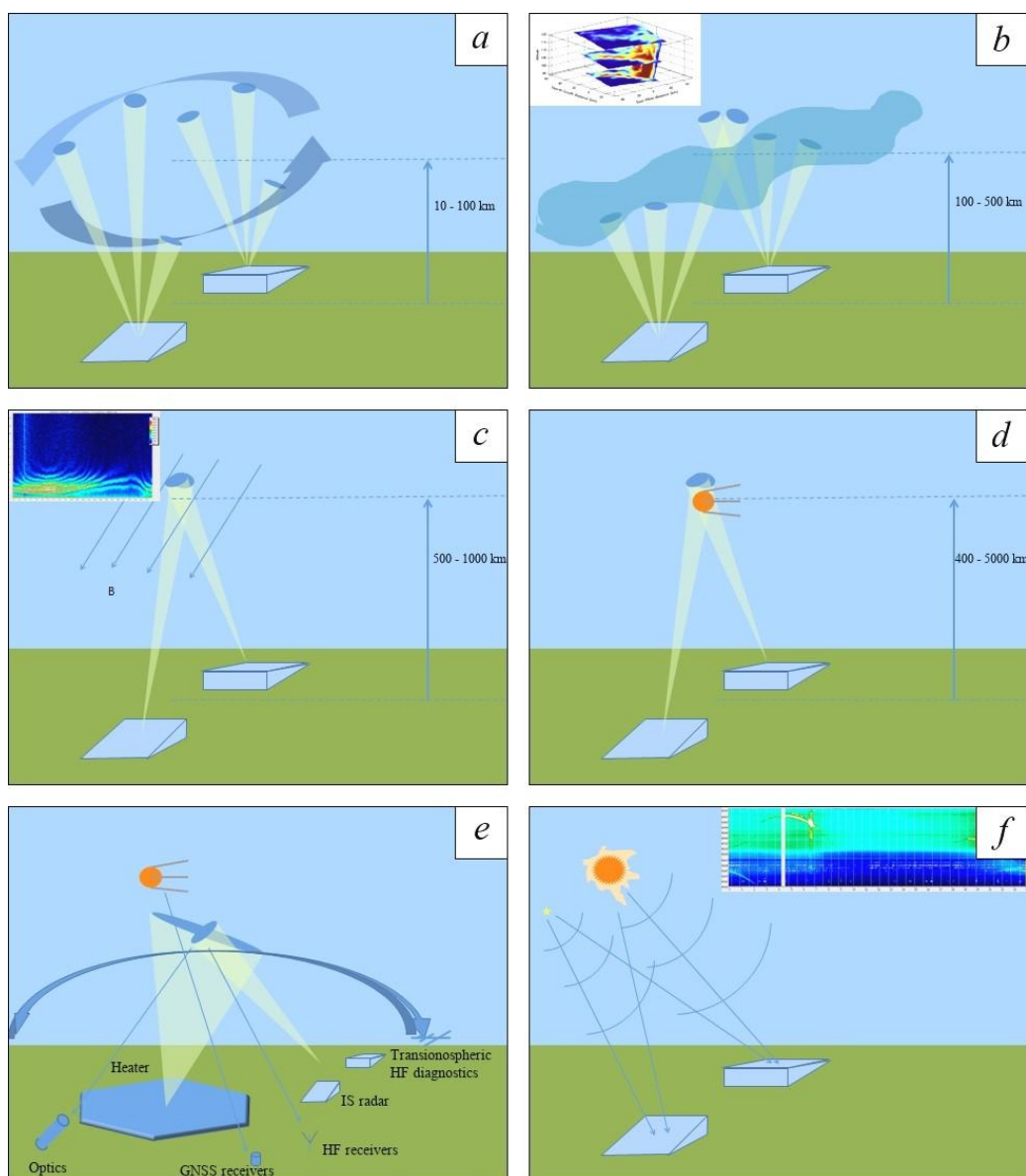
Figure 13. NHC RAS: IS-MST Radar. Operating modes of IS-MST Radar: MST mode (*a*); IS-1 mode (*b*); IS-2 mode (*c*), SO monitoring mode (*d*); cooperative observation mode (*e*), radioastronomical (passive) mode (*f*) [Medvedev et al., 2020]
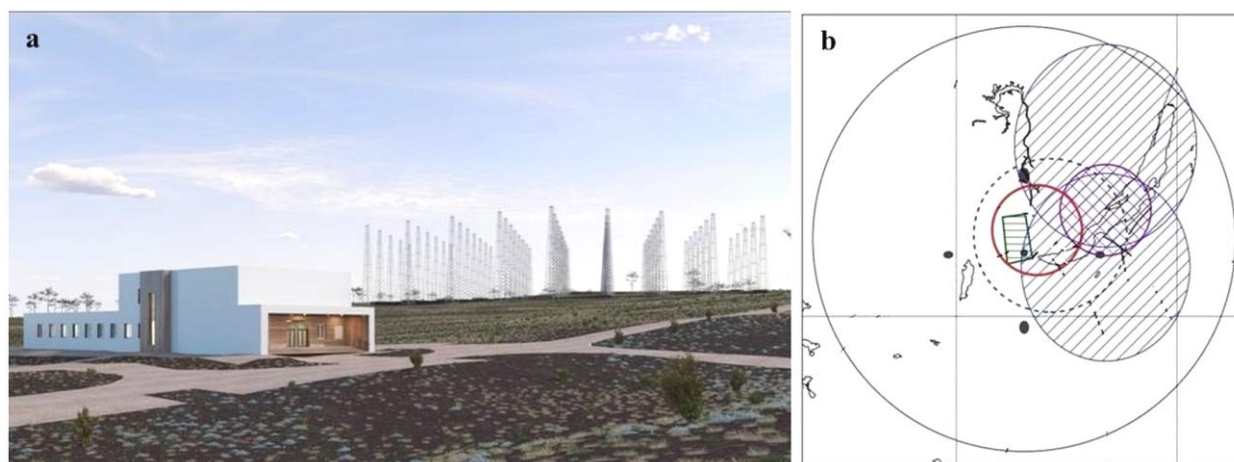

Figure 14. NHC RAS: Heating Facility. General view of the Heating Facility (*a*). Fields of view of the NHC RAS instruments at an altitude of 250 km are (*b*): red circle for the Heating Facility; blue ellipses with right hatching for the IS-MST Radar; purple circle with left hatching for the MS lidar; green trapezium with horizontal hatching for the existing Irkutsk IS-radar; green dashed circle for the existing ionosonde DPS-4; black circle for the all-sky camera; gray ellipses for the Fabry — Perot interferometer [Vasilyev et al., 2020a]
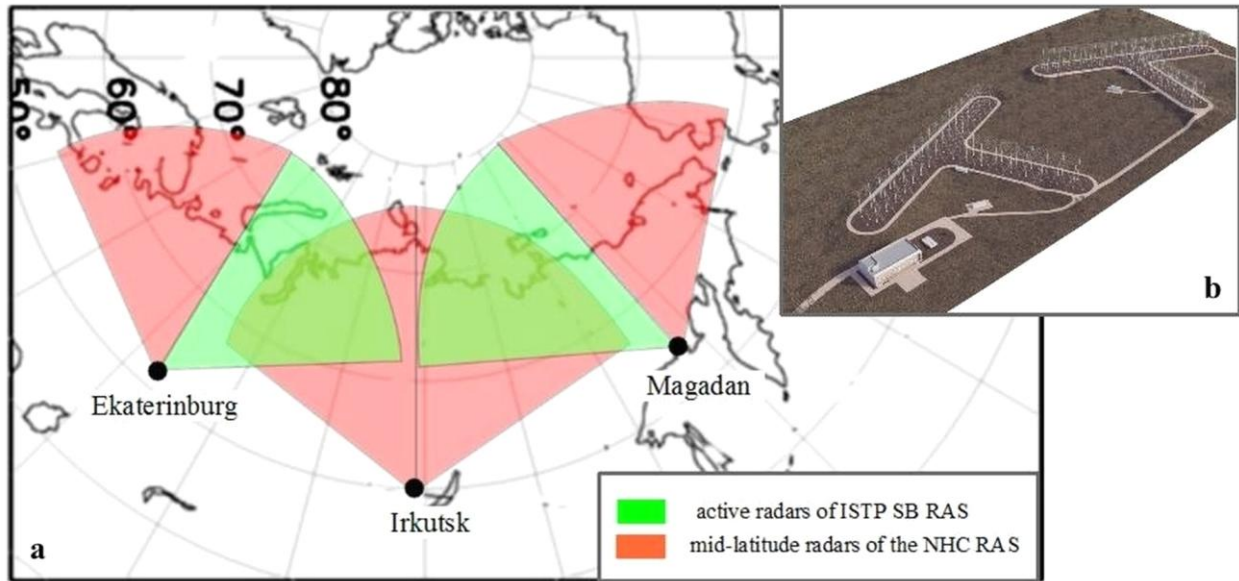
Figure 15. NHC RAS: Network of Coherent Ionospheric Radars. Position of coherent radars and their fields of view (*a*). General view of coherent radar of NHC RAS (*b*)

Lidar Optical Complex (LOC)

Lidar Optical Complex (LOC) is designed to study profile characteristics of physical parameters (temperature, density, wind) and composition (gas components, aerosol) of the middle and upper atmosphere, which are formed under the influence of natural processes and anthropogenic impacts [Matvienko et al., 2020; Vasilyev et al., 2020b]. The optical complex combines active laser systems [Matvienko et al., 2020] and passive optical instruments for recording the atmospheric emission [Vasilyev et al., 2020b]. The Lidar Optical Complex will allow solving basic problems in atmospheric research at different altitudes, along with important practical problems in the field of environmental ecology and global climate change.

The mesostratospheric lidar

The study of the upper atmosphere, including the mesosphere and the thermosphere, requires lidar systems with large optics and high-power lasers. Such a mesostratospheric (MS) lidar (Figure 16) will be developed as part of NHC RAS with the use of theoretical and experimental developments, received at V.E. Zuev Institute of Atmospheric Optics of the Siberian Branch of the Russian Academy of Sciences (IAO SB RAS) [Matvienko et al., 2020]. The MS lidar should allow us to measure profiles of thermodynamic parameters of the atmosphere and distribution of the aerosol-gas composition in the altitude range 10–100 km. The proposed version of the MS lidar utilizes different laser sources within 350–1100 nm range and corresponding narrowband high-sensitivity detectors of lidar signals. The wide spectral range is necessary for realizing various laser sensing methods when obtaining information about remote atmospheric layers. The problem of combining various measurement methods for one receiving antenna will be solved by spectral selection and using the multilobe antenna pattern.

The passive optical instrument

The passive optical instruments (Figure 17) include [Vasilyev et al., 2020b] Fabry — Perot interferometers with diameter of etalon 70 mm, equipped with automatically interchangeable light filters and an automatically controlled periscope input window having a sensitivity sufficient to detect wind and temperature variations in the upper atmosphere at a level of 5 m/s and 5 K respectively; all-sky cameras with spatial resolution ~0.1°–0.5° and sensitivity in several Rayleigh, equipped with automatically interchangeable light filters; high-speed photometers with a field of view of ~10° and time resolution of 1 ms; diffraction spectrometers in visible and infrared spectral ranges with ~0.1 nm spectral resolution and sensitivity sufficient to observe variations in the intensity of lines in several Rayleigh. The complex of passive optical instruments has been put into operation and carries out regular measurements at the Geophysical Observatory of ISTP SB RAS (GPO ISTP RAS). Figure 17, *c* shows SAR-arcs detected at GPO ISTP RAS (midlatitudes) with an all-sky camera at a wavelength of 630 nm during the April 23, 2023 strong geomagnetic storm.

The Data Center

The Data Center to be established in Irkutsk will provide collection, real-time processing, and storage of data from NHC RAS instruments; it will also allow for data transfer to users (Figure 18). Its computing power and hardware as well as software architecture should ensure compliance with the requirements for speed, storage capacity (at least 100 000 terabytes per year), generation of necessary warnings, indices, and other indicators of the state of the Sun and near-Earth space.

The main goals of Data Center are: carrying out experiments to the benefits of scientific organizations (Shared Equipment Center); preparing data products for end users (customers); space weather conditions: warnings and alarms for consumers; online control of working modes of the instruments of NHC RAS; collecting data from NHC RAS instruments; data processing; data storage.
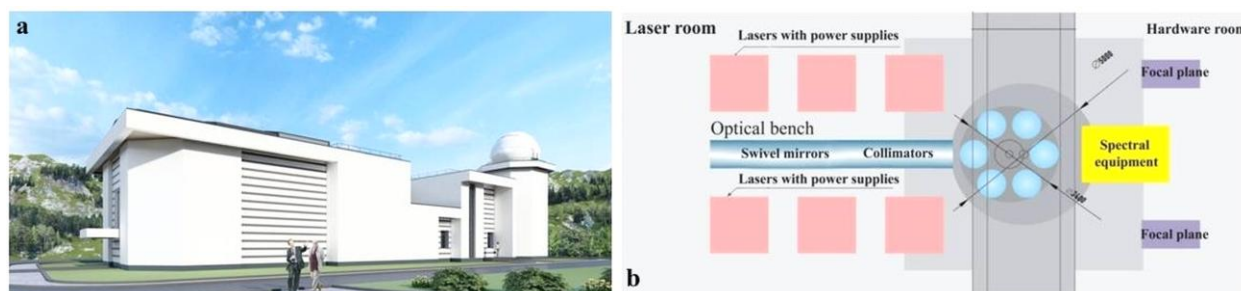
Figure 16. NHC RAS: Mesostratospheric lidar. General view of MS lidar building (*a*); arrangement of the main elements of the MS lidar (*b*) [Matvienko et al., 2020]

Figure 17. NHC RAS: Complex of passive optical instruments at GPO ISTP RAS. Building (*a*); an all-sky camera in the dome space (*b*); SAR-arcs detected with the all-sky camera at a wavelength of 630 nm during the April 23, 2023 strong geomagnetic storm (*c*)

Figure 18. NHC RAS: Data Center. General view of Data Center building

The National Heliogeophysical Complex will facilitate the transition to a qualitatively new level of development of basic and applied research in solar-terrestrial physics, and ensure high-level implementation of these works for the next 25–30 years. The geographical location of the complex, its multifunctionality and technical equipment will allow Russian scientists to participate in international programs including IMCP and the Chinese-Russian Joint Research Center.

CONCLUSION

The foundation of the Chinese-Russian Joint Research Center on Space Weather in 2000 reflected the main trends in society and science. The center's activities focus on addressing fundamental issues in modern solar-terrestrial physics, such as quantitative description of the processes in complex interconnected system Sun — interplanetary medium — magnetosphere — ionosphere — atmosphere, assessment of capabilities of predicting interactions

within this system, development of effective models for forecasting the state of the atmosphere and near-Earth space. The Joint Research Center is aimed at the study of all major space weather events from the Sun to the magnetosphere, ionosphere, and atmosphere.

In 2024, the Chinese-Russian Joint Research Center on Space Weather celebrated its 24th anniversary. We have been working together for two solar cycles already. Founded by ISTP SB RAS and NSSC CAS, the Joint Research Center has united more than 10 scientific institutes in Russia and China. About 60 scientific projects have been implemented and more than 400 joint scientific articles have been published. As part of the Joint Research Center's work, the following important results were obtained. Simultaneously at the Siberian Solar Radio Telescope (Russia) and the Huairou Solar Observing Station (China), zebra patterns in the microwave range were recorded for the first time. This allowed us to determine not only spectral, but also spatial characteristics of the event. For the first time, data was collected on the evolution of wave processes in small angular solar magnetic structures linked to umbral flashes. The spatial patterns of the magnetic helicity reversals in the Sun were shown to reflect the processes which contribute to generation and evolution of the large-scale magnetic fields. New patterns of Earth's magnetosphere saturation process were obtained: stopping the growth of the electromagnetic energy flux through the magnetosphere boundary and the polar cap from the solar wind with its unusual intensification during superstorms. Local empirical models of regular ionospheric variations at high, mid-, and low latitudes were created based on long-term ionospheric measurements with vertical sounding ionosondes in Norilsk, Irkutsk and on Hainan island. Coordinated studies of the ionospheric effects of geomagnetic storms in 2000–2017 were performed at the meridional chain of ionospheric stations in Russia and China. The medium-latitude ionosphere was found to exhibit properties of high-latitude ionosphere during superstorms. Additionally, there are differences in the East Asian ionospheric response to geomagnetic storms at high and low solar activity. Furthermore, there is longitudinal alternation of positive and negative ionospheric response during the recovery phase of some storms.

The future work of the Joint Research Center will be closely linked to the implementation of major unique projects in China and Russia: the International Meridian Circle Program (IMCP) led by NSSC CAS, and the National Heliogeophysical Complex of the Russian Academy of Sciences (NHC RAS) led by ISTP SB RAS.

IMCP connects 120° E and 60° W meridian chains of ground-based observatories to enhance the ability to monitor space environment worldwide. Currently, institutes from more than 10 countries (in particular China, Russia, Brazil, Australia, Canada) as well as some international scientific associations (EISCAT, SCOSTEP, SuperDARN) participate in the program. IMCP is designed to track propagation of space weather events from the Sun to Earth as well as to monitor various disturbances generated within the Earth system that impact near-Earth space. The IMCP observation system will provide monitoring and better understanding of the interactions between solar activities and terrestrial processes.

NHC RAS is a complex of large heliogeophysical instruments of new generation. NHC RAS is being deployed by ISTP SB RAS in the Eastern Siberia. The complex includes five big scientific instruments: Large Solar Telescope-Coronagraph, Multiwave Radioheliograph, Radiophysical Complex for Atmospheric and Ionospheric Research, Network of Coherent Ionospheric Radars, Lidar Optical Complex. NHC RAS should provide solutions to the most important problems of solar-terrestrial physics, considering the Sun — Earth system as a uniform and interrelated one. NHC RAS is aimed at studying solar activity and its impact on space weather; studying the magnetosphere — ionosphere — atmosphere system and effects imposed on it by solar factors and meteorological and lithospheric processes; studying the effects of space factors on operation of spacecraft and various engineering systems; monitoring of near-Earth space, spacecraft and space debris; developing methods for solar activity and near-Earth space monitoring and prediction to the benefit of different consumers. NHC RAS can make a significant contribution to IMCP for observations at middle and high latitudes at 120° E meridian.

After many years of collaboration, we can conclude that the Chinese-Russian Joint Research Center on Space Weather has proven its usefulness and continues its work in studying the Sun, solar-terrestrial relations, and near-Earth space. The Joint Research Center invites all interested institutions to further cooperation and development.

We would like to thank all those who took part in establishment of the Chinese-Russian Joint Research Center on Space Weather, and facilitated its successful work.

REFERENCES

Altyntsev A.T., Kuznetsov A.A., Meshalkina N.S., Rudenko G.V., Yan Yihua. On the origin of microwave zebra pattern. *Astron. Astrophys.* 2005a, vol. 431, pp. 1037–1046. DOI: 10.1051/0004-6361:20048337.

Altyntsev A.T., Kuznetsov A.A., Meshalkina N.S., Yan Yihua. Observations of "zebra" pattern in cm-range with spatial resolution. *Adv. Space Res.* 2005b, vol. 35, pp. 1789–1794. DOI: 10.1016/j.asr.2005.01.018.

Altyntsev A.T., Lesovoi S.V., Globa M.V., Gubin A.V., Kochanov A.A., Grechnev V.V., Ivanov E.F., et al. Multiwave Siberian Radioheliograph. *Solar-Terr. Phys.* 2020, vol. 6, iss. 2, pp. 30–40. DOI: 10.12737/stp-62202003.

Berngardt O.I., Kurkin V.I., Kushnarev D.S., Grkovich K.V., Fedorov R.R., Orlov A.I., Kharchenko V.V. ISTP SB RAS decameter radars. *Solar-Terr. Phys.* 2020, vol. 6, iss. 2, pp. 63–73. DOI: 10.12737/stp-62202006.

Blanc M., Bounhir A., Donovan E., and 31 co-authors. Science objectives and observation system for the International Meridian Circle. *Taikong ISSI-BJ Magazine.* 2020, no. 19.

Blanc M. The International Meridian Circles Program. A major opportunity for science, space weather monitoring and international collaboration. *CEDAR Workshop 2023*, San Diego, June 25–30, 2023.

Demidov M.L., Wang X.F., Wang D.G., Deng Y.Y. On the Measurements of full-disk longitudinal magnetograms at Huairou Solar Observing Station. *Solar Phys.* 2018, vol. 293, A146. DOI: 10.1007/s11207-018-1366-6.

Grigoryev V.M., Demidov M.L., Kolobov D.Yu., Pulyaev V.A., Skomorovsky V.I., Chuprakov S.A. AMOS team. Project of the Large Solar Telescope with mirror 3 m in diameter. *Solar-Terr. Phys.* 2020, vol. 6, iss. 2, pp. 14–29. DOI: 10.12737/stp-62202002.

Hong Gao, Jiyao Xu, Mikhalev A.V., Wei Yuan, Medvedeva I.V. The estimate of the peak density of atomic oxygen between 2000 and 2004 at 52° N. *Proc. SPIE*. 2009, vol. 7296, 72960M, pp. 72960M-1–72960M-6. DOI: 10.1117/12.823817.

Hu Y.Q., Peng Z., Wang C., Kan J.R. Magnetic merging line and reconnection voltage versus IMF clock angle: Results from global MHD simulations. *J. Geophys. Res.* 2009, vol. 114, A08220. DOI: 10.1029/2009JA014118.

Liu W., Wang C., Shen X., Wu J., Blanc M., Yan Y., Fu S., et al. Yang F. International Meridian Circle Program. *Chin. J. Space Sci.* 2020, vol. 40, no. 5, pp. 723–725. DOI: 10.11728/cjss2020.05.723.

Liu W., Blanc M., Wang C., Xu J., Li H., Ren L., Liu Z., et al. Progress of International Meridian Circle Program. *Chin. J. Space Sci.* 2022, vol. 42, no. 4, pp. 584–587. DOI: 10.11728/cjss2022.04.yg10.

Matvienko G.G., Marichev V.N., Bobrovnikov S.M., Yakovlev S.V., Chistilin A.Yu., Sautkin V.A. Mesostratospheric lidar for the heliogeophysical complex. *Solar-Terr. Phys.* 2020, vol. 6, iss. 2, pp. 74–83. DOI: 10.12737/ stp-62202007.

Medvedev A.V., Potekhin A.P., Setov A.G., Kushnarev D.S., Lebedev V.P. All-atmosphere IS-MST radar. *Solar-Terr. Phys.* 2020, vol. 6, iss. 2, pp. 41–48. DOI: 10.12737/stp-62202004.

Mishin V.V., Mishin V.M., Karavaev Yu., Han J.P., Wang C. Saturation of the Poynting flux and the finite compressibility of the magnetosphere during superstorms: Results of the magnetogram inversion technique and global PPMLR-MHD model. *Geophys. Res. Lett.* 2016, vol. 43, pp. 6734–6741. DOI: 10.1002/2016GL069649.

Pipin V.V., Zhang H., Sokoloff D.D., Kuzanyan K.M., Gao Y. The origin of the helicity hemispheric sign rule reversals in the mean-field solar-type dynamo. *Monthly Not. Royal Astron. Soc.* 2013, vol. 435, pp. 2581–2588. DOI: 10.1093/mnras/stt1465.

Pirog O.M., Besprozvannaya A.S., Shchuka T.I. Dependence of the location of the main ionospheric through poleward edge on geomagnetic activity indexes and IMF parameters. *Studies on Geomagnetism, Aeronomy, and the Physics of the Sun*. 1997, vol. 105, pp. 122–128. (In Russian).

Pirog O.M., Polekh N.M., Romanova E.B., Zherebtsov G.A., Shi J.K., Wang X. Study of ionospheric response to magnetic superstorms in the East Asian sector. *J. Atmos. and Solar Terr. Phys.* 2010, vol. 72, no. 2-3, pp. 164–175. DOI: 10.1016/j.jastp.2009.11.004.

Rakhmatullin R.A. Substorm in geomagnetic pulsations. Experiments at meridional chains of stations on the Eurasian continent in 1973–2003. *Thesis for the degree of Doctor of Science (Phys&Math)*. Irkutsk, 2010, 312 p. (In Russian).

Ratovsky K.G., Shi J.K., Oinats A.V., Romanova E.B. Comparative study of high-latitude, mid-latitude and low-latitude ionosphere on basis of local empirical models. *Adv. Space Res.* 2014, vol. 54, no. 3, pp. 509–516. DOI: 10.1016/j.asr.2014.02.019.

Shi J.K., Wang G.J., Reinisch B.W., Shang S.P., Wang X., Zherebtsov G.A., Potekhin A. Relationship between strong range spread F and ionospheric scintillations observed in Hainan from 2003 to 2007. *J. Geophys. Res.* 2011, vol. 116, A08306. DOI: 10.1029/2011JA016806.

Sych R., Wang M. Fine wave dynamics in umbral flash sources. *Astron. Astrophys.* 2018, vol. 618, id. A123. DOI: 10.1051/0004-6361/201732139.

The 20th Anniversary of China-Russia Joint Research Center on Space Weather. Irkutsk, Vostsibpechat Publ., 2021, 234 p.

Vasilyev R.V., Setov A.G., Frolov V.L., Ratovsky K.G., Beletsky A.B., Oinats A.V., Yasyukevich Yu.V., Medvedev A.V. Modern heating facility for research into the mid-latitude ionosphere. *Solar-Terrestrial Phys.* 2020a, vol. 6, iss. 2, pp. 49–62. DOI: 10.12737/stp-62202005.

Vasilyev R.V., Artamonov M.F., Beletsky A.B., Zorkaltseva O.S., Komarova E.S., Medvedeva I.V., Mikhalev A.V., et al. Scientific goals of optical instruments of the National Heliogeophysical Complex. *Solar-Terr. Phys.* 2020b, vol. 6, iss. 2, pp. 84–97. DOI: 10.12737/stp-62202008.

Wang C., Han J.P., Li H., Peng Z., Richardson J.D. Solar wind-magnetosphere energy coupling function fitting: Results from a global MHD simulation. *J. Geophys. Res.: Space Phys.* 2014, vol. 119, pp. 6199–6212. DOI: 10.1002/2014JA019834.

Wang Chi, Chen Zhiqing, Xu Jiyao. Introduction to Chinese Meridian Project — Phase II. *Chin. J. Space Sci.* 2020, vol. 40, no. 5, pp. 718–722. DOI: 10.11728/cjss2020.05.718.

Wang Chi, Xu Jiyao, Lu Daren, Yue Xinan, Xue Xianghui, Chen Gang, Yan Jingye, et al. Construction Progress of Chinese Meridian Project Phase II. *Chin. J. Space Sci.* 2022, vol. 42, no. 4, pp. 539–545. DOI: 10.11728/cjss2022.04.yg09.

Wang Chi, Michel Blanc, Zhang Shunrong, Denardini Clezio Marcos, Liu William, Shen Xuhui, Wu Jian, et al. Progress of International Meridian Circle Program. *Chin. J. Space Sci.* 2024, vol. 44, no. 4, pp. 1–5. DOI: 10.11728/cjss2024.04.2024-yg24.

Yuan D., Nakariakov V.M., Huang Z., Li B., Su J., Yan Y., Tan B. Oscillations in a sunspot with light bridges. *Astrophys. J.* 2014, vol. 792, no. 1. DOI: 10.1088/0004-637X/792/1/41.

Zherebtsov G.A., Pirog O.M., Razuvaev O.I. Structure and dynamics of the high-latitude ionosphere. *Studies on Geomagnetism, Aeronomy, and the Physics of the Sun*. 1986, vol. 76, pp. 165–177. (In Russian).

Zherebtsov G.A. Complex of heliogeophysical instruments of new generation. *Solar-Terr. Phys.* 2020, vol. 6, iss. 2, pp. 3–13. DOI: 10.12737/stp-62202001.

Zherebtsov G.A., Shi Jiankui, Perevalova N.P., Polekh N.M., Zolotukhina N.A. *Ionospheric disturbances in East-Asian region*. Moscow, GEOS Publ., 2021, 339 p.

URL: http://imcp.ac.cn/en/about/planning/ (accessed March 10, 2025).

URL: https://www.meridianproject.ac.cn/mcmp/ (accessed March 10, 2025).

URL: https://www.meridianproject.ac.cn/en/ (accessed March 10, 2025).

URL: https://www.meridianproject.ac.cn/bi/ (accessed March 10, 2025).

URL: http://imcp.ac.cn/en/about/objectives/ (accessed March 10, 2025).

URL: http://imcp.ac.cn/en/ (accessed March 10, 2025).

URL: http://imcp.ac.cn/en/about/sw/ (accessed March 10, 2025).

URL: http://ngkran.ru/ (accessed March 10, 2025).

URL: http://badary.iszf.irk.ru (accessed March 10, 2025).

How to cite this article

Medvedev A.V., Zherebtsov G.A., Perevalova N.P. Chinese-Russian Joint Research Center on Space Weather: Results and prospects. *Sol.-Terr. Phys.* 2025, vol. 11, iss. 3, pp. 98–113. DOI: 10.12737/stp-113202512.

THE RAYLEIGH — TAYLOR INSTABILITY AS A TRIGGER OF SOLAR FLARES

A.V. Stepanov
Central Astronomical Observatory at Pulkovo,
St. Petersburg, Russia, stepanov@gaoran.ru
Ioffe Institute,
St. Petersburg, Russia

V.V. Zaitsev
Institute of Applied Physics RAS,
Nizhny Novgorod, Russia, za130@ipfran.ru

Abstract. The review of authors' papers is devoted to the essential role of the Rayleigh — Taylor instability (RTI) as a trigger of flare energy release. We have analyzed two cases of RTI: near coronal loop footpoints and at the loop top. RTI near loop footpoints requires pre-heating of chromospheric plasma. This pre-heating can be realized due to Joule dissipation in partially ionized plasma under condition of the Cowling resistivity. RTI at the loop top arises in current-carrying coronal loop loaded by prominence. We have determined the conditions of RTI as a flare trigger in both cases. It is shown that RTI generates super-Dreicer electric field in the chromospheric parts of a loop. This is the promising solution of longstanding "number problem" of particle acceleration. RTI can be also a cause of prompt (~10 s) hot onset precursor events (HOPE).

Keywords: Sun, flare trigger, Joule dissipation, particle acceleration.

INTRODUCTION

The epigraph to this review article is a quotation from Cornelis de Jager "Flares are different". Indeed, the observed variety of flares does not fit into the Procrustean bed of the standard model. In recent decades, it has been found that in most flares flare plasma is heated before the appearance of hard X-ray caused by electrons accelerated in a flare [Veronig et al., 2002; Sharykin, Kosovichev, 2015; Meshalkina, Altyntsev, 2024]. Moreover, in some cases there is unusually rapid (~10 s) pre-flare heating of chromospheric plasma up to 10–15 MK at coronal magnetic loop footpoints [Hudson et al., 2021]. A number of recent works have examined the nature of hot onset precursor events (HOPE) (see, e.g., [da Silva et al., 2023; Battaglia et al., 2023]). Nevertheless, the mechanism of the rapid heating has not been determined yet.

The problem of explaining the huge number of charged particles accelerated in a flare remains unclear in the physics of solar flares [Hoyng et al., 1976]. It has been established that a solar flare in the impulsive phase produces ~10^{37} energetic (>20 keV) electrons per second, and the total number of such electrons during the impulsive phase (~100 s) is 10^{39}[Miller et al., 1997]. This exceeds the number of thermal electrons in the coronal part of the magnetic loop: $(1\div5)10^{37}$ [Emslie, Henoux, 1995]. In giant flares, the number of electrons with energies >20 keV can be as large as 10^{41} [Kane et al., 1995], i.e. the entire plasma in the flare loop should be in acceleration mode. One possible solution to this problem is acceleration in denser layers of the solar atmosphere.

An important problem is to identify the trigger of solar flares. A number of possible flare triggers have been discussed in the literature: thermal trigger [Syrovatskii, 1976; Ledentsov, 2021], topological trigger [Somov, 2008; Kusano et al., 2012], interaction between magnetic loops [Kumar et al., 2010], trigger prominence [Pustil'nik, 1974; Zaitsev, Stepanov, 1992]. In this paper, we investigate the role of Rayleigh — Taylor instability (RTI) as a solar flare trigger in the typical magnetic configuration — the current-carrying flare loop. We examine two cases of RTI development: near loop footpoints and at its top due to prominence activity. We also study two important consequences of RTI development as a flare trigger: plasma heating due to Joule dissipation and acceleration of charged particles.

RAYLEIGH — TAYLOR INSTABILITY AT FLARE LOOP FOOTPOINT

We proceed from the representation of a flare loop as an equivalent electric circuit [Alfvén, Carlqvist, 1967], when an electric current is generated by convective motions in the photosphere, and the current flowing through the loop is closed either through the photosphere at the level of $\tau_{5000}=1$ [Zaitsev, Stepanov, 1992; Zaitsev et al., 2020] or through the loop surface [Melrose, 1991]. Figure 1 schematically shows a flare loop footpoint located in the partially ionized chromosphere. RTI is caused by centrifugal acceleration with an appropriate magnetic field curvature with radius R_c [Zaitsev, Stepanov, 2015]:

$$\vec{g}_c = \frac{\vec{f}_c}{\rho} = \frac{2k_B T}{m_i R_c^2}\frac{n}{n+n_a}\vec{R}_c, \qquad (1)$$

where ρ is the plasma number density; k_B is the Boltzmann constant; T is the plasma temperature at the outer boundary of the flux tube; n, n_a are electron and neutral atom densities respectively. The appropriate curvature of the magnetic field of a loop is formed in the region of a sharp increase in the width of the loop due to a decrease in external pressure; therefore, the vertical size of the RTI region can be estimated as $l\approx(0.5\div1.0)\,10^8$ cm. The dynamic pressure gradient of the convective flow
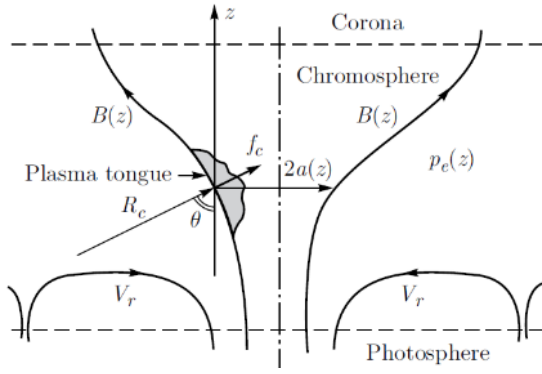
Figure 1. Scheme of plasma injection from the chromosphere into the magnetic loop footpoint during the development of RTI: f_c is the centrifugal force; $a(z)$ is the radius of the magnetic flux tube; p_e is the external gas pressure; θ is the angle between the direction of the radius of curvature and the vertical [Zaitsev, Stepanov, 2015]

also acts on the outer boundary of the tube. $-m_i(n+n_a)\partial V_r^2/\partial r$. Assuming $V_r(r,t) = -V_0(t)r/a$, we obtain the condition for RTI development (ballooning mode) $g_c + \frac{2V_0^2}{a}\sin\theta - g\cos\theta > 0$, which at $H(z) = \frac{k_B T_e(z)}{m_i g} > a(z)$ takes the form [Zaitsev, Stepanov, 2015]:

$$\frac{nT}{2(n+n_a)T_e} + \frac{8HV_0^2(t)}{a^2 g} > 1. \quad (2)$$

Here, T_e is the temperature inside the magnetic flux tube; g is acceleration of gravity on the Sun. It follows from (2) that ballooning instability develops when the outer shell of the flux tube is heated and the convective plasma flow velocity (dynamic force) increases sharply. To determine the temperature to which the outer shell should be heated, we can use the modified Saha formula for hydrogen atom [Brown, 1973]:

$$\frac{(n+n_a)x^2}{1-x} = $$
$$= 7.2 \cdot 10^{18} T^{1/2} \exp\left(-6.583 - \frac{1.185 \cdot 10^5}{T}\right), \quad (3)$$

where $x = n/(n+n_a)$ is the degree of ionization. It follows from (3) that for a chromospheric layer with a density $n+n_a = 10^{15}$ cm^{-3} instability criterion (2) is fulfilled at relatively low plasma stream velocities $V_0(t)$ if the flux tube shell is heated to $T \approx 2.5 \cdot 10^4$ K. The degree of ionization x runs to 90 %, and the instability criterion takes the form $xT/(2T_e) \approx 2.6 > 1$. In this case, the typical RTI time in the magnetic flux tube with radius $a \approx (3 \div 5)10^7$ cm

$$\tau_{RT} \approx \left(3^{3/2} a T_e/4\pi T g\right)^{1/2} \approx 10 \text{ s.} \quad (4)$$

This value is of the order of a/V_{Ti} that takes the external plasma tongue to penetrate the magnetic flux tube with the thermal velocity of ions.

The Rayleigh—Taylor instability causes disturbance

of the magnetic field of a loop and compression of the current channel leading to amplification of current and its increased dissipation due to ion-neutral particle collisions in chromospheric plasma.

ELECTRON ACCELERATION IN INDUCED ELECTRIC FIELDS

Electric field acceleration of charged particles is most effective. When the chromospheric plasma tongue penetrates into the loop footpoint at a velocity $V_r(r,t) = -V_0(t)r/a$ the magnetic field components B_z and $B_\varphi = 2I/(ca)$, and hence the current, according to $\partial\vec{B}/\partial t = \text{rot}\left[\vec{V}\times\vec{B}\right]$, evolve as follows:

$$B_\varphi(r,t) = B_{\varphi 0}\frac{r}{a}\exp\left(\frac{2}{a}\int_0^t V_0(t')dt'\right),$$
$$B_z(r,t) = const \cdot \exp\left(\frac{2}{a}\int_0^t V_0(t')dt'\right). \quad (5)$$

From Formula (5) and $\text{rot}\vec{E} = -(1/c)\partial\vec{B}/\partial t$, we can show that with the development of RTI the induced electric field $\vec{E} = -(1/c)\left[\vec{V}\times\vec{B}\right]$ is perpendicular to the magnetic field, so it does not accelerate charged particles. However, during the time $\tau_A \approx l/V_A \approx 5 \div 10$ s, where $l \approx (0.5 \div 1.0)10^8$ cm is the vertical extent of the RTI region, the magnetic field tension pulse B_φ "escapes" from the instability region at an Alfvén velocity V_A as a pulse of longitudinal electric current

$$\frac{\partial^2 B_\varphi}{\partial t^2} = \frac{B_{z0}^2}{4\pi\rho}\frac{\partial^2 B_\varphi}{\partial z^2}. \quad (6)$$

The magnetic pressure pulse $B_z(r,t)$ remains in the region of plasma tongue penetration, exciting FMS oscillations (Figure 2).

If the current is low ($B_\varphi^2 \leq 8\pi p$, where p is the plasma gas pressure), the magnetic field disturbance is balanced by the gas pressure disturbance and $E_z = 0$. An electric current pulse propagates along the loop as a linear Alfvén wave. At $B_\varphi^2 \gg 8\pi p$, an induced electric field appears which is directed along the magnetic field of the loop B_{z0}. This is due to the fact that at $B_\varphi^2 \gg 8\pi p$ magnetic field disturbances are no longer balanced by the gas pressure gradient as in the linear Alfvén pulse, but velocity perturbations occur along the flux tube radius and along the undisturbed magnetic field B_{z0}, which lead to the generation of the electric field component B_φ nonlinear in field and current along the flux tube axis [Zaitsev et al., 2016]:

$$\frac{\partial E_z}{\partial r} = -\frac{1}{c}\frac{B_\varphi^2}{4\pi\rho V_A^2}\frac{\partial B_\varphi}{\partial t}. \quad (7)$$

The electric field average with respect to the loop cross-section

$$\overline{E_z} = \frac{2I_0^2 V_A}{5c^4 B_{z0}^2} \frac{\partial I_0}{\partial \xi}, \; \xi = z - V_A t. \tag{8}$$

For example, for $n_a = 10^{14}$ cm^{-3}, $B_{z0} = 300$ G, $I_0 = 10^{10}$ A, find $\overline{E_z} \approx 0.1$ V/cm, i.e. electrons can accelerate at a length $l \approx (0.5 \div 1.0) 10^8$ cm to an energy of ~10 MeV. The ratio of the maximum field to the Dreiser field $E_D = 6 \cdot 10^{-8} n/T$ V/cm, when plasma electrons go into escape mode, is [Zaitsev et al., 2016]

$$\frac{E_{zm}}{E_D} = 2.2 \cdot 10^8 \frac{T I_0^3 (A)}{a^2 B_{z0} n^{3/2} \Delta \xi}. \tag{9}$$

Figure 3 displays generation regions of electric fields, large and small Dreiser fields for typical conditions in the chromosphere.

Why are electric fields of the order of the Dreiser field necessary for effective acceleration of particles in a
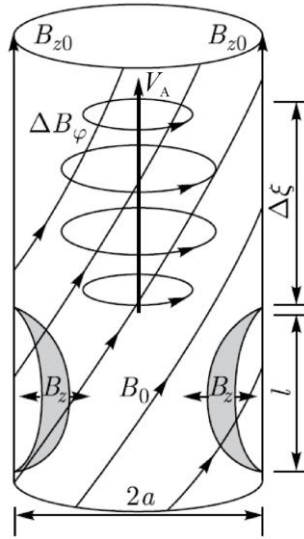

Figure 2. Magnetic field disturbance in the flux tube due to the development of RTI. Here, *l* is the vertical size of the penetrating external plasma tongue; *a* is the radius of the magnetic flux tube; $\Delta\xi$ is the size of the electric current pulse along B_{z0} [Zaitsev et al., 2016]
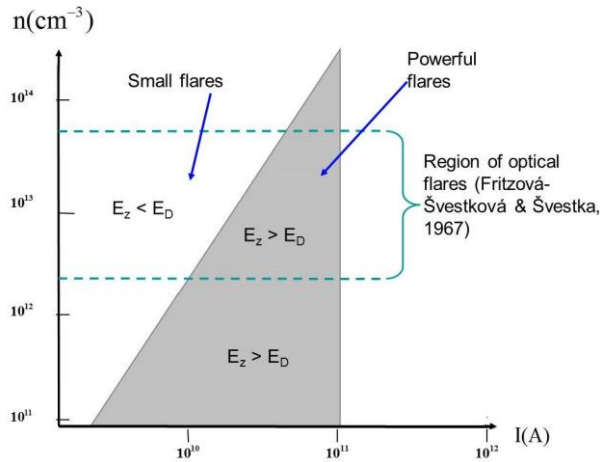

Figure 3. Plasma number density — electric current plot for $a = 10^7$ cm, $B_{z0} = 2 \cdot 10^3$ G, $T = 2 \cdot 10^4$ K, $\delta\Delta\xi = 5 \cdot 10^7$ cm. Regions of sub- and super-Dreicer electric fields (gray) are shown which are formed at the leading edge of a current pulse propagating along a magnetic loop from the RTI region [Zaitsev et al., 2016]

flare? In the chromospheric part of the loop, the number of particles in the column from the temperature minimum to the transition region between the chromosphere and the corona averages ~$5 \cdot 10^{39}$. This is enough to provide injection of the required number of electrons ~10^{39} into the acceleration mode [Miller et al., 1997]. Since the total number of accelerated electrons does not differ much from the total number of particles in the chromospheric part of the loop, this indicates a high efficiency of the acceleration mechanism when the number density of accelerated electrons is comparable in order of magnitude to the background plasma number density. This means that when accelerated by regular electric fields, the fields should either be close to or exceed the Dreiser field. That is why, in sufficiently powerful flares, acceleration of electrons should most likely occur in the chromosphere. Otherwise, it is difficult to explain the high number density of accelerated electrons $n \sim 10^{10} - 10^{11}$ cm^{-3} with an energy >20 keV. Electric fields larger than the Dreiser field can appear at the front of an electric current pulse generated in a loop due to the development of RTI if the current amplitude exceeds 10^{10}A (see Figure 3). The presented results on particle acceleration in the chromosphere can be considered as *déjà vu* — return to the concept of a chromospheric flare [Giovanelli, 1946; Fritzova-Švestková, Švestka 1967].

FLARE ENERGY RELEASE INITIATED BY PROMINENCE

Some authors (see, e.g., [Zimovets et al., 2020]) believe that a shortcoming of the current interruption model is the inability to explain the observed energy release at the loop top, which occurs in hard X-ray "above-the-loop-top flare" [Masuda et al., 1994]. We show that RTI caused by prominence at flare loop tops can explain this phenomenon. For the first time, the possibility of initiating a flare in magnetic loops loaded with prominence (filament) was observed by Pustil'nik [1974] under the assumption of magnetic reconnection. In fact, a dense $(n_a + n \sim 10^{11} - 10^{12}$ cm$^{-3})$ and relatively cold $(T \sim 0.01$ MK) prominence of thickness $D \approx (3 \div 10)10^8$ cm, located above a flare loop or an arcade of loops with $T \sim (1 \div 10)$ MK and $n \sim 10^9$ cm^{-3}, represents a classical RTI pattern: heavy liquid over light (Figure 4). An appropriate magnetic field curvature is also available. As a result, partially ionized plasma tongues penetrate into the hot current-carrying loop, which lead to increased Joule dissipation under the Cowling resistivity and to acceleration of charged particles, described in the previous section, in induced electric fields. If loops are sequentially arranged in height (see Figure 4), there may occur a Masuda flare effect since the increased plasma number density provides a target thick enough for generating hard X-ray by electrons accelerated at loop tops. This is, briefly, our scenario of a flare trigger due to prominence-induced RTI.

Accordingly, we make some estimates. RTI (ballooning mode) occurs if the prominence thickness $D > D_c = B^2/(10\pi\rho g)$ [Pustil'nik, 1974]. Given $\rho = m_i (n_a + n) = 5 \cdot 10^{-13}$g/cm^3 and $B = 10$ G, we find $D_c = 2 \cdot 10^8$ cm, which is less than the observed filament thickness.

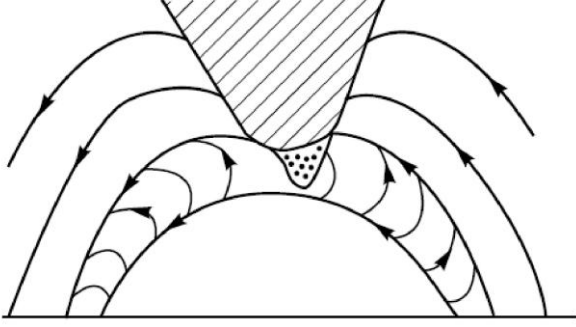The Joule dissipation rate per unit volume of magnetic flux tube is determined as [Stepanov, Zaitsev, 2018]

Figure 4. Flare loop-prominence interaction. The tongue of dense partially ionized plasma of prominence penetrates a loop due to RTI [Zaitsev, Stepanov, 1992]

$$q = \left(\mathbf{E} + \frac{1}{c} \mathbf{V} \times \mathbf{B} \right) \mathbf{j} =$$
$$= \frac{j_z^2}{\sigma} + \frac{F^2 B_\varphi^2 j_z^2}{(2-F) c^2 n m_i v_{ia}'} \ \text{erg/(cm}^3 \text{s)}, \tag{10}$$

where $j_z = I/(\pi a^2)$, $\sigma = ne^2/(m_e v_{ei})$ is the classical conductivity (Spitzer), $F = n_a/(n+n_a)$, $B_\varphi = 2I/(ca)$, $v_{ia}' \approx 1.6 \cdot 10^{-11} F(n+n_a)\sqrt{T}$. The second term in (10) describes dissipation due to the Cowling resistivity associated with ion-atom collisions, which in the case of injection of neutral particles from a prominence to a magnetic loop is predominant. Then, the dissipation rate can be represented as

$$q = \frac{4 F^2 I^4}{(2-F) \pi^2 c^4 a^6 n m_i v_{ia}'} \ \text{erg/cm}^3 \text{s} \tag{11}$$

Assuming $I=10^{11}$A, $F=0.5$, the loop radius in the corona $a=10^8$ cm, $n=10^9$ cm^{-3}, $T=10^4$ K, we obtain $q \approx 4 \cdot 10^3$ erg/(cm^{3}s). If the energy release region at the loop top is $\sim 3 \cdot 10^{25}$ cm^3, we get an energy release capacity of $\sim 10^{29}$ erg/s.

The number of energetic electrons accelerated at the top of the current–carrying loop when the prominence plasma tongue penetrates it can be estimated as $N \approx 2\pi n \Delta x D V_{Ti} \Delta t$. For the time $\Delta t \approx 100$ s at $n \approx 3 \cdot 10^{11}$ cm^{-3}, the length of the tongue penetrating the loop top $\Delta x \approx D \approx 3 \cdot 10^8$ cm, $V_{Ti}(T=10^4$ K$) \approx 10^6$ cm/s, we have $N \approx 2 \cdot 10^{37}$. This number of accelerated electrons corresponds to a medium power flare.

PULSE HEATING OF THE CHROMOSPHERE AND PROMPT FLARE PRECURSORS

Among HOPEs, there are also unusually prompt flare precursors. For example, Hudson et al. [2021] using observational data from GOES and RHESSI have shown that before the flare impulsive phase on January 7, 2017 the chromospheric coronal magnetic loop footpoints rapidly, for ~10 s, heated up to a temperature 10–15 MK, being almost the same for 1.5 min. The emis-

sion measure of radiating loop footpoints slowly increased and, according to GOES data, ran to $n^2 V \approx 10^{47}$ cm^{-3}. With loop footpoint volumes of $V \approx 5 \cdot 10^{23} \div 10^{25}$ cm^3, this leads to an estimate of plasma number density $n \approx (3.0 \div 4.5) 10^{11}$ cm^3 near the precursor region, which is typical of the chromosphere. During the heating phase, the chromosphere was not heated by accelerated electrons. A similar result has been obtained in a number of other papers [Awasthi, Jain, 2011; Battaglia et al., 2023]. Thus, pre-flare heating is not related to collisional heating of the active region by non-thermal electrons, which contradicts the standard flare model.

We assume that the pre-flare heating is linked to a sharp increase in the longitudinal electric current (B_φ) during the development of RTI, described in the previous sections, at loop footpoints. A pulse of high-amplitude longitudinal electric current remains in the chromosphere for $\tau_A \approx l/V_A \approx 5 \div 10$ s. During this time, the current heats the chromospheric footpoint to $T \sim 10^7$ K, forming an X-ray flare precursor. Then, the pulse of the longitudinal electric current leaves the instability region as a nonlinear Alfvén wave (see Figure 2) with the induced electric field that accelerates electrons to energies sufficient to form a solar flare hard X-ray source. This is a possible scenario for a flare with a precursor [Zaitsev, Stepanov, 2025].

Explore the conditions for the formation of such a prompt flare precursor. First, from (11), find the time of heating of magnetic loop footpoints to $T \geq 10^7$ K by electric currents. We can ignore dissipation due to the Spitzer resistivity since at $\sim 3 \cdot 10^{11}$ A such resistivity is significant only for heights <1000 km [Stepanov et al., 2024]. When estimating the heating time, neglect the radiative losses caused by high temperatures, as well as the thermal conductivity along the loop, which is suppressed by a significant azimuthal magnetic field component B_φ associated with the longitudinal current j_z. Assume that at $T > 10^6$ K the relative number density of neutrals depends on temperature in the same way as in the quasi-stationary corona, i.e. $F \approx 0.15/T$ [Verner, Ferland, 1996; Zaitsev, 2015]. From the heat balance equation

$$\frac{1}{\gamma-1} \frac{\partial p}{\partial t} = 2.6 \cdot 10^{-9} \frac{I^4}{n^2 a^2 T^{3/2}},$$
$$p = 2 k_B nT, \gamma = \frac{5}{3} \tag{12}$$

determine the temperature dependence on time

$$T^{5/2} - T_0^{5/2} = 3.25 \cdot 10^{-9} (\gamma-1) \frac{I^4}{k_B n^3 a^6} t. \tag{13}$$

From (13), find the heating time of the chromospheric footpoints $t_H \approx 10^4$ s ~ 3 hr to $T \geq 10^7$ K at $I = 10^{12}$ A, $n = 4 \cdot 10^{11}$ cm^{-3} and $a = 3 \cdot 10^7$ cm. Such a long heating time means that we cannot use the formula for the relative number density of neutrals for the quasi-stationary corona, but we should take into account the

pulsed nature of heating and the nonstationarity of ionization process. The rate of change in the plasma electron density during neutral atom ionization by electron impact can be estimated from the equation

$$\frac{dn}{dt} = n n_a \left\langle \sigma_H V_{Te} \right\rangle. \tag{14}$$

The hydrogen atom ionization cross-section $\sigma_H \approx 2 \cdot 10^{-17}$ cm^2 at $T \approx 10^7$ K [Andreev, 2010]. The heating time of precursor plasma by electric current $\tau_H \approx 10$ s. During this time, plasma at the loop footpoint is only partially ionized, retaining a certain number of neutrals. The number density of neutrals at the heating stage is estimated from Equation (14):

$$n_a \approx \frac{\partial n / \partial t}{n \left\langle \sigma_H V_{Te} \right\rangle} \approx \frac{1}{\tau_H \left\langle \sigma_H V_{Te} \right\rangle} \approx 4 \cdot 10^6 \text{ cm}^{-3}. \tag{15}$$

With the plasma number density $n \approx 4 \cdot 10^{11}$ cm^{-3} in the precursor generation region, the relative number density of neutrals $F = n_a / n = 10^{-5}$. It is three orders of magnitude higher than the relative number density of neutrals in the corona with $T = 10^7$ K $\left(F \approx 0.15 / T \approx 10^{-8}\right)$. This difference is caused by the fact that when a strong electric current is pulsed on the heating rate is higher than the ionization rate (ionization does not keep up with heating). Therefore, when a current pulse "escapes" from the flare precursor region in the form of a nonlinear Alfvén wave, the residual number density of neutrals in this region remains quite high [Zaitsev, Stepanov, 2025]. To determine the current required to heat the precursor to $T \approx 10^7$ K during the time τ_H 10 s at $F \approx 10^{-5}$, we use Equation (12) from which we find the heating time.

$$\tau \approx \frac{1.6 \cdot 10^{-8} n^3 a^6 T^{3/2}}{F I^4} \text{ s}. \tag{16}$$

It follows from (16) that for the region with $n = 4 \cdot 10^{11}$ cm^{-3}, $a = 3 \cdot 10^7$ cm, $F = 10^{-5}$ plasma heating to $T \approx 10^7$ K during the time $\tau_H \leq 10$ s is possible at $I \geq 10^{12}$ A. For the plasma number density $n = 10^{11}$ cm^{-3}, the critical current $I \geq 5 \cdot 10^{11}$ A. Such electric currents are recorded in flare precursors [Wang et al., 2017]. Since the heating time is $\sim I^{-4}$, prompt X-ray precursors at currents lower than 10^{11} A are unlikely to exist.

CONCLUSION

We have shown that the Rayleigh — Taylor instability is a flare trigger both at loop footpoints and at their tops. RTI at the loop footpoint leads to the intrusion of the surrounding chromospheric plasma into the loop at a velocity $\sim V_{Ti}$ during the time $\sim a / V_{Ti}$ ~10 s, with the longitudinal electric current increasing $I_z = I_0 \exp\left(\frac{2}{a} \int_0^t V(t') dt'\right)$.

Joule dissipation with increased Cowling resistivity causes the chromosphere to heat up at loop footpoints and a significant number of electrons to accelerate to energies ~1–3

MeV in induced electric fields. At the same time, for $\sim 10^{38}$–10^{39} electrons to accelerate during a flare, electric fields should be either close to the Dreicer field or higher (super-Dreicer). Our results on energy release and particle acceleration in the chromosphere can be considered as *déjà vu* — return to the concept of a chromospheric flare.

The Rayleigh—Taylor instability at tops of flare loops, loaded with a dense cold filament, initiates phenomena similar to those described for loop footpoints. In this case, the filament injects a significant number of neutral particles into current-carrying magnetic loops, which dramatically increase the Joule dissipation at loop tops, accompanied by charged particle acceleration. Thus, we can explain flares of the "above-the-loop-top" type [Masuda et al., 1994] in the current-carrying magnetic loop model.

An important consequence of RTI as a solar flare trigger is the possibility of explaining prompt (~10 s) hot (10–15 MK) solar flare precursors. We have shown that if the pulse current exceeds 10^{11} A, the Joule plasma heating rate overtakes the ionization rate, which leads to increased electric current dissipation. Note that preheating of flare plasma to a temperature >12 MK is also a necessary condition for accelerating high-energy (>100 MeV) protons [Struminsky et al., 2024]. Moreover, understanding the physical nature of the solar flare trigger is of paramount importance for predicting space weather and mitigating its impact on technological infrastructure.

REFERENCES

Alfvén H., Carlqvist P. Currents in the solar atmosphere and a theory of solar flares. *Solar Phys.* 1967, vol. 1, p. 220–228. DOI: 10.1007/BF00150857.

Andreev G.V. Calculation of ionization cross-section by electron shock for hydrogen and nitrogen atoms. *Physical-Chemical Kinetics in Gas Dynamics*. 2010, vol. 9, pp. 1–2. (In Russian).

Awasthi A.K., Jain R. Multi-wavelength diagnostics of precursor phase in solar flares. *First Asia-Pacific Solar Physics Meeting. Astron. Soc. India Conf.* 2011, vol. 2, pp. 297–305.

Battaglia A.F., Hudson H., Warmuth A., et al. The existence of hot X-ray onsets in solar flares. *Astron. Astrophys.* 2023, vol. 679, article number A139. DOI: 10.1051/0004-6361/202347706.

Brown J.C. On the ionization of hydrogen in optical flares. *Solar Phys.* 1973, vol. 29, pp. 421–427. DOI: 10.1007/BF00150822.

da Silva D. F., Hui L., Simoes P.J.A., et al. Statistical analysis of the onset temperature of solar flares in 2010–2011. *Monthly Notices of the Royal Astronomical Society.* 2023, vol. 525, iss. 3, pp. 4143–4148. DOI: 10.1093/mnras/stad2244.

Emslie A.G., Henoux J.-C. The electrical current structure associated with solar flare electrons accelerated by large-scale electric fields. *Astrophys. J.* 1995, vol. 446, p. 371. DOI: 10.1086/175796.

Fritzová-Švestková L., Švestka Z. Electron density in flares. II Results of measurement. *Solar Phys.* 1967, vol. 2, pp. 87–97. DOI: 10.1007/BF00155894.

Giovanelli R.G. A theory of chromospheric flares. *Nature.* 1946, vol. 158, pp. 81–82. DOI: 10.1038/158081a0.

Hoyng P., Brown J.C., van Beek H.F. High time resolution analysis of solar hard X-ray flares observed on board the ESRO TD-1A satellite, *Solar Phys.* 1976, vol. 48, P.197–254. DOI: 10.1007/BF00151992.

Hudson H., Simoes P.J.A., Fletcher L., et al. Hot X-ray onsets of solar flares. *Monthly Notices of the Royal Astronomical Society.* 2021, vol. 501, iss. 1, pp. 1273–1281. DOI: 10.1093/ mnras/staa3664.

Kane S.R., Hurley K., McTiernan J.M., et al. Energy release and dissipation during giant solar flares. *Astrophys. J. Lett.* 1995, vol. 446, p. L47. DOI: 10.1086/187927.

Kumar P., Srivastava A.K., Somov, B.V., et al. Evidence of solar flare triggering due to loop-loop interaction caused by foot-point shear motion. *Astrophys. J.* 2010, vol. 723, pp. 1651–1664. DOI: 10.1088/0004-637X/723/2/1651.

Kusano K., Bamba Y., Yamamoto T.T. Magnetic field structures triggering solar flares and coronal mass ejections. *Astrophys. J.* 2012, vol. 760, no. 1, p. 31. DOI: 10.1088/0004-637X/760/1/31.

Ledentsov L. Thermal trigger for solar flares I: Fragmentation of the preflare current layer. *Solar Phys.* 2021, vol. 296, article number 74. DOI: 10.1007/s11207-021-01817-1.

Masuda S., Kosugi T., Hara H., et al. A loop-top hard X-ray source in a compact solar flare as evidence for magnetic reconnection. *Nature.* 1994, vol. 371, pp. 495–497. DOI: 10.1038/371495a0.

Meshalkina N.S., Altyntsev A.T. Heating manifestations at the onset of the 29 June 2012 flare. *Solar-Terrestrial Physics.* 2024, vol. 10, iss. 3, pp/ 1–17. DOI: 10.12737/stp-103202402.

Melrose D.B. Neutralized and unneutralized current patterns in the solar corona. *Astrophys. J.* 1991, vol. 381, p. 306. DOI: 10.1086/170652.

Miller J.A., Cargill P.J., Emslie A.G., et al. Critical issues for understanding particle acceleration in impulsive solar flares. *J. Geophys. Res.* 1997, vol. 102, pp. 14631–14659. DOI: 10.1029/97JA00976.

Pustil'nik L.A. Instability of quiescent prominences and the origin of solar flares. *Soviet Astronomy.* 1974, vol. 17, p. 763.

Sharykin I.N., Kosovichev A.G. Dynamics of electric currents, magnetic field topology, and helioseismic response of a solar flare. *Astrophys. J.* 2015, vol. 808, no.1. DOI: 10.1088/0004-637X/808/1/72.

Somov B.V. Magnetic reconnection and topological trigger in physics of large solar flares. ?2008, vol. 17, no. 2-3, pp. 421–454. DOI: 10.48550/arXiv.0901.4697.

Stepanov A.V., Zaitsev V.V. *Magnetospheres of Active Regions of the Sun and Stars.* Moscow, Fizmatlit Publ., 2018, 387 p. (In Russian).

Stepanov A.V., Zaitsev V.V., Kupriyanova E.G. Features of electric current dissipation in the solar atmosphere. *Geomagnetism and Aeronomy.* 2024, vol. 64, pp. 1203–1214. DOI: 10.1134/S001679322470030.

Struminsky A.B. Sadovsky A.M., Grogoryeva I.Yu. Criteria for forecasting proton events from real time solar observations. *Geomagnetism and Aeronomy.* 2024, vol. 64, no. 2, pp. 139–149. DOI: 10.1134/S0016793223600984.

Syrovatskii S.I. Current sheet characteristics and thermal trigger of solar flares. *Soviet Astronomy Letters.* 1976, vol. 2, p. 13.

Verner D.A., Ferland C.J. Atomic data for astrophysics. I. Radiative recombination rates for H-like, He-like, Li-like, and Na-like ions over a broad range of temperature. *Astrophys. J. Suppl. Ser.* 1996, vol. 103, no. 2, pp. 467–473. DOI: 10.1086/192284.

Veronig A., Vršnak B., Dennis B.R., et al. Investigation of the Neupert effect in solar flares. I. Statistical properties and the evaporation model. *Astron. Astrophys.* 2002, vol. 392, no. 2, pp. 699–712. DOI: 10.1051/0004-6361:20020947.

Wang H., Liu Ch., Ahn K., et al. High-resolution observations of flare precursors in the low solar atmosphere. *Nature Astronomy.* 2017, vol. 1, article number 0085. DOI: 10.1038/s41550-017-0085.

Zaitsev V.V. Ultrafine magnetic structures in the chromosphere. *Geomagnetism and Aeronomy.* 2015, vol. 55, pp. 846–849. DOI: 10.1134/S0016793215070294.

Zaitsev V.V., Stepanov A.V. Towards the circuit theory of solar flares. *Solar Phys.* 1992, vol. 139, pp. 343–356. DOI: 10.1007/BF00159158.

Zaitsev V.V., Urpo S., Stepanov A.V. Temporal dynamics of Joule heating and DC-electric field acceleration in single flare loop. *Astron. Astrophys.* 2000, vol. 357, pp. 1105–1114.

Zaitsev V.V., Stepanov A.V. Particle acceleration and plasma heating in the chromosphere. *Solar Phys.* 2015, vol. 290, pp. 3559–3572. DOI: 10.1007/s11207-015-0731-y.

Zaitsev V.V., Stepanov A.V. On the nature of fast X-ray precursors of solar flares. *Astronomy Lett.* 2025, vol. 51, no. 1. (In print).

Zaitsev V.V., Kronshtadtov P.V., Stepanov A.V. Rayleigh — Taylor instability and excitation of super-Dreicer electric fields in the solar chromosphere. *Solar Phys.* 2016, vol. 291, pp. 3451–3459. DOI: 10.1007/s11207-016-0983-1.

Zaitsev V.V., Stepanov A.V., Kronshtadtov P.V. On the possibility of heating the solar corona by heat fluxes from coronal magnetic structures. *Solar Phys.* 2020, vol. 295, article number 166. DOI: 10.1007/s11207-020-01732-x.

Zimovets I.V., Sharykin I.N., Gan W.Q. Relationships between photospheric vertical electric currents and hard X-ray sources in solar flares: Statistical study. *Astrophys. J.* 2020, vol. 891, no. 2. DOI: 10.3847/1538-4357/ab75be.

OBSERVATIONS OF LARGE-SCALE SOLAR MAGNETIC FIELDS
WITH A NEW CHINESE TELESCOPE CONSTRUCTED FOR THE INTERNATIONAL
MERIDIAN CIRCLE PROGRAM (IMCP)

M.L. Demidov (ID)
Institute of Solar-Terrestrial Physics SB RAS,
Irkutsk, Россия, demid@iszf.irk.ru
National Astronomical Observatories,
Chinese Academy of Sciences,
Beijing, China

X.F. Wang
National Astronomical Observatories,
Chinese Academy of Sciences,
Beijing, China, wxf@nao.cas.cn
State Key Laboratory of Solar Activity and Space Weather,
National Space Science Center,
Chinese Academy of Sciences,
Beijing, China

Y.Z. Sun
National Astronomical Observatories,
Chinese Academy of Sciences,
Beijing, China, syz@nao.cas.cn
State Key Laboratory of Solar Activity and Space Weather,
National Space Science Center,
Chinese Academy of Sciences,
Beijing, China

Y.Y. Deng
National Astronomical Observatories,
Chinese Academy of Sciences,
Beijing, China, dyy@nao.cas.cn
State Key Laboratory of Solar Activity and Space Weather,
National Space Science Center,
Chinese Academy of Sciences,
Beijing, China
School of Astronomy and Space Science,
University of Chinese Academy of Sciences,
Beijing, China

Abstract. One of the very important international events in space science that has happened recently is the launch of the International Meridian Circle Program (IMCP). A key element of IMCP is a quite new instrument — the Solar Full-disk Multi-layer Magnetograph (SFMM) installed at Gan Yu Solar Station (GYSS) of the Purple Mountain Observatory (Jiangsu Province). The main objective of this telescope is to provide data on distribution of magnetic fields across the solar surface, which is necessary for prediction of some space weather (SW) parameters since this information is actually the low boundary condition for corresponding numerical simulations.

There are plans to construct a network of such telescopes (similar to GONG or to ngGONG), so it is very important to test how reliable the measurements of weak large-scale magnetic fields (LSMF) are with these instruments. It is just LSMF, not strong magnetic fields in active regions (which are relatively easy to measure), that determines the structure of the heliosphere. To do this, using first observations with SFMM at GYSS, is the main purpose of this study.

After a brief description of the instrument and some methodical issues, we present the results of comparison of SFMM observations with the Wilcox Solar Observatory (WSO) data. WSO measurements of LSMF are the most reliable in the world, and the results of such comparison are extremely important. We have found out that the correlation coefficient is high enough ($\approx$0.70) if we consider the whole range of measured strengths, but it is lower ($\approx$0.57) if the consideration is rerstricted only to relatively weak ($|B|\leq$10.0 G) fields. Note that there is a significant difference between regression coefficients (R) for these two cases: $R\approx$5.1 in first case and only $R\approx$1.8 in the second one. The reason of this is still unclear and will be the subject of future investigations.

Keywords: the Sun, solar magnetic field, space weather, telescope.

INTRODUCTION

Space weather (SW) is a rapidly developing branch of modern science that deals with detection and prediction of plasma parameters in near-Earth space and in the interplanetary medium, which originated from the Sun. Many aspects of SW are crucially important for a larger number of applied problems such as geomagnetic activity. No wonder it is precisely with SW that many modern large projects are connected. Two of them are carried out in China. The first is the International Meridian Circle Program, (IMCP), which has been launched recently; the second is the Advanced Space-based Solar Observatory (ASO-S, Chinese nickname Kuafu-1). It was launched on 8 October 2022. One of the ASO-S instruments is the Full-disk Vector Magnetograph (FMG), designed for full-disk observations of solar magnetic fields.

A key element of IMCP is a quite new instrument — the Solar Full-disk Multi-layer Magnetograph (SFMM), installed at Gan Yu Solar Station (GYSS) of the Purple Mountain Observatory, Jiangsu Province (see Figure 1). The new telescope was briefly described at the 15th Russian-Chinese Workshop on Space Weather [Sun et al., 2024]. The telescope is designed for observing magnetic fields and other parameters in the photosphere and chromosphere (it is therefore called "multi-layer"), covering the full disk quasi-simultaneously in four spectral lines: FeI 532.419, Hβ 486.134, Hα 656.28, and CaII 854.21 nm. Actually, SFMM consists of two telescopes on the same mount: the first one (Full-disk Magnetograph Telescope) is designed for magnetic observations in the first couple of lines; and the other (Full-disk Chromospheric Telescope), for observations of velocities and intensities in the second couple.

The aperture of the objective lens of this magnetograph telescope is 120 mm (the aperture of the chromospheric telescope is 200 mm), and the spatial resolution is higher than 2 arcsec. It alternately measures the solar magnetic field in two spectral lines: FeI 532.419 and Hβ 486.134 nm. For the FeI line there are 6 measurement positions in regular observations (and 21 in special) ranging from –0.016 to +0.016 nm from line center; for the Hβ line there are 12 measurement positions from –0.05 to +0.05 nm. The exposure time at one wavelength position is ~5–20 ms. The scanning time for a single spectral line is less than 15 min.

It is obvious that in some aspects SFMM reminds the old SMAT (Solar Magnetism and Activity Telescope) facility at Huairou Solar Observing Station (HSOS): it utilizes a DKDP electro-optical crystal as a polarization analyzer (PA), it uses the same spectral line FeI 532.419 nm, but it has as well a fundamental difference — Liquid Crystal Variable Retarder (LCVR) — an LCVR-based Lyot filter with fast scanning of the spectral line profile.

There are plans to develop a Chinese network of SFMM-like telescopes (similar to GONG or to ngGONG);

Figure 1. General view of the SFMM telescope at Gan Yu Solar Station of the Purple Mountain Observatory, Jiangsu Province. At the right bottom corner is a strip with sea

therefore, it is very important to test how reliable the measurements of weak large-scale magnetic fields (LSMF) are with these instruments. It is precisely LSMF, rather than strong magnetic fields in active regions which are relatively easy to measure (see the most recent comparison of local magnetic fields with Chinese data in Xu et al., [2024]), that determines the structure of the heliosphere (actually, LSMF synoptic maps provide low boundary conditions for corresponding numerical simulations [Demidov et al., 2023]). Especially if to take into account that observations of LSMF with SMAT (made in one wing of line profile) had some problems [Demidov et al., 2018]. The objective of this study is to make such a test, using first SFMM observations (at present, we consider only line-of-sight or longitudinal component).

RESULTS

It has long been recognized by solar physics community that the most reliable observations of LSMF are provided by the Wilcox Solar Observatory (WSO). So it makes an obvious sense to compare SFMM measurements with WSO ones. Note that at SFMM the direct method of measurements is used for calculating the magnetic field strength at every pixel of a solar image [Chen et al., 2025]. It reminds the center-of-gravity (COG) method [Uitenbroek, 2003], but it is based on the detection of the difference ($2\Delta\lambda$) between wave length positions of the minimum intensity of the corresponding Zeeman-components when PA is running. Remind that for the linear Zeeman effect the shift value of splitted components (relative to the case without magnetic field B) is determined by the formula

$$\Delta\lambda[\text{nm}] = \pm 4.668 \cdot 10^{-8} \, g_{\text{eff}} \lambda^2 \, B[\text{T}],$$

where g_{eff} is the effective Lande factor. So for the spectral line FeI 532.419 nm with Lande factor $g=1.5$ we have

$$\Delta\lambda[\text{cm}] = \pm 1.92 \cdot 10^{-9} \, B[\text{T}].$$

For this study, we have used one of the best SFMM (but typical) observations made on April 18, 2023, when a number of scanning points along the line profile was as many as 21. The original matrix of data has a size 2048×2048 px. However, for comparison with low spatial resolution WSO data such high resolution is not needed, and we have remapped them through different smoothing. Since we are planning to compare SFMM data with observations made at the telescope STOP of the Sayan Solar Observatory with spatial resolution 21×21 px, the lowest SFMM spatial resolution used here is the same. Remind that WSO original measurements are performed with 3 arcmin aperture, and the scanning grid consists of 11 scan lines in the north-south direction and 21 east-west positions at the equator.

Some following figures show how SFMM full-disk magnetograms look like with a different spatial resolution and with different scales of color bars. Figure 2 presents a magnetogram with spatial resolution 256×256 px and with a linear color bar. We can see that only strong magnetic fields in active regions are visible, and it is hardly possible to say something about weaker

magnetic fields on the rest of the surface. Much more informative is Figure 3, where the same magnetogram but with a non-linear color scale bar is presented. In this case, we can see large-scale features of weak magnetic fields, which, as has been mentioned above, determine the structure of the open magnetic flux, which, in turn, builds the structure of the helio-magnetosphere. At last, Figure 4 exhibits the same magnetogram with a non-linear color scale bar with a spatial resolution 21×21 px in the mosaic form. It is this data with such a spatial resolution that will be used in the following. Note that here SFMM magnetogram fortunately does not show any strange artificial large-scale structures, which were
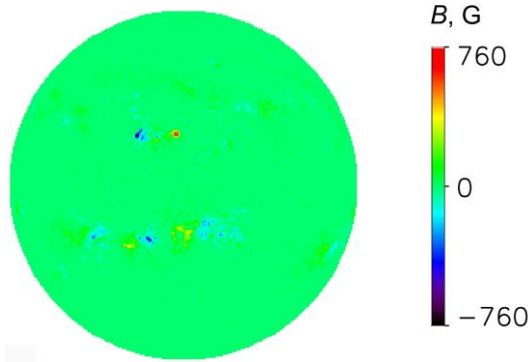

Figure 2. Full-disk magnetogram of longitudinal solar magnetic fields observed with SFMM telescope on April 18, 2023. The spectral line is FeI 532.419 nm; the remapped spatial resolution is 256×256 px
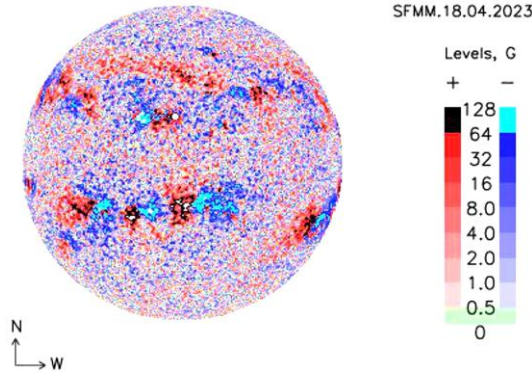

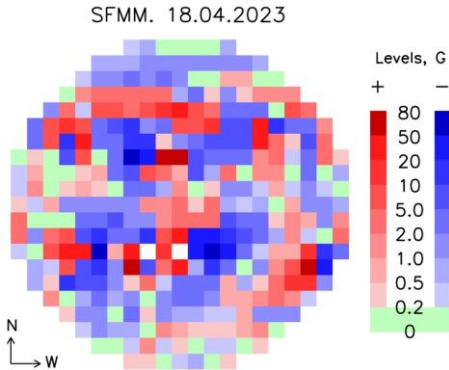*Figure 3*. Same as in Figure 2 but with a non-linear color scale bar

Figure 4. Same as in *Figure* 3, but with spatial resolution 21 by 21 px and with other levels of scale on the non-linear color bar

found in SMAT data [Demidov et al., 2018] (see, e.g., the left bottom panel in Figure 1). It is a good indicator that SFMM probably does not have systematical field-of-view errors that SMAT has.

Unfortunately, WSO does not have any observations of magnetograms for April 18, 2023, so it is impossible to make a direct comparison between SFMM and WSO full-disk observations. But we can use a WSO synoptic map for similar analysis. Indeed, the central meridian of the SFMM magnetogram for Carrington Rotation (CR) 2269 has a longitude ≈30°, so we can employ for comparison a part of the SFMM magnetogram and the corresponding data at the beginning of the synoptic map. Figure 5 shows the WSO synoptic map in latitude-longitude coordinates. Figure 6 displays a part of the SFMM magnetogram in Carrington coordinates for the range of longitudes 0°–90°. The results of comparison between the overlapping (SFMM-WSO) points (for WSO from λ=0° to λ=90°) are presented in Figure 7.

The correlation coefficient is seen to be rather high ($\rho=0.7$), which suggests that SFMM observations are quite reliable. The question arises about a big difference between amplitudes of magnetic field strengths: for SFMM, they are by five times higher than for WSO. Why it is happening is still unclear. It is most likely to be somehow connected with the use of different spectral lines at SFMM and WSO (WSO employs FeI 525.02 nm line with the Lande factor $g=3.0$). The question of comparison between solar magnetic field measurements in different spectral lines is separate and very complicated; it deserves a special consideration. Furthermore, this question is important for solving the open magnetic flux problem [Linker et al., 2017]. It is worth noting here that Wang et al. [2022] suggested to correct WSO observations by a factor of 4.5 (at the disk center) (that is close to the value we have just obtained) to compensate for signal saturation in the extremely sensitive FeI 525.02 nm line. The SFMM observations in the FeI 532.419 nm line with $g=1.5$ should not be affected by saturation.

If we look at Figure 7 more carefully, we find that points of small values do not follow this regression. To explore this question in more detail, we analyze points with magnetic field strengths $|B| \leq 10$ G separately. The results are presented in Figure 8. As expected, the correlation coefficient in this case becomes lower ($\rho=0.57$), but is still high enough. What is more important is that
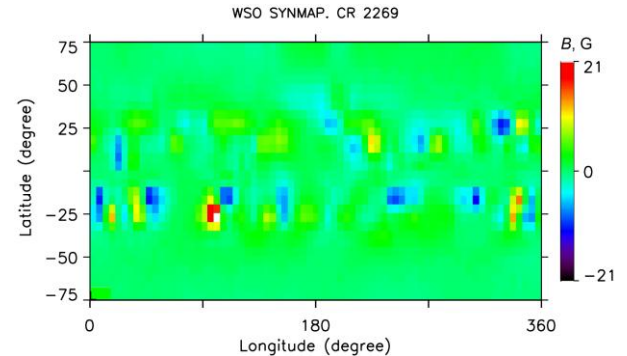

Figure 5. Synoptic map for Carrington Rotation (CR) 2269, observations of the solar magnetic field at the Wilcox Solar Observatory (WSO)
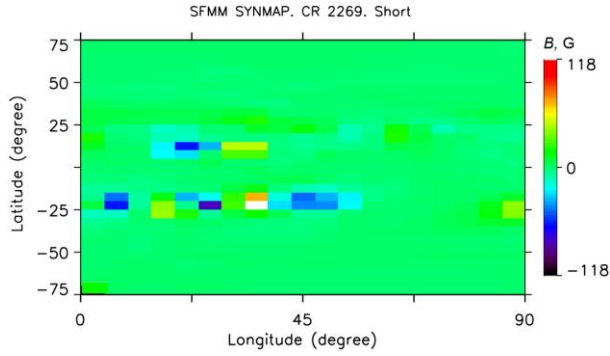
Figure 6. Part of the SFMM magnetogram (April 18, 2023) in Carrington coordinates for the range of longitudes $0° - 90°$ for CR 2269
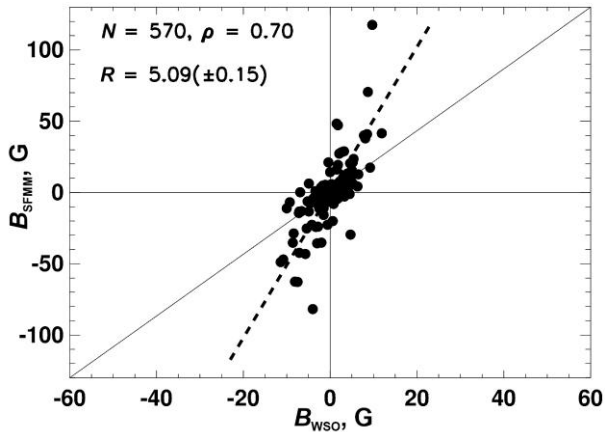

Figure 7. Comparison between SFMM and WSO data sets for a part of CR 2269, $0° \div 90°$ longitude range: *N* indicates the number of point pairs (px); ρ is the correlation coefficient; *R* is the linear regression coefficient (dashed line). The solid line is $R = 1.0$
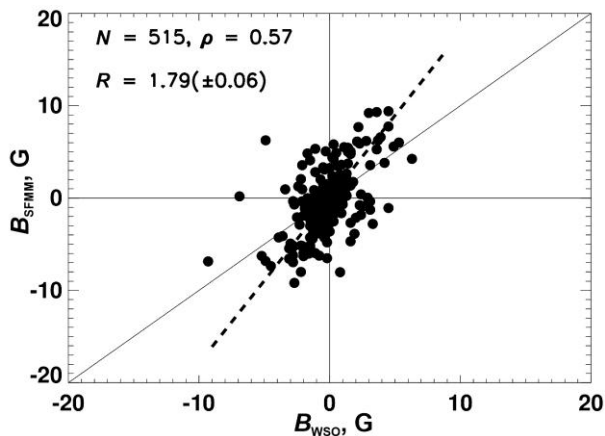

Figure 8. The same as in Figure 7, but for points with magnetic field strength $|B| \leq 10$ G for both data sets. ρ is the correlation coefficient; *R* is the linear regression coefficient (dashed line). The solid line is $R = 1.0$

the regression coefficient decreases very significantly ($R \approx 1.8$), which raises a question as to the need for using different coefficients in cross-calibration of SFMM-WSO observations for weak and strong magnetic fields. In the future, to improve the accuracy of observations of weak magnetic fields, it is necessary to employ measurements in the "deep integration" mode.

CONCLUSION

At present, for many aspects of human civilization existence and development it is very important to know and predict conditions in near-Earth space and often far beyond. This branch of science is called space weather. To monitor parameters of high layers of the atmosphere, ionosphere and magnetosphere, many facilities are used around the world. One of the most ambitious projects is the International Meridian Circle Program (IMCP), developed and realized in China. Since many parameters detected by IMCP instruments strongly depend on conditions on the Sun, it is extremely important to obtain information about such processes. That is why, under ICMP a special instrument — the Solar Full-disk Multi-layer Magnetograph (SFMM) — was developed. One of the most important aims of this instrument is to provide the full-disk solar magnetograms.

The purpose of this study is to test the reliability of measurements of large-scale magnetic fields (LSMF) with this new instrument. LSMFs are rather weak, and it is a big challenge to measure them. By comparing SFMM data with Wilcox Solar Observatory (WSO) observations (which are considered as the most reliable), we have drawn a conclusion that correspondence between these two data sets is fairly close.

The next natural step is to construct SFMM-based synoptic maps and to use them for calculating the solar wind velocity and other space weather parameters. This is our task for the nearest future.

REFERENCES

Chen J., Su J., Xie W., Deng Y., Bai X., et al. Direct measurement of the longitudinal magnetic field in the solar photosphere with the Zeeman effect. *Solar Phys.* 2025, vol. 300, iss. 4, article id. 49.
DOI: 10.10007/s11207-025-02455-7.

Demidov M.L., Wang X.F., Wang D.G., Deng, Y.Y. On the measurements of full-disk longitudinal magnetograms at Huairou solar observing station. *Solar Phys.* 2018, vol. 293, iss. 10, article id. 146, p. 18.
DOI: 10.10007/s11207-018-1366-6.

Demidov M.L., Hanaoka Y., Wang X.F., Kirichkov P.N. On the differences in the ambient solar wind speed forecasting caused by using synoptic maps from different observatories. *Solar Phys.* 2023, vol. 298, article id. 120, p. 14.
DOI: 10.10007/s11207-023-02206-6.

Linker J.A., Caplan R.M., Downs C., P. Riley, Z. Mikic, et al. The open flux problem. *Astroph. J.* 2017, vol. 848, no.1, p. 11. DOI: 10.3847/1538-4357/aa8a70.

Sun Y., Tong L., Deng Y., Wang D., Wang X., et al. Development of the full-disk vector magnetographs for the Meridian Project II. *The 15th Russian-Chinese Workshop on Space Weather*. *Irkutsk. Russia,* 2024, p. 46.

Uitenbroek H. The accuracy of the center-of-gravity method for measuring velocity and magnetic field strength in the solar photosphere. *Astrophys. J.* 2003, vol. 592. p. 1225–1233. DOI: 10.1086/375736.

Wang Y.-M., Ulrich R.K., Harvey J.W. Magnetograph saturation and open flux problem. *Astroph. J.* 2022, vol. 926, article id. 113, p. 14 DOI: 10.3847/1538-4357/ac4491.

Xu H., Su J., Liu S., et al. Comparison of line-of-sight magnetic field observed by ASO-S/FMG, SDO/HMI and HSOS/SMAT. *Solar Phys.* 2024, vol. 299, article id. 17. DOI: 10.1007/s11207-024-02260-8.

URL: http://wso.stanford.edu (accessed April 23, 2025).

How to cite this article

MONITORING OF SPACE WEATHER EFFECTS WITH SOZVEZDIE-270 NANOSATELLITE CONSTELLATION OF MOSCOW UNIVERSITY

A.V. Bogomolov
Lomonosov Moscow State University,
Skobeltsyn Institute of Nuclear Physics,
Moscow, Russia, aabboogg@srd.sinp.msu.ru

V.V. Bogomolov
Lomonosov Moscow State University,
Skobeltsyn Institute of Nuclear Physics,
Moscow, Russia, bogovit@rambler.ru
Lomonosov Moscow State University,
Faculty of Physics, Moscow, Russia

A.F. Iyudin
Lomonosov Moscow State University,
Skobeltsyn Institute of Nuclear Physics,
Moscow, Russia, aiyudin@srd.sinp.msu.ru

V.V. Kalegaev
Lomonosov Moscow State University,
Skobeltsyn Institute of Nuclear Physics,
Moscow, Russia, klg@dec1.sinp.msu.ru
Lomonosov Moscow State University,
Faculty of Physics, Moscow, Russia

I.N. Myagkova
Lomonosov Moscow State University,
Skobeltsyn Institute of Nuclear Physics,
Moscow, Russia, irina@srd.sinp.msu.ru

V.I. Osedlo
Lomonosov Moscow State University,
Skobeltsyn Institute of Nuclear Physics,
Moscow, Russia, osedlo@mail.ru

S.I. Svertilov
Lomonosov Moscow State University,
Skobeltsyn Institute of Nuclear Physics,
Moscow, Russia, sis@coronas.ru
Lomonosov Moscow State University,
Faculty of Physics, Moscow, Russia

I.V. Yashin
Lomonosov Moscow State University,
Skobeltsyn Institute of Nuclear Physics,
Moscow, Russia, ivn@eas.sinp.msu.ru

Abstract. The space project Sozvezdie-270 of Moscow University is in progress now. It involves the deployment of a CubeSat nanosatellites constellation. To the present, 20 satellites have been launched, 9 of them continue to function in near-Earth orbit; one more will be launched in the near future. Instruments were developed specifically for the experiments on board small spacecraft of the CubeSat format, which provide measurements of fluxes and spectra of charged particles, primarily electrons of relativistic and sub-relativistic energies, as well as gamma quanta. Along with the space constellation, a network of ground receiving stations is also being created. A multi-satellite constellation gives a number of advantages in studying dynamic processes in near-Earth space. In particular, it makes possible to carry out simultaneous measurements of charged particle fluxes with instruments of the same type at different points in near-Earth space. Such measurements provide unique information about the flux of sub-relativistic electrons, including variations due to precipitation of electrons, which is of great importance for understanding the mechanisms of acceleration and losses of trapped and quasi-trapped electrons in Earth's radiation belts (ERB).

We discuss various recent space weather manifestations associated with increased solar flare activity. Among such effects is the filling of the polar caps with particles of solar cosmic rays, dynamic processes in outer ERB during magnetic storms, rapid variations in electron fluxes due to precipitation.

Keywords: space weather, Earth's radiation belts, solar cosmic rays, nanosatellites, CubeSat.

INTRODUCTION

Space weather is a relatively young branch of physics, which studies extremely variable conditions in near-Earth space (NES). These variations are caused by active processes on the Sun, conditions in the interplanetary medium (variations in interplanetary magnetic field (IMF) and solar wind (SW) parameters) and in the magnetosphere—ionosphere—thermosphere system, as well as their influence on Earth and human activity. Adverse changes in NES can reduce the efficiency and reliability of spacecraft and ground-based systems, which, in turn, can lead to heavy losses due to problems in operating communication systems, navigation, power systems, and reconnaissance satellites [Baker, 2001; Belov et al., 2004; Iucci et al., 2005; Romanova et al., 2005; Potapov et al., 2016; Novikov, Voronina, 2021]. That is why space weather has become one of the fastest-growing areas of research over the past few decades [Daglis,

2001; Cole, 2003; Schrijver et al., 2015; McGranaghan et al., 2021]. Nowadays, space weather forecast centers have been established by several national governments and research institutes (e.g., [Wei et al., 2003; Lundstedt, 2006; Wilkinson, 2009]).

One of the main space weather effects includes variations in energetic charged particle fluxes in various NES regions [Kudela, 2013]. At the same time, variations in particle and quantum fluxes recorded by instruments can be caused either by a satellite crossing a compact region with increased particle density (so-called spatial effects) or by an increase (or decrease) in intensity (temporal effects). In turn, both spatial and temporal effects can be related to acceleration of particles and their precipitation from the regions of trapped radiation — Earth's radiation belts (ERB), as well as to penetration of particles accelerated in solar flares into the magnetosphere, i.e. the so-called solar cosmic rays (SCRs) [Dorman, Miroshnichenko, 1968].

Experimental measurements of energetic charged particle fluxes in NES began in the early years of the space age [Vernov et al., 1958]. From these measurements, empirical models of ERB were developed in the 1970s and 80s. These models describe the spatial and energy distribution of omnidirectional fluxes of protons with energies from hundreds of keV to hundreds of MeV and electrons with energies from tens of keV to ~7–10 MeV in a large region of NES from ~250 km to geostationary and highly elliptical orbits. The most well-known models are AP8, AE8 (USA), and AP9/AE9 [Ginet et al., 2013] based on newer experimental data. SINP MSU has also developed ERB models [Kuznetsov et al., 2014], which formed the basis for domestic standards regulating methods of assessing radiation conditions of satellite flight.

However, these models are stationary. Variations in particle fluxes are reflected in them only by setting fluxes for minimum and maximum solar activity, whereas the corresponding fluxes differ only for some energies a maximum of several times. At the same time, real charged particle fluxes in the vicinity of Earth, even under geomagnetically quiet conditions, are subjected to fairly significant medium- and long-term variations associated with solar and geomagnetic activity, variations in the geomagnetic field and the density of the upper atmosphere. Also noteworthy are rapid variations in cosmic ray fluxes, which primarily include short-term (with characteristic times of less than a few seconds) variations in electron fluxes of sub-relativistic and relativistic energies (from hundreds of keV to ~10 MeV).

In order to construct an adequate dynamic pattern of three-dimensional distribution of energetic radiation fluxes in NES, we should consider their time variations, including short-term variations in high-energy electron fluxes. In this case, the central problem is to figure out whether the detected variations in particle fluxes result from spatial or temporal effects. This problem is difficult to resolve with a single spacecraft. This requires simultaneous measurements with several spacecraft, which can be implemented using a multi-satellite constellation. Such problems are most effectively solved by comparative analysis of data from several spacecraft operating in both close and significantly different orbits. Such a strategy may be implemented as follows:

1) Sequential passage of closely spaced satellites through the same region, which allows the most reliable separation of spatial and temporal effects;

2) Simultaneous measurements on different L shells needed to restore the dynamic pattern of distribution of the trapped particle flux in a wide range of orbits, which, in particular, allows us to observe a shift of ERB maximum during geomagnetic disturbances;

3) Simultaneous measurements at one altitude by instruments of the same type installed on several satellites shifted in longitude relative to each other, which allows us to assess the influence of the local time factor on the particle flux dynamics.

Some of these problems can be solved by grouping several simultaneously launched spacecraft with identical detectors; the others, by analyzing data from one or more nanosatellites together with data from a larger spacecraft equipped with a complex of instruments providing detailed measurements of particle fluxes, the electromagnetic field, and other magnetospheric plasma parameters. It seems that standard-format micro- and nanosatellites, including CubeSats, are the most suitable spacecraft for implementing the multi-satellite measurement strategy considered. Such satellites are relatively cheap and do not require complex development stages and special tests. As a rule, they are launched into orbit by the associated launch, which also considerably reduces the cost of the mission. At the same time, there is no need to completely duplicate the functionality of large spacecraft. The advantage of the micro- and nanosatellite constellation lies precisely in the possibility for examining in more detail the time variations of different cosmic radiation components in various NES regions [Caspi et al., 2022].

1. MULTI-SATELLITE MISSION SOZVEZDIE-270 OF MOSCOW UNIVERSITY

In recent years, Moscow State University has been implementing its own space program, which involves monitoring charged particle fluxes in NES, as well as solar X-rays and gamma rays — electromagnetic transients of different nature. Noteworthy in this regard is the successful launch of such satellites as Universitetskiy—Tatiana [Sadovnichy et al., 2011], Universitetskiy—Tatiana-2 [Sadovnichy et al., 2011], Vernov [Panasyuk et al., 2016a, b], and Lomonosov [Sadovnichii et al., 2017]. The next step in this direction is a new project of Moscow University Sozvezdie-270, which intends to deploy a constellation of nanosatellites. By the end of 2024, 20 CubeSat nanosatellites had been launched (starting in 2018), 9 of which continue to operate in polar orbit at a height of ~500 km. Among them is the Avion spacecraft, launched on June 27, 2023, which provided the maximum amount of scientific data.

At present, the satellite constellation, deployed under the Sozvezdie-270 project, operates in the monitoring mode for individual events, but in the future it is

expected to be expanded, as well as to create a network of receiving stations distributed along the meridians, which will allow us to quickly obtain large amount of data and thus to turn to monitoring of cosmic radiation in near real-time mode. At least five ground-based receiving stations should be deployed using antennas operating in VHF, S, and X bands in the regions from Kaliningrad to Kamchatka. As a result, a unified system consisting of space and ground segments will be developed. It should ensure spacecraft control, as well as regular data reception from the constellation's satellites located at different NES points, and will significantly increase the amount of transmitted information. The main purpose of the multi-satellite constellation is to monitor cosmic radiation and electromagnetic transients of atmospheric, astrophysical, and solar origin.

To conduct experiments with CubeSat satellites, various instruments have been developed for detecting energetic charged particles, hard X-rays and gamma rays, as well as optical (ultraviolet and red) airglow.

To date, measurements with the satellite constellation of Moscow University have provided important information about the effects associated with various manifestations of solar flare activity and its impact on geomagnetic conditions in NES. Among such phenomena is penetration of SCRs into the polar caps, which leads to a significant change in radiation fields in the inner magnetosphere. In this regard, an important part is also played by a change in the spatial structure of the distribution of high-energy electron fluxes in outer ERB due to magnetic storms, which, in turn, are caused by changes in IMF and SW parameters due to active processes on the Sun. Another direction in the study of radiation conditions in NES is to examine the dynamics of sub-relativistic electron fluxes in the regions of precipitation from inner ($L \sim 1.6 \div 1.8$) and outer ERBs.

Bellow, we discuss examples of observations of these phenomena, made using mainly instruments on board Avion SC and some other satellites of Sozvezdie-270. There are three detector modules of the DeCoR type installed on board Avion SC: DeCoR-1, DeCoR-2, and DeCoR-3 [Bogomolov et al., 2020]. The DeCoR instruments are scintillation spectrometers that utilize a combination of a thin layer of plastic scintillator and a thicker CsI(Tl) crystal as a detector element. In front of the CsI(Tl) crystal is a thin layer of plastic scintillator, which simultaneously serves as a detector of charged particles (mostly electrons) and an active protection of the CsI(Tl) channel, which uses the separation of events in different scintillators by the shape of the light pulse at the output of the photodetectors. Hard X-rays is detected by CsI(Tl) scintillation crystals.

The detectors installed on Avion differ in the size of the sensitive region optimized for solving specific scientific problems. In particular, DeCoR-2 is optimized for recording and studying cosmic gamma-ray bursts of different nature. It has an effective area increased to ~65 cm^2, which is necessary to increase sensitivity and improve temporal resolution, determined primarily by the statistics of detected gamma-rays. The DeCoR-2 module is a composite scintillation detector (phoswich) consisting of a 3 mm plastic scintillator and a 9 mm CsI(Tl) crystal. Both scintillators are viewed by an assembly of silicon photomultipliers (SiPM), which ensures separate recording of gamma quanta and electrons in the energy release range in scintillators from 20 keV to 1 MeV. This separation is important when conducting an experiment to study gamma-ray bursts in a polar orbit.

In addition to DeCoR-2, two more detector modules are included in the equipment complex to ensure more accurate measurements. The DeCoR-1 module with scintillators having an area of ~18 cm^2, viewed by two vacuum photomultipliers (PMT), is designed to study changes in the electron flux in the energy release range from 50 keV to 2 MeV. It is completely analogous to the DeCoR instruments employed for the experiments carried out by VDNKh-80, Norby, Descartes, and other CubeSats [Bogomolov et al., 2020]. The DeCoR-3 module was added to expand the range of detected gamma rays to the high-energy range, i.e. up to 5 MeV. Its main purpose is to measure energy spectra of solar flare gamma rays and cosmic gamma-ray bursts. The detecting element of this unit is a CsI(Tl) scintillation crystal $30 \times 30 \times 30$ mm^3, which is viewed by two vacuum PMT systems.

Data from each DeCoR module is recorded both as monitoring frames (count rate on several channels) and a detailed event-by-event record. The volume of scientific data transmitted from the Avion DeCoR instruments is ~5 MB per day. The main type of transmitted data is frames in monitoring mode with a time resolution of 1 s, and during the flight it is possible to repeatedly change this value, both up and down. The lower threshold for detecting quanta is several tens of keV, it can also be changed during flight, taking into account background conditions in near-Earth orbit, while the detectors can be configured differently.

The data from the CubeSat satellites of the MSU constellation, including the Avion spacecraft, are available in the form of graphs and tables on the SINP MSU space weather website [https://swx.sinp.msu.ru/tools/davisat.php].

2. EXAMPLES OF OBSERVATIONS OF SPACE WEATHER EFFECTS

2.1. Solar cosmic rays

As an example illustrating the possibilities of experiments on detection of SCR events by CubeSat nanosatellites, let us consider two increases in solar electron fluxes in the polar caps: the former began immediately after midnight on June 8, 2024; the latter, around midnight on June 12, 2024 (Figure 1). The top panel exhibits time dependences of count rates N of >300 keV electrons, obtained by DeCoR-1 and DeCoR-3 on board Avion SC (dark blue and purple dots respectively). Measurements are shown in the polar caps — regions of open field lines to which SCRs penetrate.

Circled marks (squares for DeCoR-1 and circles for DeCoR-3) represent measurements in the southern polar cap; uncircled marks, in the northern one. Curves of SCR electron fluxes are seen to be not completely identical
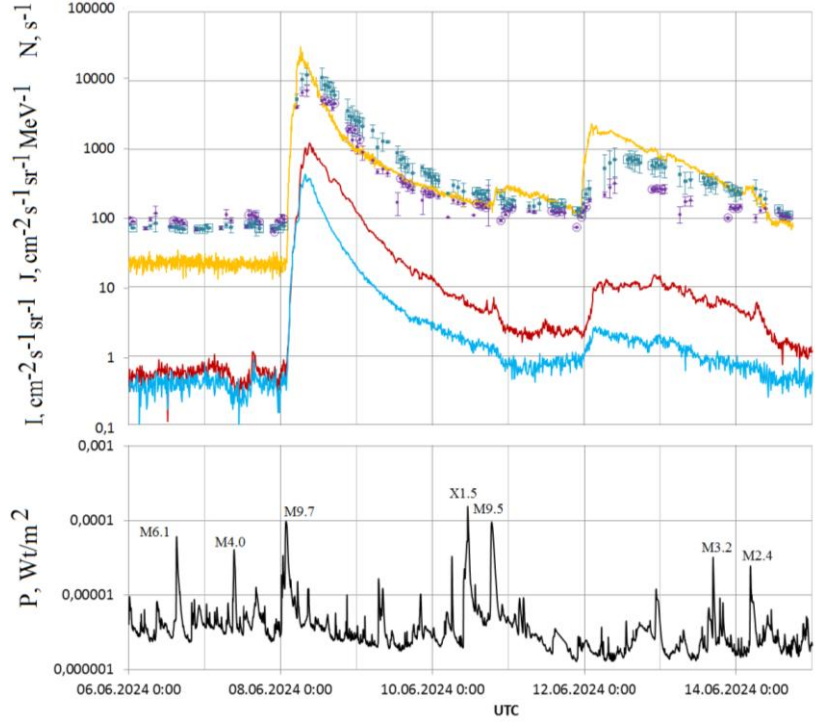
A.V. Bogomolov, V.V. Bogomolov, A.F. Iyudin, V.V. Kalegaev, I.N. Myagkova, V.I. Osedlo, S.I. Svertillov, I.V. Yashin

Figure 1. Time dependences (at the top) of count rates *N* of >300 keV electrons obtained by DeCoR-1 and DeCoR-3 on board Avion SC (dark blue and purple dots respectively; circled marks correspond to measurements in the southern polar cap; uncircled, in the northern one); time dependence of 175–315 keV electron flux *J* derived during an experiment on board ACE SC (yellow curve), and time dependences of proton fluxes *I* with an energy 9–20 MeV (red curve) and 20–40 MeV (blue curve), derived during an experiment on board Electro-L2 SC; at the bottom is the time dependence of X-ray fluxes from GOES data

in the northern and southern caps during this event, i.e. there is an asymmetry that may be linked both to anisotropy of the fluxes and to different orientations of the instruments relative to geomagnetic field lines. Simultaneously with Avion measurements, the top panel shows the time dependence of *J* electron flux with an energy 175–315 keV, obtained during an experiment on board ACE SC (yellow curve), and time dependences of *I* proton fluxes with an energy 9–20 MeV (red curve) and 20–40 MeV (blue curve), obtained by the SKIF instrument during an experiment on board Electro-L2 SC operating in geostationary orbit. The bottom panel displays the time dependence of X-ray fluxes from GOES-16 SC. The time dependences of SCR electron fluxes in the polar caps and at the L1 point are seen to be in fairly good agreement, as observed during earlier experiments [Kuznetsov et al., 2003]. Note that the possibility of obtaining data on SCR electron fluxes near Earth is an advantage of experiments in circular polar orbits since such data cannot be collected during experiments at geostationary orbit due to the fact that it is located in outer ERB.

The source of the first increase in SCRs (June 8 – June 10) was a solar flare of M9.8 class according to the GOES classification (see the bottom panel in Figure 1). The flare began on June 8, 2024 at 01:23 UT in active region (AR) AR13697, which was located in the southern hemisphere near the western limb (coordinates of the flare S18W69) during the flare. It was quite long — the soft X-ray emission maximum was recorded at 01:49 UT; the end of the flare, at 02:07 UT. The flare

was accompanied by a coronal mass ejection (CME), which was recorded on June 8, 2024 at 01:48 UT. Figure 1 shows that the time dependences of SCR proton fluxes according to Electro-L2 data and SCR electron fluxes according to ACE and Avion data are similar, although not identical, and have a profile characteristic of SCR events from western flares — a rapid increase in SCR particle flux and a much longer gradual decrease. It can be seen that the increase in the solar proton flux according to Electro-L2 data began immediately after the soft X-ray burst at ~02:10 UT, the maximum proton flux caused by this event in the above range was detected on June 8 at 06:20 UT.

The second rather intense SCR event (see Figure 1) began on June 12, 2024 around midnight. Its source was a post-limb flare that probably occurred in AR13697 as the flare that triggered the above SCR event. This flare was also accompanied by halo-type CME with an initial velocity of ~2000 km/s, which was recorded on June 11, 2024 at 23:20 UT. As in the first SCR event considered, simultaneously with increases in SCR electron fluxes in the polar caps (Avion) and at L1 (ACE) on June 11–12, 2024 near midnight, the SKIF instrument installed on the Electro-L2 geostationary satellite also detected an increase, i.e. SCR protons and electrons arrived at Earth's orbit in both SCR events.

In conclusion of this section, we would like to note that, despite many years of observation of SCR events, the creation of SPE catalogs and theoretical models, some problems remain unresolved. So, even in the above short time period (see Figure 1), it is apparent

that neither the most intense X1.5 flare occurring in AR13697 during this period on June 10, 2024, nor the subsequent M9.5 class flare (again in the same AR) belong to significant SPEs comparable in amplitude to the two SCR events discussed above for protons and electrons. There is a need for further experimental studies of SCR events, which will be useful in developing theoretical and predictive models.

2.2. Dynamics of Earth's outer radiation belt during a magnetic storm

Another significant manifestation of space weather, which can also be monitored by CubeSat nanosatellites during experiments, is a change in outer ERB during magnetic storms. Let us take a closer look at the outer ERB dynamics, using Avion data for the period from August 11 to August 15, 2024, when there was fairly high geomagnetic activity.

Figure 2 plots time dependences of count rates of >300 keV electrons recorded by DeCoR-1 on board Avion SC (purple line, left scale) and the McIllwain parameter L (yellow line, right scale) for the time intervals on August 10, 2024 from 21:27 to 23:42, on August 12, 2024 from 21:15 to 23:30, and on August 14, 2024 from 21:03 to 23:18 UT before, during, and after the magnetic storm that began at the end of August 11, 2024. The given intervals are chosen in such a way as to exclude the longitude effect since for each of the three time intervals the spacecraft passes along the same longitudes.

The obtained time dependences of count rates of outer ERB electrons are seen to change with time.

Let us examine geomagnetic conditions of this time in-

terval in more detail. A strong disturbance of IMF, probably caused by the arrival of an interplanetary coronal mass ejection (ICME) at Earth, which resulted from the merger of several, at least three, CMEs that left the Sun from August 8 to August 10, 2024. The maximum ejection velocity recorded by LASCO (SOHO) on August 8, 2024 at 19:48 UT was 789 km/s, the maximum SW velocity at Earth's orbit was ~520 km/s; and its maximum density, ~35 cm^{-3}.

The storm main phase began on August 11–12, 2024 around midnight. The maximum amplitude of *Dst* variation of ~−203 nT was observed on August 12 at 17:00, with maximum K_p being 8. The geomagnetic indices K_p and *Dst* for August 9–16, 2024 are shown in Figure 3. Colored arrows represent the time points when data on outer ERB was obtained (see Figure 4).

The left panel of Figure 4 plots L dependences of the measurement point proportional to the magnetic latitude, electron count rates before (blue line), during (red line), and after (green line) the August 11–12, 2024 magnetic disturbance for the time intervals (see arrows in Figure 3). In the right panel are maps with a projection of the Avion orbit onto Earth for observations presented in the left panels. The curves were obtained from observations for the following time intervals that correspond to the intersection of the satellite's orbit with ERB (see Figure 2), when the spacecraft moved from the polar region to the equator. The top panel presents data on August 10, 2024 at 21:46–22:10, August 12 at 21:31–21:55, and August 14 at 21:16–21:40 UT, i.e. in the Northern Hemisphere. The bottom panel displays data on August 10, 2024 at 22:30–23:00, on August 12, 2024 at 22:15–22:45, and on August 14 at 22:00–22:30 UT, i.e. in the Southern Hemisphere.
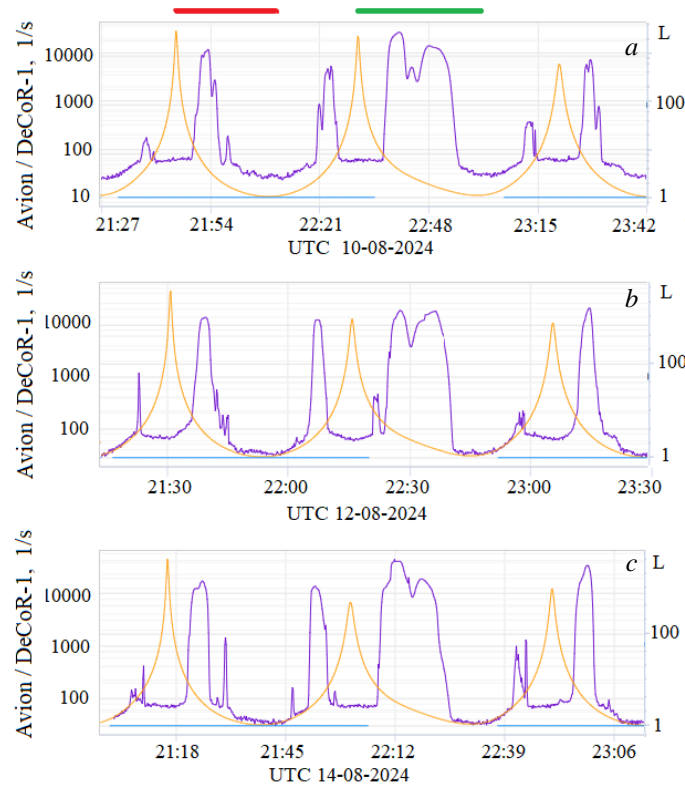

Figure 2. Time dependences of electron count rates by Avion DeCoR-1 (purple line, left scale) and the McIlvaine parameter L (yellow line, right scale) on August 10 (*a*), August 12 (*b*), and August 14, 2024 (*c*). Horizontal red and green lines indicate the time intervals used in Figure 4 (see below)
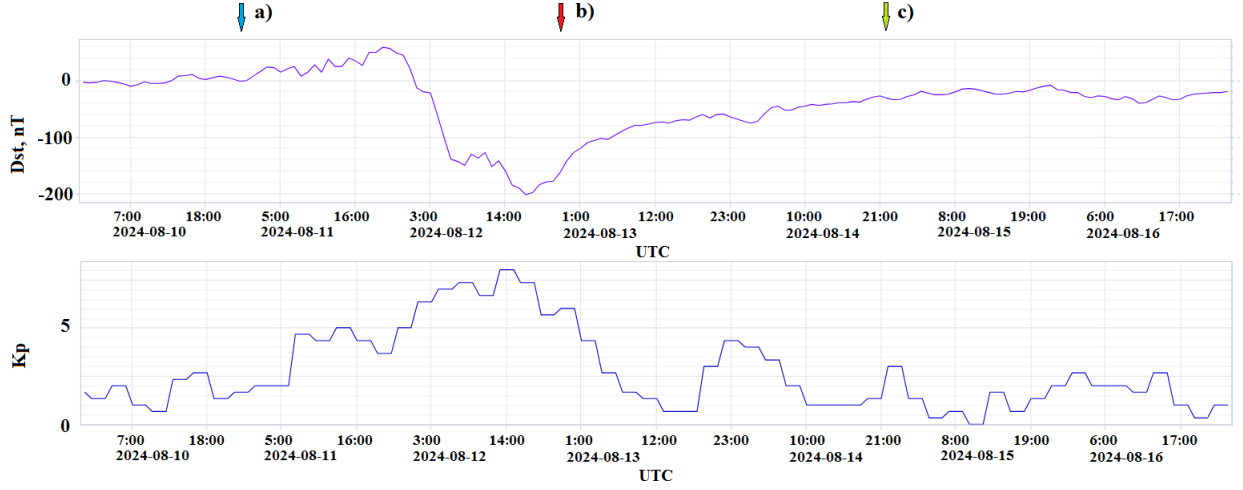
A.V. Bogomolov, V.V. Bogomolov, A.F. Iyudin, V.V. Kalegaev, I.N. Myagkova, V.I. Osedlo, S.I. Svertillov, I.V. Yashin

Figure 3. Time dependences of the geomagnetic activity indices *Dst* (top) and K_{p} (bottom). Arrows indicate measurement moments on the Avion spacecraft, shown in Figure 4
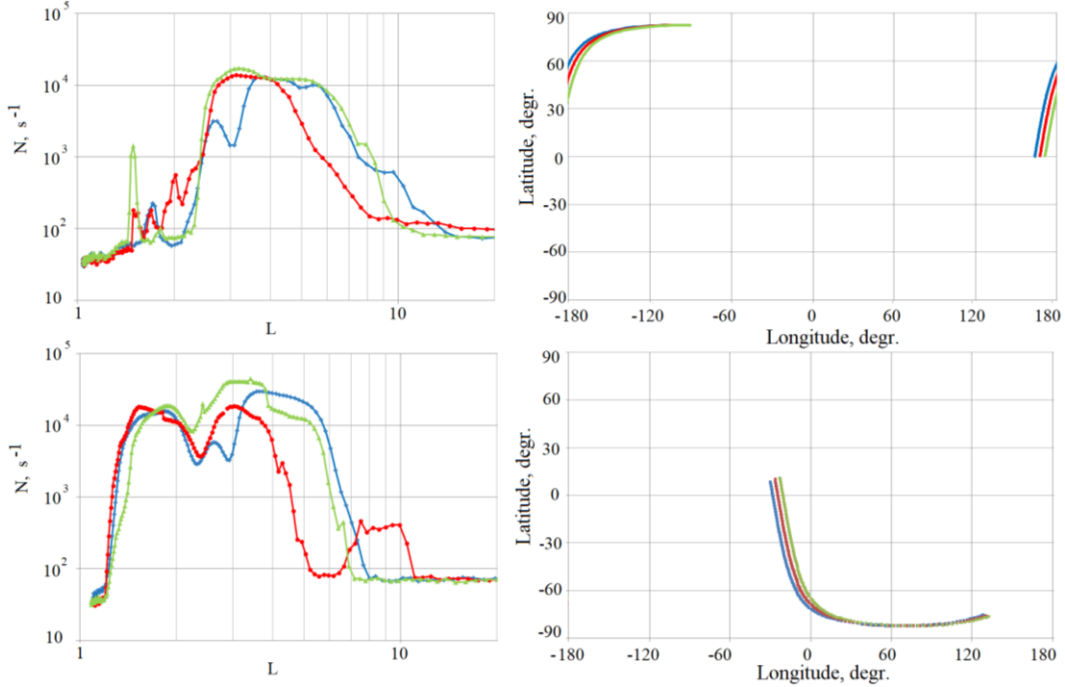

Figure 4. On the left: *L* dependences of electron count rates before (blue line), during (red line), and after (green line) the August 11–12, 2024 magnetic disturbance for the time intervals denoted in Figure 2 by the red line (top panel) and the green line (bottom panel). On the right: maps with a projection of the Avion orbit onto Earth for observations presented in the left panels

It can be observed that in the Northern Hemisphere at the maximum of the storm the intensity of outer ERB remained virtually unchanged, but its maximum shifted closer to Earth, from *L*=4 to *L*=3, where there was a gap between outer and inner belts before the storm. The high-latitude boundary of outer ERB also shifted to smaller *L* — from *L*~8÷9 to *L*~6÷7. In the Southern Hemisphere, at the maximum of the storm, the intensity of sub-relativistic electron fluxes decreased several times, the equatorial boundary, as in the Northern Hemisphere, shifted to smaller *L*, i.e. in both hemispheres, the gap was filled with particles. In the Southern Hemisphere, the polar boundary of outer ERB shifted from *L*~7÷8 to *L*~5÷6. Since the equatorial boundary of the outer belt shifted less in both hemispheres, it can be said that by the end of the storm main phase the outer belt seemed to compress. Also noteworthy in the Southern Hemisphere is an additional high-latitude increase in electron fluxes in the *L* region from 8 to 10. Clarifying the nature of such high-latitude increases requires further research.

At the end of the recovery phase (on August 14), the high-latitude boundary of outer ERB returned to the pre-storm level in both hemispheres. In the Southern Hemisphere, the intensity at the maximum, which remained closer to Earth than before the storm, increased. The polar boundary of outer ERB returned to the pre-storm level in both hemispheres, the pre-storm gap region remained filled with particles, i.e. the space filled with electrons of outer ERB under the action of the geomagnetic storm increased in this case, as was repeatedly observed during other experiments (e.g., [Myagkova et al., 2021]).

2.3. Electron precipitation from the inner belt

The third problem in terms of space weather phenomena is the study of variations of precipitation from inner ERB. As an example, let us examine variations in the electron count rate in the region of precipitation from inner ERB ($L\sim1.6\div1.8$). Before the magnetic storm, there was one peak of intensity at $L\sim1.7$ (blue curve in Figure 4). Two additional peaks appeared during the storm, at $L\sim1.6$ and $L\sim2$ (red curve in Figure 4). After the end of the storm, the amplitude of the peak at $L\sim1.6$ increased significantly after its end (green curve in Figure 4). Note that the peaks near 1.6 were observed on August 12 at ~21:44 and on August 14 at ~21:30 UT, i.e. approximately at the same time. Thus, the question arises whether the dynamics of the count rate of sub-relativistic electrons precipitating from inner ERB at $L\sim1.6$ is related to geomagnetic activity or there are other factors.

To answer this question, we analyzed Avion measurements made during the August 8, 2024 magnetic storm and during the quiet period on September 25 – October 3, 2024. Time dependences of the count rate of >300 keV electrons derived from measurements performed by Avion with the aid of DeCoR-1 are shown in Figure 5. We also analyzed data from the Altair CubeSat, obtained on December 13, 2024, also during the magnetically quiet period.

A map of the Avion and Altair CubeSats' orbits projected onto Earth for these measurements is presented in Figure 6. Since the spacecrafts' orbits are close to sun-synchronous, they pass through the same regions at approximately the same UT. Circles mark regions where sub-relativistic electrons precipitated from inner ERB.

The L dependences of >300 keV electron count rates, obtained using the Avion and Altair CubeSats (see trajectories in Figure 6), are plotted in Figure 7. The green line indicates Avion spacecraft data received on August 14,
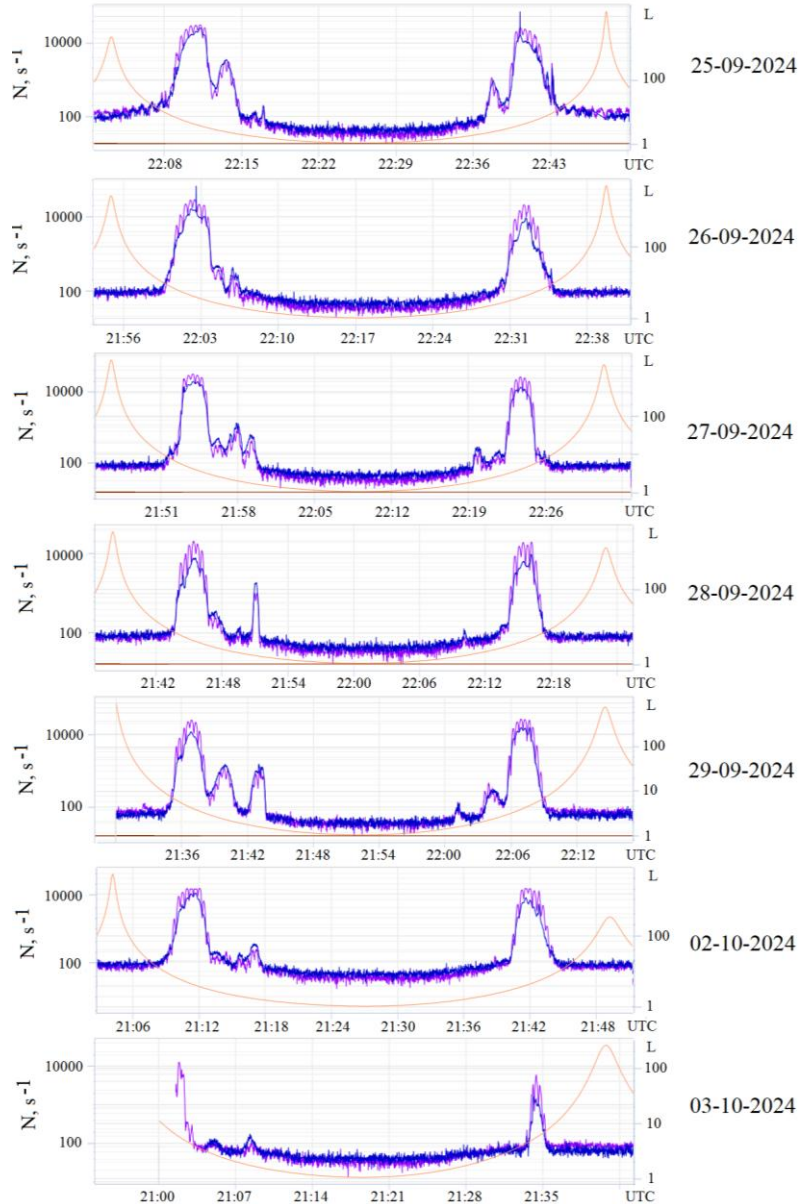

Figure 5. Time dependences of count rates of electrons from Avion DeCoR-1 (purple line, left scale) and DeCoR-3 (blue line, left scale), as well as the McIllwain parameter L (orange line, right scale) for magnetically quiet periods
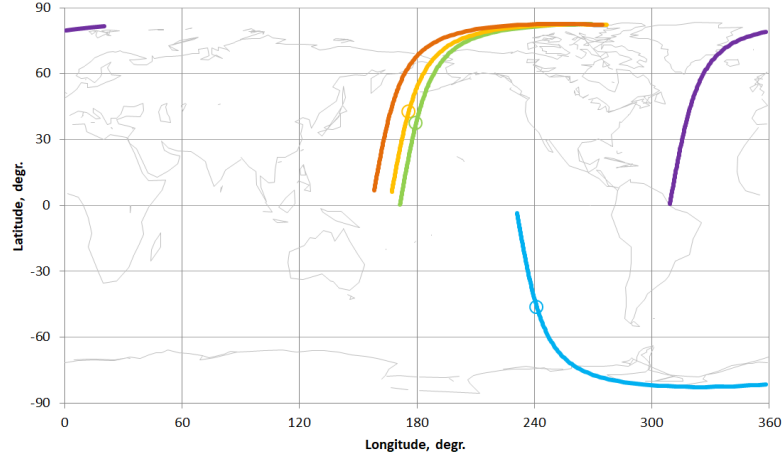
Figure 6. Map with a projection of the Avion and Altair CubeSats's orbits onto Earth: the green line is the Avion orbit on August 14, 2024 at 21:16–21:40; the yellow line is the Avion orbit on September 28, 2024 at 21:38–22:00; the purple line is the Avion orbit on September 28, 2024 at 12:06–12:30; orange line, the Altair orbit on December 13, 2024 at 09:48–10:11; blue line, the Altair orbit on December 13, 2024 at 16:53–17:17 UT. Circles mark the regions where sub-relativistic electrons precipitate from the inner belt
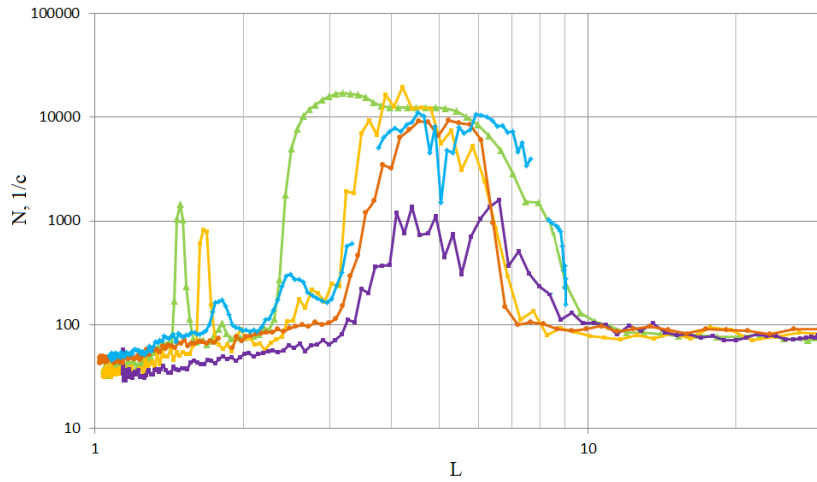

Figure 7. Dependences of electron counting rates on L, obtained on the Avion and Altair CubeSats for the measurements shown in Figures 5 and 6. The green line is Avion on August 14, 2024 at 21:16–21:40 UT (after the magnetic storm); the yellow line is Avion on September 28, 2024 at 21:38–22:00 UT (similar orbit and UT); the purple line, Avion on September 28, 2024 at 12:06–12:30 UT (different orbit and UT); the red line, Altair on December 13, 2024 at 09:48–10:11 UT (similar orbit, different UT); the blue line, Altair on December 13, 2024 at 16:53–17:17 UT (different orbit, similar UT)

2024 at 21:16–21:40 UT (after the magnetic storm that began on August 11, 2024); the yellow line (Avion), on September 28, 2024 at 21:38–22:00 UT (similar orbit and UT, Dst=–11 nT, K_p=2+); the purple line (Avion), on September 28, 2024 at 12:06–12:30 UT (different orbit and UT, Dst=3 nT, K_p=2–); the red line (Altair), on December 13, 2024 at 09:48–10:11 UT (similar orbit, different UT, Dst=1 nT, K_p=1+); the blue line (Altair), on December 13, 2024 at 16:53–17:17 UT (different orbit, similar UT, Dst=–6 nT, K_p=1+).

The above Figures show that in the regions under study (at L~1.7) there were short-term sharp increases (peaks) in >300 keV electron fluxes both before the onset of the magnetic storm (August 10), during the magnetic storm (August 12), and during the magnetically quiet period in December 2024 (data from the Altair CubeSat). At the same time, during the magnetic storm in August, another peak appeared at L~1.6, which reached a much higher amplitude on August 14, and the peak at L~1.7 ceased to be observed. Combination of

these facts suggests that the August 11–12, 2024 geomagnetic storm was so strong that it caused a disturbance not only in outer ERB, but also in the inner one, which led to a change in the distribution of sub-relativistic electron fluxes in the precipitation region.

If we consider this region as a whole, i.e. from L~1.6÷1.9, it should be noted that sharp increases in sub-relativistic electron fluxes on these L shells can occur in the region of 180° E both during magnetic storms and during magnetically quiet periods, and reach maximum values in the evening (UT).

In order to determine whether the observed intensity maxima of precipitating electrons are due to certain UT or reflect the spatial distribution of fluxes on certain drift shells or in certain geographic regions, we analyzed measurements at orbits intersecting the shells L~1.6÷1.9 at other longitudes (purple curve in Figures 6, 7).

Figure 7 shows that at ~320°–330° longitudes around noon (UT) there were no increases in intensity at L~1.6÷1.7, which allows us to conclude that precipita-

tion at these longitudes is probably linked either to a certain geographic region or to a certain UT interval.

To analyze both possibilities, we have compared electron count rates measured when different spacecraft passed through the same region, crossing it at different points (UT). To do this, in addition to Avion data, Figures 6, 7 plot two more trajectories and two additional sub-relativistic electron count rate profiles as function of L (red and blue lines). They were obtained from measurements made by DeCoR-2 (it also measured the count rates of >300 keV electrons) on board the Altair CubeSat, whose orbit is analogous to that of Avion. The red curve in Figure 7 represents the L dependence of electron flux, measured when Altair crossed the same region at $L{\sim}1.6$ as Avion, but much earlier (09:48–10:11 UT). In this case, the electron flux did not increase at $L{<}2$. However, a peak at $L{\sim}1.8$ was detected during other Altair passes, the L dependence for one of which is indicated by the blue line in Figure 7. At that time (16:53–17:17 UT), Altair moved from the southern polar cap to the equator over the Pacific Ocean. These results allow us to conclude that significant peaks at $L{\sim}1.6{\div}1.9$ are observed in different geographic regions, but during certain periods (UT), i.e. mainly in the afternoon and evening.

Note that significant fluxes of sub-relativistic electrons at $L{\sim}1.6{\div}1.9$ were previously detected by the OHZORA [Nagata et al., 1988], CORONAS-I satellites [Bashkirov et al., 1999; Kuznetsov, Myagkova, 2001; Kuznetsov, Myagkova, 2002], and the Mir orbital station [Bogomolov et al., 2005]. In particular, Kuznetsov, Myagkova [2002] have shown that electrons at $L{\sim}1.6$ are generally recorded at longitudes 110°–200°, 200°–290° from 10 to 24 UT. Kuznetsov and Myagkova [2002] conclude that precipitation at $L{\sim}1.6$ may be caused by thunderstorm activity, yet it is not unlikely that the precipitation may be linked to variations in the geomagnetic activity indices. We can say that the results of measurements of sub-relativistic electron fluxes at $L{\sim}1.6{\div}1.9$ with the Moscow University SC constellation do not contradict these conclusions.

CONCLUSION

In this paper, we have provided examples of observation of some space weather phenomena during experiments conducted with instruments developed at SINP MSU and installed on CubeSats of the Sozvezdie-270 constellation. In particular, we have demonstrated possibilities of measuring solar electron fluxes in NES for SCR events, have carried out observations of filling of the polar caps with SCR particles, which were used to obtain time dependences of the average count rate of sub-relativistic electrons in the polar caps during the June 8–10 and 12–14, 2024 SCR events. These dependences agree well with time variations of SCR electron fluxes at the L1 libration point, which were measured by ACE, as well as with the SCR proton profile from Electro-L2 data. We also acquired data on the dynamics of spatial distributions of sub-relativistic electron fluxes in outer ERB during the August 11–12, 2024 strong magnetic storm, which showed that during the magnetic storm main phase the outer ERB region seemed to compress. This is due to

the smaller shift in the equatorial boundary of the belt (to the region of the pre-storm location of the gap) as compared to the more noticeable shift in the polar boundary of ERB. During the recovery phase, the polar boundary returns to the position observed before the storm, whereas the equatorial boundary continues to remain close to Earth, due to which the region occupied by sub-relativistic electrons of outer ERB expands.

Also noteworthy are the results of studies into the dynamics of fluxes of sub-relativistic electrons precipitating from inner ERB at $L{\sim}1.6{\div}1.8$. We have shown that significant fluxes on these drift shells are generally observed in different geographic regions during a certain UT period at different geomagnetic activity levels. At the same time, in the case of the severe magnetic storm on August 11, 12, 2024, the spatial distribution of electron fluxes in the precipitation region underwent some variations. The results do not contradict the conclusions drawn earlier from OHZORA and CORONAS-I observations. Particularly noteworthy is that observations from different satellites of the Moscow University multi-satellite constellation Sozvezdie-270 have been used for the first time to obtain a more complete picture of the dynamics and spatial structure of precipitating electrons. Naturally, in order to draw certain conclusions on the dynamics and mechanisms of sub-relativistic electron precipitation from inner ERB, further research is needed to which satellite measurements can make a significant contribution. In this regard, the role of Sozvezdie-270 is very important.

REFERENCES

Baker D.N. Satellite anomalies due to space storms. *Space Storms and Space Weather Hazards*. 2001, vol. 38. Springer, Dordrecht. DOI: 10.1007/978-94-010-0983-6_11.

Bashkirov V.F., Denisov Y.I., Gotselyuk Y.V., et al. Trapped and quasi-trapped radiation observed by "CORONAS-I" satellite. *Radiation Measurements*. 1999, vol. 30, no. 5, pp. 537–546.

Belov A.V., Villoresi J., Dorman L.I., M.I. et al. Effect of the space on operation of satellites. *Geomagnetism and Aeronomy*. 2004, vol. 44, no. 4, pp. 461–468.

Bogomolov A.V., Denisov Y.I., Kolesov G.Y., et al. Fluxes of quasi-trapped electrons with energies >0.08 MeV in the near-earth space on drift shells $L{<}2$. *Cosmic Res.* 2005, vol. 43, no. 5, pp. 307–313.

Bogomolov V.V., Bogomolov A.V., Dement'ev Yu.N., Eremeev V.E., et al. A first experience of space radiation monitoring in the multi-satellite experiment of Moscow University in the framework of the Universat-SOCRAT project. Moscow University *Physics Bulletin*. 2020, vol. 73, no. 6, pp. 676–683. DOI: 10.3103/S0027134920060089.

Caspi A., Barthelemy M., Bussy-Virat C.D., et al. Small satellite mission concepts for space weather research and as pathfinders for operations. *Space Weather*, 2022, vol. 20, iss. 2, e2020SW002554. DOI: 10.1029/2020SW002554.

Cole D.G. Space weather: Its effects and predictability. *Space Sci. Rev.* 2003, vol. 107, pp. 295–302.

A.V. Bogomolov, V.V. Bogomolov, A.F. Iyudin, V.V. Kalegaev, I.N. Myagkova, V.I. Osedlo, S.I. Svertillov, I.V. Yashin

DOI: 10.1023/A:1025500513499.

Daglis I.A. *Space Storms and Space Weather Hazards*. Kluwer, Dordrecht, Boston, 2001. DOI: 10.1007/978-94-010-0983-6.

Dorman L.I., Miroshnichenko L.I. *Solar Cosmic Rays*. Moscow: Nauka, 1968, 468 p. (In Russian).

Ginet G.P., O'Brien T.P., Huston S.L. AE9, AP9 and SPM: New models for specifying the trapped energetic particle and space plasma environment. *Space Sci. Rev*. 2013, vol. 179, pp. 579–615 DOI: 10.1007/s11214-013-9964y.

Iucci N., Levitin A., Belov E., Eroshenko E.A. Space weather conditions and spacecraft anomalies in different orbits. *Space Weather*. 2005, vol. 3, S01001. DOI: 10.1029/2003SW000056.

Kudela K. Space weather near Earth and energetic particles: selected results. *Journal of Physics: Conf. Series*. 2013, vol. 409, iss. 1, article id. 012017. DOI: 10.1088/1742-6596/409/1/012017.

Kuznetsov S.N., Myagkova I.N. Fluxes of quasi-trapped particles under the Earth's radiation belts. *Geomagnetism and Aeronomy*. 2001, vol. 41, no. 1, pp. 10–13.

Kuznetsov S.N., Myagkova I.N. Quasi-trapped electron fluxes (>0.5 MeV) under the radiation belts: analysis of their connection with geomagnetic indices. *J. Atmos. Solar-Terr. Phys*. 2002, vol. 64, no. 5-6. pp. 601–605.

Kuznetsov S.N., Bogomolov A.V., Denisov Y.I., et al. The solar flare of November 4, 2001, and its manifestations in energetic particles from CORONAS-F data. *Solar System Res*. 2003, vol. 37, pp. 121–127. DOI: 10.1023/A:1023384425209.

Kuznetsov N.V., Nymmik R.A., Panasyuk M.I., Popova E. Working model of flows of space charged particles and new experimental data. *Voprosy atomnoi nauki i tekhniki* [Problems of Atomic Science and Technology. Ser. Physics of Radiation Effects…] 2014, no. 1, pp. 44–48. (In Russian).

Lundstedt H. The Sun, space weather and GIC effects in Sweden. *Adv. Space Res*. 2006, vol. 37, no. 6, pp. 1182–1191. DOI: 10.1016/j.asr.2005.10.023.

McGranaghan R.M., Camporeale E., Georgoulis M., Anastasiadis A. Space weather research in the digital age and across the full data lifecycle: Introduction to the topical issue. *J. Space Weather and Space Climate*. 2021, vol. 11, p. 50. DOI: 10.1051/swsc/2021037.

Myagkova I.N., Bogomolov A.V., Eremeev V.E., et al. Dynamics of the Radiation Environment in the Near-Earth space in September–November 2020 according to the Meteor-M and Electro-L Satellite Data. *Cosmic Res*. 2021, vol. 59, iss. 6, pp. 433–445. DOI: 10.1134/S0010952521060071.

Nagata K., Kohno T., Murakami H., Nakamoto A., Hasebe N., Kikuchi J., Doke T. Electron (0.19–3.2 MeV) and proton (0.58–35 MeV) precipitations observed by OHZORA satellite at low latitude zones *L*=1.6–1.8. *Planet. Space Sci*. 1988, vol. 36, pp. 591–606.

Novikov L.S., Voronina E.N. Interaction of spacecraft with the environment. Moscow: KDU, 2021.

Panasyuk M.I., Svertilov S.I., Bogomolov V.V., et al. Experiment on the Vernov satellite: Transient energetic processes in the Earth atmosphere and magnetosphere. Pt 1. Description of the experiment. *Cosmic Res*. 2016a, vol. 54, no. 4, pp. 261–269. DOI: 10.1134/S0010952516040043.

Panasyuk M.I., Svertilov S.I., Bogomolov V.V., et al. Experiment on-the Vernov satellite: Transient energetic processes in the Earth atmosphere and magnetosphere. Pt 2. First results. *Cosmic Res*. 2016b, vol. 54, no. 5, pp. 343–350. DOI: 10.1134/S0010952516050051.

Potapov A., Ryzhakova L., Tsegmed B. A new approach to predict and estimate enhancements of "killer" electron flux at geosynchronous orbit. *Acta Astronaut*. 2016, vol. 126, pp. 47–51. DOI: 10.1016/j.actaastro.2016.04.017.

Romanova N.V., Pilipenko V.A., Yagova N.V., et al. Statistical correlation of the rate of failures on geosynchronous satellites with fluxes of energetic electrons and protons. *Cosmic Res*. 2005, vol. 43, pp. 179–185. DOI: 10.10604-005-0032-6.

Sadovnichii V.A., Panasyuk M.I., Yashin I.V., et al. Investigations of the space environment aboard the Universitetsky-Tat'yana and Universitetsky—Tat'yana-2 microsatellites. *Solar System Res*. 2011, vol. 45, no. 1, pp. 3–29.

Sadovnichii V.A., Panasyuk M.I., Amelyushkin A.M., et al. "Lomonosov" satellite — space observatory to study extreme phenomena in space. *Space Sci. Rev*. 2017, vol. 212, no. 3-4. pp. 1705–1738. DOI: 10.1007/s11214-017-0425-x.

Schrijver C.J., Kauristie K., Aylward A.D., et al. Understanding space weather to shield society: A global road map 772 for 2015–2025 commissioned by COSPAR and ILWS. *Adv. Space Res*. 2015, vol. 55, pp. 2745–2807. DOI: 10.1016/j.asr.2015.03.023.

Vernov S.N., Grigorov N.L., Logachev YU.I., Chudakov A.Ye. Changes in cosmic radiation on an artificial Earth satellite. *Doklady Akademii Nauk*. 1958, vol. 120, no. 6, pp. 1231–1233. (In Russian).

Wei F., Feng X., Guo J.S., Fan, Q., Wu, J. Space weather research in China. *Adv. in Space Environment Res*. Springer, Dordrecht. 2003, pp. 327–334. DOI: 10.1007/978-94-007-1069-6_31.

Wilkinson P. Space weather studies in Australia. *Space Weather: The Intern. J. Research and Applications*. 2009, vol. 7, S06002. DOI: 10.1029/2009SW000485.

URL: https://swx.sinp.msu.ru/tools/davisat.php/ (accessed July, 22, 2025).

SPACE WEATHER RESEARCH IN YAKUTIA

A.V. Moiseev (iD)
*Yu.G. Shafer Institute of Cosmophysical Research
and Aeronomy SB RAS,
Yakutsk, Russia, moiseev@ikfia.ysn.ru*

A.Yu. Gololobov (iD)
*Yu.G. Shafer Institute of Cosmophysical Research
and Aeronomy SB RAS,
Yakutsk, Russia, golart87@gmail.com*

I.B. Ievenko (iD)
*Yu.G. Shafer Institute of Cosmophysical Research
and Aeronomy SB RAS,
Yakutsk, Russia, ievenko@ikfia.ysn.ru*

A.A. Korsakov (iD)
*Yu.G. Shafer Institute of Cosmophysical Research
and Aeronomy SB RAS,
Yakutsk, Russia, korsakovaa@ikfia.ysn.ru*

I.S. Petukhov (iD)
*Yu.G. Shafer Institute of Cosmophysical Research
and Aeronomy SB RAS,
Yakutsk, Russia, i_van@ikfia.ysn.ru*

S.A. Starodubtsev (iD)
*Yu.G. Shafer Institute of Cosmophysical Research
and Aeronomy SB RAS,
Yakutsk, Russia, starodub@ikfia.ysn.ru*

Abstract. The article reports on the studies of various manifestations of space weather (SW) on Earth, conducted by SHICRA SB RAS at the network of geophysical stations located in Yakutia. It is noted that the Institute researchers study various phenomena occurring in the solar wind and Earth's magnetosphere such as magnetic clouds, Forbush effects, magnetic storms, substorms and associated subauroral glow, as well as high-latitude impulses in the dayside magnetosphere and sudden phase anomalies in the lower ionosphere. In addition to the data from the network of stations in Yakutia, data from other domestic and foreign stations, as well as direct measurements of the parameters of the interplanetary medium and magnetosphere, carried out on various spacecraft, are used to study these phenome-

na. The paper also describes physical models of magnetic clouds in the solar wind, high-latitude disturbed ionosphere, and methods for short-term forecasting of SW based on cosmic ray (CR) measurements developed at SHICRA SB RAS.

Keywords: geomagnetic Pc5 pulsations, equivalent current systems, azimuthal and meridional propagation, space weather monitoring, space weather forecast, lower ionosphere, solar flare, VLF signal, sudden phase anomaly.

INTRODUCTION.
SPACE WEATHER MONITORING
AND FORECASTING IN RUSSIA

With the development of high technologies, space physics research has become of great importance for fundamental and applied science. Nowadays, space weather monitoring and forecast play an equally important role in the successful operation of space technology and human safety than the ordinary weather forecast. The term "space weather" (SW) refers to the state of near-Earth space (NES). In contemporary Russia, the information on the state of NES is generally provided by geophysical stations located at high latitudes of the Russian Arctic. The number of these stations is limited due to difficulties with staff, logistics, high electricity and heat tariffs in the Arctic. In addition, these stations belong to scientific organizations subordinate to different departments such as the Ministry of Education and Science of the Russian Federation and Roshydromet. As a result, SW monitoring and forecasting is carried out by a number of Russian scientific organizations (IZMIRAN, IKI RAS, SINP MSU, LPI RAS, ISTP SB RAS, IPG, AARI, SHICRA SB RAS,

IKIR FEB RAS, etc.). Despite the SW problem importance, this work has not yet been coordinated, and each organization does it independently. By contrast, SW issues are given much more attention abroad. As far back as 1995, the National Space Weather Program was created in the United States (National Space Weather Program. Strategic Plan. Office of Federal Coordinator for Meteorological Services and Supporting Research FCM-P30-1995. Washington DC. 1995); in 2001, the European ILWS (International Living with a Star) Program was launched. China keeps up with them and has also created the National Space Science Center, Chinese Academy of Science [http://eng.sepc.ac.cn/]. The importance of this problem is emphasized by the creation of the scientific journals "Space Weather" and "Space Weather and Space Climate", which very quickly became highly rated. Also noteworthy are the ground-based instruments for studying SW: a developed network of geophysical stations in the Western Hemisphere compared to the Eastern one. By contrast, the SW problem is poorly addressed in present-day Russia. The number of scientific events in the country that draw attention to this problem, such as conferences on SW held by the Joint Russian-Chinese Scientific Center for SW, is very

limited. Thus, scientific organizations engaged in SW research in Russia work under such difficult conditions.

This paper describes the network of geophysical stations of the Yu.G. Shafer Institute of Cosmophysical Research and Aeronomy SB RAS in Yakutia and presents the results of SW research the Institute carries out.

1. GEOPHYSICAL NETWORK OF STATIONS IN YAKUTIA

The main experimental measurements for studying the physical picture of phenomena in the subauroral and auroral zones are carried out on the basis of the unique meridional network of SHICRA SB RAS geophysical stations in the territory of Yakutia (Figure 1). Geophysical phenomena during substorms and magnetic storms often cover a significant latitudinal and longitudinal interval. Therefore, in a number of situations only the ground-based method of recording SW manifestations can provide general information about magnetospheric processes.

The experimental base includes a network of stations in Yakutia, among which the following stationary polygons should be highlighted:

* Yakutsk EAS Array named after D.D. Krasilnikov (Oktyomtsy);
* Yakutsk cosmic ray spectrograph named after A.I. Kuzmin (Yakutsk);
* Tixie Polar Geocosmophysical Observatory (Tixie Bay);
* Complex geophysical station Zhigansk (Zhigansk);
* The Maimaga optical station named after V.M. Ignatiev (Maimaga);
* Magnetic observatory and ionospheric station Yakutsk (Yakutsk);
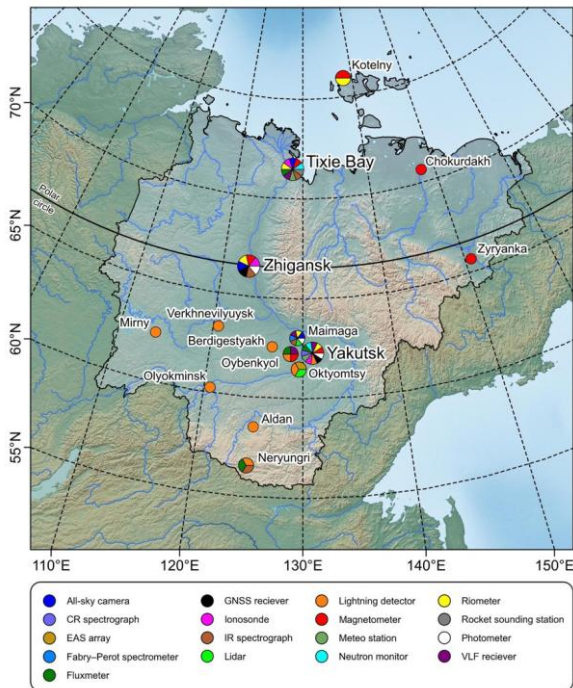* Radiophysical station "Oybenkyol" (Oybenkyol).

Figure 1. Stations of the meridional geophysical network in Yakutia in geographic coordinates. Measurement types are shown in color in the legend (for 2024)

According to types of spatial measurements, the following networks of stations can be distinguished in Yakutia:

* network of magnetometric stations;
* network of riometric stations;
* network of stations for measuring the atmospheric electric field intensity;
* network of stations monitoring thunderstorm activity in Yakutia.

In the area of research into the geomagnetic field and magnetospheric electromagnetic disturbances, SHICRA SB RAS participates in three large international projects — INTERMAGNET [http://www.intermagnet.org], MAGDAS [http://magdas2.serc.kyushu-u.ac.jp/station/index.html], and PWING [http://www.isee.nagoya-u.ac.jp/dimr/PWING/en/], and also conducts joint research with the group of low-frequency radio emissions of the Georgia Institute of Technology, Atlanta, USA. Consequently, SHICRA SB RAS stations are equipped with modern scientific instruments from the world's leading manufacturers.

2. RESULTS OF SPACE WEATHER RESEARCH AND FORECAST

Below we present the results obtained by studying SW phenomena experimentally and via modeling, as well as the result of SW forecast from satellite measurements.

2.1. Comparative analysis of meridional and azimuthal propagation of Pc5 pulsations and their current systems based on ground and satellite observations

One of the daytime impulsive high-latitude phenomena is Travelling Convection Vortices (TCVs) [Glassmeier, 1992]. TCV is a structure consisting of a pair of oppositely directed vortices in the magnetosphere, connected by field-aligned currents with vortices in the ionosphere. During its development, TCV shifts azimuthally from noon to dawn sector and along the meridian poleward. The location of magnetospheric and ionospheric TCVs, as well as the field-aligned currents connecting them in the pre-noon sector, is shown in Figure 2, *a* from [Tavares, Santiago, 1999], with arrows V_{EW} and V_{conv} indicating TCV propagation in the azimuthal direction and plasma convection respectively. According to ground-based and satellite observations, TCV consists of 2–3 pulses of opposite polarities with 5–10 min periods; TCVs are observed locally on the dayside at high latitudes. It is important to study the dynamics of TCVs in terms of SW since they cause geomagnetic field variability $|dB/dt|$ in the absence of magnetic storms and can affect technical infrastructure at high latitudes [Pilipenko et al., 2023].

Moiseev et al. [2024a] have used ground observations in 8 events to compare TCV velocities by phase delays of Pc5 pulsations and by the motion of their equivalent current systems. Figure 2, *b*, *c* presents histograms of meridional velocities; and Figure 2, *d*, *e*, of azimuthal velocities. On the ordinate axis in Figure 2, *b*, *d* is the number of measurements of Pc5 pulsation velocities
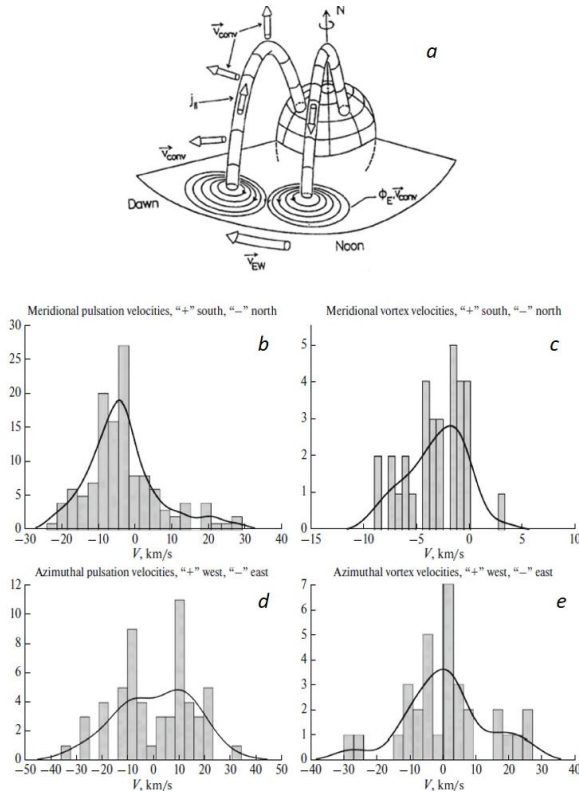
Figure 2. Travelling convection vortices in the magnetosphere and ionosphere (*a*); histograms of propagation velocities of geomagnetic pulsations and equivalent current vortices; meridional velocities (*b, c*); azimuthal velocities (*d, e*)

on the ordinate axis in Figure 2, *c, e* is the number of measurements of vortex propagation velocities. The histograms show a smoothing line as the result of a nonparametric method for estimating the density of random variable (Kernel Density Estimation). It is evident from the histograms that propagation of pulsations and vortices is similar: along the meridian, pulsations and vortices predominantly propagate to the north. In most cases, propagation velocities of pulsations and vortices were ~5 km/s and 2 km/s respectively, whereas in azimuth, pulsations and vortices propagate to the west, their propagation velocities were ~10 km/s and 3 km/s respectively. However, in the distribution of azimuthal velocities of both pulsations and vortices there are comparable maxima corresponding to eastward propagation: the velocity of pulsations is 10 km/s, and that of vortices is 5 km/s. Moiseev et al. [2024b] have studied TCV propagation, using satellite and ground-based observations. Pulsations in the magnetosphere and ionosphere, and equivalent current vortices in the ionosphere were found to propagate in the azimuthal direction from the day side to the night side. The propagation velocities according to ground observations are 5–25 km/s; according to satellite observations, 114–236 km/s.

The results of the work show that the dynamics of equivalent current systems correspond to the dynamics of pulsations, and they can be utilized to study propagation as an additional method, especially when it is impossible to determine propagation velocities from phase delays, but it is necessary to take into account the difference between velocities of pulsations and vortices.

TCVs are recorded in an extended longitude sector (up to 12 hours). It is assumed that the observed dynamics of Pc5 pulsations and vortices reflects propagation of MHD waves in the magnetosphere, not only from the day side to the night side, but also in the opposite direction (from the night side to the noon side).

2.2. Study of the magnitude of sudden phase anomalies on VLF radio paths during solar flares

Changes in lower ionosphere parameters are sensitive to space weather events [Silber, Price, 2017]. Very low frequency (VLF 3–30 kHz) radio waves propagate for a long distance as in a waveguide due to reflection from water, ground, and lower ionosphere. An increase in the X-ray flux intensity during solar flares leads to sudden ionospheric disturbances (SIDs). A sharp increase in the electron density during SIDs causes sudden phase anomalies (SPAs) of VLF radio signals during daytime propagation in the Earth — ionosphere waveguide [Kumar, Kumar, 2018]. Recording of VLF signal parameters allows ionosphere research to be conducted with high resolution both in time and space. The Antarctic-Arctic Radiation-belt (Dynamic) Deposition-VLF Atmospheric Research Consortium is widely known, it provides continuous observations of the lower ionosphere in the polar regions [Clilverd et al., 2009]. The problem of high-resolution VLF monitoring of large, hard-to-reach areas of the Pacific Ocean and Northern Asia remains unresolved [Wendt et al., 2024]. VLF observations in Yakutia are described below.

In Yakutsk (62.02° N, 129.70° E) and in the Polar Geocosmophysical Observatory (PGO) in Tixie Bay (71.60° N, 128.90° E), SHICRA SB RAS records signals from VLF radio transmitters. The phase variations of signals from the transmitters Khabarovsk (Russia, RSDN-20 system, 50.07° N, 136.6° E, signal frequency 11.904 kHz) and NWC (Australia, 21.82° S, 114.17° E, signal frequency 19.8 kHz) have been selected for the analysis [Kozlov et al., 2025]. Radio propagation paths Khabarovsk—Yakutsk (the length is 1.4 Mm) and NWC—Yakutsk (the length is 9.4 Mm) cover the East Asia territory. SPAs of signals from the Khabarovsk and NWC transmitters recorded in Yakutsk are plotted in Figure 3 as a function of solar X-ray flux. Changes in the VLF signal phase Φ relative to the undisturbed value are reduced to the propagation path length unit (deg/Mm). The value P is the maximum X-ray flux intensity (0.1–0.8 nm) during a solar flare (W/m^2). The value $\cos X$ is the cosine of a solar zenith angle X averaged along the entire propagation path. The solar zenith angle X was calculated from geographic coordinates along each of the radio paths with a step of 200 km by the algorithm [http://stjarnhimlen.se/comp/tutorial.html].

The standard deviations of residuals are 1.37 deg/Mm (the Khabarovsk—Yakutsk propagation path) and 1.73 deg/Mm (the NWC—Yakutsk propagation path). The reliability level of model SPA parameters is not lower than 98 % (the Fisher criterion). The SPA model parameters were applied to solar flares for the VLF propagation paths. The X-ray flux during solar flares can be estimated by the ground-based method, using VLF data [George et al., 2019; Korsakov et al., 2021].
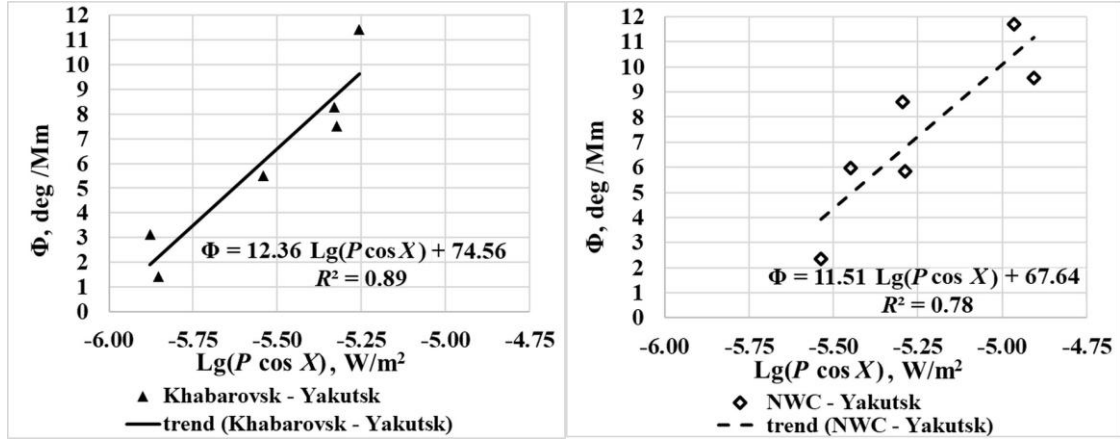
Figure 3. Sudden phase anomalies Φ of signals from transmitters Khabarovsk (left) and NWC (right) recorded in Yakutsk as a function of solar X-ray flux

2.3. Relationship of the SAR arc to the energetic ion flux boundary inside the plasmasphere and the plasmapause based on ground and satellite observations

Stable auroral red (SAR) arcs occur during magnetic storms due to overlap of the ring current with the outer plasmasphere, where energetic ion fluxes heat plasmaspheric electrons. SAR arcs are optical manifestations of SW in Earth's atmosphere. The resulting downward flux of superthermal electrons along magnetic field lines increases the ambient electron temperature at altitudes of the ionospheric F2 region in the form of a subauroral electron temperature peak (T_e peak). As a result, the intensity of the red line of atomic oxygen in the SAR arc, which reflects the plasmapause, increases [Cole, 1965, 1970; Cornwall et al., 1971; Kozyra et al., 1997]. Long-term observations of subauroral glow at the Yakutsk meridian have shown that under conditions of low magnetic activity ($Dst \geq -50$ nT, $K_p \leq 3-4$) SAR arcs appear during individual substorms and are observed at corrected geomagnetic latitudes (CGMLat) 55–60° [Ievenko, 1999; Ievenko, Alekseev, 2004]. During periods of high geomagnetic activity, SAR arcs are recorded at lower latitudes.

Below are the results of comparison of SAR arc observations by the digital all-sky camera (All-sky imager "Keo Sentry") at the station Maimaga (CGMLat=58°, CGMLon=202°) with data from simultaneous recording of plasmapause and energetic ion fluxes on board the Van Allen Probe B (VAP-B) satellite at the beginning of the major magnetic storm on March 17, 2015 [Ievenko, 2020; Ievenko, Parnikov, 2020].

The ground-based and satellite observations in Figure 4 show the following.

1. An intense SAR arc was observed equatorward of the diffuse aurorae at low auroral activity at CGMLat=52−59° in the dusk MLT sector. Variations in the intensity and location of the red arc during the period considered were insignificant (*a*).

2. At 12:10:10 UT (~18:52 MLT), the equatorial edge of the red arc at CGMLon~179° coincided with the boundary of the flux of energetic H⁺ and O⁺ ions

inside the plasmasphere at $L \sim 2.8$, as measured by VAP-B at ~17:36 MLT (*b*).

3. At 12:45:10 UT (~19:05 MLT), the polar edge of the arc at CGMLon~174° was due to a sharp decrease in the electron density to ~100 cm⁻³ (plasmapause) at $L \sim 4.0$ at ~19:05 MLT (*b*).

4. The width and location of the SAR arc were in good agreement with the intense T_e peak, as measured by DMSP-19 in the dusk MLT sector at ~11:54 UT (*c*). Electron temperature measurements verify ground-based observations of the SAR arc.

2.4. Study of ionospheric disturbances based on numerical modeling of large-scale structure of the ionosphere

The high-latitude ionosphere has a complex structure and is characterized by the presence of regular large-scale structural features such as the tongue of ionization and polar cavity at high latitudes, polar and auroral peaks in the daytime cusp region and in the night sector, as well as the main ionospheric trough (MIT) at subauroral latitudes [Mizun, 1980]. The ionosphere depends significantly on SW. Thus, during geomagnetic storms, the configurations of these structural features become more complex, which is mainly caused by the disturbance of the large-scale electric field of magnetospheric convection controlled by the orientation of the interplanetary magnetic field (IMF). Changes in the electron density distribution in turn affect radio wave propagation and the positioning accuracy of global navigation satellite systems (GNSS).

SHICRA SB RAS conducts research into the large-scale structure of the ionosphere and the processes occurring in it, using the developed non-stationary three-dimensional model of the ionosphere in Euler variables [Kolesnik, Golikov, 1982; Golikov et al., 2005, 2012, 2016]. Below are the results of the study into the effect of magnetospheric convection on the large-scale structure of the ionosphere during a moderate geomagnetic storm for winter conditions ($\delta = -23°$). Two diametrically opposed scenarios are considered: 1) with the onset of the storm at 16 UT; 2) with the onset of the storm at 04 UT.

Figure 5 illustrates variations in the IMF B_z component (*a*) and geomagnetic activity indices *Dst* and *AL* (*b*) and spatiotemporal distributions of the electron density at the F2 maximum altitude (n_mF2) at different moments of universal time (UT) at the onset of the storm at 16 UT (*c−e*) and 04 UT (*f−h*). Under quiet conditions (Figure 5, *c*), the convection region is seen to partially enter the illuminated zone above the terminator at 16 UT, which leads to transfer of plasma from the dayside ionosphere to the night side and the formation of an ionization tongue. In polar latitudes ($\Phi_M \geq 80°$), a region of low n_mF2 is formed — a polar cavity surrounded by ionization in the auroral oval (Figure 5, *c*). In the latitudinal variation in the dusk sector in the full shadow region [Kolesnik, Golikov, 1982], a deep concentration trough is observed: the main ionospheric trough (MIT) (Figure 5, *c*). After the onset of the disturbance, convection intensifies and its area of action increases (Figure 5, *d*, *e*). This causes an increase in the area of overlap of the convection region with the illuminated ionosphere and hence an increase in the transfer of dayside ionization to the night side by the antisunward flow, subsequent extension of the ionization tongue in the day-night direction, and the disappearance of the polar cavity at 19 UT. At 22 UT, the depth of MIT decreases, and MIT shifts southward by ~5°÷10°.
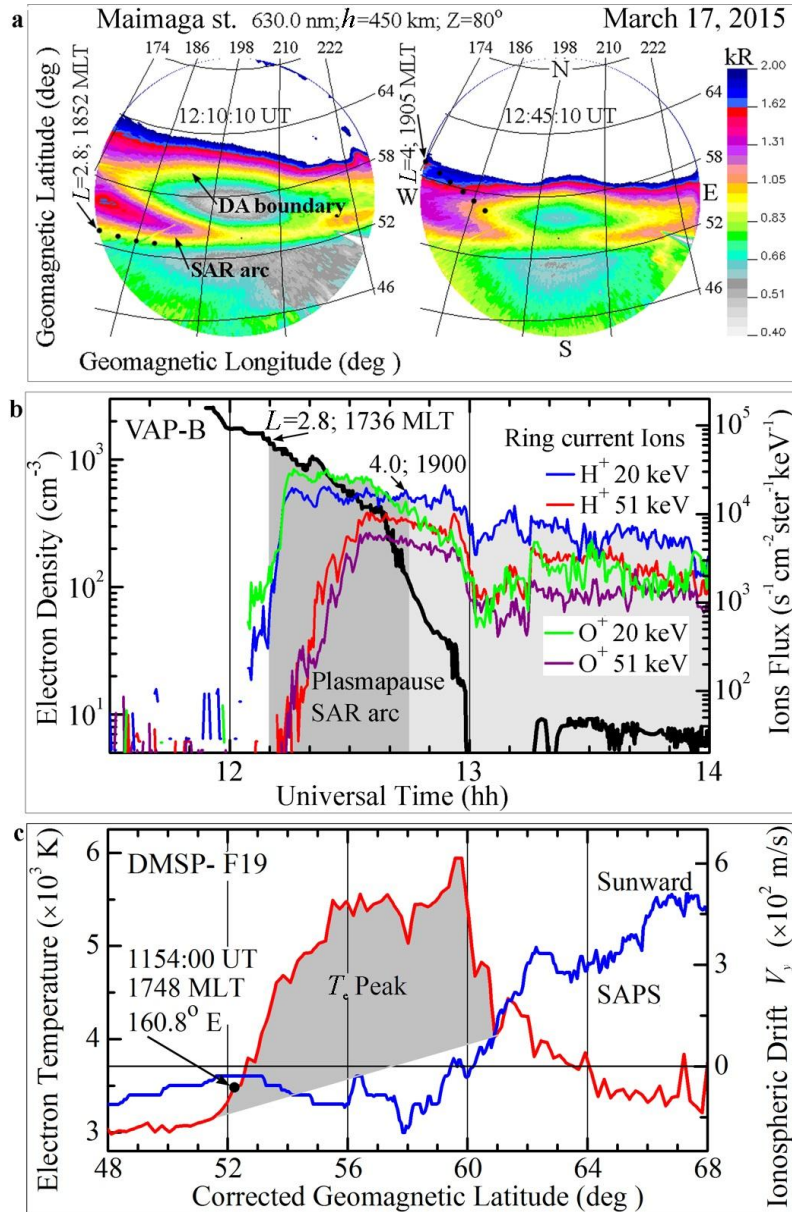

Figure 4. SAR arc at Maimaga station during recording of plasmapause energetic ion fluxes and T_e peak on board the VAP-B and DMSP-F19 satellites, respectively, on March 17, 2015. All sky images in the 630.0 nm emission projected onto Earth's surface for the glow altitude of 450 km (Z≤80°) in corrected geomagnetic coordinates (*a*). The color scale of the emission intensity is given only up to two kilorayleigh (kR) for better display of the SAR arc. The density of thermal electrons and fluxes of energetic protons and oxygen ions (*b*). The dark gray column shows the region of VAP-B measurements, which was conjugate with the observed SAR arc. Latitudinal distribution (*c*) of electron temperature and ionospheric drift in the F region based on DMSP-19 measurements in the dusk MLT sector. The bold dot marks the location of the equatorial boundary of the T_e peak, with magnetic longitude and MLT indicated
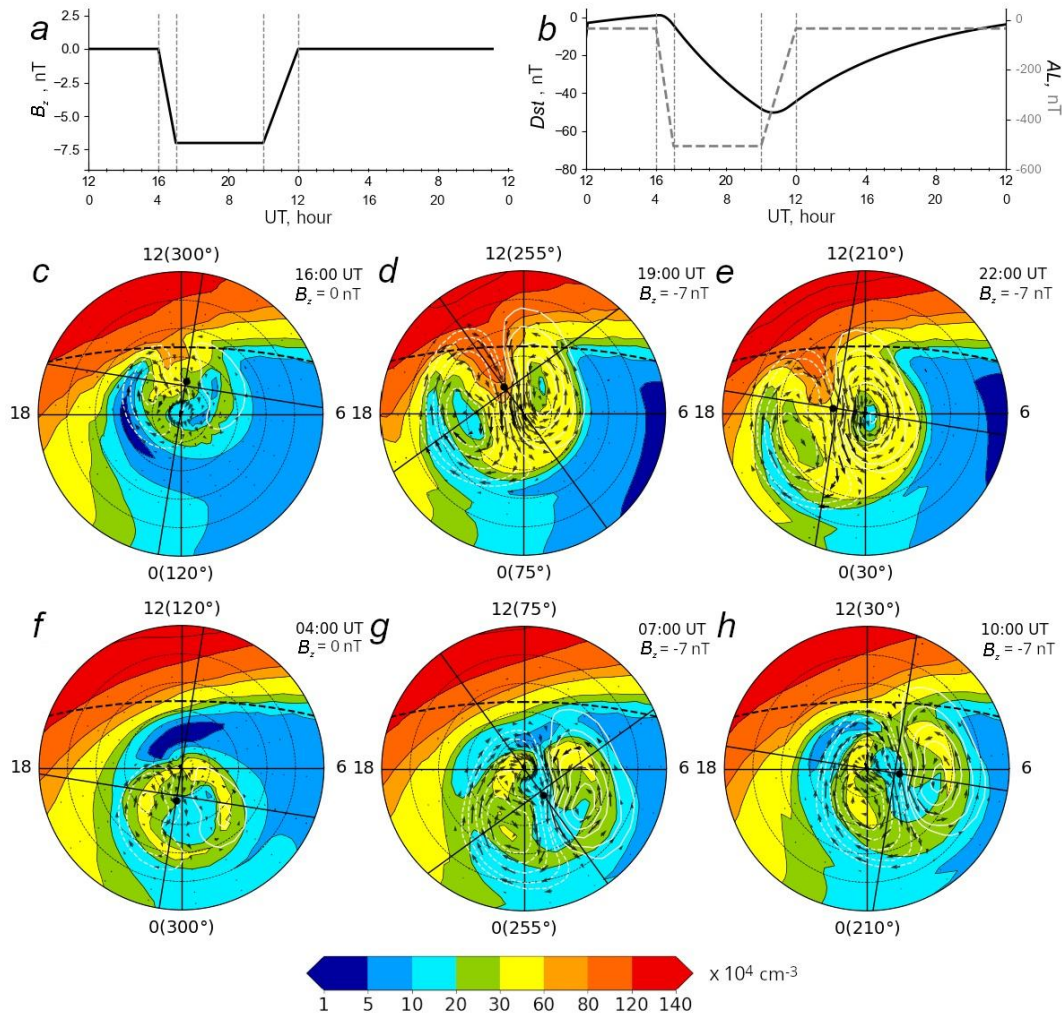
Figure 5. IMF B_z component (*a*), geomagnetic activity indices *Dst* and *AL* (*b*), and spatiotemporal distributions of the electron density at the height of the F2 maximum (n_mF2) at different moments of universal time at the onset of the storm at 16 UT (*c–e*) and 04 UT (*f–h*). Concentric circles denote the geographic latitudes of the Northern Hemisphere drawn through 10°. The lower boundary corresponds to 40° N. The numbers near the outer circle are local time and next to them in brackets are geographic longitude. The dashed line (upper) is the position of the terminator at the zenith angle χ=90°. The intersection point of two mutually perpendicular lines is the geomagnetic pole, which is 11.5° away from the geographic pole. The arrows indicate drift velocities of ionospheric plasma caused by the electric field of magnetospheric convection. White isolines show the electric field potentials calculated by the Weimer model [Weimer, 1996]. Charged particle precipitation is specified using the APM PGIA model [Vorobjev et al., 2013]

The storm onset at 04 UT is diametrically opposite to the magnetic storm onset at 16 UT (Figure 5, *f–h*). In this case, the Eastern Hemisphere is on the day side. As can be seen, at 04 UT the geomagnetic pole and with it the convection and precipitation region are located entirely on the night side (Figure 5, *f*). As a result, the ionization tongue is seen to separate from the dayside ionosphere. In the latitudinal variation on the dayside in the range 70–80° N, a great dip in n_mF2 is observed — a daytime dip (Figure 5, *f*) [Kolesnik, Golikov, 1984]. At CGMLat above ~80°, a polar cavity is formed, where n_mF2≤10^4 cm^{-3}. After the disturbance starts, the increase in magnetospheric convection leads to the expansion of the detached tongue of ionization and to the smoothing of the auroral peaks of n_mF2 (Figure 5, *g, h*). At 07 UT, convection covers the daytime trough and significantly increases n_mF2 compared to their values under quiet conditions (Figure 5, *g, f*).

Thus, magnetospheric convection during a moderate magnetic storm causes a change in the shapes and sizes of the main large-scale structural features of the ionosphere and depends on the time of the geomagnetic storm onset due to the displacement of the geographic and geomagnetic poles. The storm effect is most pronounced in the case of storm onset at 16 UT, when the disturbed electric field of magnetospheric convection enhances the transfer of plasma from the dayside ionosphere to the night side. The results are presented in more detail in [Gololobov, Golikov, 2024; Gololobov et al., 2025].

2.5. Explanation of Forbush decreases in cosmic rays based on a physical model

Large-scale coronal mass ejections (CMEs) are one of the largest energetic events on the Sun and an important factor in SW affecting geomagnetic activity, the

spatiotemporal distribution of CRs, and solar wind plasma properties. The modern approach to determining the properties of ejections and their identification in interplanetary space is usually based on the use of local spacecraft measurements. Since the number and spatial coverage of such spacecraft are fairly limited, there is a need for alternative sources of information, for example, CR measurements, which, due to high mobility, contain information about large-scale properties of the medium.

Part of CME is magnetic clouds (MCs) — areas filled with a helical magnetic field. Due to its force-free structure, such a field is preserved at large distances. Some MCs are oriented in such a way that in the vicinity of Earth, regular IMF will have a high intensity and a long-term southern orientation, which is a necessary condition for the occurrence of a geomagnetic storm.

To determine properties of MC from observed characteristics of CRs, it is necessary to describe their interaction. We have proposed an electromagnetic mechanism for such interaction. In this mechanism, particle scattering is neglected, and propagation is determined only by the magnetic field of the ejection and the electric field induced in the moving plasma. By calculating trajectories of CRs from the point of interest to the source (the point where the characteristics have not yet been altered by the Sun), it is possible to determine the change in their energy and the corresponding change in intensity. For theoretical calculations, an MC model has also been proposed which allows us to identify the magnetic field at an arbitrary point at any time.

The calculations have shown that the energy losses during the motion of CRs in the induced electric field, although small, are monotonous; hence, the longer the particle moves in interplanetary space, the more energy it loses, which leads to a decrease in the recorded intensity of CRs (Figure 6, *a*).

Since the calculations allow us to determine the CR distribution function, knowing it, we can find not only the zero moment (the integral intensity), but also higher moments: the first — the vector anisotropy (Figure 6, *b*), and the second — the tensor anisotropy (Figure 6, *c*, *d*). The CR anisotropy inside MC increases, which is consistent with experimental observations. Comparison of the experimental results with calculations suggests that the adopted assumptions and the constructed models are adequate. The method and the results obtained on its basis are described in more detail in [Petukhova et al., 2019, 2020].

In the future, it is planned to take into account in the model not only the magnetic field of MC, but also the effect of the coronal mass ejection plasma, the region of compressed solar wind, and the shock wave on CRs. This will allow a more accurate determination of ejection properties long before it arrives at Earth's orbit and hence refinement of space weather forecast.

2.6. Forecast of geoeffective disturbances from satellite and ground cosmic ray measurements

Since 2009, SHICRA SB RAS has been conducting an experiment on short-term (1–2 days) forecasting of the arrival of large-scale SW disturbances into the Earth orbit, such as interplanetary shock waves (ISWs) and high-speed SW streams, using measurements from the global network of CR stations, which include SHICRA SB RAS stations Yakutsk and Tixie Bay, as well as real-time spacecraft (SC) measurements of interplanetary medium parameters.

In this paper, we illustrate the capabilities of the ISW forecast from 1 hr [ftp://ftp.swpc.noaa.gov/pub/lists/ace2/] and 1 min ACE SC data [ftp://ftp.swpc.noaa.gov/pub/lists/ace/]. This SC is located near the libration point L1 at a distance of ~1 500 000 km from Earth toward the Sun. The flight time of large-scale SW disturbances from the location of ACE SC to Earth's magnetosphere is on average ~1 hr, which is clearly insufficient for taking any preventive measures to prevent possible negative effects of SW changes on various technical space or ground systems. However, the forecast method we developed using data from this SC allows us to receive a warning about upcoming changes in SW much longer in advance, ~1 day.

Of all the experiments conducted on board ACE SC, we use data from the MAG, SWEPAM, and EPAM experiments. In the latter case, the data is from measurements of proton fluxes in 8 different differential energy channels with energies from 47 to 4800 keV, which are measured by the LEMS120 detector. Note that all data is primary and so should be analyzed with a certain caution, and possible risks associated with their use must be assumed.

At present, we have already accumulated the necessary knowledge to construct a physical picture of the occurrence of fluctuations (or short-term variations with periods less than 3 hrs) of CR in order to apply it to a forecast of the arrival of large-scale solar wind disturbances at the Earth orbit [Berezhko, Starodubtsev, 1988; Starodubtsev et al., 1996; Grigoryev et al., 2008]. In brief, the knowledge boils down to the following.

In many cases, significant CR fluxes with ~1 MeV energies are often observed in the region before large-scale solar wind disturbances, e.g. ISWs or high-speed solar wind streams. Moreover, compared to the background, these CRs are characterized by large values of both the fluxes and their gradients. This leads to the development of plasma instabilities, which in turn are converted into MHD waves of various types. If fast magnetosonic waves develop in interplanetary space before the aforementioned solar wind disturbances, they, in turn, modulate the isotropic part of the CR distribution function in a wide energy range (from tens of keV to units of GeV) and hence lead to the emergence of CR fluctuations. Nonetheless, since CR fluctuations have a low amplitude (less than 1 %), then to isolate them against the background of the persistent noise, it is necessary to correctly apply spectral analysis methods [Starodubtsev et al., 2023]. One of the methods for forecasting SW developed at SHICRA SB RAS from CR measurements is based on these concepts.

The fluctuation extraction technique involves calculating the coherence between CR flux measurements in different differential channels in the EPAM/LEMS120 experiment. According to the results obtained in [Grigo-
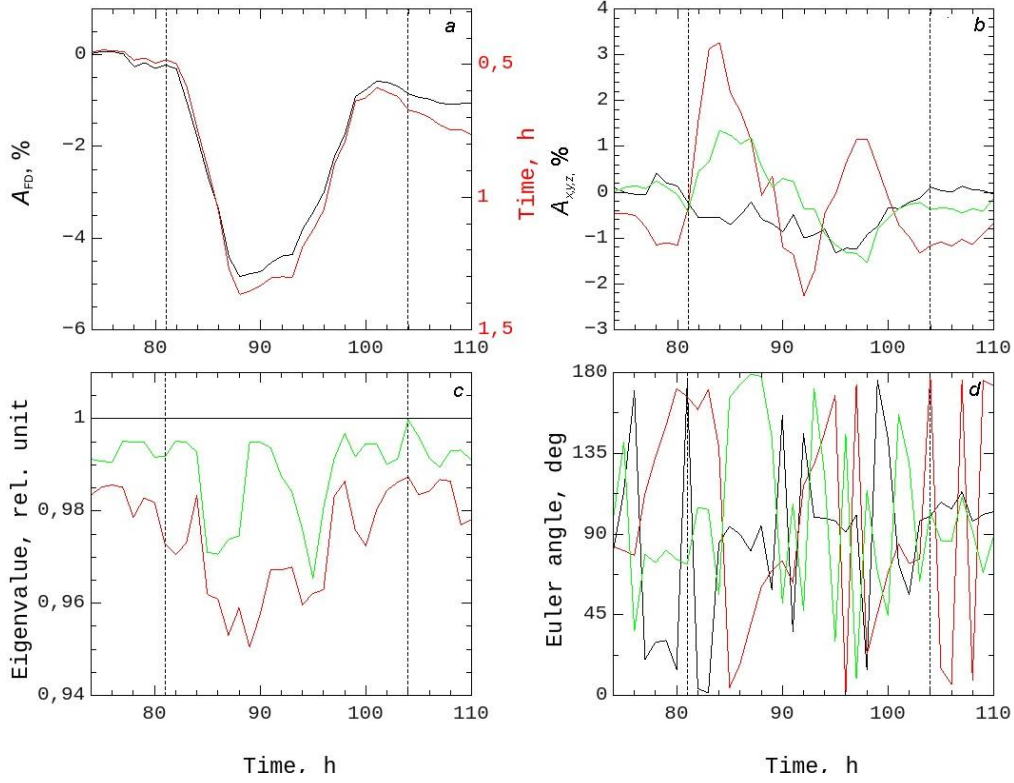
Figure 6. Characteristics of the Forbush decrease in time: *a* — the amplitude of the Forbush decrease is shown by the black curve (left scale); and the average time of CR transition from the surrounding space to MC, by the red curve (right scale); *b* — vector anisotropy component (black curve — A_x; red curve — A_y; green curve — A_z); *c* — relative eigenvalues (the maximum eigenvalue, indicated by the black line, is 1; green curve is the average; red curve is the smallest); *d* — three Euler angles defining the orientation of the ellipsoid (black and red curves are α1, α2; green curve, α3). B_m=11.6 nT is maximum magnetic field strength when MC crosses Earth. Dashed vertical lines are the leading and trailing boundaries of MC

ryev et al., 2008], there is a significant CR coherence value between CRs with different energies in the frequency range above 10^{-4} Hz in the case of significant CR fluxes in the region of the ISW pre-front. Our experience shows that for forecasting purposes it is necessary for the coherence to exceed a certain critical level equal to 0.85, and it is sufficient for this to occur not in the entire range, but at individual frequencies that correspond to the inertial section of the MHD wave turbulence spectrum, where fast magnetosonic waves are observed. Therefore, as a precursor of the arrival of interplanetary disturbances of the solar wind at the Earth orbit we utilize a maximum coherence coefficient (Coher MAX) between measurements in the energy channels P2 and P5. As an example, let us consider the ISW event of May 10, 2024. Figure 7, *a–e* presents 1-hr measurement data on the IMF modulus and B_z component (*a*), solar wind density (*b*), temperature (*c*), and velocity (*d*), as well as *Dst* (*e*) for the event under study from May 8 to 13, 2024. It is evident that at the leading edge of strong ISW at ~18:00 UT on May 10, 2024, all parameters significantly exceeded their average values. In this case, the IMF modulus *B* was more than 40 nT, the B_z component was less than –16 nT, the solar wind plasma density $n \approx 33$ cm^{-3}, its temperature $T \approx 5 \cdot 10^5$ K, and the solar wind speed *U* was as high as 680 km/s (Figure 7, *a–d*). Since this was a complex event in all respects, caused by almost simultaneous arrival of multiple CMEs at Earth [Hayakawa et al., 2025; Lazzús, Salfate,

2024; Ram et al., 2024], all SW parameters subsequently changed even more dramatically. The passage of this
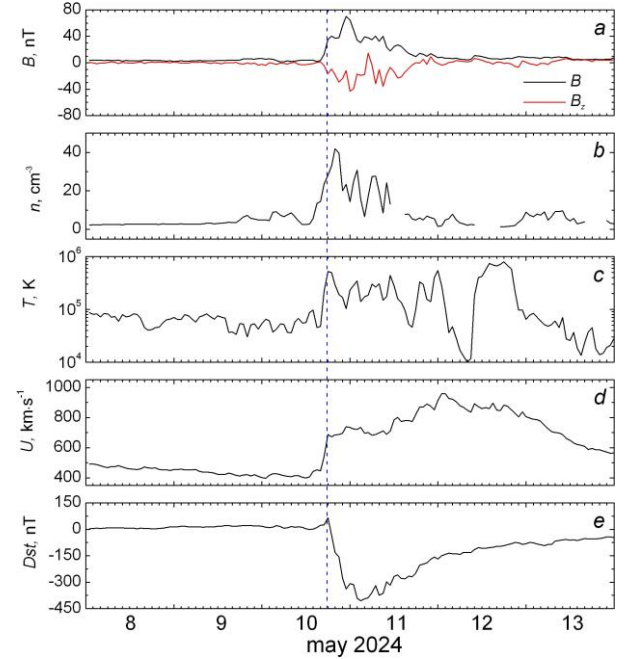

Figure 7. Variations in the IMF modulus *B* and B_z component (*a*), density *n* (*b*), temperature *T* (*c*) and solar wind velocity *U* (*d*), as well as the *Dst* index (*d*) for May 8–13, 2024, as measured by ACE SC. The vertical dashed line indicates the arrival of ISW at ACE SC and the storm sudden commencement (SSC)

strong ISW caused a powerful geomagnetic storm with SSC (Figure 7, *e*). This storm began at 17:05 UT on May 10, 2024. As a result of the passage of multiple CMEs through the Earth orbit, *Dst* at the storm minimum decreased to –406 nT [https://omniweb.gsfc.nasa.gov/ow.html]. It was the most powerful geomagnetic storm observed in the last two decades since the famous event of November 20, 2003, which is known in the scientific literature as the Halloween Event [Piersanti et al., 2025].

Figure 8 presents the results of the ISW arrival forecast and it needs some explanations. The names of the experiments and the corresponding SC on board which they are conducted are given at the top of the figure. Further, from top to bottom, the large panels show the time dependence of the variations in the IMF modulus B and *Bz* component, the SW plasma velocity *U* and density n, the low-energy CR flux *J*, and the maximum value of the coherence coefficient between measurements in the P2 and P5 energy channels (Coher MAX). Vertical lines designate the universal time (UT), which is given

under the bottom panel as day of the year. Four bottom small panels from left to right exhibit the current values of the IMF power spectrum density and the power function approximating it, as well as the coherence coefficients depending on the frequency between *B* and *U*, *B* and *n*, and between P2 and P5. Note that the coherence values between *B* and *U* reflect the contribution of Alfvén waves to the observed power spectrum of IMF; *B* and *n*, that of fast magnetosonic waves. Inscriptions below these panels contain information about the fact of using data in real time and the time of creating the figure. In the case of generating a forecast, a red inscription appears in Figure 8, which states that an interplanetary disturbance is expected to arrive at the spacecraft within ~1 day.

It is evident from Figure 8 that, as expected, increased low-energy CR fluxes were observed in this event in the region of the strong ISW pre-front. It can therefore be expected that they will generate fast magnetosonic waves in the region of the ISW pre-front, which will modulate the isotropic part of the CR flux and
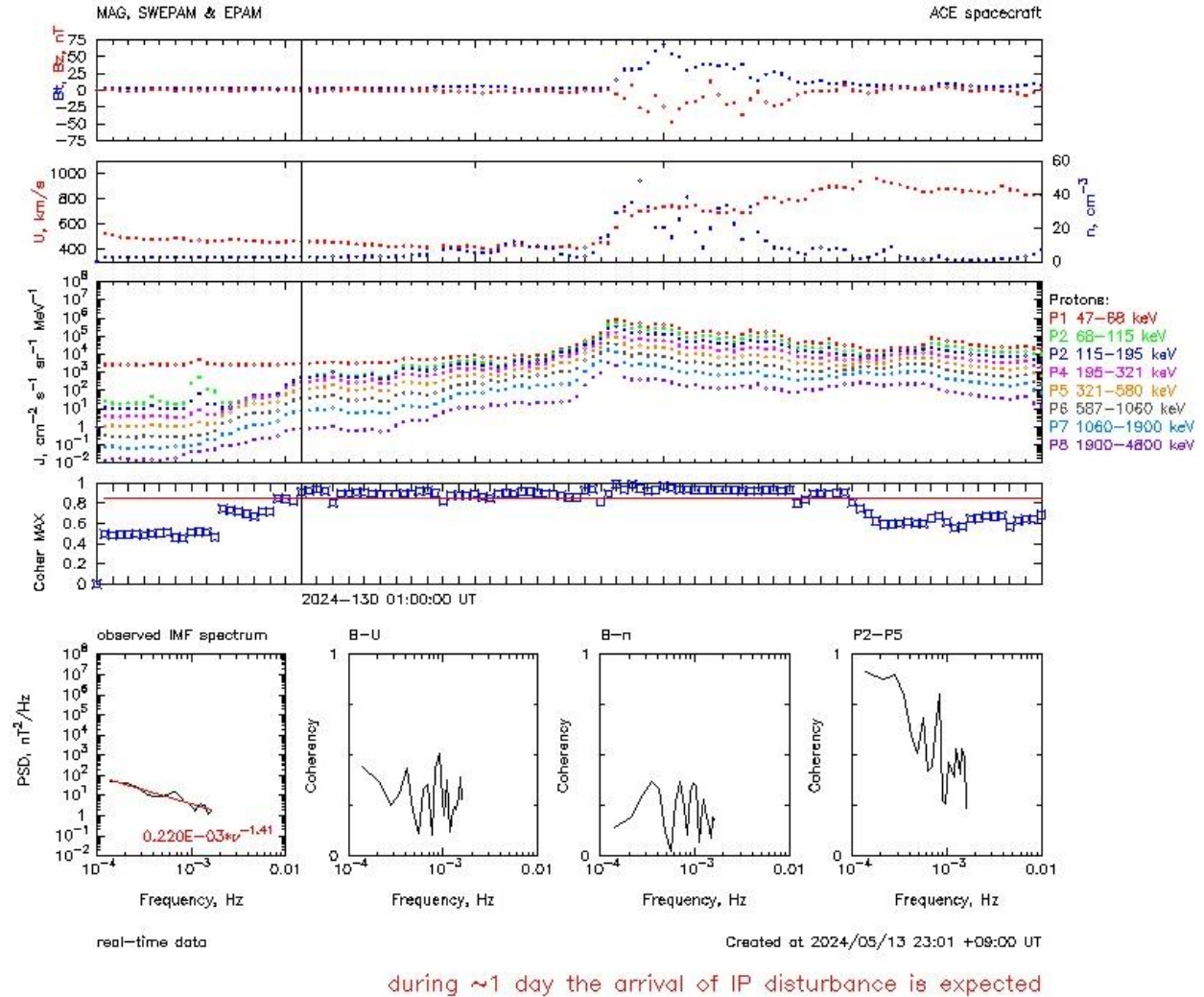

Figure 8. Variations in the IMF modulus *B* and the *Bz* component (top panel), the solar wind plasma velocity *U* and density n (second panel from the top), the low-energy CR flux *J* (third panel from the top), the maximum value of the coherence coefficient between measurements of the *J* energy channels P2 and P5 (fourth panel from the top, the red horizontal line indicates the critical level) depending on time. The vertical lines show the current time. A legend is given for the differential CR energy channels. Four bottom panels from left to right present the current values: the density of the IMF power spectrum and the power function approximating it; the coherence coefficients between *B* and *U*, *B* and *n*, and between P4 and P5

lead to the occurrence of fluctuations a sufficiently long time before the arrival of ISW. Indeed, the first maximum values of coherence between the channels of recording of proton fluxes P2 and P5 with energies 115–195 and 1060–1900 keV respectively, exceeding the critical level were observed at 01:00 UT on May 9, 2024, 36 hours before the arrival of ISW at ACE SC and remained above this level until 22:00 UT on May 11, i.e. until the SW parameters were disturbed (see Figure 8).

Thus, based on ACE SC measurements of CR fluxes with a lead time of 36 hours, a forecast was given for the arrival of a large-scale SW disturbance of the ISW type at the Earth orbit on May 10, 2024. Our experience shows that in such cases the accuracy of the forecast is ~80 %.

Note also that SHICRA SB RAS has been continuously monitoring near-Earth space in real time for many years. For this purpose, measurement data is employed from ACE SC and on the CR intensity from the stations Yakutsk and Tixie Bay. All calculations are performed automatically once per hour, using the *cron* daemon program under the control of the Linux operating system. All output information, including measurement data and calculation results in graphical form, is available at [https://www.ysn.ru/~starodub/CosmicRayFluctuations/index.html].

CONCLUSION

The SW phenomena of different spatial scales have been studied: global (magnetic storm), local (TCV, substorm). Local phenomena are recorded in the daytime (TCV) and nighttime sectors (substorm). We have examined the formation of disturbances in the solar wind and their development in the magnetosphere. Using the example of a strong magnetic storm in May 2024, the result of a short-term forecast of the arrival of a large-scale solar wind disturbance of the ISW type at the Earth orbit with a lead time of 36 hours has been shown.

SHICRA SB RAS is ready to participate in international projects, as well as in collaborations with Russian scientific organizations in the field of space weather.

REFERENCES

Berezhko E.G., Starodubtsev S.A. Nature of the dynamics of the cosmic-ray fluctuation spectrum. *Bull. Academy of Sciences of USSR. Ser. Physics.* 1988, vol. 52, pp. 2361–2363.

Clilverd M.A., Rodger C.J., Thomson N.R., Brundell J.B., Ulich T., Lichtenberger J., Cobbett N., et al. Remote sensing space weather events: Antarctic-Arctic radiation-belt (dynamic) deposition-VLF atmospheric research Konsortium network. *Space Weather.* 2009, vol. 7, iss. 4, S04001. DOI: 10.1029/2008SW000412.

Cole K.D. Stable auroral red arcs, sinks for energy of *Dst* main phase. *J. Geophys. Res.* 1965, vol.70, iss. 7, pp. 1689–1706.

Cole K.D. Magnetospheric processes leading to mid-latitude auroras. *Ann. Geophys.* 1970, vol. 26, iss. 1, pp. 187–193.

Cornwall J.M., Coroniti F.V., Thorne R.M. Unified theory of

SAR arc formation at the plasmapause. *J. Geophys. Res.* 1971, vol. 76, iss. 19, pp. 4428–4445.

George H.E., Rodger C.J., Clilverd M.A., Cresswell-Moorcock K., Brundell J.B., Thomson N.R. Developing a nowcasting capability for X-Class solar flares using VLF radiowave propagation changes. *Space Weather.* 2019, vol. 17, iss. 12, pp. 1783–1799. DOI: 10.1029/2019SW002297.

Glassmeier K.-H. Traveling magnetospheric convection twin vortices: Observations and theory. *Ann. Geophys.* 1992, vol. 10, iss. 8, pp. 547–565.

Golikov I.A., Kolesnik A.G., Chernyshov V.I., Popov V.I. Mathematical model of the F2 region of the high-latitude ionosphere taking into account the thermal regime. *Bull. Yakutsk State University*, 2005, vol. 2, iss. 3. pp. 61–69.

Golikov I.A., Gololobov A.Yu., Popov V.I. Numerical modeling of the thermal regime of the high-latitude ionosphere. *Bull. North-Eastern Federal University*, 2012, vol. 9, iss. 3, pp. 22–28.

Golikov I.A., Gololobov A.Yu., Popov V.I. Modeling the electron temperature distribution in F2 region of high-latitude ionosphere for winter solstice conditions. *Sol.-Terr. Phys.* 2016, vol. 2, iss. 4, pp. 54–61. DOI: 10.12737/19424.

Gololobov A.Yu., Golikov I.A. Numerical modeling of the influence of IMF on the large-scale structure of the ionosphere taking into account the misalignment of the poles. *Bull. North-Eastern Federal University*. 2024, vol. 21, iss. 1, pp. 45–57. DOI: 10.25587/2222-5404-2024-21-1-45-57.

Gololobov A.Yu., Golikov I.A., Popov V.I. Modeling of the influennce of magnetospheric storm on the large-scale structure of the high-latitude ionosphere for winter solstice conditions. *Sol.-Terr. Phys.* 2025, vol. 11, iss. 2, pp. 88–98. DOI: 10.12737/stp-112202509.

Grigoryev A.V., Starodubtsev S.A., Grigoryev V.G., Usoskin I.G., Mursula K. Fluctuations of cosmic rays and IMF in the vicinity of interplanetary shocks. *Adv. Space Res.* 2008, vol. 41, iss. 6, pp. 955–961. DOI: 10.1016/j.asr.2007.04.044.

Hayakawa H., Ebihara Y., Mishev A., Koldobskiy S., Kusano K., Bechet S., Yashiro S., et al. The solar and geomagnetic storms in 2024 May: A flash data report. *Astrophys. J.* 2025, vol. 979, iss. 1, 26 p. DOI: 10.3847/1538-4357/ad9335.

Ievenko I.B. Effects of magnetospheric activity on the plasmasphere as inferred from observations of diffuse aurorae and SAR arcs. *Geomagnetism and Aeronomy.* 1999, vol. 39, iss. 6, pp. 697–703.

Ievenko, I.B. SAR-arc observation during the overlap registration of an energetic plasma with a plasmapause aboard the Van Allen Probe. *J. Atmos. Solar-Terr. Phys.* 2020, vol. 209, 105386. DOI: 10.1016/j.jastp.2020.105386.

Ievenko I.B., Alekseyev V.N. Effect of the substorm and storm on the SAR arc dynamics: A statistical analysis. *Geomagnetism and Aeronomy.* 2004, vol. 44, iss. 5, pp. 592−603.

Ievenko I.B., Parnikov S.G. Ground-based and satellite observations of the SAR arc in the MLT evening sector at the beginning of the magnetic storm on March 17, 2015. *Geomagnetism and Aeronomy.* 2020, vol. 60, iss. 6, pp. 737–746. DOI: 10.1134/S0016793220050096.

Kolesnik A.G., Golikov I.A. Three-dimensional model of the high-latitude F region taking into account the displacement between geographical and geomagnetic coordinates. *Geomagnetism and Aeronomy*. 1982, vol. 22, iss. 3, pp. 435–439.

Korsakov A.A., Kozlov V.I., Karimov R.R. Sudden phase anomalies of VLF radio transmitters signals (11.9 kHz) of RSDN-20 system registered in Yakutsk during 2009–2017. *Proc. SPIE, 27th International Symposium on Atmospheric and Ocean Optics, Atmospheric Physics.* Moscow, Russian Federation, 2021, 119167X. DOI: 10.1117/12.2603367.

Kozlov V.I., Starodubtsev S.A., Grigoryev V.G., Baishev D.G., Makarov G.A., Pavlov E.A., Karimov R.R., et al. Analysis of helio- and geophysical events in October–November 2021 from comprehensive observations of SHICRA SB RAS. *Sol.-Terr. Phys.* 2025, vol. 11, iss. 1, pp. 7–26. DOI: 10.12737/stp-111202502.

Kozyra J.U., Nagy A.F., Slater D.W. High-altitude energy source(s) for stable auroral red arcs. *Rev. Geophys.* 1997, vol. 35, iss. 2, pp. 155–190.

Kumar A., Kumar S. Solar flare effects on D-region ionosphere using VLF measurements during low- and high-solar activity phases of solar cycle 24. *Earth, Planets and Space.* 2018, vol. 70, iss. 29, pp. 1–14. DOI: 10.1186/s40623-018-0794-8.

Lazzús J.A., Salfate I. Report on the effects of the May 2024 Mother's day geomagnetic storm observed from Chile. *J. Atmos. Solar–Terr. Phys.* 2024, vol. 261, 106304. DOI: 10.1016/j.jastp.2024.106304.

Mizun Yu.G. *Polar Ionosphere*. Leningrad: Nauka Publ., 1980, 216 p.

Moiseev A.V., Popov V.I., Starodubtsev S.A. Comparative analysis of the propagation of magnetic variations and equivalent current vortices of geomagnetic Pc5 pulsations along the meridian and azimuth. *Geomagnetism and Aeronomy*, 2024a, vol. 64, iss. 4, pp. 548–566. DOI: 10.31857/S0016794024040093.

Moiseev A.V., Popov V.I., Starodubtsev S.A. Investigating azimuthal propagation of Ps5 geomagnetic pulsations and their equivalent current vortices from ground-based and satellite data. *Sol.-Terr. Phys.* 2024b, vol. 10, iss. 3, pp. 97–107. DOI: 10.12737/stp-103202412.

Petukhova A.S., Petukhov I.S., Petukhov S.I. Theory of the formation of Forbush decrease in a magnetic cloud: Dependence of Forbush decrease characteristics on magnetic cloud parameters. *Astrophys. J.* 2019, vol. 880, iss. 1, art. no. 17. DOI: 10.3847/1538-4357/ab2889.

Petukhova A.S., Petukhov I.S., Petukhov S.I. Forbush decrease characteristics in a magnetic cloud. *Space Weather.* 2020, vol. 18, iss. 12, art. no. e02616. DOI: 10.1029/2020SW002616.

Piersanti M., Oliveira D.M., D'Angelo G., Diego P., Napoletanj G., Zesta E. On the geoelectric field response to the SSC of the May 2024 super storm over Europe. *Space Weather.* 2025, vol. 23, e2024SW004191. DOI: 10.1029/2024SW004191.

Pilipenko V.A., Chernikov A.A., Soloviev A.A., Yagova N., Sakharov Y., Kudin D.V., Kostarev D., et al. Influence of space weather on the reliability of the transport system functioning at high latitudes. *Russian J. Earth Sciences.* 2023, vol. 23, ES2008. DOI: 10.2205/2023ES000824.

Ram T., Veenadhari S., Dimri B., Bulusu J., Bagiya M., Gurubaran S., Parihar N., et al. Super-intense geomagnetic storm on 10–11 May 2024: Possible mechanisms and impacts. *Space Weather.* 2024, vol. 22, e2024SW004126. DOI: 10.1029/2024SW004126.

Silber I., Price C. On the use of VLF narrowband measurements to study the lower ionosphere and the mesosphere–lower thermosphere. *Surveys in Geophysics.* 2017, vol. 38, iss. 2, pp. 407–441. DOI: 10.1007/s10712-016-9396-9.

Starodubtsev S.A., Transkii I.A., Verigin M.I., Kotova G.A. Intensity fluctuations of cosmic rays and of the interplanetary magnetic field in the region of interaction of solar-wind streams with different velocities. *Geomagnetism and Aeronomy*. 1996, vol. 36, pp. 241–245.

Starodubtsev S.A., Zverev A.S., Gololobov P.Yu., Grigoriyev V.G. Cosmic ray fluctuations and MHD waves in the solar wind. *Sol.-Terr. Phys.* 2023, vol. 9, iss. 2, pp. 73–80. DOI: 10.12737/stp-92202309.

Tavares M., Santiago M.A.M. What are traveling convection vortices? *Brazilian J. Physics.* 1999, vol. 29, iss. 3, pp. 524–528.

Vorobjev V.G., Yagodkina O.I., Katkalov Yu.V. Auroral precipitation model and its application to ionospheric and magnetospheric studies. *J. Atmos. Solar-Terr. Phys.* 2013, vol. 102, pp. 157–171. DOI: 10.1016/j.jastp.2013.05.007.

Weimer D.R. A flexible, IMG dependent model of high-latitude electric potentials having "space weather" applications. *Geophys. Res. Lett.* 1996, vol. 23, no. 18, pp. 2549–2552.

Wendt V., Schneider H., Banyś D., Hansen M., Clilverd M.A., Raita T. Why does the October effect not occur at night? *Geophys. Res. Lett.* 2024, vol. 51, iss. 7, pp. e2023GL107445. DOI: 10.1029/2023GL107445.

URL: http://eng.sepc.ac.cn/ (accessed February 10, 2025).

URL: http://www.intermagnet.org (accessed February 10, 2025).

URL: http://magdas2.serc.kyushu-u.ac.jp/station/index.html (accessed February 10, 2025).

URL: http://www.isee.nagoya-u.ac.jp/dimr/PWING/en/ (accessed February 10, 2025).

URL: http://stjarnhimlen.se/comp/tutorial.html (accessed February 10, 2025).

URL: ftp://ftp.swpc.noaa.gov/pub/lists/ace2/ (accessed February 10, 2025).

URL: ftp://ftp.swpc.noaa.gov/pub/lists/ace/ (accessed February 10, 2025).

URL: https://omniweb.gsfc.nasa.gov/ow.html (accessed February 10, 2025).

URL: https://www.ysn.ru/~starodub/CosmicRayFluctuations/index.html (accessed February 10, 2025).